Self-assembled Perylene Bisimides for water splitting devices

UNIVERSITY OF LIVERPOOL

Benjamin Greeves

March 2023

Supervisor: Prof. Alexander Cowan

Thesis submitted to the University of Liverpool in partial fulfilment of the degree of Doctor in Philosophy

Abstract

The ability to harness and store the energy supplied by the powerhouse of our solar system (our sun) has taken billions of years to develop, and is best exhibited by plant based organisms that dominate our natural world. It is hoped that artificial solar fuel generation can yield complex carbon-based sugars as exhibited in nature, or perhaps the classic fuels such as hydrogen, the very fuel which supplies our own sun.

Water splitting is a leading example of a solar fuel generating process, and yields two useful molecules in the form of hydrogen and oxygen. This thesis centres around a particularly interesting class of organic aromatic molecules known as Perylene Bisimides (PBIs), in a field that has been dominated by inorganic semiconductors since its inception. PBIs have been shown to be versatile constituents of solar devices in literature, but within this thesis there is a real emphasis on understanding what makes these molecules active, and how structure is the key.

PBIs are deployed as organic photocatalysts for hydrogen evolution, coupled with a platinum nanoparticle co-catalyst to perform proton reduction. A small library of different amino acid functionalised PBIs were chosen for this study, each with their own hydrophobicity and steric bulk which has an influence on their ability to form self-assembled structures in water. We uncovered a fascinating relationship between structure types observed in the UV-Vis spectra and the ability to evolve hydrogen. This structure type was found to be trackable through the pH range chosen for these experimental conditions, and even could be applied to those not originally chosen for the fitting conditions.

Having demonstrated which amino acid functionalised PBIs were able to evolve hydrogen due to a complex structural relationship, we endeavoured to relate this to photophysical processes using transient absorption spectroscopy. Using two PBIs from our photocatalyst study: one that was able to evolve hydrogen; and one that was not. We were able to reveal the relative lifetimes of the proposed active species for hydrogen evolution. In addition, our original hypothesis involving different structure types and relative states of mixing between electronic states was shown to have excellent agreement with our spectroscopic data. In fact, our long lived excited states that resulted in hydrogen evolution were shown to be due to the

formation of an excimer like state, due to the self-assembled structures that formed at a particular pH.

PBIs form large extended self-assembled networks that can help charge separate excitons and enable effective charge transfer and catalysis, which make them an excellent candidate for organic photoanodes to yield oxygen gas. Amino acid functionalised PBI (also used previously for photocatalysis) have been characterised as photoanodes for water oxidation with a Faradaic efficiency of 56 % in the initial device. A combination of structural and electrochemical techniques has allowed for the development of a new PBI-L based photoanode, which produced promising photocurrents for an organic thin film device (200 μAcm^{-2}). However, integrating a suitable water oxidation catalyst proved a serious challenge, with a lack of stability and self-oxidation plaguing the device.

Acknowledgements

First and foremost, thank you to everyone who has supported me throughout the PhD, it has been a long journey filled with ups and downs which has eventually led to this thesis.

Thank you to Alex for giving me the opportunity to call the Cowan group my home for the last four years. The faces may have changed over the years but it remains a real family and a great place to do science. Thank you for being the supervisor I really needed over the PhD, from time to time giving me a push to finish projects (and thesis') and being able to turn them into work I am really proud of.

Thanks again to the Cowan group past and present, without whom the lab and office would have been a much quieter experience.

Special thanks to my collaborators at the University of Glasgow, in particular Dr Daniel McDowall and Prof Dave Adams for providing the PBIs which made every day a lot more purple.

Thanks to all the squash ballers over the years, especially James Smith and Khezar Saeed who made those frequent squash trips a real highlight of the PhD.

Thank you to my family and friends who supported me throughout the PhD, as I couldn't have done it without you all.

A special final thank you to my wife Sophie for being there for me every day since we met, without her endless support (mental, motivational, and financial) carrying me through the PhD, to now dragging me over the finish line. Thank you for sticking with me through the whole process, which has now finally come to an end.

Abbreviations:

- CB- Conduction band
- COF- Covalent organic framework
- CS- Charge separation
- CT- Charge transfer
- CV- Cyclic voltammograms
- DS- Dye sensitization
- FE- Faradaic efficiency
- FE- Frenkel exciton
- FTO- Fluorine doped tin oxide
- GC- Gas chromatography
- GSB- Ground state bleach
- HER- Hydrogen evolution reaction
- HOMO- Highest occupied molecular orbital
- IPCE- Incident photon to current efficiency
- LSV- Linear sweep voltammetry
- LUMO- Lowest unoccupied molecular orbital
- NIR- Near infra-red
- NP- Nanoparticles
- OER- Oxygen evolution reaction
- PBI- Perylene bisimide
- PBI-X- Perylene bisimide with an amino acid sidechain
- PVP- Polyvinylpyrrolidone
- SAXS- Small angle x-ray scattering
- SB-CS – Symmetry breaking charge separation
- SE- Stimulated emission
- SWV- Square wave voltammetry
- TA- Transient absorption
- VB- Valence band
- WOC- Water oxidation catalyst

Table of Contents

Chapter 1: Introductory chapter

Solar fuels

The ability to store solar energy in the form of a fuel is perhaps one of the greatest challenges to ever face science. The sun is the powerhouse of our solar system and delivers a sustainable source of energy, which can be converted to electricity for an instant source of energy or stored in the form of chemical bonds as fuel. The ever-increasing demand for renewable energy is fuelled by a rapidly increasing global population, in addition to socioeconomic development and record high gas prices. The issue currently plaguing the solar industry is the lack of ability to efficiently absorb and store the incident solar energy that strikes the earth every single day. By its very nature this energy source is intermittent due to the earth's rotation around the sun, in addition to weather implications such as cloud cover reducing the light intensity on the surface. Therefore, the reality remains that harvesting this source of energy in the form of a chemical fuel or chemical feedstock, which can release the energy stored within its chemical bonds when required, is the limiting factor for the future of solar energy usage.

Water oxidation, half equation: $2H_2O \rightarrow O_2 + 4H^+ + 4e^-$ $\quad\quad\quad$ $E^O = 1.23V$ vs RHE

Proton reduction half equation: $4H^+ + 4e^- \rightarrow 2H_2$ $\quad\quad\quad$ $E^O = 0$ V vs RHE

Overall: $2H_2O \rightarrow 2H_2 + O_2$ $\quad\quad\quad$ $E^O_{cell} = 1.23$ V

Equation 1- Overall water splitting with potential difference defined to be +1.23V

Potential solar fuels include hydrogen (widely produced from fossil fuels) via water splitting,[1–3] alcohols via carbon dioxide reduction,[4–6] and less conventional nitrogen fixation products such as ammonia and hydrazine. Hydrogen is perhaps the most traditional fuel due to its wide usage throughout the chemical industry, albeit largely from non-renewable sources. Hydrogen combustion has the advantage of being considered a clean process, due to only evolving water vapour, and is also an energy dense fuel due to a highly exothermic reaction upon burning and its low atomic mass. A hydrogen fuel cell is an electrochemical device which makes use of the chemical fuel to yield electricity (figure 1). Hydrogen is supplied to the anode, with air at the cathode, which is separated by a membrane permeable to protons, and

a suitable electrolyte to carry charge. Figure 1 demonstrates how a seemingly simple cell design schematic can yield and immediate source of energy. The major potential application for this is in transport, replacing common combustion engines with fuel cells. However, the lack of readily available hydrogen, derived from a renewable source, limits the widespread usage.
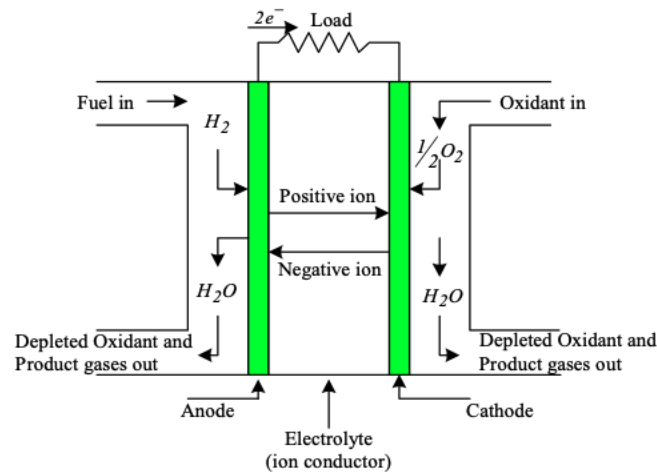
Figure 1- Hydrogen fuel cell from Nema et al.[7]

Semiconductors

The two main routes for solar fuel generation explored in this project are through the design and functionalisation of organic photocatalysis and photoelectrodes. However, there are other avenues available in both organic and inorganic device fields, such as using traditional photovoltaic solar cells in conjugation with an electrolyser to generate hydrogen.[8] Inorganic semiconductors have dominated the field since its inception in 1972 by Fujishima and Honda, who achieved electrochemical photolysis of water at a semiconductor electrode using TiO_2.[9] This publication has led to a vast quantity of research that has spun out into many directions,[10–16] from some systems developing multi-layered devices to effectively transport charges (figure 2),[17–21] to simpler devices containing a dispersed semiconductor in solution equipped with a suitable water oxidation catalyst.
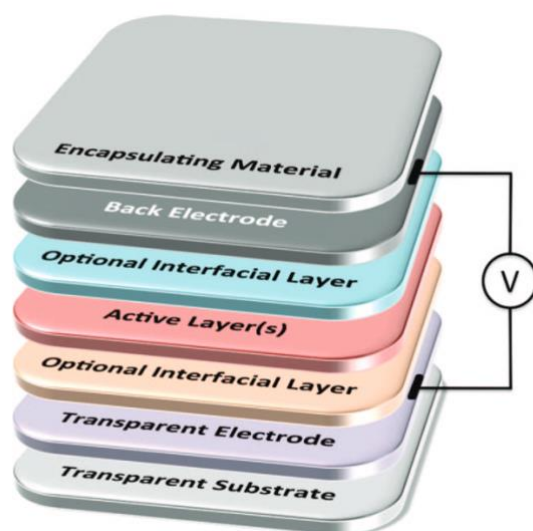
Figure 2- An example from literature of a multi-layered organic device schematic capable of performing water oxidation.[13]

Upon illumination with light of the correct frequency, a semiconductor can generate an electron-hole pair, known as an exciton. The correct frequency is required to bridge the band gap between the valence band (VB) and the conduction band (CB), and promote an electron into a higher energy state, leaving behind a hole, an area with no electron density in a position where an electron can occupy, with extraordinary oxidising power. For water to be oxidised it requires two holes to yield half an equivalent of oxygen (otherwise known as the oxygen evolution reaction or OER), with subsequent electrons being used to perform reduction reactions, [5,22,23] such as the hydrogen evolution reaction (HER). But due to the excitonic nature of organic semiconductors,[23] the electron and hole are tightly bound by coulombic forces of attraction, which must be overcome to enable effective charge separation and subsequent transport. Therefore, charge recombination is the likely pathway for many excitons generated by light absorption of the correct frequency, making the process inherently inefficient. Inorganic semiconductors often have higher dielectric constant than their organic counterparts, meaning excitons are less tightly bound, enabling greater charge separation. Despite this, organic devices boast superior scalability due to their lower costs, and ease of functionalisation. Dye sensitized cells often exhibit the best of both worlds, making use of organic dyes to absorb incident light to then transfer charge carriers to inorganic semiconductors such as the aforementioned TiO_2.[24–26]

In addition to low dielectric constants, another issue plaguing the field is the low charge carrier diffusion distances, which meant that excitonic species cannot travel large distances spatially without relaxing.[27] This distance has been shown to be shorter than the penetration of light through a material film, limiting the efficiency of the device further, and leading to concerns over thicknesses of films and how that affects light absorption properties. In a multi-layered device, the exciton is generated too far away from the interface between two materials known as a heterojunction, rendering its generation a wasteful process. In a homogenous device, this boundary could be a defect or surface of a material that encounters water. The point being that if the charges are not generated in the correct region of the system, it will be unlikely to yield successful charge transfer. Applying these processes to devices which intend to split water require that each of these criteria are satisfied. The device can absorb light of the correct wavelength, and generate charge electrons and holes, which are able overcome charge separation, and be transferred to a suitable catalyst. The most kinetically demanding process in water splitting is water oxidation, due to the need for two molecules of water and four hole equivalents to produce a single molecule of oxygen. In addition, the band gap of the chosen material must be sufficiently large to not yield thermally generated excitation, but not too large that only highly energetic UV-light can effectively excite it. Another consideration is the relative positions of the bands relative to that of proton reduction and water oxidation processes. Therefore, the choice and design of the material is paramount for it to split water successfully.

Organic Photoelectrodes

Within an electrochemical device there are two electron mediated processes which can occur, oxidation; the loss of electrons, or reduction; the gain of electrons. At the anode oxidation occurs giving rise to free electrons which flow around the circuit formed in the system. Within a photoanode electrons can be supplied due to successful charge separation as a result of photoexcitation with incident light. In the field of water splitting, water oxidation occurs at the photoanode due to the presence of holes at the interface upon illumination. At the cathode reduction occurs as the flow of electrons from the anode reach the positive terminal. Photocathodes can perform proton reduction to yield hydrogen, [28–31] but due to the kinetic complexity of water oxidation, the field of photoanodes takes precedent. The balance of

charge is maintained by a suitable electrolyte system, without which an imbalance would be created, and no charge would flow. In an ideal device one half would perform water oxidation, whilst the other performed proton reduction and thus yield complete water splitting. However due to the inherent difficulty of performing water oxidation, considerable efforts have been placed into boosting the photoanode side of the device.

Three common types of photoanode based devices are known.[15,32–36] Firstly, the simplest are n-type semiconductor-based devices (n-type due to mobile charge carriers being electrons, p-types are used for photocathodes) which use a single band gap to provide the photovoltage required to oxidise water, with a metal cathode (often platinum) is used as a counter electrode. Tandem based devices use two materials with different band gaps to perform both water oxidation and proton reduction, making use of both a photoanode and photocathode. Thirdly, there are many examples of dye sensitization (DS) within the field. These use organic based dyes to absorb the light, and then transfer electrons to a suitable semiconductor acceptor, liberating the hole to perform water oxidation at the dye interface. Beyond this PV based derivates are known, which use a mixture of materials (often inorganic based) to perform water oxidation. These different devices are illustrated by figure 3.
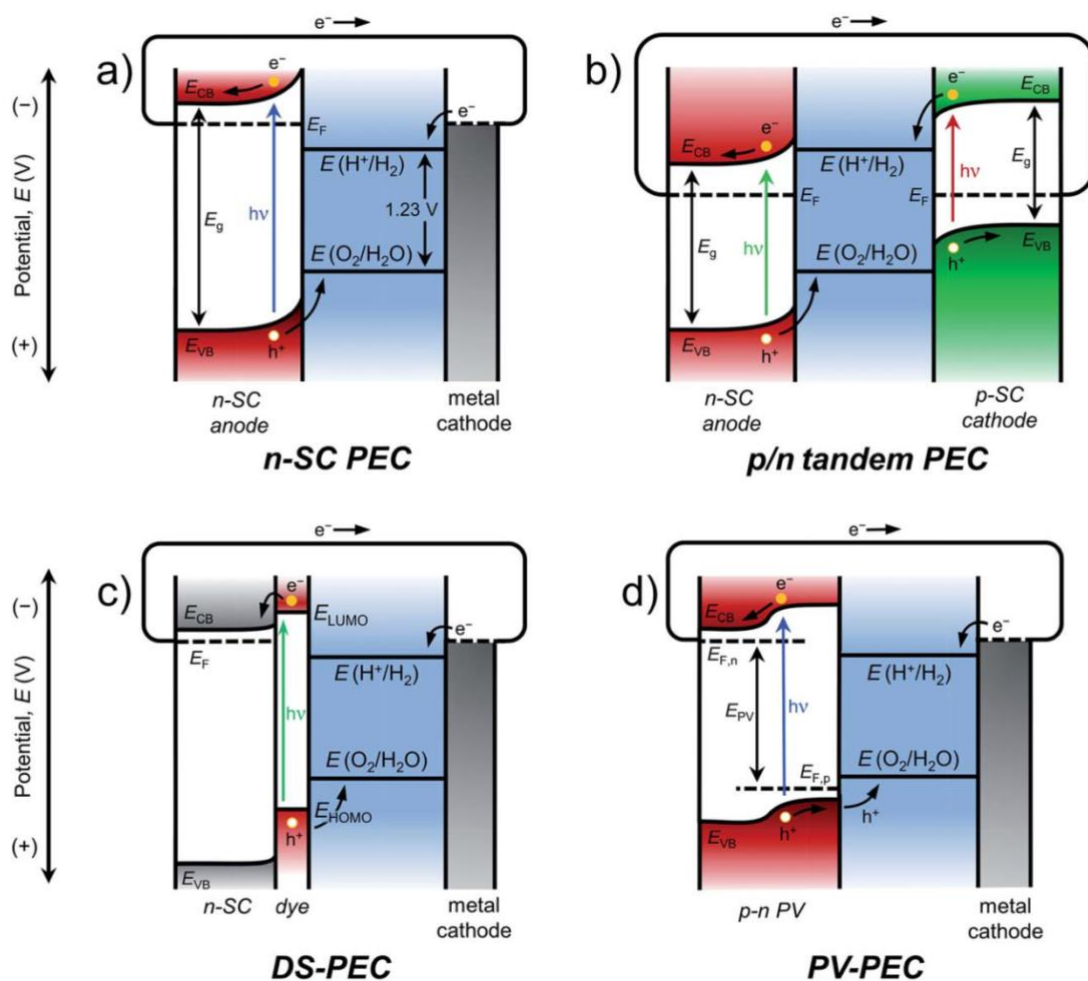
Figure 3- Comparing between different photoanode devices in the form of photoelectrolysis cells (PECs).[37]

Some notable examples include a polymer bulk heterojunction photoanode from Sivula *et al.,* which contained a donor acceptor mixture of naphthalene diimide (NDI) and benzodithiophene-based polymers.[34] Organic semiconductors can be polymeric or molecular in design, meaning there are both intra and intermolecular forces to consider when designing a device. Not only can long polymer chains with physical bonds entangle, but also significant pi-pi stacking can occur in large aromatic structures such as the NDI unit used. Jang *et al.* combatted the inherent instability of organic semiconductors in water by using an extensive metal-based protection layer (using Ni foils and Gallium indium eutectic) which was also able to enhance charge transport within the device.[38] Whereas Sartorel *et al.* preferred the use of a pentacyclic quinoid dye sensitized SnO_2 to drive oxygen evolution, making use of an integrated Ru catalyst.[39]

Literature example of organic based photoanodes attempt to boast superior performance metrics to one another, in order to establish their own niche within the field. The most important of which are the photocurrent density (change in current because of light on, light off measurements), Faradaic efficiency (to quantify how much of the charge is being used to form the intended product) and also incident photon to current efficiency (IPCE). These metrics are essentials universal within the field, and help determine the overall success of the device, and in this case how well it evolves oxygen. Some devices may boast high photocurrents on the mA scale, but may have low hole mobility meaning the liberated holes are unable to perform water oxidation, and instead simply oxidise the organic materials and degrade the device. In addition, many devices may require UV light to perform at optimum conditions, limiting the true scalability due to the narrow window of wavelengths available from true sunlight. The FE is perhaps the most valuable calculation that can be performed as it directly determines how much of the photocurrent is being used to evolve oxygen, but due to the total concentration of oxygen being produced being very low in some cases, quantification can be a challenge. A so called 'generator-collector' method is often used in these cases,[40–42] allowing for a direct comparison of charge passed in both working electrodes systems for the reactions of water oxidation and oxygen reduction.

The UV-Vis spectrum of a desired light absorbing material is of paramount importance when trying to understand how a material behaves when it encounters light. In order to absorb the light of a selected wavelength there must be an available transition. Organic chromophores used in as light absorbers commonly contain a large quantity of double bonds, and aromatics to absorb a large amount of light in the visible region. Once the chromophore absorbs a photon and enters the excited state, there may be a subtle change in the resultant UV-Vis spectrum as a result of the population in the excited state having a difference in light absorbing capabilities. This can result in a change in the UV-Vis spectrum, either a negative or positive feature. The nature of excited species can be probed further using other spectroscopic techniques, such as transient absorption spectroscopy (TAS), which can provide the lifetimes of excited species and how they contribute (or not) to eventual charge separation and transfer. The ability to harvest light is an important metric in calculating the

incident photon current efficiency (IPCE) of a device, allowing for other efficiencies like charge transfer to be calculated as a result.

Successful photoanodes often require optimisation to more efficiently evolve oxygen. This can range from improving the light harvesting by using a thicker layer, or by performing synthetic modifications. Addition of a water oxidation catalyst (WOCs) is often crucial to the device's overall efficiency due to the lack of driving force often exhibited by organic devices for water oxidation, because of low photovoltage and a need for applied bias. In theory, many materials can perform water oxidation with 1.23 V applied, but the activation energy for such a reaction is too high for the step to feasibly occur. A suitable water oxidation catalyst can lower the activation energy for this process, despite a lower driving force. Despite the significant drive to move to organic based semiconductors to reduce costs, many leading WOCs define used in literature still use expensive platinum group metals such as IrO_x and RuO_x. This is in part due to their unparalleled stability at extremes of pH, but also unrivalled activity with relatively simple preparation. Acid stability is somewhat unique to IrO_x based complexes which have been shown to survive many cycles with little degradation and loss of performance. So, while it may be possible to move away from more traditional metal-based semiconductors as light absorbers, at this point the success of many devices still hinges upon the use of Iridium, a wildly expensive and rare element.

Multi-layered devices are just one option when it comes to trying to overcome the myriad of problems that one must overcome to design successful system. Electron transport layers and hole transport layers are often used to enable enhanced transport, with ZnO often used as an electron transport layer in a multitude of solar devices.[21] This can lead to energy diagrams becoming rather complicated with many steps occurring in sequence for successful charge transfer to be shown via ever popular layer diagrams (figure 4). Despite the convoluted diagrams what is clear is that there are many intricate steps and considerations which go in to optimising a successful device.
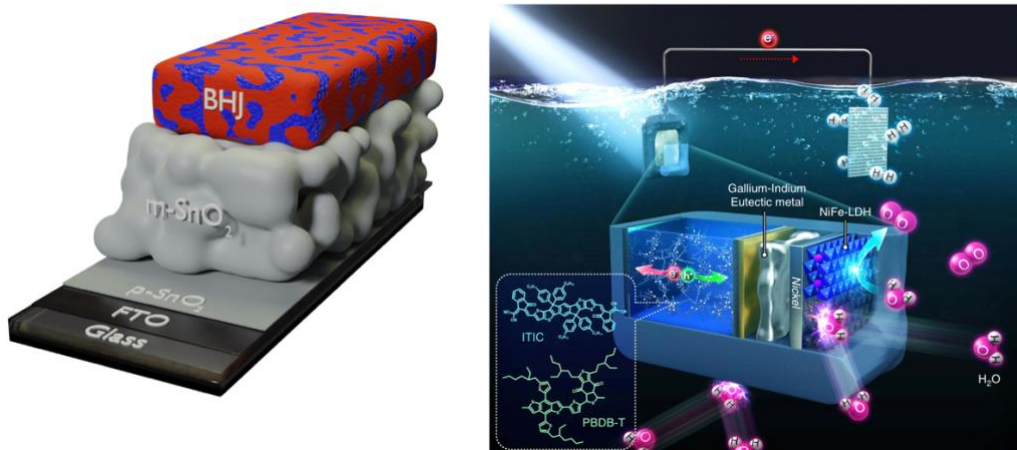
Figure 4- Images from literature of multi layered devices.[32,38]

Photocatalysts

Many organic semiconductors used as photoanodes can also be applied as light absorbers in photocatalytic evolution of hydrogen and oxygen, in addition to the aiding the decomposition of harmful pollutants and waste products.[43–45] In principle many these systems are like their photoanode counterparts, simply without an external circuit and therefore any applied bias. Common examples within the field include porphyrins,[46–48] perylenes,[49] graphitic carbon nitride,[50] phthalocyanines,[51–55] or covalent organic frameworks (COFs). Once again these are often large aromatic chromophores that also dominate the photoanode field. The history of photocatalysis is slightly different however, beginning with catalysts in a homogeneous state, before moving to a more support-based structure using polymer or silica gel.[56] The current state of the art centres around using nanostructuring to enable enhanced charge separation and transfer. Nanostructuring entails the design or control of the architecture of the material, leading to dimensional control (can be 1D, 2D, or even 3D). This introduction will largely focus on organic particles dispersed in solution. Other examples include heterojunction based photocatalysts with multiple band gaps. (figure 5)
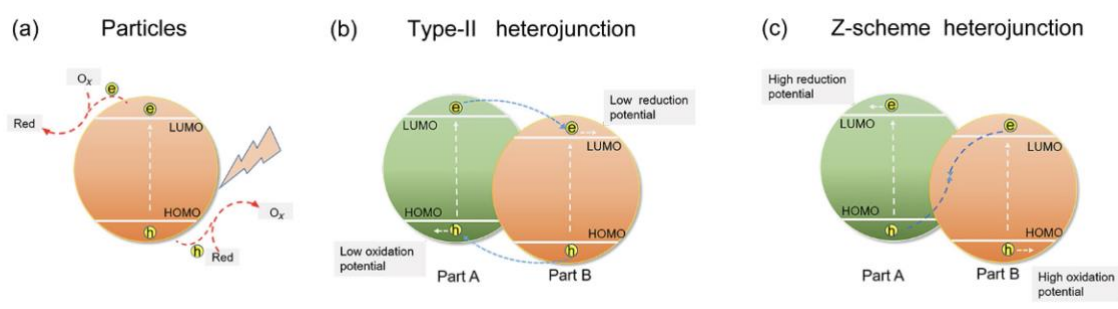
Figure 5- Schematic diagram from literature displaying different approaches to forming organic photocatalysts. Reproduced with permission.[57]

Organic photocatalysts for water splitting are often suspended or dispersed within a water-based medium, in addition to a suitable catalyst and often a hole scavenger. For the desired HER a suitable proton reduction catalyst would often be platinum,[58] either in the form of nanoparticles or a more reactive substrate. The role of the hole scavenger in theory is simple, as it acts as a sacrificial electron donor and combines with a hole generated upon illumination, to liberate a photoexcited electron. But the choice of hole scavenger can often be complex, and even yield different reaction times and mechanisms.[59] Some examples of hole scavengers include alcohols such as methanol or ethanol, EDTA, acetic acid and salicylic acid. Due to the acidic nature of a number of these compounds they will inherently influence the pH of the photocatalytic mixture, and therefore the pH sensitive proton reduction reaction itself.

Due to the lack of electrical contacts to form an electrode, the catalyst surface itself must act as the reaction centre for redox mediated reactions and be able to transfer charges to the suitable catalyst. The reactive species itself comes from the excited photocatalyst, often in the form of a singlet excited species or triplet species. The initial excited species can also form reactive intermediates such as radicals. Radical anions are likely to transfer their additional electron due to their highly reductive properties, whereas radical cations will seek to be reduced themselves and return to a neutrally charged state. The timescales of these reactions are typically on the ultrafast timescale, and require intense study using TAS.

For a successful reaction the active species must live long enough to pass on its charge to the next stage of the reaction, whether this is a neighbouring molecule or an eventual catalyst. Therefore, the design of how these neighbours interact is a key consideration, as the molecules are often not suspended alone in solution, but in fact for molecular aggregates that influence the aqueous media that solvate them. Organic molecules are known to self-assemble and aggregate together, due to the intensely hydrophobic aromatics which act as chromophores encouraging networks of pi-pi stacking (in addition to Van der Waals and hydrogen bonding networks), and liberating water molecules into the bulk of solution. The nature of these aggregates can influence hydrogen evolving capabilities of the dispersions,[49] leading to complex structural relationships which can be probed or stimulated by external

sources such as sonication.[47] Because of this delicate relationship there is a large emphasis on the synthesis of photocatalysts with high purity, free of any reactive agents which may influence assembly or catalysis.

The typical metric for measuring the success of a photocatalyst is the rate of evolution per hour per gram of material used (from $mmol\,g^{-1}h^{-1}$ or $\mu mol\,g^{-1}h^{-1}$). In our water splitting devices we are looking for a yield of oxygen or hydrogen, depending on which of the half equations is being targeted. For overall water splitting coupled organic materials with complementary energy bands are required,[60] but at this point of research, sacrificial electron donors are still required to maintain the process. High throughput methodologies are often employed to test a wide variety of variables in a shorter space of time,[49,55,61,62] sometimes using robotics to perform the experiments.[63] While this research technique will not be available for every group working in the field, there is no denying the data driven approach which has led to leading rates of evolution for hydrogen.[63]

Figure 5- An image of the autonomous robot performing photocatalysis experiments. Taken from literature with permission.[63]

Organic photocatalysis for water splitting is a thriving field globally[57,62,64–67], but the loss of activity over time and the need for hole scavengers are both undeniable issues that need to

be solved for the application of larger scales.[68] Organic semiconductors present a myriad of structural moieties and chromophores which can be used to aid to separation and transport of charge, the biggest issue is the number of different variables that can affect how these molecules behave in the solution phase. A large section of the field is driven by ground-breaking hydrogen evolution rates, and perhaps less by understanding why processes or mechanisms occur from a structural and electronic perspective. This aspect will be explored further within this thesis.

Perylene Bisimides

Perylene Bisimides (PBIs, also known as perylene diimides or PDIs) are large aromatic molecules based around the perylene dyes, first used in the 1950s.[69] Due to their intense colour as a result of high extinction coefficients in the visible region, and appropriately sized band gap, PBIs have been used as organic semiconductors over the last 30 years. In addition, PBIs boast impressive thermal and photochemical stability, with a wide range of synthetic variation. Common synthetic routes centre around using perylene-3,4,9,10-tetracarboxylic dianhydride (PTCDA) a highly crystalline material, which can be functionalised with amines to form symmetrical imides.[70] Further substitution can occur at the bay or ortho positions,[70–76] typically via halogenation, which can then lead to more labile substitution of other functional groups.[70 70,77] As a consequence there are is a vast library of PBI based devices in the organic semiconductor field,[78–81] in addition to uses in sensors,[82] and even biochemistry.[83]
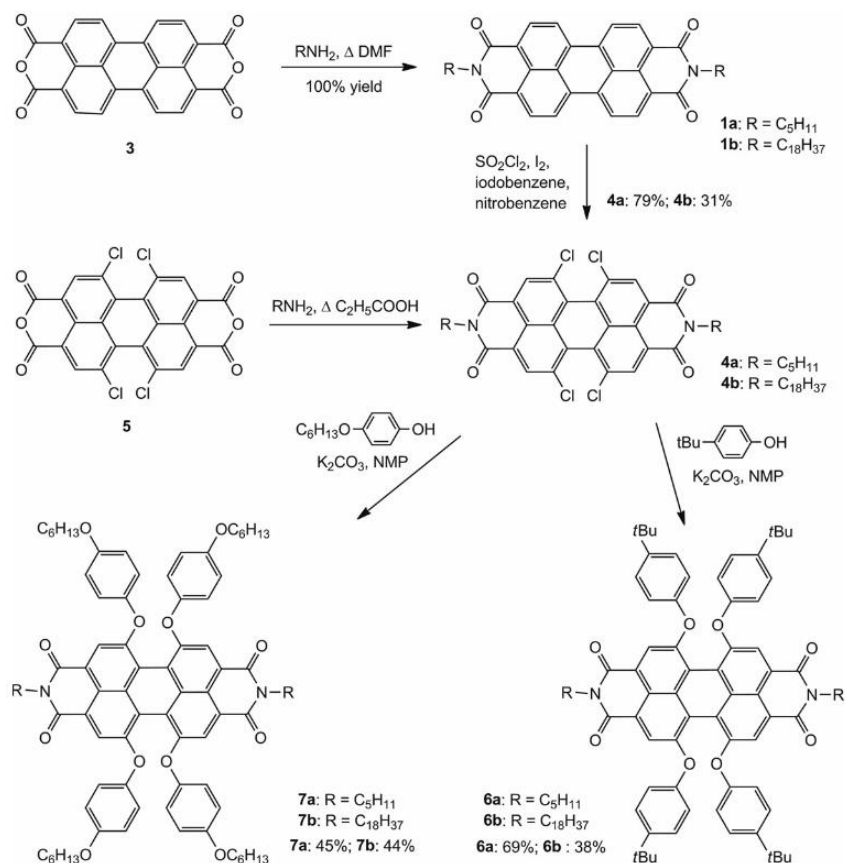
Figure 6- PBI reaction scheme which indicates some of the possible pathways available for additional functionalisation. Taken from literature with permission.[70]

The positions of the HOMO and LUMO are highly sensitive to the nature of the functional groups which are attached to the PBI core. The aromatic perylene core is highly electron rich, and also intensely hydrophobic, whereas the imide groups are strongly electron withdrawing, and can be further functionalised with hydrophilic groups to increase the solubility of the PBI molecule in water. A few examples of functionalisation from literature are shown in figure 6, and display the shift in position of the relative HOMO-LUMO gap. Despite functionality shifting the position of the HOMO-LUMO gap, the gap itself does not change dramatically without the introduction of significant bulk, or the use of a group that changes the chain of conjugation, and therefore the aromaticity across the core (such as a pyrrolidinyl group in figure 7).[84] Functionalisation at the imide position has less of an effect on the electron density at the core due to the break in the chain with the presence of the electron deficient nitrogen.
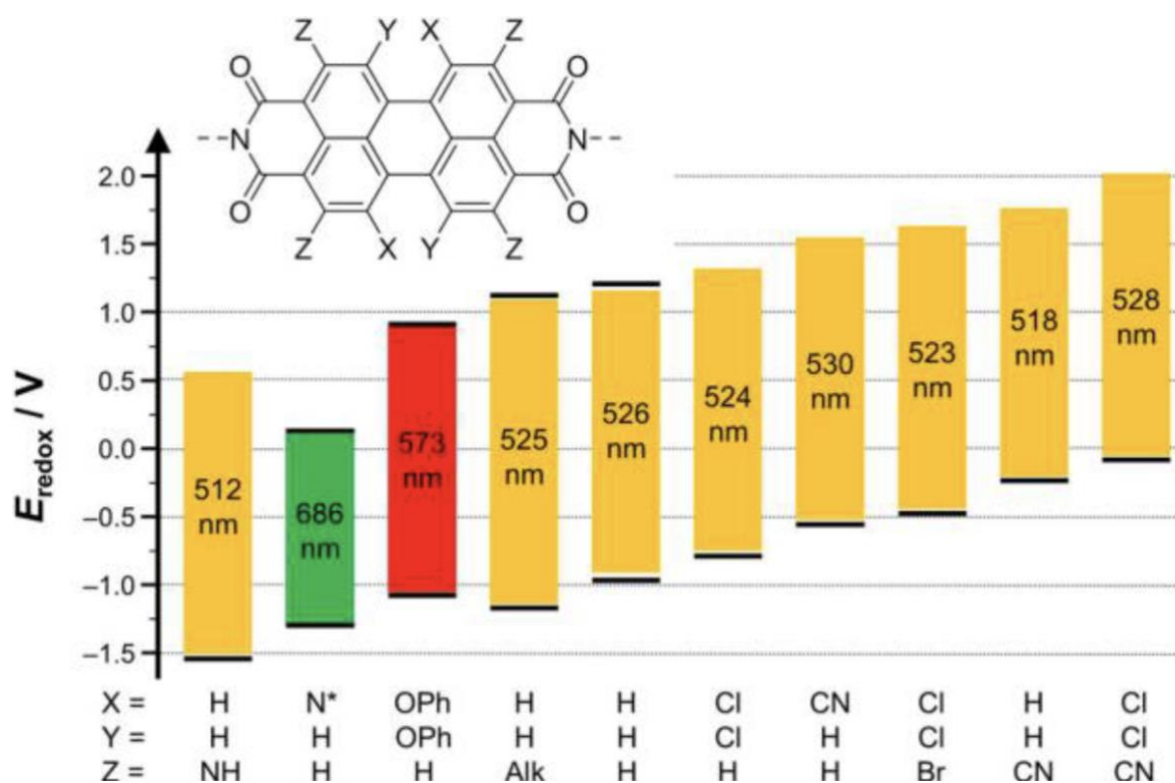
Figure 7 –An energy diagram of how different substituents on the PBI core can affect the relative energy gap and position, depending on position. N* denotes a pyrrolidinyl group. From Wurthner et al.[84]

UV-Vis spectroscopy and self-assembly of PBIs

The nature of the UV-Vis spectra of PBIs is truly fascinating, as it can be influenced by many competing factors which influence the transitions possible for the PBI core. Figure 8 displays a typical spectrum for a dilute PBI functionalised with an amino acid, and in addition a spectrum at a much higher concentration. The spectra are dominated by the S_0-S_1 transition at three distinct yet close lying vibronic modes (0-0', 0-1', 0-2') between 400-600 nm,[85] and contains the S_0-S_2 transition in the UV region. The relative intensities and width of these peaks are known to change greatly due to self-assembly. This phenomenon is known to affect all PBIs in solution to some degree (above 10^{-7} M),[85] due to the intensely hydrophobic cores contrasting strongly with the hydrophilic tails at either end of a PBI molecule (amino acids in this PBI example, figure 8). Water molecules that solvate the PBI molecules in solution are at a higher energy than those of the bulk, thus creating an energetic driving force to release these water molecules into the bulk. Aggregation is the process where individual PBI units are known to stack closely together to extended fibres, thus reducing the number of water molecules that are required to solvate the structure. This release is known as the hydrophobic

effect and is driven by a massive increase in entropy as a result of the water molecules in the solvation cage being released to the bulk. Self-assembly occurs upon the application of a suitable trigger, such as solvent switch, pH change, or salt addition.
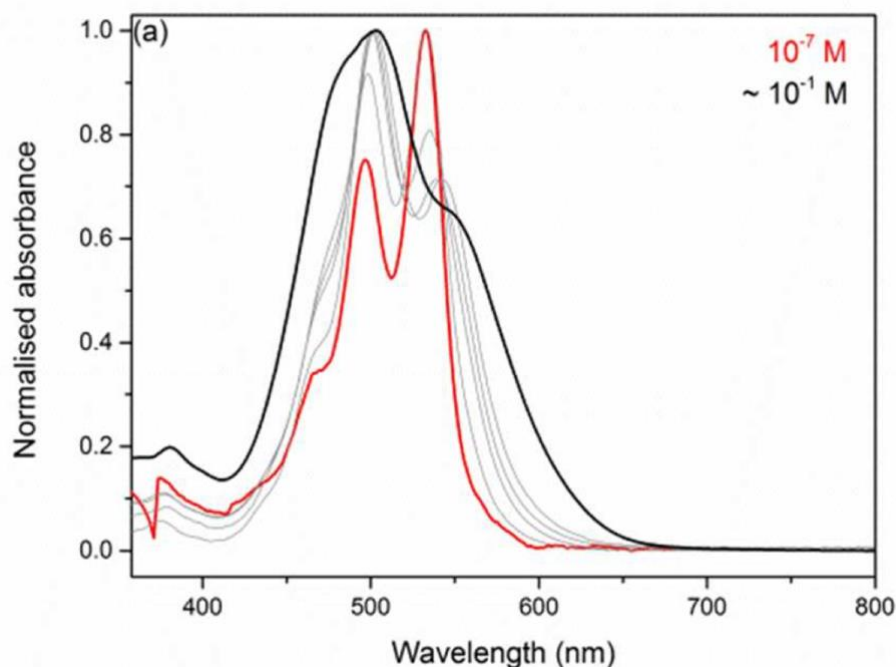
Figure 8- PBI-A UV-vis spectrum from literature at two different concentrations.[85]

Aggregation has a huge effect on the UV-Vis spectra of PBI solutions, as they become significantly broadened relative to a dilute monomer, with a clear shift in vibrionic intensity ratios. This shift can help describe the aggregates in classic Kasha theory, as either H or J aggregates, which are known to behave differently and therefore have attracted a huge amount of research interest.[86–91] The absorption bands of PBIs can either shift to shorter (hypsochromically) or longer (bathochromically) wavelengths, which indicate whether they are comprised of H or J aggregates respectively. In terms of aggregates this is perhaps best explained by figure 9, which displays how individual PBI molecules stack in a face to face (H-aggregate), or head to tail (J-aggregate) configuration. This classic theory of describing aggregates and their associated excitons has been challenged by Spano *et al.* over the last 10 years and will be explored further in chapter 3.[86,91–95]
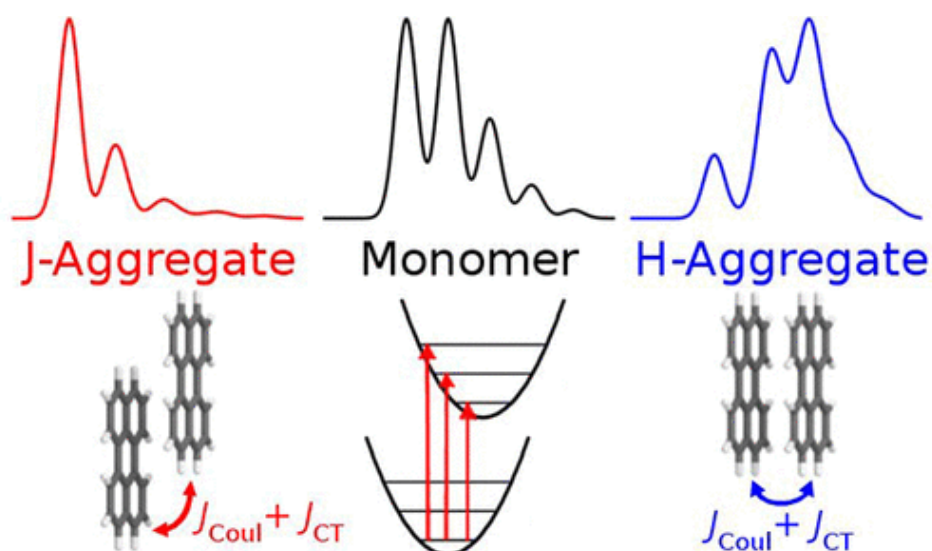
Figure 9- Diagram of H and J aggregate stacking patterns, along with the effects on the UV-Vis spectra. From Spano et al.[93]

Upon illumination with an appropriate light source PBI molecules are known to excite to the singlet state, a typically short-lived species with a broad feature in the UV-Vis spectrum. This unpaired singlet state has the potential to transfer to a triplet state, via intersystem crossing. However, in PBI excited species' a particularly low-lying species is formed,[84] leading to low triplet state yields. Instead, persistent radical species are known to form onto the PBI core, in the form of radical anion, cation, and dianions.[96–102] These species are also accessible via chemical and electroreduction,[23,84] with characteristic peaks in the UV-Vis spectra. In some cases, these radical species are so stable that they can exist in air, for minutes to hours of time after being generated.[85,103,104] Due to possessing an additional electron, radical anion and dianions are strongly reductive species. This reductive power makes them particularly appealing for a wide variety of optoelectronic applications, such as of performing charge transfer reactions to yield hydrogen in the HER (with a suitable co-catalyst).[49,105] However due to the low dielectric constants associated with organic semiconductors like PBIs the excited species are often excitonic in nature, and unable to diffuse over sufficient distances to perform reduction reactions in high yield. Self-assembled structures with many PBI units stacked together can enable this separation of charge, and also create a suitable diffusion network to deliver charges to suitable catalysts without physical bonds between them.
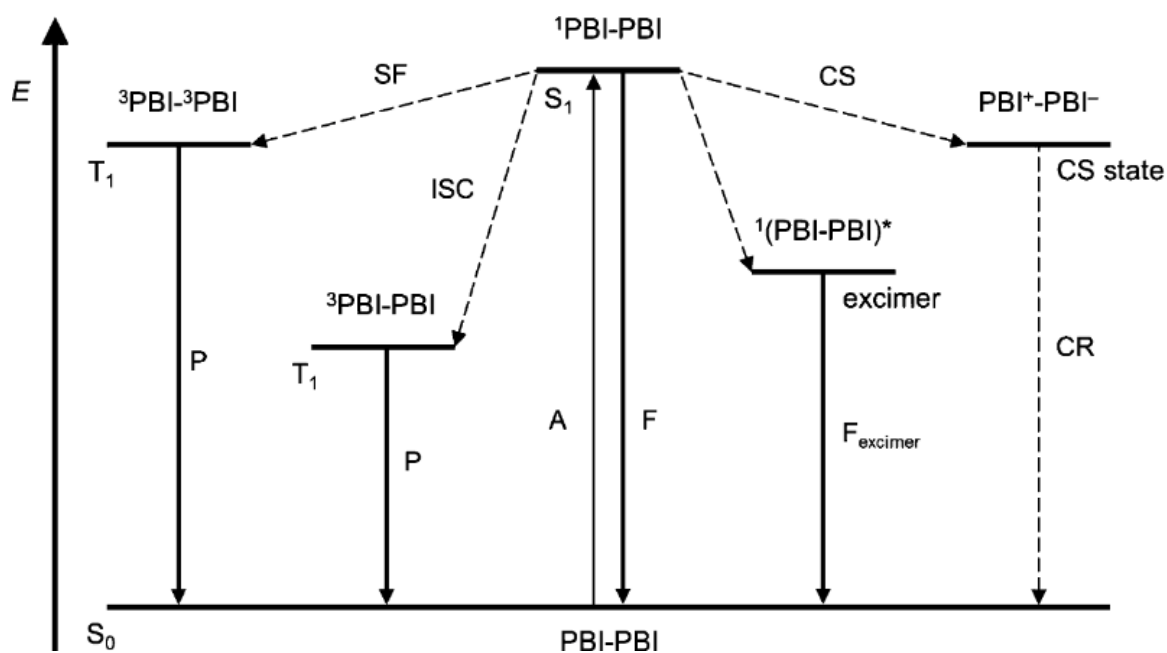
Figure 10- Diagram of possible excited state pathways for a PBI dimer. Taken from literature with permission.[84] *A, absorption; F, fluorescence; SF, singlet fission; ISC, intersystem crossing; P, phosphorescence; CS, charge separation; CR, charge recombination.*

Chapter 2: Exploring the role of self-assembly of perylene bisimides as photocatalysts in the hydrogen evolution reaction

This chapter is based upon a collaborative project with the University of Glasgow, published in Adv. Energy Mater. 2020, 2002469. PBI gelators were synthesised by D McDowall. SAXS analysis and sampling was performed by D McDowall. High throughput photocatalysis experiments were performed together. All electrochemical and spectroscopic measurements were carried out myself.

Introduction

Perylene imide-based photocatalytic devices have become increasingly common within the last 10 years, due to their low cost and highly absorbing organic cores, which provide many synthetic avenues for functionalization.[71,106–110] Despite their prevalence in many light absorbing systems, perylene based devices are often plagued by low quantum efficiencies,[13,111] due to excitonic recombination as a result of attractive coulombic forces that limit charge separation. As a result, significant molecular, and supramolecular design is required to produce a suitable device. This has produced significant diversity in the literature; with PBIs frequently employed as light absorbers in dye sensitized systems,[50,112–114] as part of donor-acceptor like structures,[75,115–117] or even by devising complex 1D nanostructures.[118–122]

Self-assembly plays a huge role in the ability of PBI systems to perform photocatalytic applications, due to the inherent tendency of PBI molecules to aggregate under various conditions or in the presence of triggers, giving opportunity for a massive variety in system design. Nanobelts,[123] nanoribbons,[124] nanohelicies,[78] nanofibers,[125,126] nanorings,[123,125] nanosheets,[127] and nanospheres,[123] are just a selection of the inventive descriptions of some of the PBI based moieties in the field. For hydrogen evolution there must be sufficient driving force for transfer of electrons from the excited energy state of the PBI system to the chosen catalyst, which is often platinum based.[105] PBIs can also be employed as photocatalysts for organic pollutant degradation.[80,128] This once again makes use of the highly absorbing PBI core to generate highly reactive charge carrying species; in this case holes, hydroxyl radicals or superoxide radicals.[45]

PBI's are often used as photosensistizers for TiO_2, to enable visible light activity, due to the well matched PBI excited state and TiO_2 band edge energies.[112] Chen *et al.* utilised synthetic modification to tune the band energies of the PBI core to maximise electron transport to TiO_2.[112] This allowed for efficient charge transfer to the TiO_2, and inhibited recombination by quenching the photogenerated holes with a large quantity of the sacrificial reagent triethanolamine, to yield photocatalytic generation of hydrogen. Marder *et al.* have performed a comprehensive review on functional modifications of PBIs and hypothesise that, in general, functionalisation of the bay area has the greatest effect on the electronic properties, and the imide position has a greater effect on the self-assembly and solubility.[71] For example electron withdrawing or donating groups attached to the bay positions can shift the relative positions of the HOMO and LUMO, thereby adding an extra layer of complexity when designing systems for photocatalysis.[72,129] Engineering the band gap can also change the absorption profile of the system, as many PBIs have been shown to be almost exclusively UV active or require multiple photons of different wavelengths.[130]

Recent reports of highly reducing charge separated radical anions generated through multi-photon processes have also been studied, such as the $(PBI^-)*$ or $(PBI^{2-})*$ generated by the sequential absorption of 2 or 3 photons in a PBI structure respectively.[130] The formation of excitonic species hinders the spatial separation of charge formed upon illumination, combining a charge separated PBI species with self-assembly allows for transport of these charges, due to the close proximity of neighbouring PBI cores as a result of extensive pi-pi stacking. Xie *et al.* have published a PBI based photosensitizer which absorbs three photons of different wavelengths to form the highly reducing $(PBI^{2-})*$ species, which can then inject an electron into TiO_2 nanoparticles (loaded with platinum) to yield hydrogen at an impressive rate of 1216 $\mu molg^{-1}h^{-1}$ (figure 11).[130] This was achieved 'in the absence of aggregation' by anchoring the PBI units to the TiO_2 nanoparticles,[130] meaning that it is possible to form highly active systems without the need for self-assembly, but it is likely that highly reducing excited anions will be required. A phosphoric acid functionalised PBI used a 'built in' electric field to enable enhanced charge separation along PBI nanofibres,[131] and this yielded an incredible 11.7 $mmolg^{-1}h^{-1}$ and quantum yield of 2.98 %. While there is no mention of the presence of

any PBI radical anions there was clear evidence of a synthetic methodology that has helped direct the self-assembly to enable electrons to travel through the stacked PBI molecules.
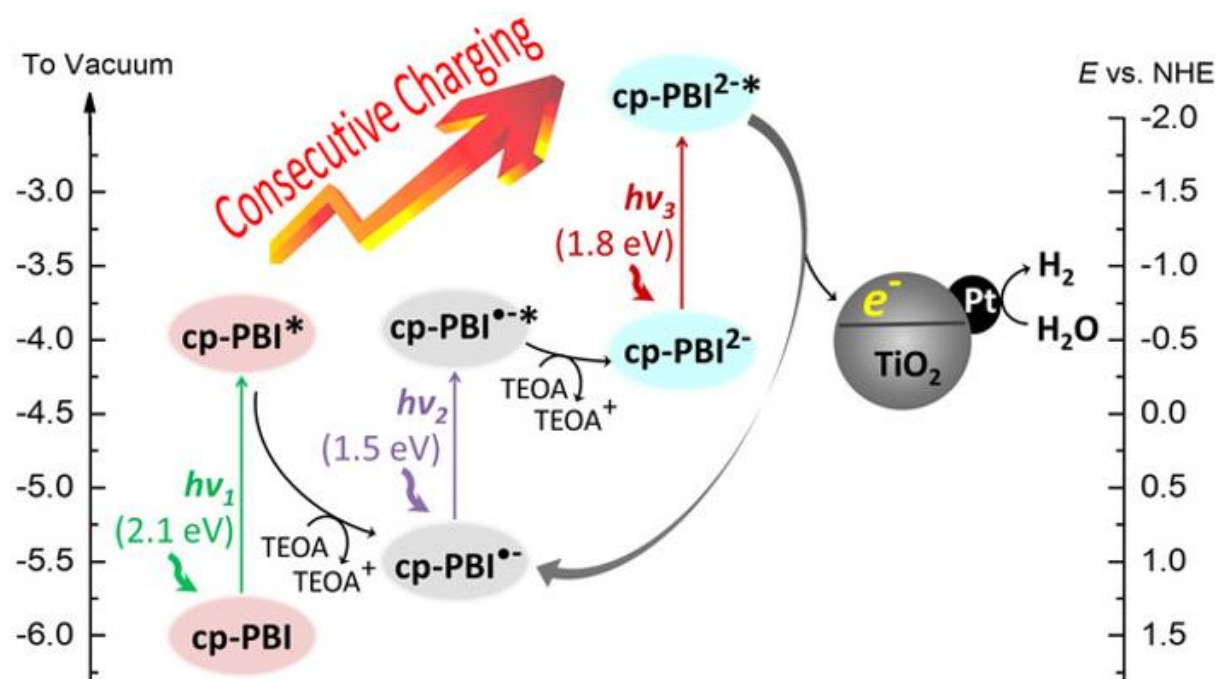
Figure 11- Diagram of the multi photon process involved in forming the excited (PBI^{2-})* radical dianion, which has sufficient reducing power to inject electrons into TiO$_2$. Reproduced from Xie et al.[130]

Stupp *et al.* have produced a number of perylene imide based photocatalysts for hydrogen evolution.[132–137] Despite being asymmetrical, the perylene monoimides (PMI) structures also self-assemble to form ribbons with a high surface charge, and yield hydrogen with dependence on the pH of the solution.[138] The importance of pH for perylene imide based systems was once again highlighted by Stupp, where a simple pH switch (and appropriate catalyst) led to a difference in the self-assembly pathway, which enabled either proton reduction or carbon dioxide reduction.[136] The PMI design was continued with a polymer chain of a variable length, which was also found to affect the rate of hydrogen evolution.[134] As expected the proposed mechanism went via exciton formation, followed by electron transfer from the ascorbate hole scavenger to yield the radical anion.[134] This mechanism was probed further in combination with Spano *et al.* ,[133] who through calculations detailed how mixing of the Frenkel exciton (FE) and charge transfer (CT) bands can lead to enhanced charge separation by effectively screening the charge to overcome the coulombic attraction between an electron and hole (figure 12). This separation was proposed to allow for an electron and

hole to reside on different neighbouring PMI molecules, as a result of extensive self-assembly which underpins this phenomenon.[133] Having separated the charges effectively the electron was then transported through the PBI structure to the chosen nickel-based catalyst. This hypothesis was underpinned by a body of work on aggregated systems by Spano over the last 10 years.[86,88,91,92,94,95,133,139,140]
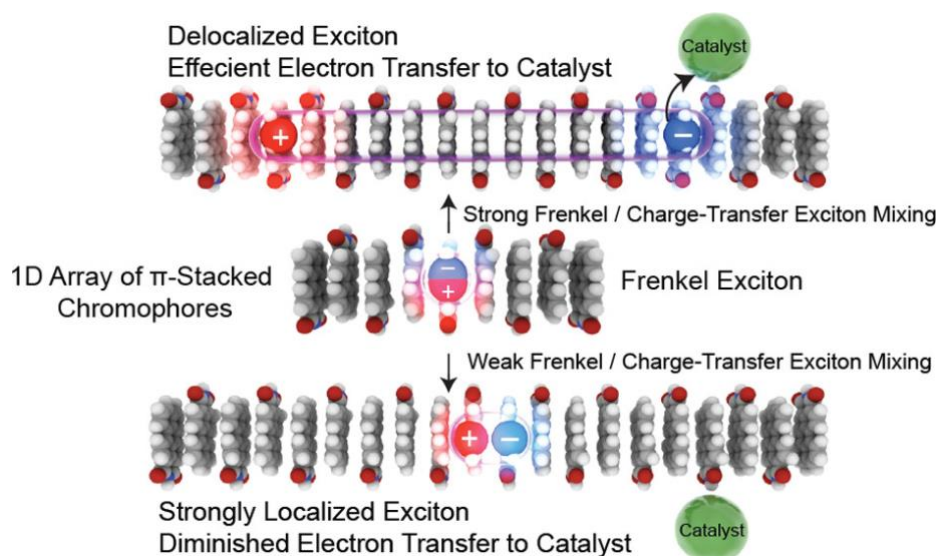
Figure 12- Diagram to illustrate how the extent of mixing of the FE and CT bands can determine the strength of charge separation and effective transfer to an appropriate catalyst. Reproduced from Spano et al with permission.[133]

The Glasgow and Liverpool teams previously examined some amino acid functionalised PBIs in great detail, in particular PBI-A.[85,104,122,141–145] . There has also been one report of PBI-F as a hydrogen evolution photocatalyst by Nolan *et al.* who found a striking pH dependence, which correlated with the extent of self-assembled structures in solution, and peaked at pH 4.5.[105] Draper *et al.* investigated the production of the radical anion and its role in transferring charge through a photoconductive PBI film,[104] using the same library of amino acids used in the high throughput study detailed in this chapter. An interesting lack of correlation between radical yield and conductivity was uncovered, and it was hypothesised that the formation of the dianion was responsible for the most active PBI samples however this has not been directly evidenced and the role of supramolecular structure in enabling activity remains unclear. Here we report (i) an expansion of the photocatalytic studies to the full library of PBI-amino acid

samples available and (ii) an assessment of the factors controlling photocatalytic activity, a topic which is further explored and expanded upon in a subsequent chapter.

High throughput photocatalytic study of amino acid functionalised PBI dispersions

Here the initial photocatalysis study centred around 8 PBIs functionalised with a different amino acids in the imide position. The 8 PBIs were dispersed in basic water (2 equivalents of sodium hydroxide) along with methanol as a hole scavenger, in addition to polyvinylpyrrolidone (PVP) capped platinum nanoparticles (made by Daniel McDowall at the University of Glasgow) to act as the proton reduction co-catalyst. Methanol was chosen to supply electrons sacrificially to enable charge separation in these typically exciton-forming species, and crucially does not significantly alter the pH of the dispersions upon addition. However, due to the inherent difference in polarity to water there were structural and photophysical implications, especially upon increasing hydrophobicity due to self-assembly. Previous control experiments performed by Dr M Nolan investigated the PBI concentration of the dispersions for catalytic activity, and we selected a concentration of 5 mg/mL (~0.01 M) due to a compromise between activity and extent of self-assembly.

The photocatalytic testing made use of a high throughput setup. While not fully automated this setup enabled rapid sample preparation and data generation which would otherwise have taken months. The initial PBI dispersion preparation was performed off-line, before capping and purging with nitrogen for 3 hours (figure 13). Once purged, the samples were transferred to the solar simulator, equipped with a roller bed, for illumination and the headspace was analysed with an auto-sampling GC.

Figure 13- (Top) Image of the purging of many PBI samples at once, before being transferred to the solar simulator. (Bottom) Image of the sample preparation of PBI dispersions. Each sample was 5 mg/mL PBI, with 20 (v/v%) methanol and contained platinum nanoparticles (1 wt.%). The samples in picture were each at a different pH and therefore display different levels of aggregation.

A range of pHs were chosen for these experiments in order to showcase the phenomenon of aggregation within PBI dispersions. At pH 10 PBIs are known to exist as short aggregates, whereas at pH 2 incredibly viscous assembled structures are present. Our intention was to track the evolution in the PBI structure and discover how it correlated with activity in the hydrogen evolving reaction (HER) with a number of different PBIs. The hydrogen evolution results for the PBIs in the initial study is shown in figure 14, with the molecular structure also depicted to illustrate the different individual functionality of each chosen amino acid.
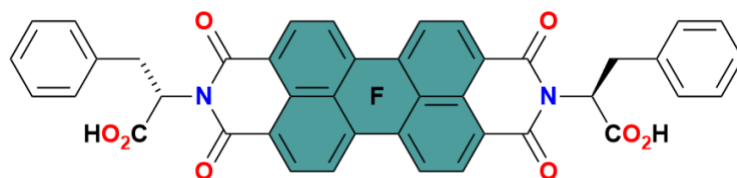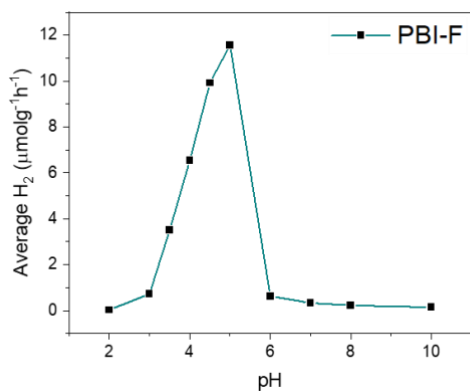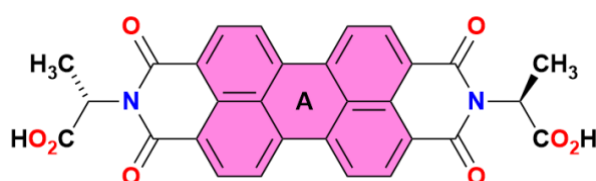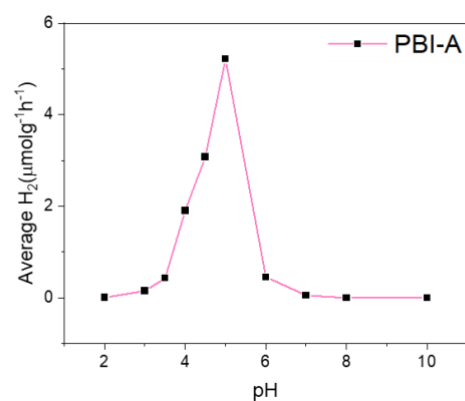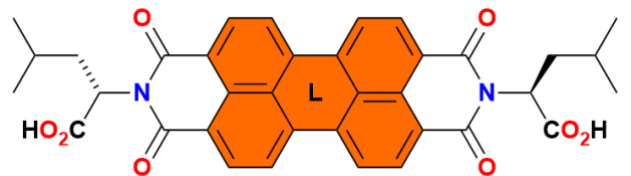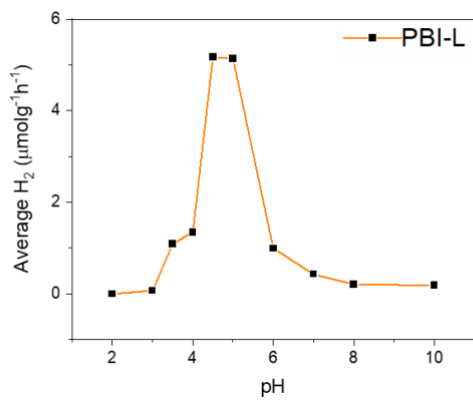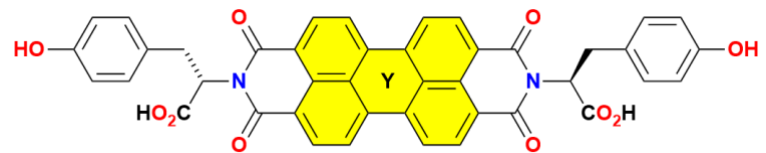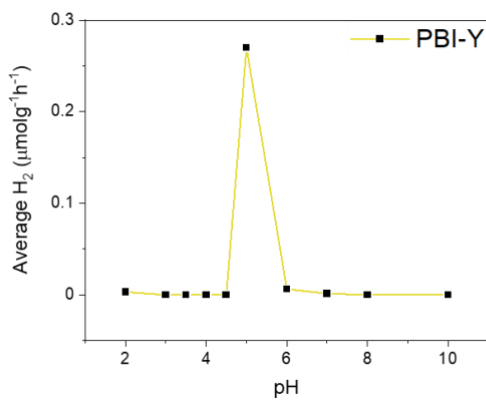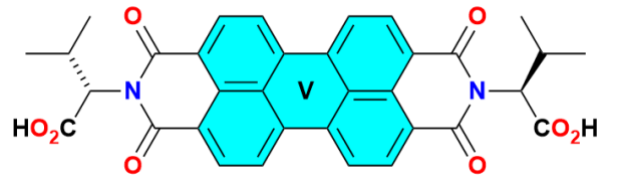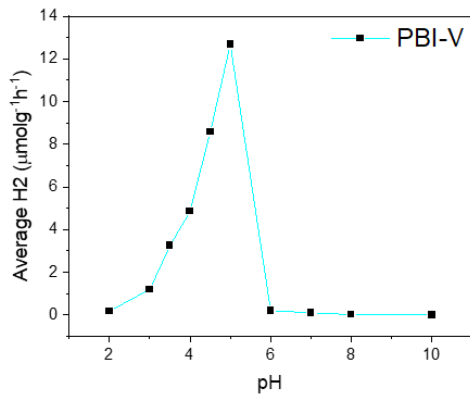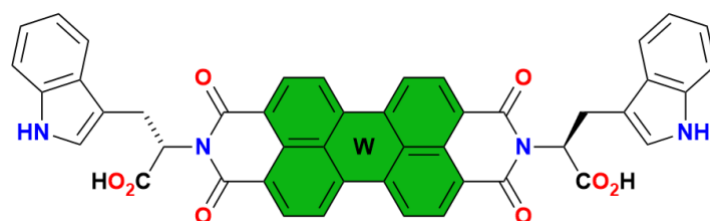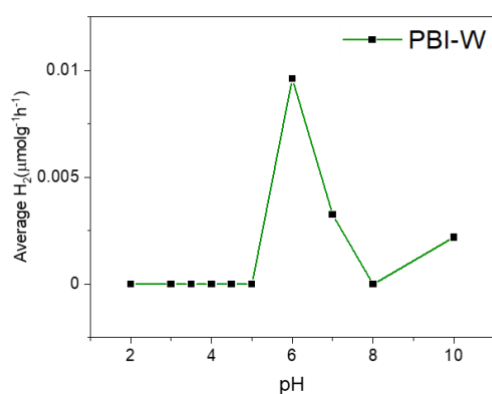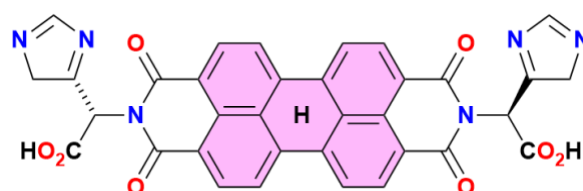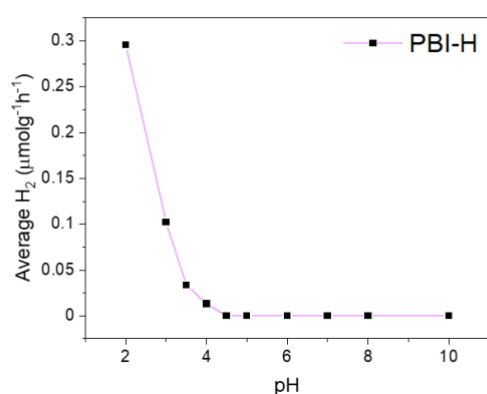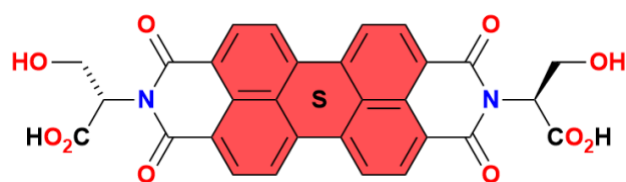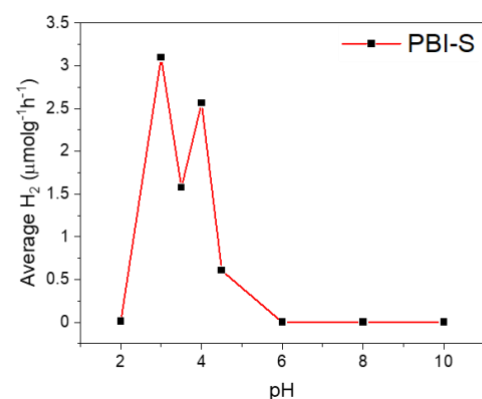
Figure 14- H₂ evolution plots for each PBI dispersion across the pH range in the study, and colour coded PBIs molecular structures with different amino acids. Amino acid single letter notation is shown in bold on the PBI ring. Constant methanol concentration of 20 (v/v%) used throughout.

Photocatalytic hydrogen evolution was measured in appreciable amounts (> 1 $\mu molg^{-1}h^{-1}$) for all but three PBIs, which were PBI-Y, PBI-H and PBI-W. Of these PBI-W had a maximum evolution rate of 0.01 $\mu molg^{-1}h^{-1}$, and from this point will be considered inactive. There was

also a clear pH dependence in all PBIs within this study, which appeared to correlate with the point of gelation (despite continuous stirring upon acid addition). When the pH ~ apparent pKa of the PBI bound amino acid (pH 5-6),[146] supramolecular structures are expected to be formed, suggesting these may be photocatalytically active, which in itself is an exciting observation.

At high pH (pH 10 for this study) there was no hydrogen evolution for any of the PBIs, which exist as doubly deprotonated carboxylates in small stacks at this pH. For most PBIs in this study the peak in activity in the HER occurs between 4-5, which coincides with the point where self-supporting hydrogels would normally form for this group of PBIs,[122,146] had they not been broken down due to continuous stirring. At this point one would expect protonation of carboxylate groups on the amino acids, which leads to rapid loss of solubility in water and aggregation of many PBI units, in a process driven by the hydrophobic effect. This delicate process can be controlled by the added amino acid functionality, due to a variability in acidity as a result of different R group appendages. Due to the differences in hydrogen evolution rate between PBI samples around the point of gelation, there appeared to be multiple factors influencing activity.

Furthermore, the activity profiles of PBI-S and PBI-H were particularly interesting due to increased activity at lower pHs, which was not typical to other PBIs in this study. In fact, below pH 4 the activity drops significantly for all other PBIs despite the continuing growth and entanglement of long PBI chains expected at these pHs. This may be due to several factors including viscosity of the dispersions as the pH is lowered, or eventual syneresis leading to separation of methanol and water layers due to the increasingly hydrophobic PBI structures. Methanol also has a lower dielectric constant than water, making it more difficult to separate charges efficiently at lower pHs.

For simplicity we classified the PBI dispersions into two categories, active or inactive. Due to the low rates of hydrogen evolution PBI-Y, PBI-H and PBI-W were classified as inactive, meaning the remaining 5 PBIs were active photocatalysts. However due to a lack of confidence in the NMR data with regards to the purity of the samples, the data from PBI-L, PBI-S and PBI-W was discarded from the discussion in the subsequent publication.[49] For photocatalysis the samples must be highly pure, especially as such small differences in

structure can have such a profound effect on the supramolecular assembly and therefore the activity of the sample. Since then, the NMR data was examined in more detail, and it was decided that the purity was sufficient for the photocatalysis results to be considered valid. Due to the uncertainty of PBI sample purity, the level of analysis for these PBIs is not at the same standard as the other 5 PBIs. Despite this there are some interesting trends and functionalities in these samples which are not present in the other data set. PBI-S for example has an additional acidic OH group (pKa of 13) on each amino acid which adds another layer of complexity to the self-assembly process, and may have resulted in a unique double peak in the hydrogen evolution data at a more acidic pH. The decrease in rate of hydrogen evolution at pH 3.5 was difficult to rationalise, but once again highlighted that structural changes were also in balance with photophysical properties.

Role of methanol concentration in controlling photocatalytic activity

Having explored 8 different PBIs with a single methanol concentration (20 v/v%) we decided to examine the role of methanol in our PBI dispersions. Methanol was primarily chosen as a sacrificial electron donor to reduce the rate of recombination in the initial excitonic species generated when a PBI species absorbs a photon but may also have a significant effect on the self-assembly and overall structure of the dispersions; due to its difference in polarity and dielectric constant with respect to water. Ultimately the optimum concentration of methanol was not known before conducting this investigation. Therefore, a range of methanol concentrations were employed in a second batch of high throughput testing, this time involving only 2 PBI's; PBI-A and PBI-Y. These two were chosen to directly compare one photocatalyst that worked well, with another that did not evolve a significant amount of hydrogen. This also allowed for examination of the secondary roles of methanol, beyond simply acting as a hole scavenger, due to effects on the assembly of supramolecular structure.
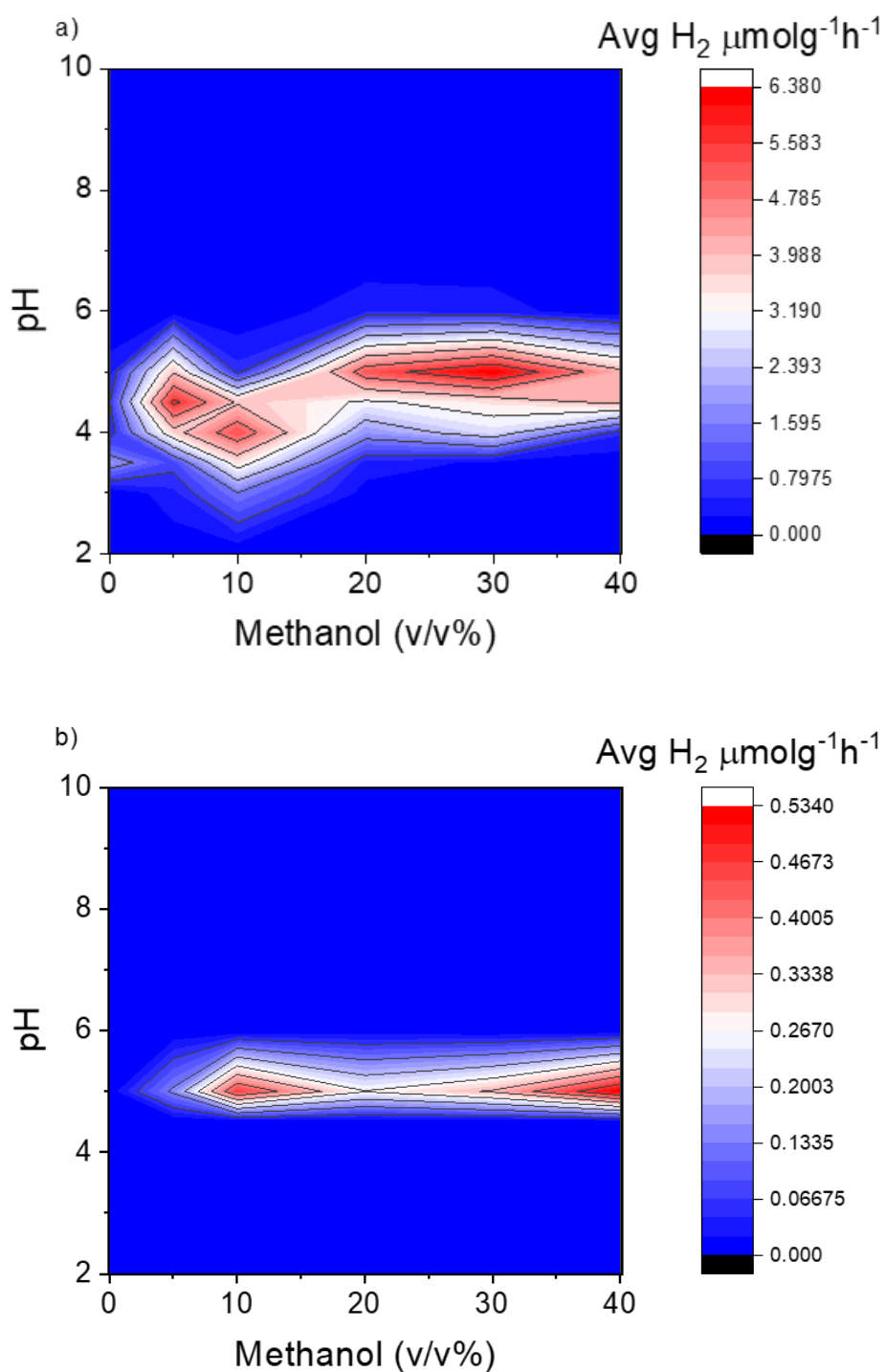
Figure 15- Contour plots of MeOH study which depict the average rate of hydrogen evolution for each dispersion pH, against the methanol concentration (v/v%). Samples of PBI-A (a) and PBI-Y (b) were 5 mg/mL and also contained platinum nanoparticles (1 mol%) along with the specified concentration of methanol. The red part of the spectrum is the most active, whereas

the dark blue is a rate of evolution of zero. Graphs scaled differently to show trends in each PBI.

The rate of hydrogen production under illumination was measured as the methanol concentration was changed (5, 10, 20, 30 and 40 %, v/v%) with all experiments using consistent concentration of 5 mg/mL PBI are shown in figure 15. Across the methanol concentration range studied the photocatalytic activity of PBI-A is consistently higher than PBI-Y. However, it is striking that there is a non-linear relationship between methanol concentration and hydrogen evolution rate for both photocatalysts. If methanol was acting solely as a photohole scavenger then it may be anticipated that photocatalytic activity would increase with methanol concentration up to a limiting value, however this is not seen here. Without the presence of the scavenger methanol, the rate of evolution would depend entirely on the ability the excited state to charge separate without the presence of a sacrificial electron donor, or scavenge an electron from another source.

The most striking observation from this data was that the most active pH for PBI-A is shown to shift depending on the concentration of methanol used, whereas PBI-Y is only significantly active at pH 5. This appears to suggest that the structures forming in PBI-A are more sensitive to the conditions present in the dispersion than PBI-Y, and PBI-Y is limited in some way to only yield a small amount of hydrogen despite many changes in dispersion conditions. PBI-A has a triple hotspot of similar activity at three different pHs, pH 4.5 for 5 %, pH 4 for 10 % and pH 5 for 30 %, which once again highlights the intricate nature of the self-assembly process and how active structures can form at different pHs in different conditions. Due to the multi-faceted role of the methanol in this study it is difficult to state conclusively whether this is due to structural or photophysical factors at this point. PBI-A was also able to produce hydrogen in the absence of methanol, with a peak performance coming at pH 3.5. On the other hand, PBI-Y was unable to form any hydrogen without the sacrificial electrons provided by methanol. The results of this study confirm that varying the concentration of methanol does not follow a simple trend of methanol only acting as a hole scavenger. The presence of methanol has been shown to increase the rate of evolution in some capacity, when compared to dispersions where it was absent. But the lack of a linear trend in either PBI reaffirms a more complex relationship.

Structural analysis of PBI dispersions

Small angle x-ray scattering study of PBI dispersions

Small angle x-ray scattering (SAXS) was used to probe the supramolecular structures forming in our dispersions and have the advantage of being able to study wet samples which underpin our dispersion design. SAXS data was collected for five PBI's (PBI-A, PBI-Y, PBI-F, PBI-H, and PBI-V) to cover the pH range used in the experiments, in addition to the methanol study of PBI-A and PBI-Y. From the extensive data gathered it is clear that self-assembly is occurring across all PBIs as a result of pH decrease, with a clear difference in aggregate size beginning at pH 6, which correlated well with samples observed by eye. At high pH there was little evidence for larger assembled structures, as signified by the low scattering intensity. As the pH was lowered to pH 6 larger aggregates began to form in all PBIs, even those that were inactive for the HER such as PBI-Y. Beyond this point very large aggregates were present in high concentrations throughout the dispersion. Figure 16 displays a cartoon of PBI structures at the various stages of self-assembly in this study.
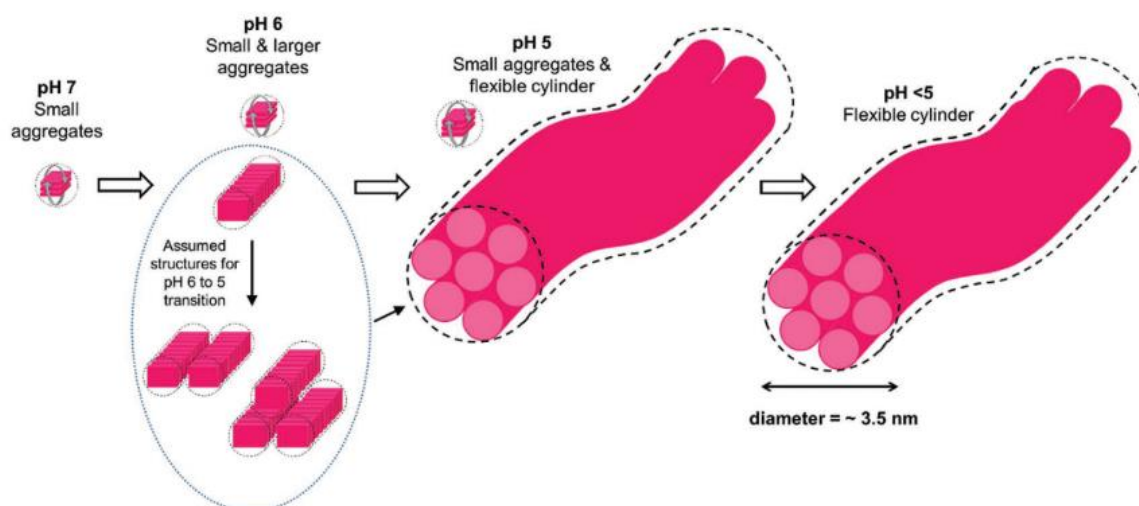
Figure 16- Cartoon of the PBI structures present in the pH range of the experiments. At high pH small aggregates are present, and as the pH is lowered the aggregates increase in size and entangle with one another to form fibres. At pH lower than 5 the size of these aggregates can reach 100s of nm in length. Reproduced with permission.[49]

SasView software was used to fit the SAXS data to structural models and allowed for significant understanding of self-assembly in the dispersions. We found that PBI-A forms small

stacks of between 2-6 PBIs at pH 10 all the way to pH 6. This is based upon the assumption that the interplane distance between PBIs is similar to that of graphite,[49,71] which is known to be around 3.4 Å.[77,147] At pH 5 the data describes a flexible cylinder forming structures up to 130 nm in length (Figure 17 and table 1), as opposed to a sphere present at higher pH; which is indicative of a small number of aggregated PBIs tumbling in solution. Below the point of aggregation at pH 5 the concentrations of these large structures increased significantly, which led to a power law being needed to fit the data (figure 17-18 tables 1 and 2). From this study it was clear that large, self-assembled structures were indeed forming for our active photocatalysts, but also revealed that the same (on the size domains probed by SAXS) large structures were forming for those that were virtually inactive in the HER. Further SAXS data and explanation is discussed in greater detail in the publication.[49]
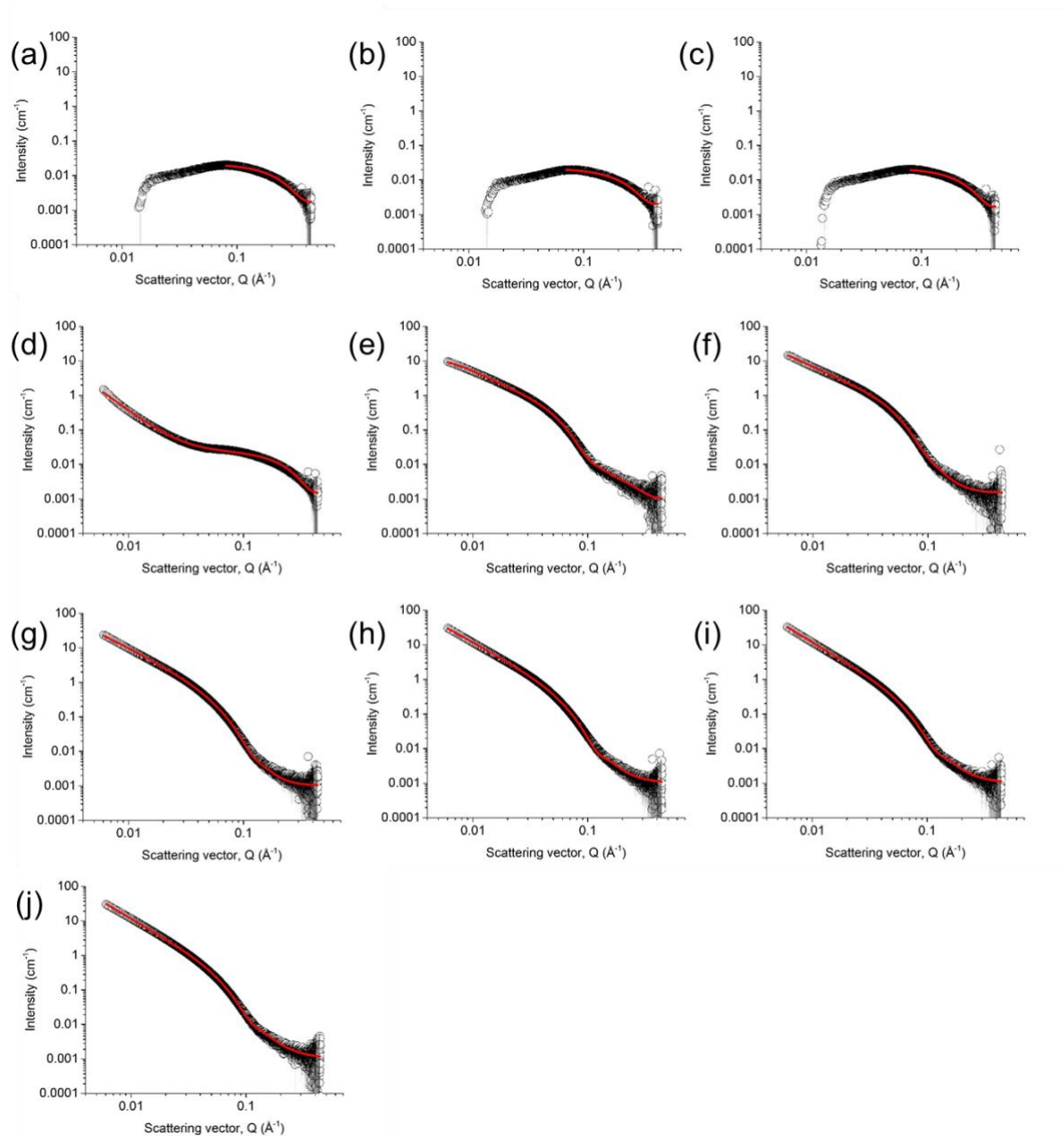
Figure 17- SAXS plots of scattering vector against scattering intensity for PBI-A across the pH range used in the photocatalysis study: (a) 10; (b) 8; (c) 7; (d) 6; (e) 5; (f) 4.5; (g) 4; (h) 3.5; (i) 3; (j) 2. Samples were 5 mg/mL with 20 v/v% methanol. Data fittings shown in red.

Model	pH	Length / nm	Kuhn length / nm	Cylinder radius / nm	Sphere radius / nm	Power law	Reduced Chi squared
Flexible cylinder with a polydispersity of radius 0.2 + power law	2	680*	5.9 ± 0.08	3.2 ± 0.01	-	2.7	3.4
Flexible cylinder with a polydispersity of radius 0.2 + power law	3	680*	5.7 ± 0.07	3.1 ± 0.01	-	2.7	1.3
Flexible cylinder with a polydispersity of radius 0.2 + power law	3.5	680*	5.6 ± 0.06	3.0 ± 0.01	-	2.7	3.7
Flexible cylinder with a polydispersity of radius 0.25	4	680*	6.3 ± 0.05	3.0	-	-	3.9
Flexible cylinder with a polydispersity of radius 0.3	4.5	220 ± 2.7	24.3 ± 0.07	3.5	-	-	3.4
Flexible cylinder with a polydispersity of radius 0.25 + Sphere	5	130 ± 0.52	22 ± 0.08	3.5	1.0†	-	2.7
Sphere + Power law	6	-	-	-	1.0	2.6 ± 0.01	1.0
Sphere	7	-	-	-	1.0	-	<1
Sphere	8	-	-	-	1.0	-	<1
Sphere	10	-	-	-	1.0	-	<1

*Table 1- PBI-A SAXS model fitting results that were illustrated in figure 17. * Errors unavailable for fitting results. Length continued to increase beyond expected level with further fittings and was therefore capped at 680 nm (beyond SAXS length measuring capability) with an added power law to describe low Q intensity. Sphere radius set to 1 nm based on high pH. Data fittings performed by Daniel McDowall and reproduced from literature paper.[49]*
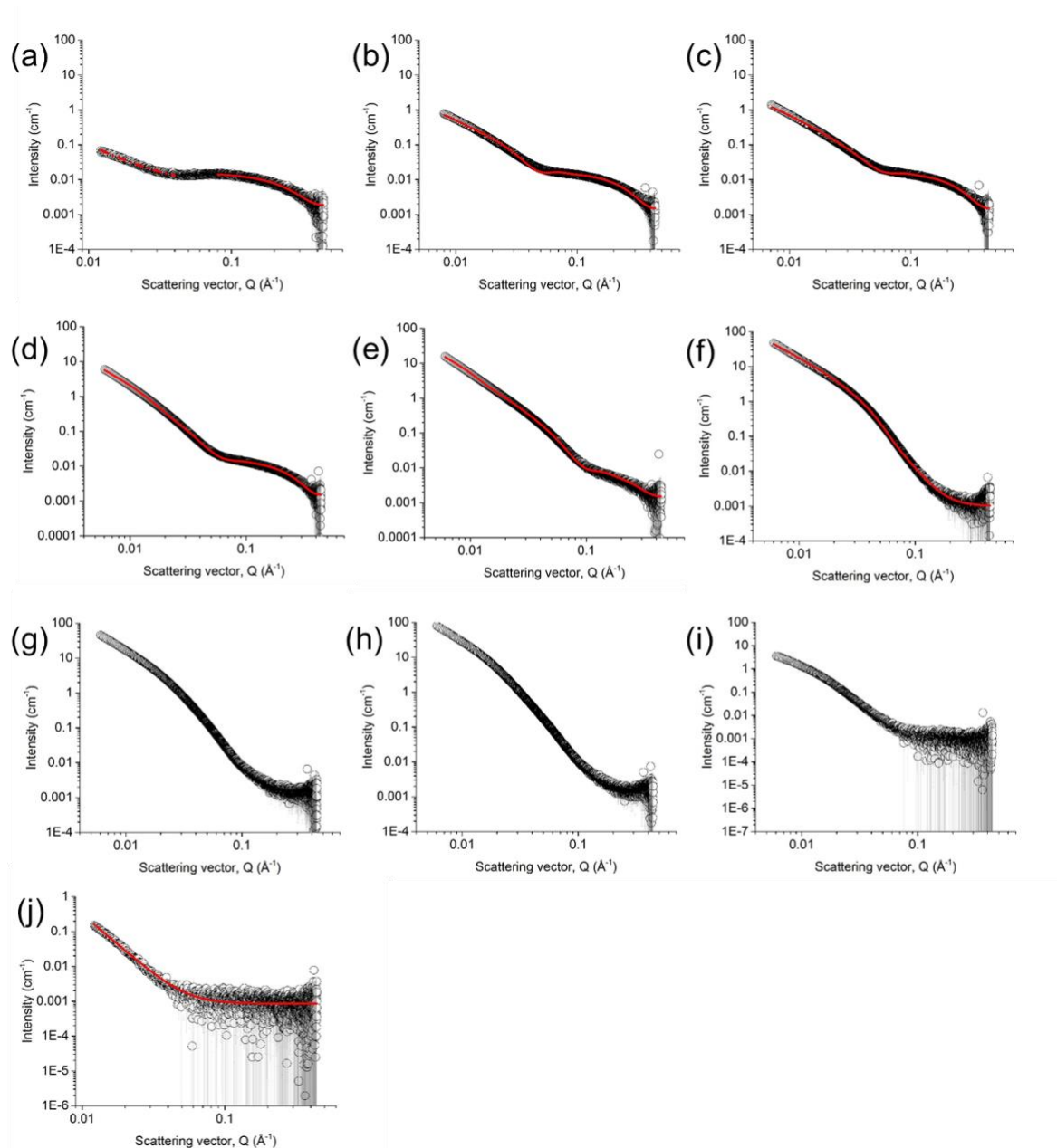
Figure 18- SAXS plots of scattering vector against scattering intensity for PBI-Y across the pH range used in the photocatalysis study: (a) 10; (b) 8; (c) 7; (d) 6; (e) 5; (f) 4.5; (g) 4; (h) 3.5; (i) 3; (j) 2. Samples were 5 mg/mL with 20 v/v% methanol. Data fittings shown in red, fittings not obtainable for all graphs due to formation of dense fibre network that could not be observed by SAXS. Performed by Daniel McDowall and reproduced from literature.[49]

Model	pH	Length / nm	Kuhn length / nm	Cylinder radius / nm	Axis ratio	Sphere radius / nm	Power law	Reduced Chi squared
Power law	2	-	-	-	-	-	3.5 ± 0.02	<1
Not fitted	3							
Not fitted	3.5							
Not fitted	4							
Flexible cylinder with a polydispersity of radius 0.35	4.5	1300*	11.1 ± 0.06	4.6 ± 0.01	-	-	-	11.7
Flexible elliptical cylinder + Sphere	5	640 ± 0.18	64.0 ± 13.08	3.2	8.0 ± 0.03	1.0	-	2.1
Flexible elliptical cylinder + Sphere	6	570*	27.7 ± 0.43	4.7 ± 0.01	3.7 ± 0.02	1.0	-	1.1
Flexible cylinder + Sphere	7	300*	10.9 ± 0.29	5.8 ±0.02	-	1.0	-	1.6
Flexible cylinder + Sphere	8	130	31.8 ± 0.80	7.0 ± 0.02	-	1.0	-	1.8
Sphere	10	-	-	-	-	1.0	-	<1
Power	10	-	-	-	-	-	1.9 ± 0.07	<1

*Table 2- PBI-Y SAXS model fitting results that were illustrated in figure 18. * Errors unavailable for fitting results. Data from pH 3-4 could not be fitted. Data fittings performed by Daniel McDowall and reproduced from literature paper.[49]*

UV-Vis spectroscopy of PBI samples

SAXS provided an insight into the extent of self-assembly, and size of structures, but it does not reveal how self-assembly affects the local electronic environment as a result of coupling between neighbouring chromophores. Figure 19 displays the UV-Vis data recorded for this study after normalisation. Due to the high concentration of PBIs used in this study a thin pathlength was required to record the UV-Vis. Spectra were recorded after samples were placed between two microscope slides and sealed with parafilm. In all cases aggregation leads to broadening of the UV/Vis spectra and a decrease in the maximum absorption coefficient a result of aggregation;[148] therefore normalisation was required to allow for a comparison between the data and we are unable to report accurate molar extinction

coefficients. Five PBIs were studied using this method at a single methanol concentration, to correlate with the data recorded in the SAXS.
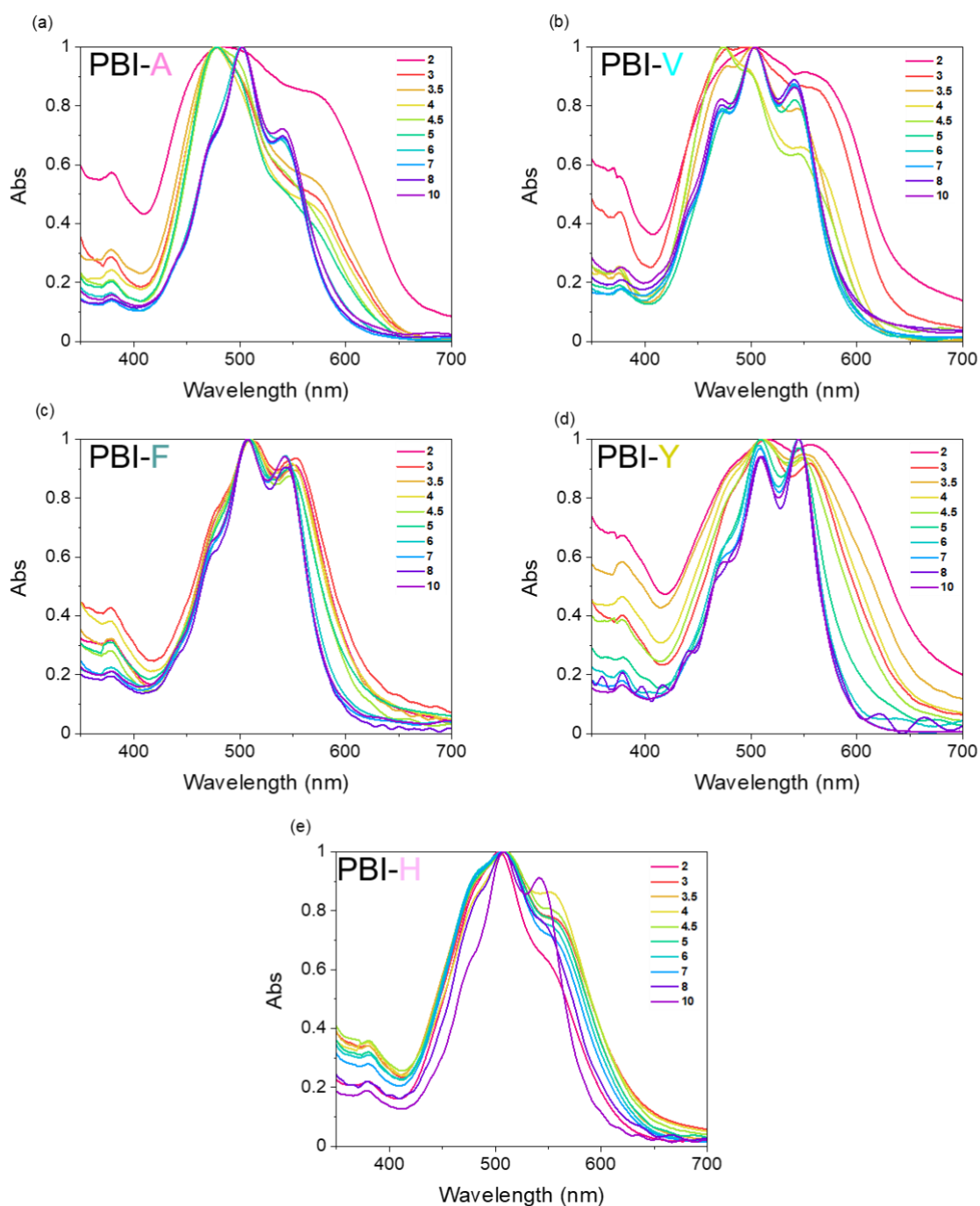
Figure 19 – UV-Vis data for the PBIs in the study; a) PBI-A, b) PBI-V, c) PBI-F, d) PBI-Y, and e) PBI-H. Photocatalysis dispersions were not diluted for this study, despite high extinction coefficients. 5 mg/mL PBI dispersion, with 20% methanol (v/v%) and Pt nanoparticles all present. Each colour represents a different pH from the study, and all data is normalised due to extinction coefficients changing with pH.

PBI aggregation has been previously shown to be highly dependent on the nature of the solvent,[148] which has a profound effect on the UV-Vis spectrum. Solvation in water in particular is known to cause extreme broadening even at low concentrations, due to the polarity of water.[85,148] Figure 20 demonstrated clear changes in intensity ratios of the vibronic modes, even at low concentration, which indicated that aggregation was still occurring. At 10^{-6} M PBI-A has the most monomer like structure of the series, which was depicted by the increasing strength of the v= 0-1 transition relative to other spectra, and displays clear evidence of aggregation with increasing concentration due to broadening and peak intensity shifts. This broadening is characteristic of self-assembled structures existing in solution, and not free molecules.[149]
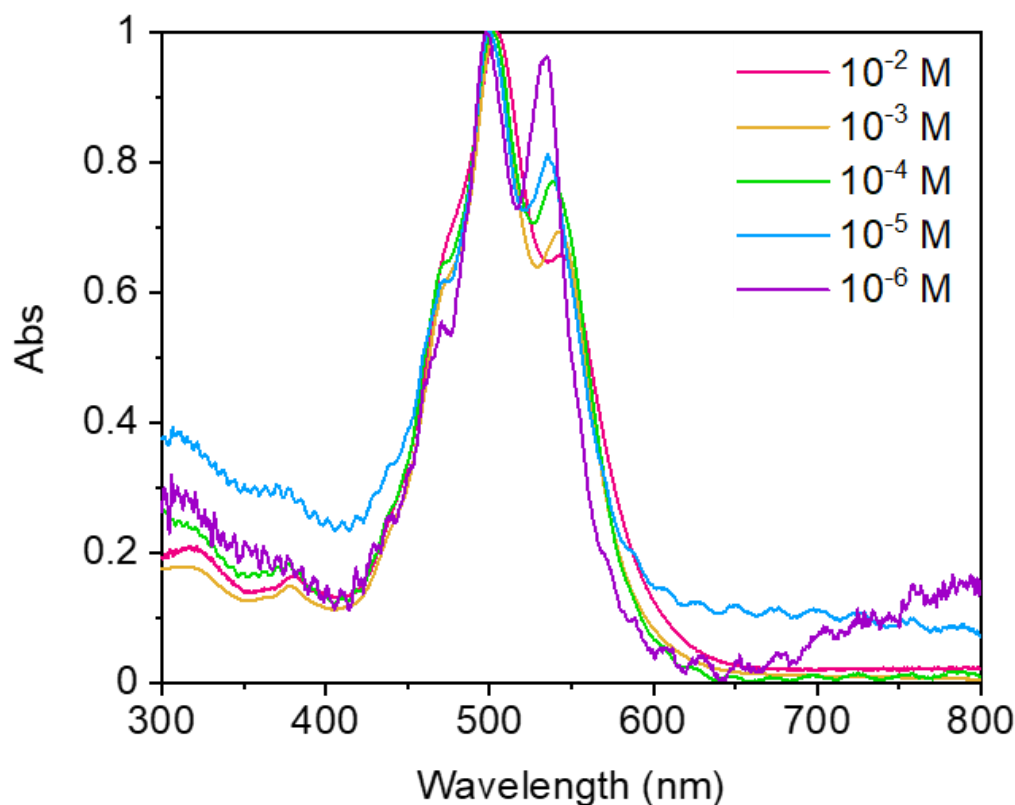
Figure 20- Dilution series of PBI-A with normalised absorbance. Initial 10^{-2} M is approximately the same concentration as used in the photocatalysis experiments (5 mg/mL ~ 0.09 M). More dilute samples had a very low absorbance and therefore produced much more noisy data.

The UV-Vis of PBI-A has previously been shown to consist of two major electronic transitions, the S_0-S_1 in the visible (450-600 nm) and the S_0-S_2 in the UV (360 nm).[85,143] In addition close-

lying vibronic transitions are used to determine the aggregation type present in the PBI species,[85,143] and can heavily impact the peak positions in the spectrum. PBI-A displays H-type aggregation due to the prominence of the 0-1' transition, with minimal contribution from the first two vibronic modes with respect to the monomer PBI spectrum (figure 20).

As the pH was lowered from pH 10 to pH 6, there was a clear hypsochromic shift in the maximum absorption from 500 nm to 480 nm, due to an increase in aggregate size with extensive face to face stacked helices throughout (PBI-A).[122] Interestingly it has previously been shown that there is little change in the structure of PBI-A aggregates as they assemble besides the length of the aggregate itself.[122] Beyond pH 5 extensive broadening of the S_o-S_1 transition in the UV/Vis occurred, to leave an incredibly broad spectrum at pH 2. This once again correlated well with what was observed by the SAXS in which large flexible cylinders were shown to dominate, as opposed to smaller aggregates or free molecules in solution. In addition to this, a power law was required to fit the large supramolecular structures present at such a high concentration, and in some cases the structures were too large and too dense to be modelled by SAXS.

PBI-V followed a similar pattern to PBI-A in the pH profile UV-Vis spectra, with initially well-defined peaks at high pH, which then shift in position as the length scale of PBI aggregates increases with lowered pH, to finally show large broadening at pH 2. PBI-F on the other hand does not show this final broad state at pH 2, and only saw small shifts in the UV-Vis spectra upon addition of an acid trigger, despite being a highly active photocatalyst for the HER in this study. PBI-Y does display the final broader state at pH 2, but does not show the same peak shifts around pH 5 that are present in the initial analysis of PBI-A. The UV-Vis profile of PBI-H is significantly different to the other PBIs in this study, with major differences at pH extremes and little change around pH 5.

Fitting UV-Vis data

PBI structures with peptide appendages have previously been shown to display multiple aggregate types simultaneously.[150] The UV/Vis spectra show a pH dependence with PBI-A in particular showing a general trend of increased broadening of the S_0-S_1 transition at lower pH, presumably indicating increased coupling between chromophores of the assembly. To elucidate our findings further and to attempt to deconvolute contributions to the spectra

arising from individual structure types we employed a similar methodology by fitting the UV-Vis spectral data to a combination of linear fittings, where each defined structure type is assumed to have a distinct UV-Vis spectrum. We determined that in PBI-A absorption spectra there were 3 different aggregate types determining its behaviour as a photocatalyst. Aggregate type 1 was characterised to be the spectrum at pH 10, type 2 was pH 4, and type 3 was pH 2. Equation 1 describes how the absorption of the fitted spectra were calculated (A_{pH}), using the coefficient of the contribution of each aggregate type C_x and the absorbance associated with it A_x. Aggregate types are denoted as such to distinguish between the aggregate types between PBIs, while they may be similar in structure it is not possible to call them the same species (figure 21).

$$\text{Equation 1: } A_{pH}(\lambda) = \sum C_x A_x(\lambda)$$
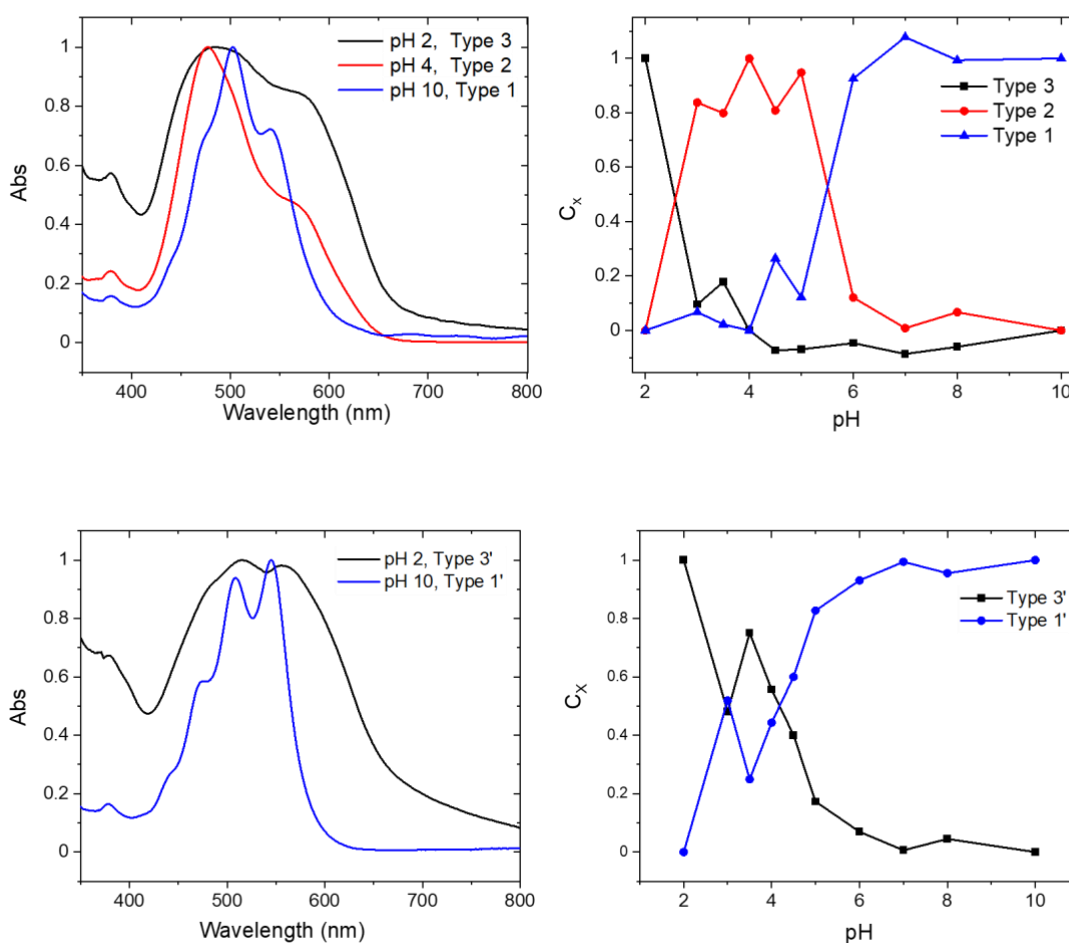
Using a plot of aggregate contribution vs pH allows for a comparison of aggregate type dominance at each pH to account for activity in the HER. At pH 10 in PBI-A and PBI-Y type 1 aggregates dominate due to short chains of PBI being present in excess. However, the significant change occurs at pH 5 in PBI-A where type 2 aggregates were found to dominate, and this coincides with the switching on point in hydrogen evolution for PBI-A. The nature of the type 2 aggregates will be discussed in detail further below but here we initially note that (i) there is a significant change in vibronic ratios when compared to either PBI-A at low concentration (figure 20) or PBI-A at high pH (type 1 aggregate) and (ii) a broadening of the UV/Vis spectra occurs, indicating a change in coupling in the self-assembled structures formed. Interestingly at the lower pH's studied we find a 3rd aggregate type is present which has a very broad UV/Vis spectrum and the 0-1 vibronic transition increases in amplitude again, suggesting a further change in the coupling between PBI-A units at pH < 3 which is not detected by SAXS. In PBI-Y we found that the spectra could be fit through a linear combination of only 2 spectra types. Type 2' aggregates were not present in PBI-Y at significant levels at any pH, thereby indicating the importance of type 2 aggregates in the success of the photocatalyst.

Another active catalyst in the study, PBI-V, observed the same trend in UV-Vis spectral fitting as PBI-A with pH (shown in figure 22) with a clear switching on in activity correlating well to dominance of type 2' aggregates around pH 5. This trend extends further to the hydrogen evolution data for PBI-V, which displayed the same profile shape as PBI-A across the pH range studied, but also produced more hydrogen at each active pH. PBI-V also displays clear evidence of the three types of aggregate contributing to the UV-Vis spectrum. PBI-F on the other hand only displays two aggregate types (type 2' and type 1'), despite being an equally active catalyst (figure 23). This observation was rationalised by the lack of broadening in the UV-Vis at low pH, when compared to PBI-A and PBI-V. The formation of the type 2' aggregates

occurred at the same pH region (around gelation point ~5) as seen in other previous active PBIs (PBI-A and PBI-V). Instead there was simply a peak shift at low pH, indicating the formation of type 2' aggregates, which did not proceed to form type 3' aggregates at low pH which for other PBI samples are indicated through the very broad UV-Vis absorption spectra.
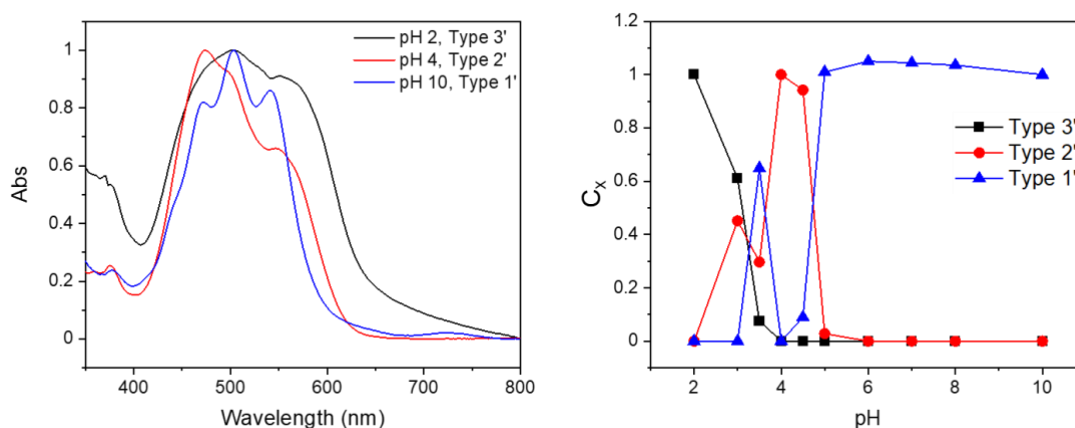
Figure 22- UV-Vis of PBI-V samples used in the photocatalysis study with fitting analysis to determine aggregate type contribution correlation with pH. Samples were 5 mg/mL, contained 20% methanol (v/v%) and platinum nanoparticles. Panel a) shows 3 aggregate types with their corresponding UV-Vis spectrum; panel b) displays the contribution of each type of aggregate in the pH range used for the study. Reproduced from literature.[49]
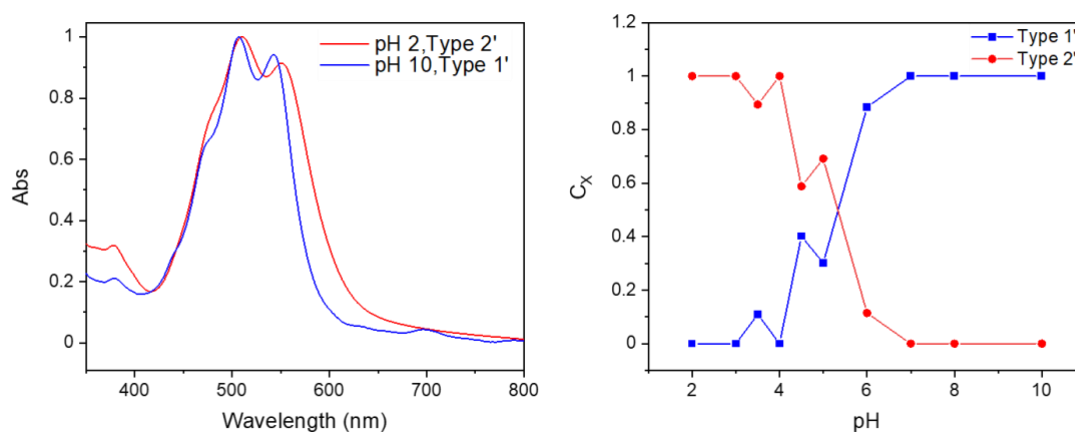

Figure 23- UV-Vis of PBI-F samples used in the photocatalysis study with fitting analysis to determine aggregate type contribution correlation with pH. Samples were 5 mg/mL, contained 20 (v/v%) methanol and platinum nanoparticles. Panel a) shows two aggregate types with their corresponding UV-Vis spectrum; panel b) displays the contribution of each type of aggregate in the pH range used for the study. Reproduced from literature paper.[49]

PBI-H shows only low levels of photocatalytic activity and fitting the UV-Vis spectra from different pH's did not yield the same 3 aggregate types shown to be crucial to the success of PBI-A (figure 24). Similar to PBI-Y, PBI-H only displays 2 aggregate types. Interestingly the spectrum for pH was so significantly different to the other PBIs it was excluded from the fitting analysis. PBI-H spectra did not display significant broadening or shifts shown in type 2 aggregates in PBI-A and PBI-V around pH 5. PBI-H has been shown to dissolve at low pH (around pH 2) due to the imidazole functional group protonation, and therefore has a significantly narrower UV-Vis spectrum as a result. This also prevented further SAXS analysis due to the dissolution of larger aggregates formed as the pH was lowered, but interestingly correlated with the only measurable quantity of hydrogen being detected in PBI-H samples. Whether this is due to a uniquely formed low pH active species, or simply a breakdown product due to instability is not clear and was not explored further. Nevertheless, this was another striking result and reaffirmed once again that without type 2 aggregates there was no significant evolution of hydrogen.
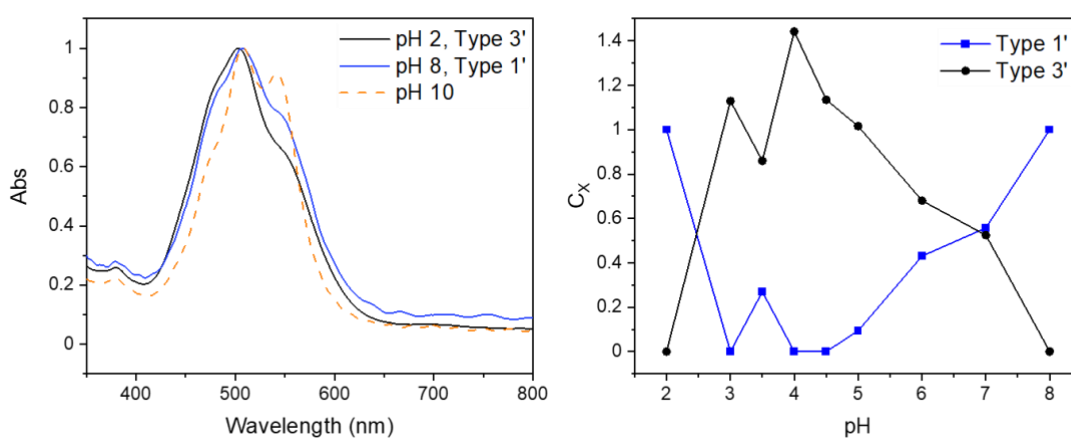
Figure 24- UV-Vis of PBI-H samples used in the photocatalysis study with fitting analysis to determine aggregate type contribution correlation with pH. Samples were 5 mg/mL, contained 20 % methanol (v/v%) and platinum nanoparticles. Panel a) shows 3 aggregate types with their corresponding UV-Vis spectrum; panel b) displays the contribution of each type of aggregate in the pH range used for the study. Reproduced from literature paper.[49]

Investigating the effects of methanol on the UV-Vis spectra

Having uncovered the importance of type 2 aggregates to the success of PBI-A with 20 (v/v%) methanol, the next logical step was to investigate its influence across the methanol

concentration scale. Figure 25 and 26 display the UV-Vis spectra for PBI-A and PBI-Y at the 6 different methanol concentrations (0, 5, 10, 20, 30, 40 v/v %). For PBI-A the spectra generally followed similar trends to what has been previously seen for 20 (v/v%) methanol, with initially sharper peaks shifting and broadening around pH 5, to leave a very broad final spectrum at pH 2. However, the spectra for 5 and 10 (v/v%) methanol did not follow this trend in quite the same way. The spectrum for 0% methanol does not show the same hypsochromic shift seen at pH 5 at 20 % (and higher concentrations), and instead the shift occurred at pH 4. Intriguingly the peak of hydrogen evolution with no hole scavenger present was 3.5, as opposed to pH 5 previously seen in the spectrum at 20 (v/v%), indicating a preference for the peak shifted structure we have named type 2. The spectrum of 5 (v/v%) methanol does possess the peak shift at pH 5 but did not show the same extreme broadening at pH 2, indicating a lack of type 3 aggregates with respect to 20 % methanol (v/v%). This appeared to demonstrate a slower rate of forming type 2 and type 3 aggregates in samples with a lower methanol concentration (with respect to pH), and therefore a lower pH was required to achieve maximum hydrogen evolution. Samples with higher concentrations of methanol (v/v%) follow the same trends of the 20 % methanol data set, and both maintain pH 5 as the optimum set of conditions.
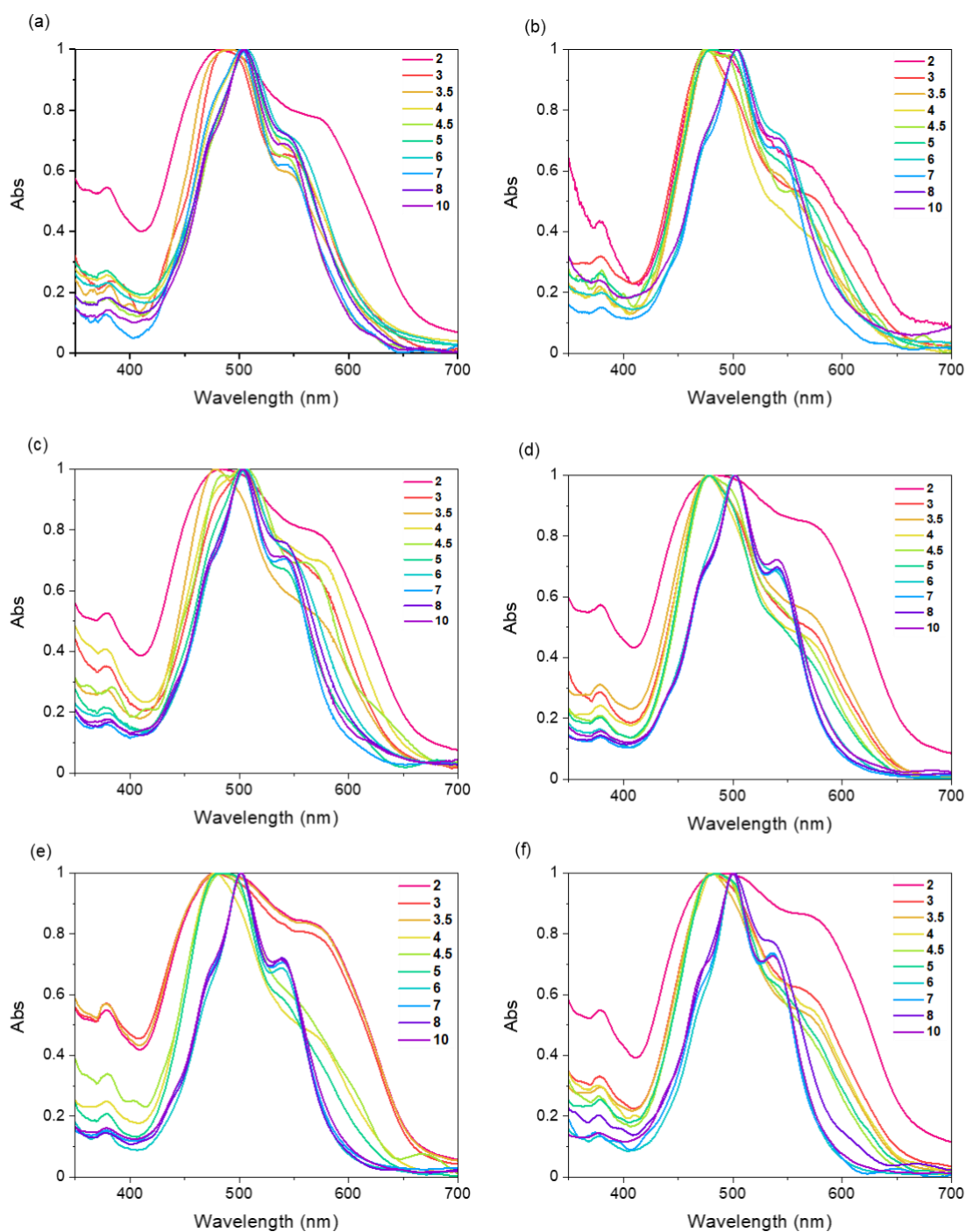
Figure 25- UV-Vis spectra of PBI-A at 5 mg/mL with platinum nanoparticles and a varied methanol concentration of a) 0%; b) 5%; c) 10%; d) 20%; e) 30%; f) 40% v/v% against pH which is shown by the spectrum of colours. Spectra were recorded using 2 glass microscope slides being pressed tightly together due to the large absorbance of the samples at high pH. Data was normalised. Reproduced from literature paper.[49]

The UV-Vis spectra of PBI-Y across the methanol study are displayed in figure 26. In general, the spectra follow the same trends shown by 20 v/v%, but there are noticeable differences in

the behaviour at extreme methanol concentrations, in particular, with no methanol present. In figure 26 a) the characteristic peaks of PBI-Y at 509 nm and 547 nm had an intensity ratio of ~1:1 at pH 10. This intensity ratio appears to change strikingly as the methanol concentration (v/v%) is increased, until at 40 (v/v%) the ratio is 2:1 at pH 10; this does not appear to happen in the spectra for PBI-A. The similarities between the 0 (v/v%) methanol spectra for both PBI-A and PBI-Y were quite striking, as they both appeared to display a less pronounced change with self-assembly before then becoming very broad at pH 2. Despite this there is no clear peak shift in the maxima for PBI-Y at any methanol concentration in the study, which appears to suggest once again a lack of type 2 aggregates. The broadness exhibited at 5 (v/v%) methanol with PBI-Y is much more apparent at higher pHs than without methanol, which indicated a clear difference in structuring as a result of the methanol. This trend continued as the methanol concentration (v/v%) increased through the study, especially when comparing the results at pH 4-5 with the spectrum containing no methanol.

It was difficult to compare these spectra by eye due to the subtle electronic and vibronic changes that occur as the conditions are delicately adjusted. Due to the nature of aggregation, the PBI molecules that are being probed by UV-Vis spectroscopy were in strikingly different conditions ranging from 2-6 PBIs, to structures too large to be probed by SAXS (>700 nm). Overall, the spectral changes in PBI-Y appear to be subtler than those that occur in PBI-A as the pH is lowered, due the lack of a well-defined peak shift around pH 5. It was also difficult to rationalise these small changes in an inactive photocatalyst that did not yield significant changes in hydrogen evolution regardless of the supramolecular state it was found in.
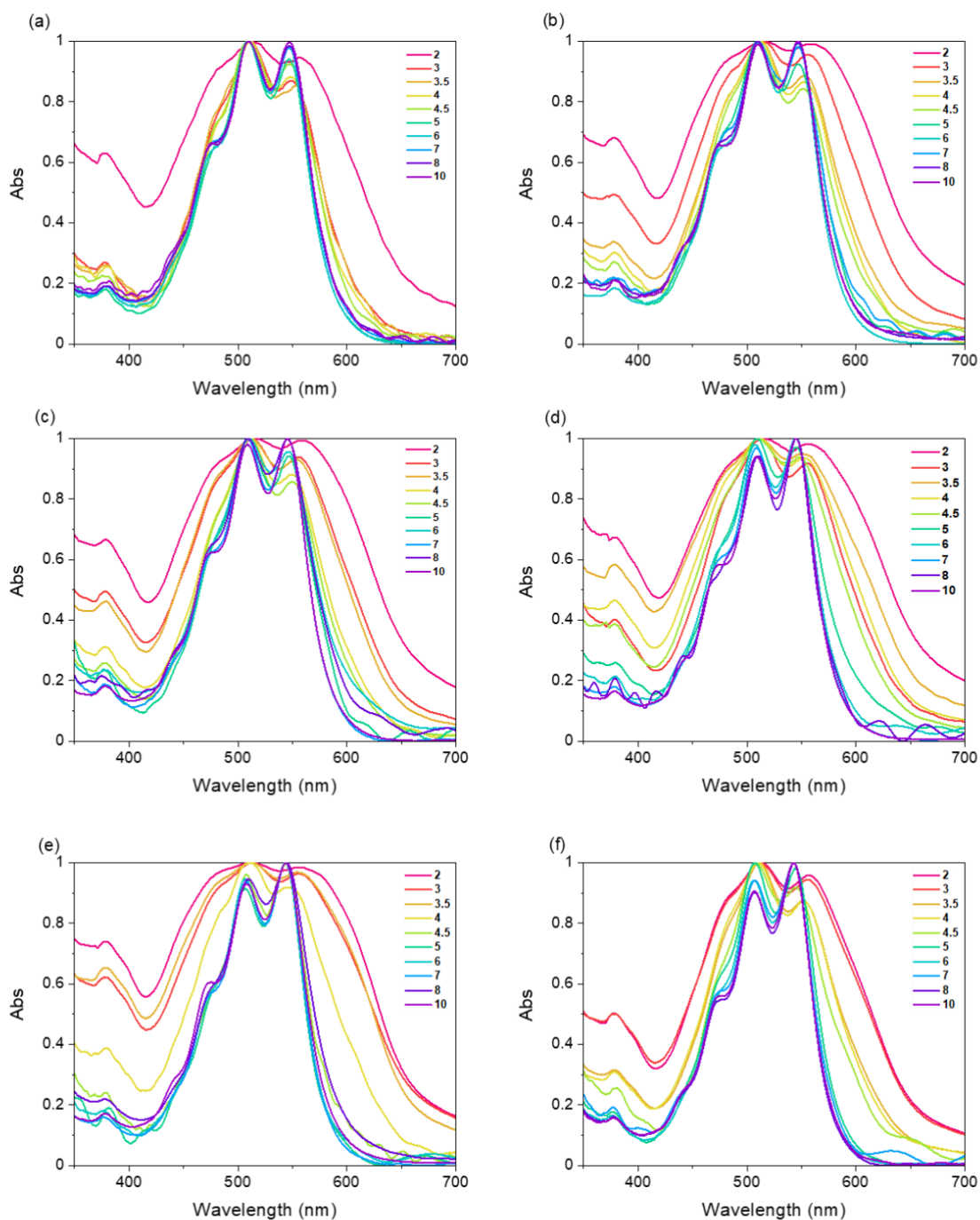
Figure 26- UV-Vis spectra of PBI-Y at 5 mg/mL with platinum nanoparticles and a varied methanol concentration of a) 0%; b) 5%; c) 10%; d) 20%; e) 30%; f) 40% v/v% against pH which is shown by the spectrum of colours. Spectra were recorded using 2 glass microscope slides being pressed tightly together due to the large absorbance of the samples at high pH. Normalised data. Reproduced from literature paper.[49]

The same fitting process was applied to the UV-Vis data of PBI-A and PBI-Y (figure 27 and 28), with special consideration applied to pH 5 as it was the most active pH for PBI-A; and the only

active pH for PBI-Y. Figure 27 demonstrates the effect of methanol on the resulting UV-Vis of PBI-A at pH 5, and it appears that samples with a lower concentration of methanol are less broad and have not undergone the characteristic hypsochromic shift. The results of the fitting procedure are visualised by the plot of concentration of type 2 aggregates vs methanol concentration, which followed the trend in hydrogen evolution very nicely. The lack of a broadening and peak shifts in low methanol concentration samples were confirmed as being due to a lack of type 2 aggregates, and therefore a lack of hydrogen at pH 5.
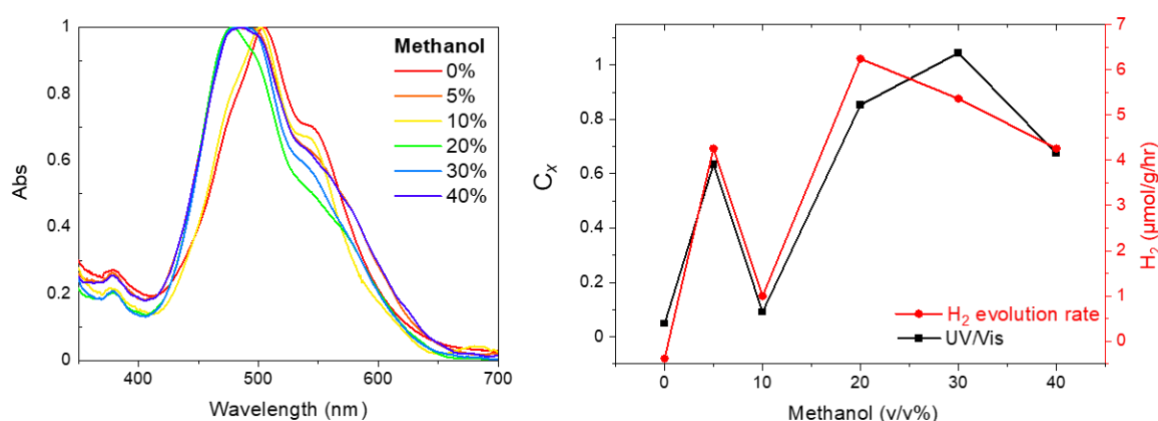
Figure 27- UV-Vis spectra of PBI-A at pH 5 across the methanol concentration window used in the photocatalysis experiments. Samples were 5 mg/mL, with a different methanol concentration shown by a different colour, along with the same concentration of Platinum nanoparticles. b) shows the concentration of type 2 aggregates at pH 5 in each sample across the different methanol concentrations used in the study, also correlated with hydrogen evolution from the pH 5 sample in red. UV-Vis data was normalised.
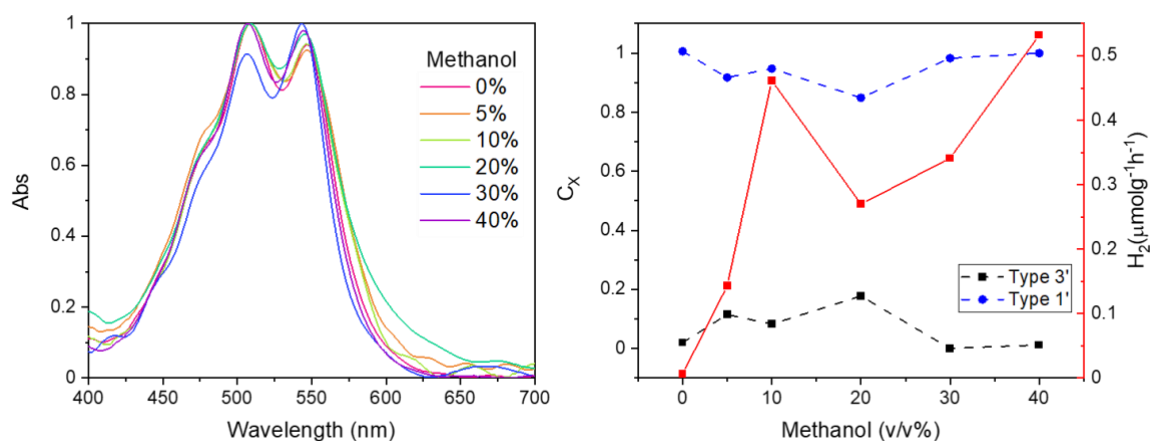
Figure 28- UV-Vis spectra of PBI-Y at pH 5 across the methanol concentration window used in the photocatalysis experiments. Samples were 5 mg/mL, with a different methanol concentration shown by a different colour, along with the same concentration of Platinum nanoparticles. b) shows the concentration aggregates at pH 5 in each sample across the different methanol concentrations used in the study, also correlated with hydrogen evolution from the pH 5 sample in red. UV-Vis data was normalised.

Understanding the photocatalytic mechanism

Electrochemistry of PBI supramolecular structures

In order to investigate the active species for hydrogen evolution in our PBI samples, a series of electrochemical measurements were carried out including cyclic voltammetry and square wave voltammetry. Electrochemical measurement of the reduction and oxidation potential of the PBI's can be used to approximate the energy of photogenerated PBI^+ and PBI^-. Figure 29 displays the Cyclic voltammograms (CVs) and square wave voltammograms (SWVs) of PBI-A and PBI-Y, along with a comparison with how the proton reduction potential changes with pH. The CVs and SWVs of PBI-A and PBI-Y at pH 10 are quite comparable, as they both clearly display the reduction of neutral PBI species to the radical anion (around -0.3 V vs normal hydrogen electrode (NHE)), followed by an additional reduction at higher applied potential which appears to be the dianion formation. At high pH, short chains of PBIs dominate in solution rather than free molecules tumbling in solution, which added an extra layer of complexity to assigning species. Due to the nature of aggregation and mixing of FE/CT states discussed earlier, we hypothesise charge delocalisation across several PBIs. As the pH is lowered and the PBI fibre length increases, there was a decrease in the current measured for the PBI reduction processes in PBI-A samples. While this may have been a surprising result, the fact that the reduction processes in both PBIs appear to be virtually pH independent was even more intriguing due to the strikingly different electronic and structural environments found in more aggregated species. One may inherently assume that the electronic mechanisms of a short chain PBI would behave differently to that of a larger stack, but electrochemical measurements have shown a lack of significant differences.
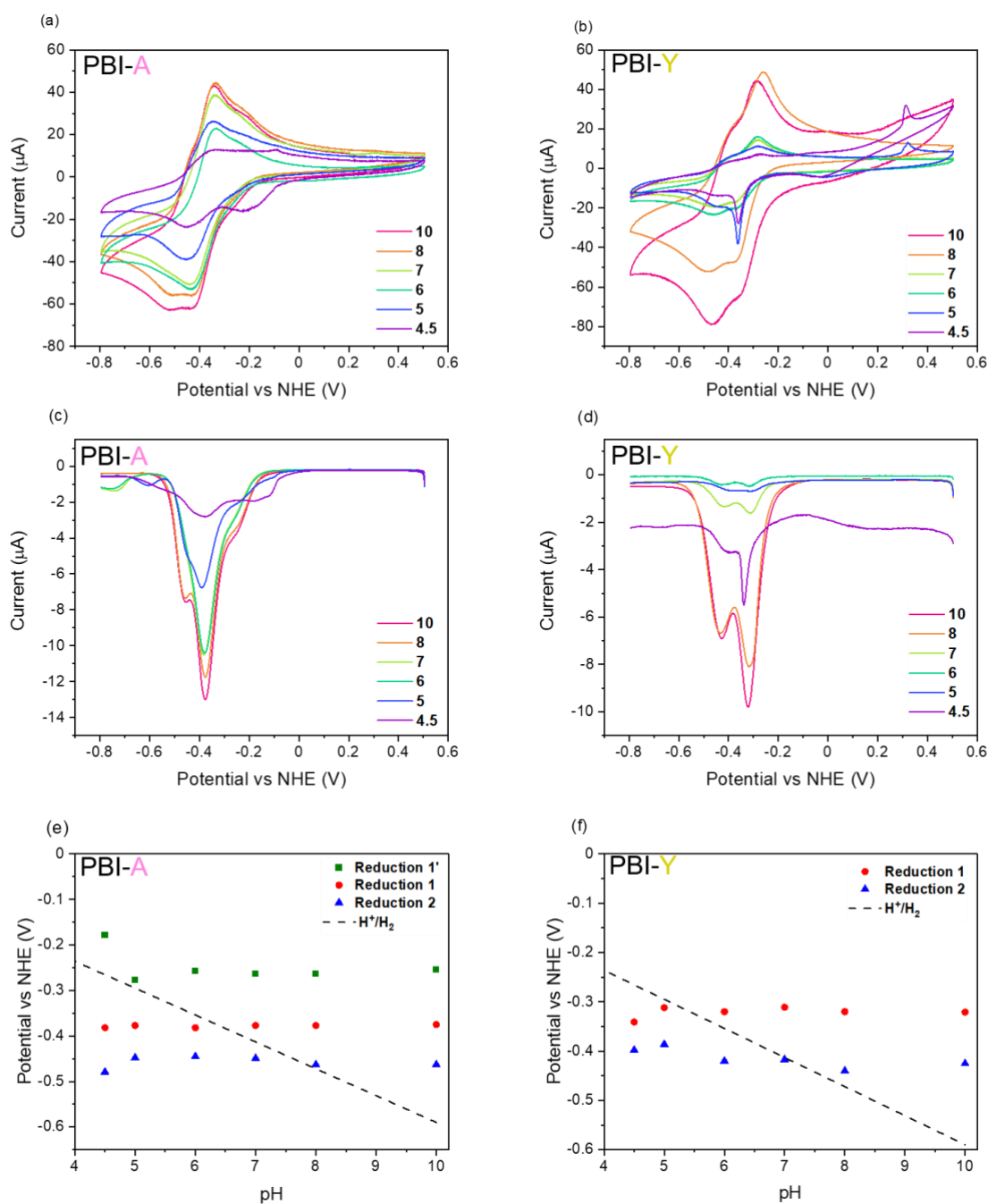
Figure 29- Electrochemistry of PBI-A vs PBI-Y photocatalysis dispersion, in the absence of platinum nanoparticles. Experiments were performed in a 40 mL vial and used a 3-electrode setup. PBI gelator solution was 5 mg/mL and contained 20 (v/v%) methanol, with a supporting electrolyte of NaCl (0.1 M). Cell was purged with N_2 for 30 minutes before experiments. Cyclic voltammograms were performed between +0.3 V to -1 V with a scan rate of 100 mVs^{-1}. SWV measurements used a 1 second equilibration time, 0.01 amplitude and a frequency of 1 Hz.

In a recent study on dilute photocatalytic samples of PBI-F, the PBI radical was reported by spectroelectrochemistry (SEC) at -0.285 V (vs Ag/AgCl) and the dianion at -0.472 (vs Ag/AgCl)

due to the characteristic emergence of peaks at 725 and 610 nm respectively.[105] While this study allows for an estimate for the nature of the reduction processes occurring, the structures present were not comparable due to the 5x dilution. In the SWV measurements for PBI-A and PBI-Y we observe 3 clear reductions in PBI-A samples, and 2 reduction processes in PBI-Y. Spectroelectrochemistry (SEC) measurements of the photocatalysis samples were not possible due to the importance of maintaining the same structure throughout all measurements without dilution. But spectroelectrochemical studies of PBI photoelectrodes are explored further in chapter 4, and confirm the presence of two reductions via UV-Vis due to the emergence of radical anion peaks at 730 and 830 nm from -0.3 V applied, and a new peak at around 620 nm from -0.5 V onwards to confirm the presence of the dianion (figure 30). While the structure of the species is not consistent, there are clear parallels between the PBI-A photocatalysis samples and photoelectrodes.
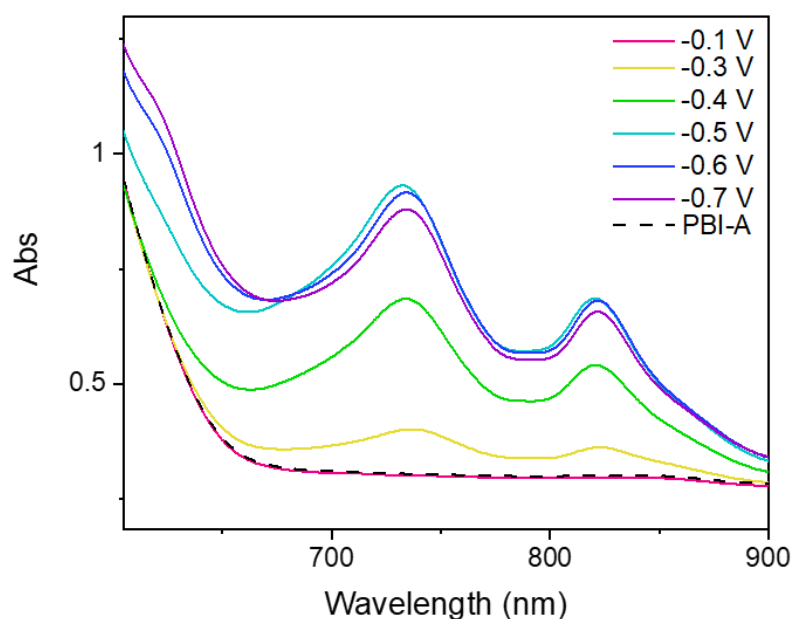
Figure 30- Spectroelectrochemical study of PBI-A photoelectrodes using UV-Vis spectrophotometry. Electrochemistry performed in a custom cuvette cell using a pH 4 KCl electrolyte (0.1 M), with a Ag/AgCl reference electrode and platinum wire counter electrode. Electrode was placed into beam of UV-Vis spectrophotometer, and spectra were recorded with applied potential.

Therefore, assigning the reduction processes to a definitive species is difficult due to the high concentration of our samples, but there were clear parallels between the dilute PBI-F measurements and our own PBI-A photoelectroderesults.[105] For example, there are 3 clear

close lying reductions for both PBI-F and PBI-A despite the proposed final species being a dianion, with a maximum of two reductions for a single molecule. This can only point to an element of aggregation influencing the electrochemical processes, making the pH independence of the reductions for PBI-A and PBI-Y even stranger. We hypothesise that the initial reduction process is the formation of the PBI radical anion from the neutral species, followed by additional reductive processes that then go on to form the PBI^{2-} at the final reduction potential. This agrees with the initial study at low dilution, which confirms the emergence of the dianion peak at 610 nm before the removal of the radical anion peaks at 725 and 820 nm.[105] In fact due to the closely stacked environment of PBI molecules, there was likely to be an element of charge delocalisation across many chromophores, as opposed to a single doubly reduced molecule forming initially. This process was illustrated by the second reduction, with a second formal charge forming upon the third reduction. The final graph of figure 29 compares the reduction potentials of the PBI samples across the pH range, along with the hydrogen reduction potential for that pH, which allows for a crude approximation of driving force for proton reduction at that pH. The rate determining step is likely to be the transfer of charges to the platinum co-catalyst through a transfer from a PBI stack, which must possess the reductive power to supply the co-catalyst with the electron to perform proton reduction. For PBI-A the first reduction does not have the driving force for proposed proton reduction at any pH, so it was unlikely to contribute to catalysis. The second reduction became feasible at pH 6, which is around the point where PBI-A begins to self-assemble, making it a contender for the active species. The third reduction of PBI-A was feasible from pH 7, where no hydrogen evolution occurs, which perhaps means the fully formed dianion is not required for active photocatalysis. pH 5 for PBI-A has a significant enough overpotential for effective photocatalysis for both reduction 2 and 3, which led to a peak in activity at that pH; but despite an increase in driving force at lower pH the rate of hydrogen evolution fell.

For PBI-Y the first reduction becomes feasible at pH 5, which was the only pH that resulted in any hydrogen, with the second reduction having significant driving force at pH 6. Assigning an active species of either the radical anion or dianion is not possible from these measurements, as it appears that driving force alone does not seem to be the limiting factor for the success of PBI photocatalysts. Both PBI-A and PBI-Y can form reduced PBI species capable of being

sufficiently reducing to evolve hydrogen, but it was clear that the structure governs the behaviour. Chapter 3 will investigate the photophysics of PBI dispersions further to uncover the origin of the activity differences.

Action spectrum of PBI-A

Measuring the incident wavelength dependent hydrogen evolution rate can provide important insights into the photocatalytic mechanisms occurring. Figure 31 shows the wavelength dependent hydrogen evolution rate for PBI-A at pH 5 (20 v/v% methanol), overlapped with the UV/Vis absorption spectrum of the photocatalytic mixture. In order to evolve hydrogen gas from these samples, there needed to be sufficient saturation of the PBI solution with H_2. This required a pre-illumination step with a Xe lamp for 3 hours, due to the incubation period. Figure 31 displays a clear preference for UV light which has been highlighted previously for these amino acid functionalised samples.[85,105] The rate of evolution also correlates with the peak absorbance of PBI-A at 490 nm, and decrease past 650 nm. Figure 32 also displays the rate of evolution for a PBI-A sample at pH 5 over a period of 25 hours, this also confirms that the relative rate of evolution was susceptible to change over the time period of illumination. Between 3-7 hours the rate of evolution was fairly constant (~5 $\mu molg^{-1}h^{-1}$) but between 7 to 25 hours the rate of evolution plateaued to an average of around 3 $\mu molg^{-1}h^{-1}$. This drop-in activity was expected due to the photooxidation of the sample over time which would likely destroy the structures required for the long lived charges to suvive.
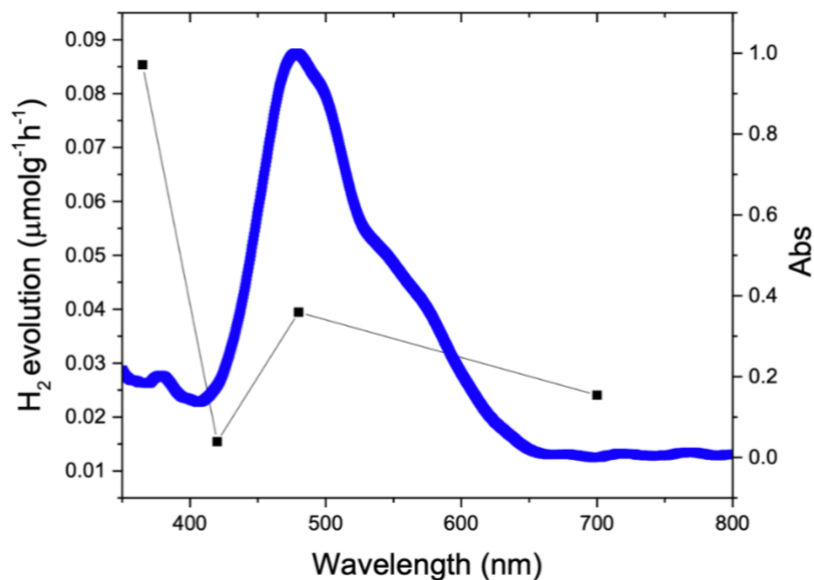
Figure 31 – Action spectrum of PBI-A after pre-illumination with a Xe lamp for 3 hours followed by illumination with a single wavelength of light for one hour. Gas analysis taken before and after illumination. UV-Vis absorbance shown in blue to allow for comparison with activity.
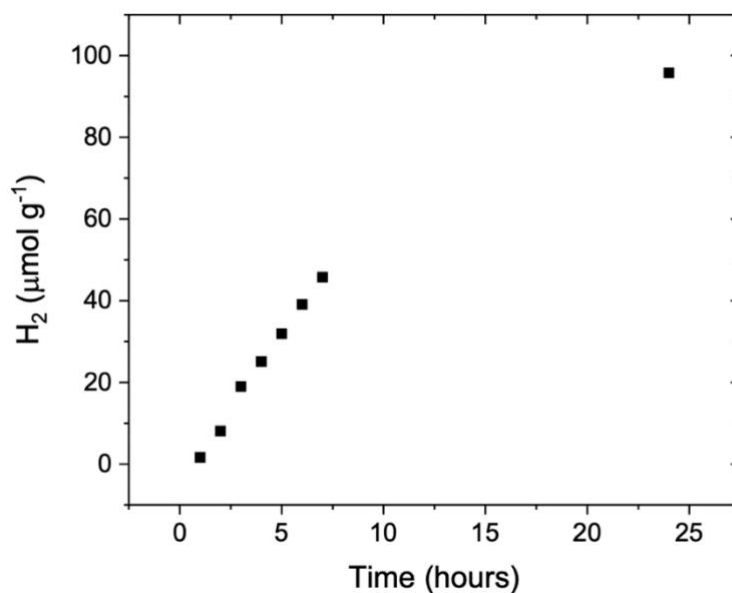
Figure 32- Hydrogen evolution over time of a pH 5 PBI-A sample with 20 % methanol (v/v%) and platinum nanoparticles. Light source used was a 300 W Xe lamp with a light intensity of 100 mWcm^{-2}, no filters were used.

Another interesting observation was the lack of correlation between generating the PBI radical anion in previous testing, and activity in the HER via proton reduction.[104] We expect the importance of charge separation and the generation of the PBI radical anion to be key to the success of PBI structures as photocatalysis, however it does not seem to be as simple as generating the largest quantity of anion. In a study by Draper *et al.* the same 8 PBIs were studied as photoconductive films that were illuminated with UV light to track the generation of the radical anion through EPR.[104] While the morphology of a PBI film may be different to that of a dispersion some parallels between the structures in each study can be made, but there appears to be little to no correlation between activity in the HER and photoconductivity via PBI radical generation. This is itself a surprising result but may just highlight the lack of true insight into the mechanism for PBI based photocatalysis, and perhaps the need for multi photon processes to generate more reducing species. Indeed, the PBI dianion is known to be EPR silent which may explain why more photoconductive samples seemed to have such low quantities of radical anion.[104]

Explaining the local packing changes exposed by the UV-Vis study

Due to the nature of aggregation, PBI chromophores come into close contact with one another and can interact. In theory this can enable charge separation and transfer through a network of PBI cores, with delivery of electrons to the platinum co-catalyst. The self-assembly process has already been demonstrated in PBI-A by SAXS; and perhaps more crucially by the broadening and peak shifts shown by UV-Vis spectroscopy. The broadening of PBI-A as the pH was lowered was indicative of more PBI chromophores interacting with one another as they stack together to form long fibres, which leads to more electronic environments being available to individual PBI molecules once a photon of light is absorbed. Solvation can also influence how charges are distributed amongst PBI molecules and stacks,[151] with water in particular having a high dielectric constant which stabilises separation of charge. In addition, the ability to separate charges over multiple PBI units (while still tightly bound) not only enhances the prospect of enhanced lifetimes, but also boosts the transport of charges through PBI stacks. A single PBI molecule in water does not have the ability to delocalise charges over multiple units, meaning that even if the hole and electron were to separate, and

survive long enough, it is unlikely that there would be effective transport to the platinum co-catalyst.

Extensive research of covalently linked PBIs have investigated how the mixing of the FE and CT bands can lead to a mixed state,[88,91,92,95,133,139,140] which enables the separation of charge. We hypothesised that the same mixing of states can occur in our PBI aggregates formed around pH 5,[49] and therefore enable charge separation without the need for physical bonds. This would explain why at pH 10, where small aggregates between 2-6 PBIs dominated, there was a lack of mixing of states, and thereby a lack of charge separation, which was demonstrated by the lack of broadening in the UV-Vis spectra from 10-6. Upon aggregation and extensive state mixing broadening was apparent in the UV-Vis at pH 5 (which we defined as type 2) and this coincides with a switching on in activity for hydrogen evolution, due to the ability to separate charges, and transport them through fibres. Below pH 5 the yield of hydrogen evolution decreased, despite this mixing. We believe this is due in part to the hydrophobicity that exists in our PBI structures in acidic media, as a result of double protonation of the amino acids at low pH; coupled to an already hydrophobic PBI core. As a result, PBI structures may separate into an almost organic layer, preferring to be solvated by the methanol instead of the water that underpins the charge separation of our photocatalysts. Without water in the structure the vast networks of PBI fibres were likely unable to fulfil the charge transporting potential due to a lack of ability to separate effectively from the initial excitonic state. But could also simply illustrate the goldilocks like structure type that is required for hydrogen evolution to be favoured in our systems.

Macromolecular aligned PBI photocatalysts: Noodles

Having confirmed the importance of self-assembly and supramolecular structure to the design of successful PBI photocatalysts, our next step was to use alignment of PBI structures to influence activity. As part of the collaboration with the University of Glasgow Daniel McDowall was investigating aligned fibres,[152] and was able to find a PBI molecule that was suitable for forming "noodles". PBI noodles were formed in a trigger medium $CaCl_2$ solution (in water) which was used to induce self-assembly instead of pH. We had no control over the arrangement of our PBI dispersions beyond changing the pH, but by forming noodles under shear forces we aimed to induce alignment to boost activity in the HER.

The structural arrangement present in a gel is usually perceived as 'random' as the fibres entangle to immobilise the solvent and increase the entropy of the system. Magnetic fields,[145,153] electric fields,[154–156] and shear forces are all known to cause alignment,[144] including some previous work with PBIs specifically.[142,144,145] Noodles were first reported using peptide amphiphiles by Stupp *et al*,[157] and using a similar methodology we were able to form PBI noodles by pipetting a PBI solution into the trigger medium of CaCl$_2$. However due to the extensional viscosity of the PBI solution required to form noodles, a different amino acid functionalised PBI was required namely PBI-I (shown in figure 33). Draper *et al* have investigated similarly functionalised PBIs (PBI-V, PBI-L and PBI-I) and uncovered an interesting higher pKa present in PBI-I, allowing it to self-assemble at a higher pH than the other PBIs in this study.[146] For the formation of noodles the pH was first adjusted to pH 6 to increase the viscosity of the samples and to allow the trigger medium to 'lock in' the proposed aligned structure under the shear forces of the pipette. Our photocatalytic samples used a PBI concentration of 5 mg/mL, however noodles were not able to form using this concentration, and a higher concentration of 10 mg/mL was required.
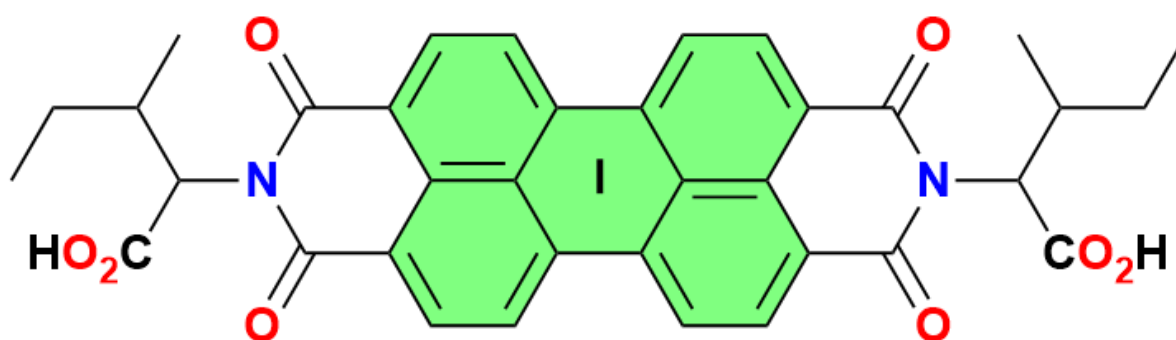
Figure 33- Diagram of PBI-I molecular structure with the PBI core highlighted in light green.

Monitoring structure alignment in PBI-I noodles

Alignment of fibres has previously been demonstrated using microscopy,[157] and through spectroscopy.[158] Due to the high concentration of the PBI solutions and the inherent high absorbance used it was difficult to design a spectroscopic experiment to test for alignment. Therefore, the microscopy setup used by Stupp *et al.* was adapted by Daniel McDowall (shown in figure 35).[157] Bright regions of PBI noodles were shown under cross polarised light as a

result of birefringence (figure 34), whereas unaligned regions appeared dark due to the light being removed by the filters. The phenomenon of birefringence results from a material that has a refractive index that depends on the polarization of the incident light. Therefore, when an incident ray of light passes through the material it produces two rays of light with a small difference in path, due to a difference in polarization. Having two polarizers at right angles to one another each side of the sample meant that without birefringence the sample would appear dark. Birefringent sections appear bright due to a change in the polarization which allowed the light through the second polariser. The brightness of the birefringent sections was also dependent on the relative rotation relative to that second polariser. This meant reproducibly quantifying the alignment of the noodles was a challenge, but we were able to check and compare the alignment between samples by fixing the camera gain throughout all videos and pictures. Images of both our experimental setup figures 34 and 35 the schematic from literature it was based upon.
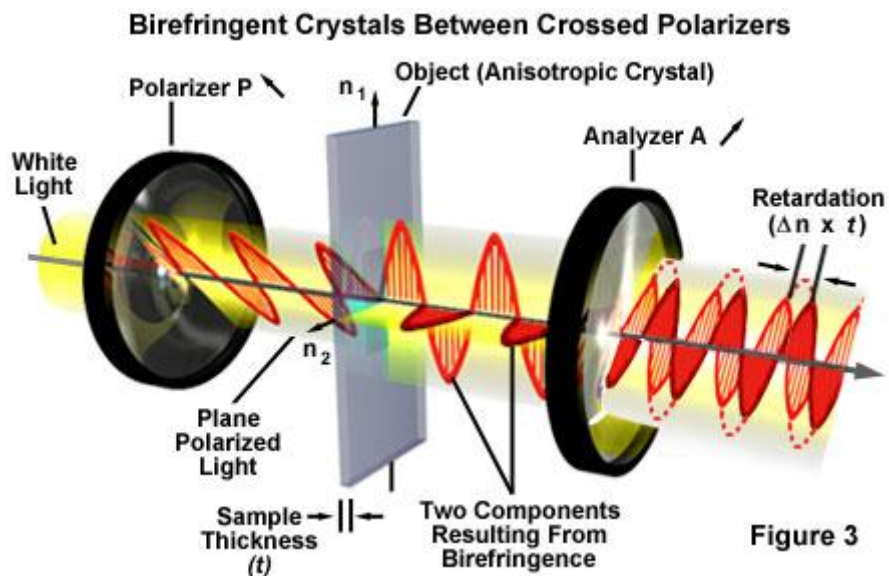
Figure 34- A diagram to illustrate the interaction between plane polarised light and a birefringent material.[159]
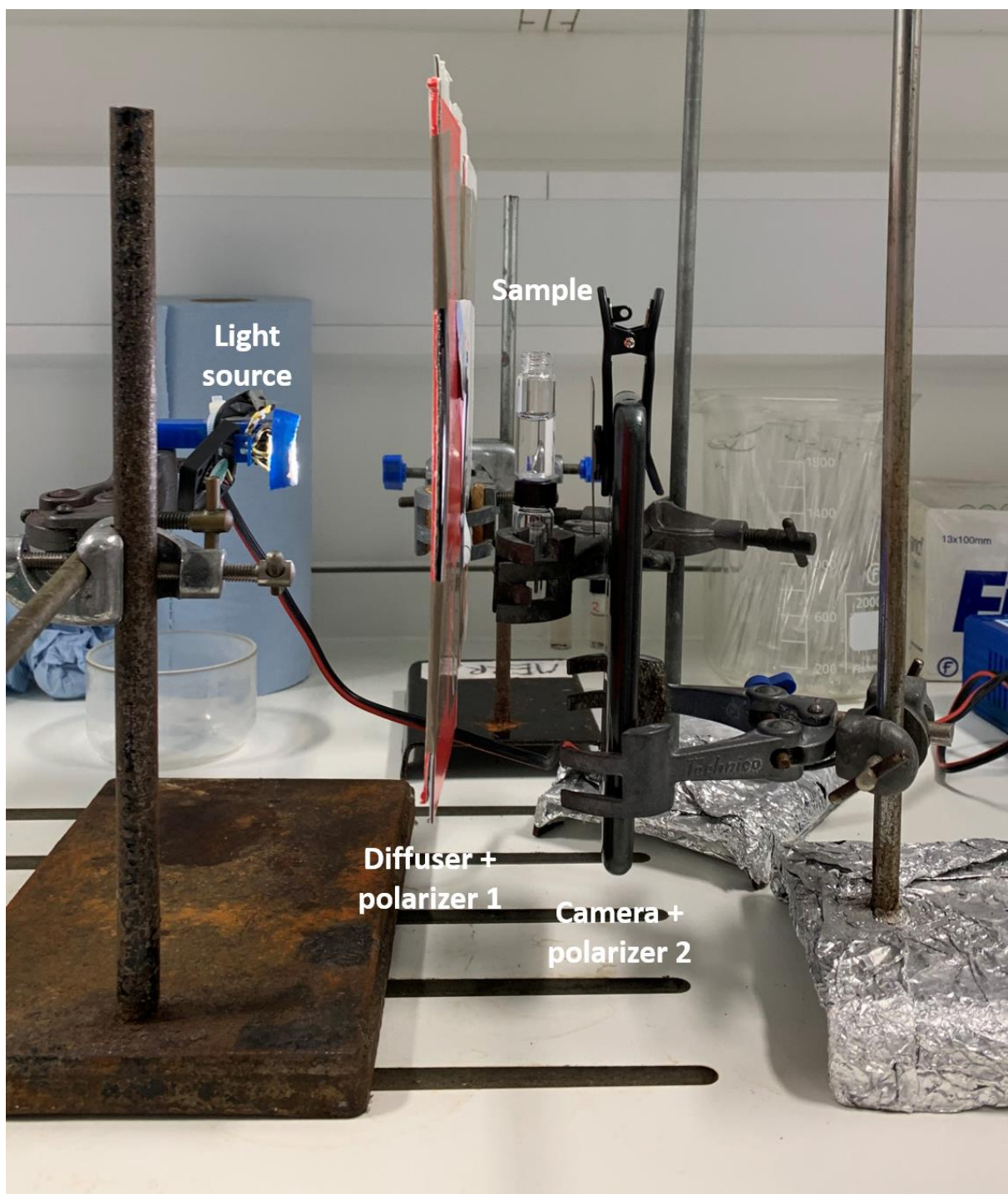
Figure 35- Image of the noodle alignment checking setup. This consisted of an LED white light source, a light diffuser (white paper), two crossed polarisers at 90º to one another and a mobile phone camera to capture the images. The sample was pipetted into the vial in front of the camera from above to allow for videos and images to be taken while the noodle was forming. Setup designed with Daniel McDowall and was used in the dark to be able to see the alignment through brightness.
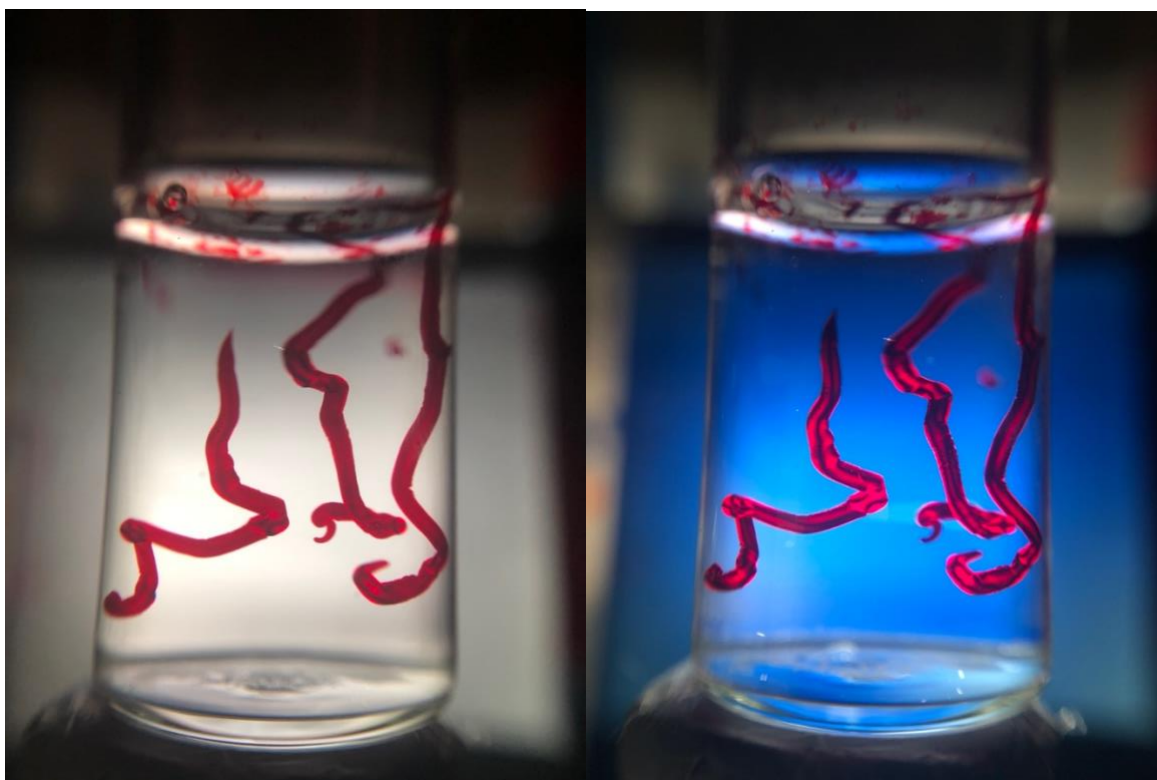
Figure 36- Images of aligned PBI-I noodles with and without the second polariser. The darker image is due to the second polariser removing the light let through by the first polariser. The birefringent sections of the noodle appear bright due to being let through the second polariser. Noodle appears to be aligned due to bright sections present in long straight section, in addition to coiled section.

Forming aligned noodles

The challenging task for forming aligned noodles was adjusting the pH of the PBI-I solution, which buffers around pH 6 due to its close lying pKa (figure 36). There was a delicate balance between forming noodles that were not that aligned, and more aligned noodles due to the level of assembly in the PBI solution. Drifting below pH 6 often led to noodles that were not homogenous, whereas above pH 6.30 there was a lack of alignment. There were also occasions where aging of the solutions appeared to be key, as shown by figure 37. For each PBI-I solution there appeared to be a slightly different sweet spot for alignment in terms of pH and aging, where some solutions formed aligned noodles on the first day after pH adjusting and some that required a lot of adjustment over periods of days.
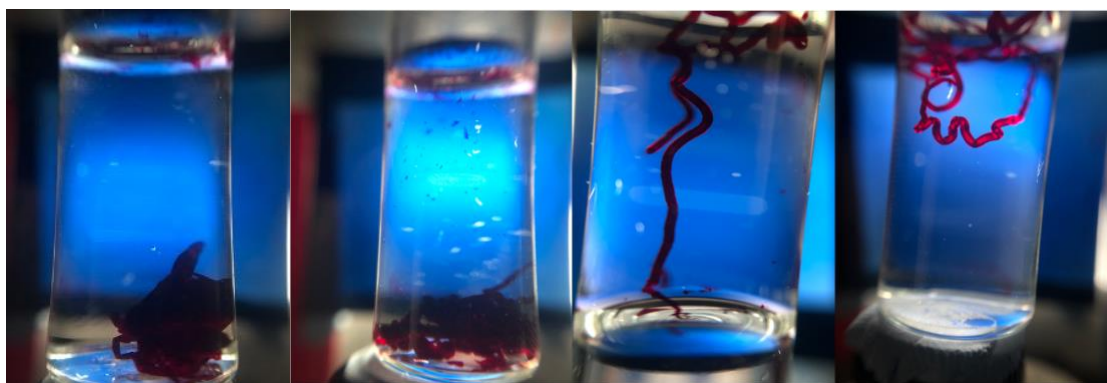
Figure 37- Images of PBI-I noodles on 4 sequential days with slight differences in pH and therefore alignment. First picture pH= 6.32, second picture pH= 6.66, third picture pH= 5.95, and the fourth picture pH= 6.12. The pH of the PBI-I solution was adjusted using low concentrations of HCl or NaOH with stirring and left overnight to sit without stirring. Brighter sections in image 4 illustrate aligned noodles.

Aligned noodles were formed by directly pipetting the PBI-I solution (10uL, adjusted to pH 6, 10 mg/mL) into a vial of the trigger medium $CaCl_2$ (50 mM in water) at a constant rate. The noodle was formed instantly and reached length scales of around a centimetre, provided the noodle did not break apart into smaller pieces. A video of the noodle forming was recorded for each experiment, the presence of aligned sections was confirmed by the bright regions. The brightest parts of the noodle are usually at 90° to the second polariser, but rotating the noodle showed the darker sections were in fact aligned in some cases due to the phase relative to the filter (which are shown by image 28). Crossed sections of aligned noodles also have the same effect as a cross polariser, and therefore appear dark (shown in figure 38), confirming the birefringent properties.

Figure 38- Image of crossed noodles, will probably just go with one of these. Crossed sections appear dark due to additional effect of polarising light due to birefringence. Red filter used to confirm difference due to birefringence and not absorbance in visible region from PBI noodles.

Hydrogen evolution from noodles

In order to employ PBI noodles as photocatalysts they required the integration of a co-catalyst and a hole scavenger. Initial tests attempted to introduce both reagents to the PBI solution before noodle formation, however due to the viscosity of the methanol being significantly different to water it was not possible to form noodles in this way. Therefore the methanol was mixed into the trigger medium containing the $CaCl_2$ dissolved in water, and the platinum nanoparticles remained in the PBI solution. The noodles produced in the trigger medium containing methanol appeared to be thinner than those pipetted simply into the $CaCl_2$ solution, but due to the necessity of having methanol as a sacrificial electron donor it was included. The pH of the trigger solution was also adjusted to pH 5, which was the most active pH for most of the PBIs tested in the high throughput study. Previous tests on PBI-I as a 5 mg/mL photocatalytic dispersion (same sample preparation as previously)[49] had already been carried out using a Xe lamp, as a proof of principle test for hydrogen evolution for PBI-I. The

tests revealed that PBI-I was an active photocatalyst with an average of 8 $\mu molg^{-1}h^{-1}$, which compared favourably with other PBIs in our previous study.

Initial testing of single noodles in 4 mL vials were performed in front of a 300 W Xe lamp with no filters but yielded no hydrogen probably due to the lower amount of PBI present in the solution. This was not wholly surprising due to the disparity In PBI concentration between a 10 µL pipetted noodle (10 mg/mL) and 5 mL of a 5 mg/mL solution. One of the primary objectives had been to try and quantify the amount of hydrogen per unit area to try and compare it with the bulk dispersions used previously. Subsequent hydrogen testing using multiple noodles confirmed that many more noodles were required than previously thought. Hydrogen was detected by gas chromatography (GC) analysis in an appreciable amount using 28 noodles in a vial, after a 3-hour illumination. Due to the fragility of the noodles the trigger solution was pre-purged with argon, and briefly opened while the noodles were pipetted in. Upon illumination there was a clear colour change within 5 minutes, as the noodles became much darker and almost black in colour (shown by figure 39). A post illumination image suggests a loss of alignment due to illumination (figure 39), as some noodles are still very bright and others very dark. This may be due to the lack of stirring, once again due to the fragile nature of the noodles. While illuminated, some noodles were blocked by noodles in front of them, and due to how absorbing they are it is unlikely much light penetrated through the noodle. The loss of alignment as a result of illumination makes it challenging to assess if alignment of supramolecular structures is beneficial for photocatalysis.

Figure 39- Image of PBI-I noodles before (L)and after (R) illumination with a Xe lamp. The bright sections in the picture before illumination demonstrate an element of alignment in the noodles as a result of shear forces. The image taken after the illumination appears to have entire noodles that appear dark which suggests they have lost alignment upon illumination.

Preparing unaligned noodles

Due to a lack of comparability between unaligned PBI dispersions and aligned noodles, the next logical step was using unaligned noodles to truly test whether alignment was boosting hydrogen evolution through our hypothesis of enhanced charge separation. We aimed to make the unaligned noodles as similar in macroscopic structure to the aligned noodles as possible but they needed to consist of supramolecular structures that are randomly orientated with respect to each other. This was inherently challenging as we wanted to use the same PBI solution to make aligned and unaligned noodles. Pipetting the same pH 6 PBI-I solution into water appeared to reduce the alignment of the noodles as although the shear force of the pipetting leads to initial alignment, due to the lack of Ca^{2+} salts to lock the structure in place and we anticipated that alignment would be rapidly lost if the sample were not immediately gelled. After one minute had passed concentrated Ca^{2+} salt was then added to prevent any further dissolution of the noodles, which appeared to be unaligned due to the

loss of brightness and dark regions (as shown by figure 40). The noodles are attempted to be grown in a single direction for ease of observation of alignment, rather than for a distinct purpose.
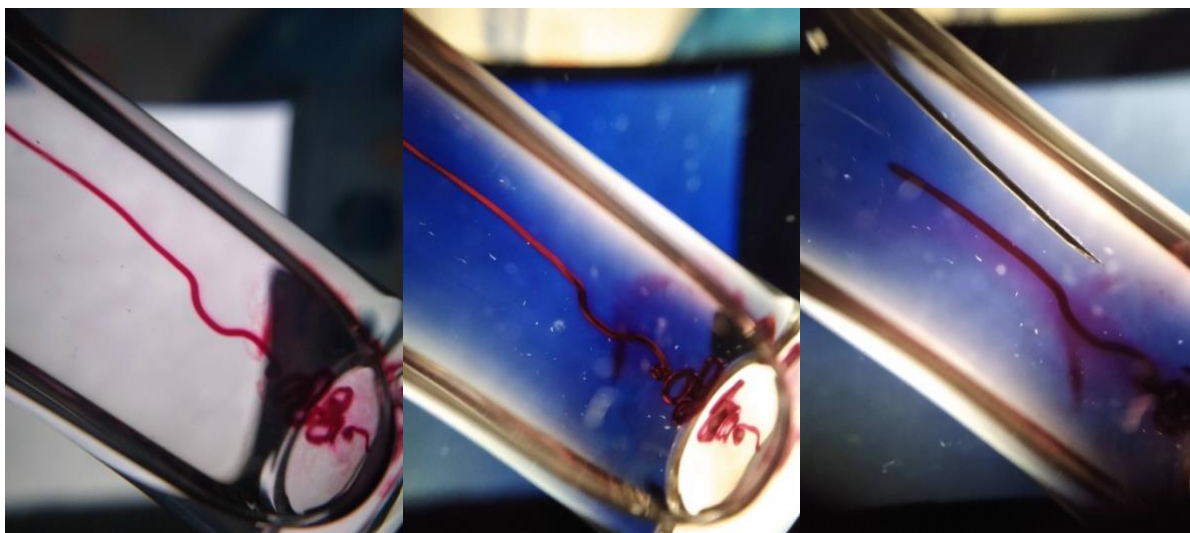
Figure 40- Images of PBI-I noodles pipetted into water over time. Image 1 shows the noodle with no crossed polarised filters and therefore provides no information about the alignment. Image 2 shows that the noodle is initially aligned as it is pipetted due to the shear forces, but image 3 displays the loss of alignment as the noodle dissolves in water.

To compare with the hydrogen-evolving aligned noodles, 28 unaligned noodles were prepared in water with methanol (20 v/v%), and then triggered by addition of the calcium salt. However due to the preparation in water the noodles began to dissolve and sank to the bottom of the vial, causing them to clump together and form a single structure (as shown by figure 41). Due to a lack of stirring the clumped structure stayed intact for the whole 3-hour illumination, but it did not yield any hydrogen. While this is an interesting outcome it was difficult to truly compare the unaligned noodle clump to free aligned noodles in solution.

Figure 41- Unaligned clump of PBI-I noodles which was used for initial photocatalysis testing to compare with aligned noodles. Clump was formed due to noodles dissolving on top of one another in water, before the addition of concentrated Ca^{2+} locked in the structure. This sample was then illuminated for 3 hours before headspace gas analysis.
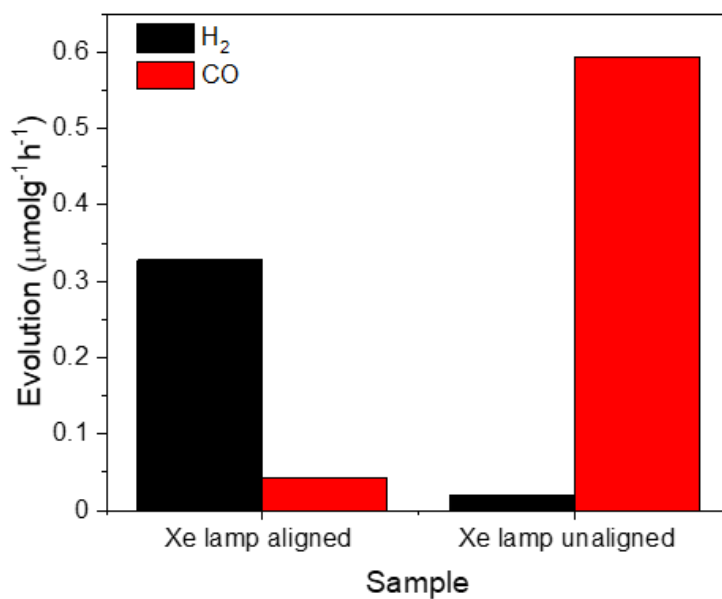
Figure 42- Hydrogen and CO evolution data from aligned and unaligned PBI-I noodles. 28 noodles were prepared in solution along with methanol. Platinum nanoparticles were present in the PBI solution. Illuminated for 3 hours using Xe lamp with no stirring.

Aligned PBI-I noodles produced an average of around 0.3 $\mu molg^{-1}h^{-1}$ while also evolving an average of 0.05 $\mu molg^{-1}h^{-1}$ of CO (figure 42). This evolution was quantified by GC injection, and calibrated using injections of a known concentration of calibrant gas. The unaligned clump of noodles did not produce any hydrogen above the detection limit, which was established when it became apparent that injections with air contained a larger than expected quantity of hydrogen gas. This was determined to be latent hydrogen present on the syringe used by other users from ongoing experiments. In addition, a much larger quantity of CO was evolved by the unaligned noodles, which may have been due to additional breakdown as a result of extended illumination of the same area of the noodle clump (lower surface area exposed to light). No CO_2 evolution was quantified due to lack of calibration and GC setup used, however it may explain why the column required baking out in between experiments.

Using the roller bed to break up and stir the noodle suspensions

Due to the unaligned noodle clumps forming in the control experiments, a change to the photocatalysis illumination was made. In place of the Xe lamp a single LED was used in combination with a roller bed set to a slow speed. This not only broke up the clumps of unaligned noodles, but effectively rotated the noodles to ensure that uniform illumination for all noodles was achieved. Initial experiments used a 365 nm UV LED (~20 $mWcm^{-2}$) with a 3-hour illumination which yielded no hydrogen above the minimum detection for either alignment type despite a higher degree of mixing (figure 43). Our PBI dispersions previously showed almost exclusive UV activity, but the change in morphology led to a change to a 490 nm LED to test visible light activity. Once again there was no hydrogen activity for either sample set. Figure 44 displays the noodles after being on the roller bed for 3 hours without any illumination; and provides clear evidence that alignment was still present in our aligned samples. There also seemed to be an element of alignment in the samples which were supposed to be unaligned, which suggested the method of making them could be improved.
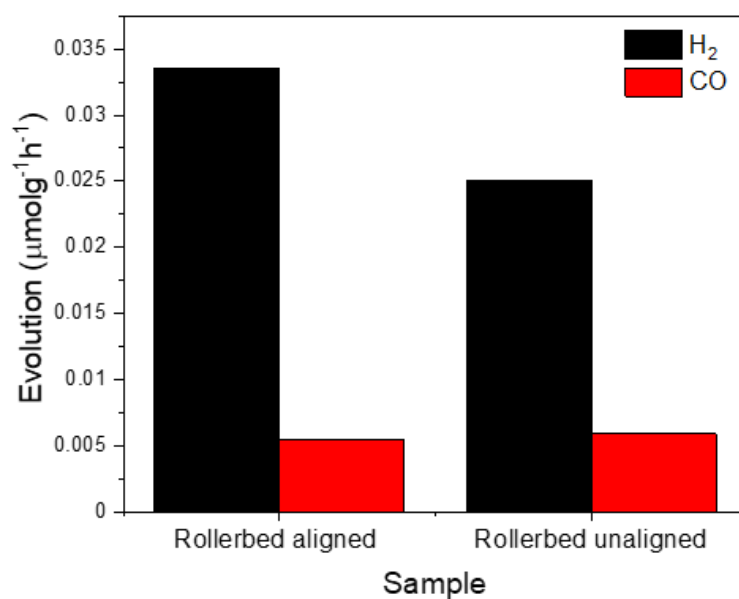
Figure 43- Hydrogen and CO evolution data from aligned and unaligned PBI-I noodles. 28 noodles were prepared in solution along with methanol. Platinum nanoparticles were present in the PBI solution. Hydrogen data shown in black, CO in red. Illuminated for 3 hours using 365 nm LED with a light intensity of 20 mWcm^{-2}, with slow stirring on a roller bed.
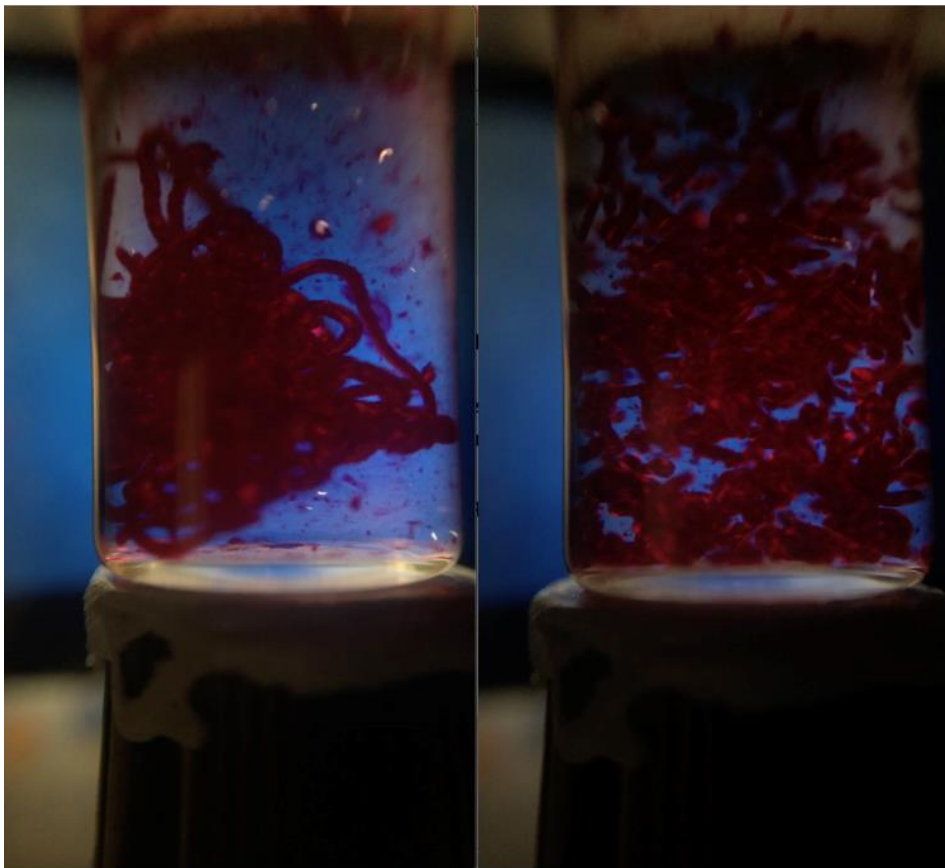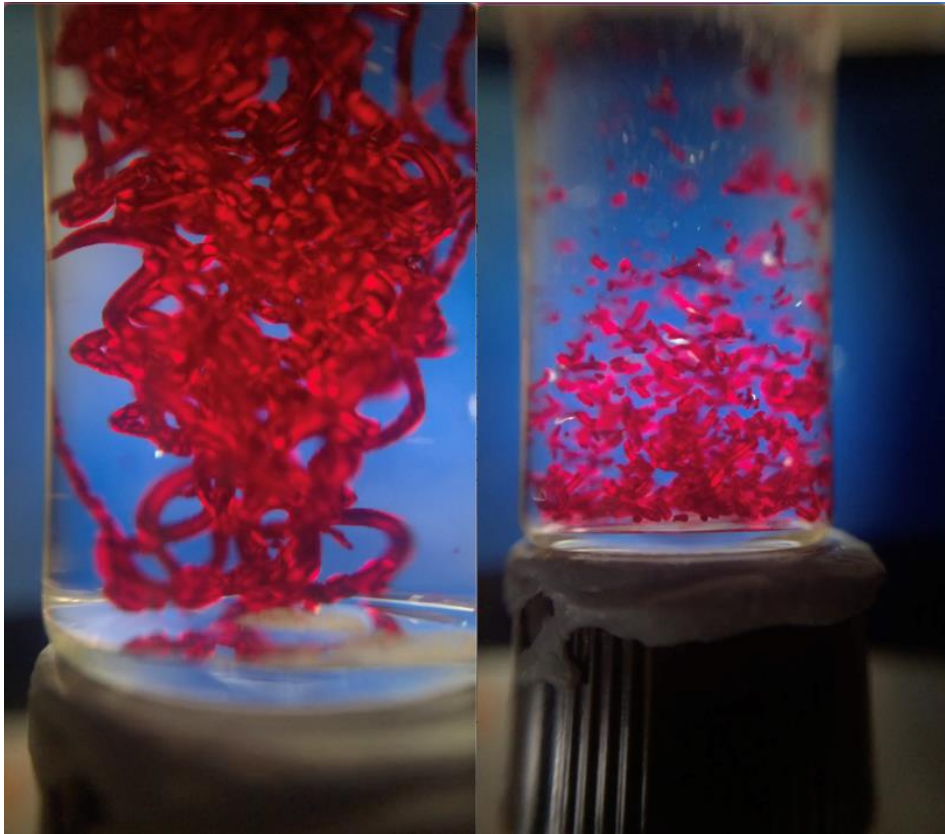
Figure 44- Noodles before and after rolled bed mixing for 3 hours. Top; Bright sections indicate birefringence and therefore alignment. Noodles are much smaller and broken up after mixing, but still bright. Bottom; unaligned clump of noodles before and after mixing.

Noodle UV-Vis and active species

Measuring the UV-Vis spectrum of the noodles was a challenge due to the high concentration of PBI solution used. Recorded spectra were obtained by squashing noodles into thin path length cuvettes, which appeared not to damage the structure; but made measuring purged samples impossible. Figure 45 displays the UV-Vis spectra of aligned and unaligned noodles along with the spectrum of the solution the noodles were made from; pH 6 adjusted 10 mg/mL PBI-I containing platinum nanoparticles (1 wt.%). Both noodle spectra appear to be broader than the solution indicating a greater degree of environments due to assembly triggered by salt-induced gelation. The spectrum of the aligned noodle also appeared to be broader than that from the unaligned noodle, which is interesting as alignment should in theory reduce the number of different environments that exist for a PBI molecule in a noodle. It should be noted however that due to the method of measuring the UV-Vis spectra of the noodles the structure may have been altered due to pressure applied when measuring the noodle samples.
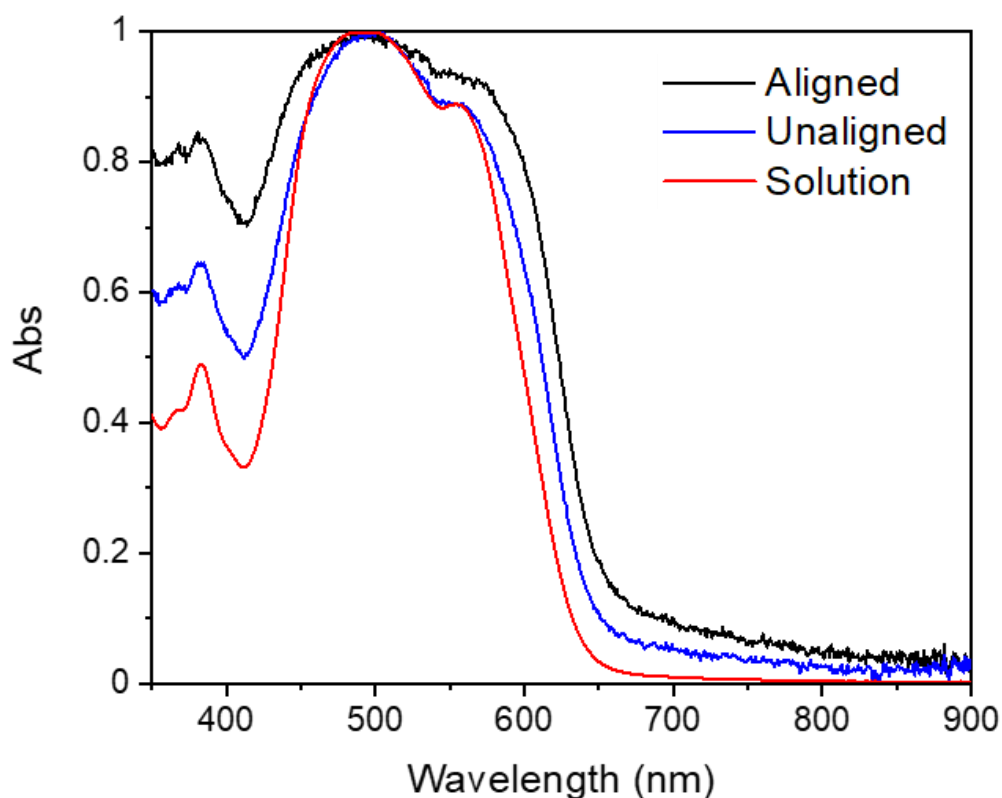
Figure 45- UV-Vis spectra of PBI-I noodles formed via salt-induced gelation method as described earlier. Solution contained 10 mg/mL PBI-I and Pt nanoparticles (1 wt. %). Aligned noodles were formed by pipetting into salt solution (50 mM in water), whereas unaligned were pipetted into water before the addition of salt. Absorption is normalised. The sharp step at 550 nm is a result of instrumentation.

PBI-I solution was illuminated with a 365 nm LED and a UV-Vis spectrum was recorded before and after to examine the species that could form within a noodle. There was clear evidence for the generation of the PBI radical anion with peaks at 725 and 810 nm which dominated the spectrum after illumination. Despite the intensity of the peaks formed upon illumination, it is difficult to infer whether a large concentration of radical anion has been generated or not, as in some cases subtle differences in the UV-Vis spectrum result from large amounts of radical anion.[104] Nevertheless the formation of the radical anion species was confirmed via photoreduction after a short illumination, thus confirming a potential charge carrying species which can form in supramolecular noodles (figure 46).
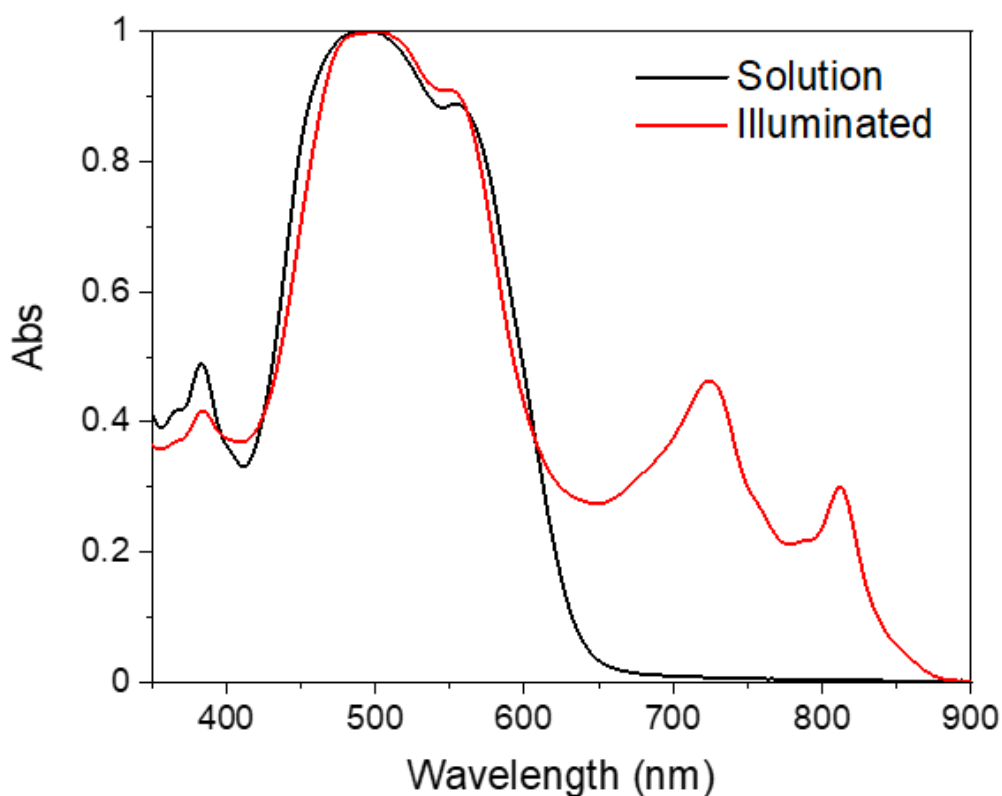
Figure 46- UV-Vis of PBI-I solution used to form noodles before and after illumination with 365 nm LED (red). Solution was 10 mg/mL PBI-I and contained Pt NP (1 wt. %). Cuvette pathlength was 0.1 mm. Absorbance data was normalised.

We were unable to pinpoint the active species responsible for photocatalytic activity in our high throughput study, however it was clear that generating a long-lived charge separated species such as a PBI radical anion was of paramount importance. The radical anion was generated in the PBI-I solution via illumination, and by chemical reduction of a PBI-I noodle shown in figure 47. The resulting spectrum of the chemically reduced noodle was more like that from the unreduced noodle than initially expected. There was a clear colour change from dark purple to lilac upon addition of the sodium dithionite, which was not picked up by UV-Vis and may have been due to the lack of stability of the reduced species when exposed to air, or due to structural changes after squashing the noodle into the thin cuvette. In contrast, the colour change that occurred post illumination from a photocatalysis experiment did not mirror that of the chemical reduction, and instead black noodles were produced that appeared to have lost alignment via photo inspection. Once again, this change was seemingly

not detected by UV-Vis as the post illumination spectrum was not significantly different to that of the noodle before illumination (figure 48).
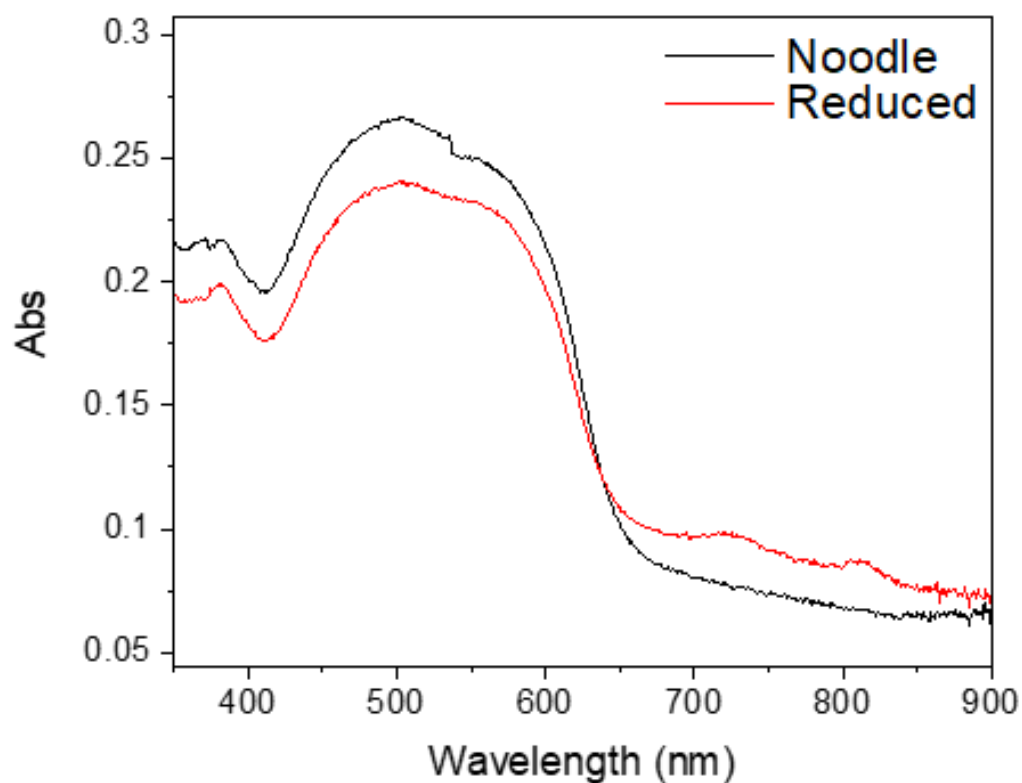
Figure 47- UV-Vis spectra of PBI-I noodles formed via salt gelation method as described earlier. Solution contained 10 mg/mL PBI-I and Pt nanoparticles (1 wt. %). The noodle was then chemically reduced using an excess of sodium dithionite solution, a subsequent spectrum was recorded and is shown in red. Step in the spectrum as a result of the instrument.
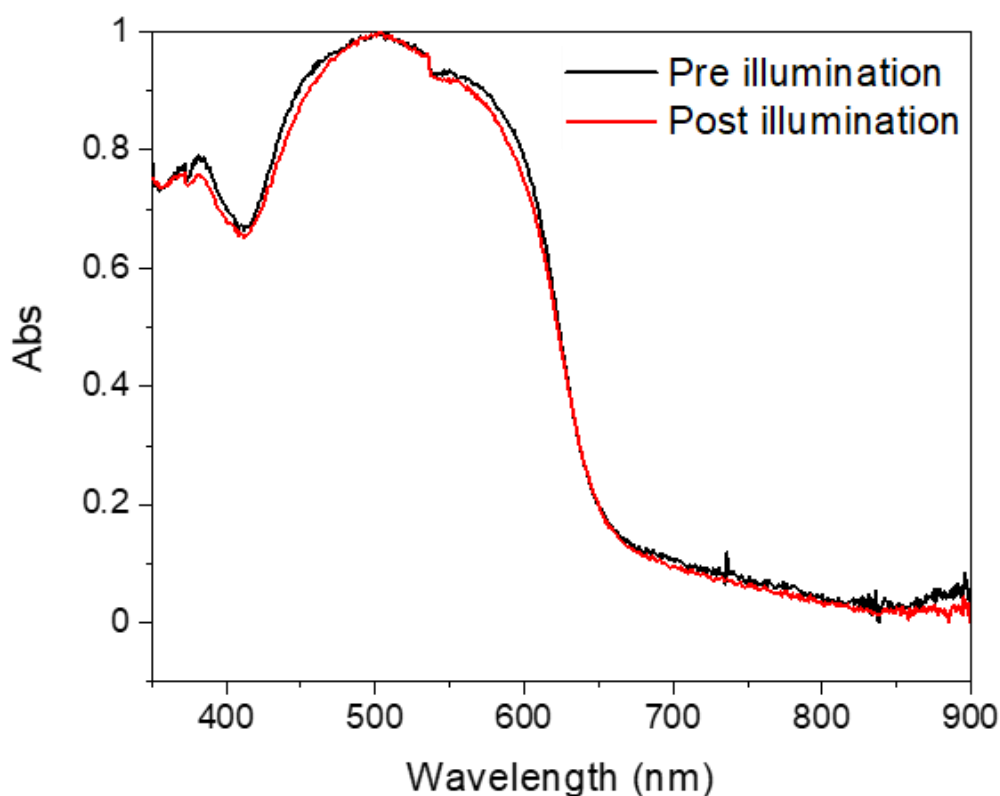
Figure 48- UV-Vis spectra of PBI-I noodles formed via salt gelation method as described earlier. Solution contained 10 mg/mL PBI-I and Pt nanoparticles (1 wt. %). Noodle was illuminated with a Xe lamp for 3 hours before a spectrum was recorded.

Lack of noodle activity in the HER

The initial noodle photocatalysis experiments were highly promising due to the detectable level of hydrogen (0.2 μmolg^{-1}h^{-1}) with 28 aligned noodles in a vial. However, the difficulties with forming unaligned noodles posed a huge issue, in combination with a lack of reliable method for quantifying the alignment besides the qualitative images generated in the birefringence experiment. A SAXS study was performed by Daniel McDowall to attempt to explore differences in the packing between aligned and unaligned samples, but ultimately this was not successful due to the perceived lack of alignment in our aligned samples. This coupled with the lack of activity in the HER despite intense illumination for multiple hours led to a rethink about the approach to the project. While there is no doubt that the noodles are an interesting modification of a well-known class of materials, the hypothesis of alignment had not been quite demonstrated beyond a series of images. A high throughput study of a series

of noodle making PBIs could have explored several key variables, to truly pin down what causes the activity or lack of it in PBI noodles. But at the time of testing only a single PBI had been identified to successfully form noodles, and the correct conditions for evolving hydrogen reproducibly were not found. In addition, the difficulty in working with the noodle solutions was extreme due to the lack of reproducibility between samples. There were many occasions where solutions made on the same day with the same materials would behave very differently when it came to adjusting the pH, which led to huge variation in the noodles produced. If all these concerns were addressed, there is still the issue of illumination which could be a whole study, due to the complexity of understanding PBI photophysics. PBIs are known to be able to absorb multiple photons of different wavelengths to form highly reducing species,[130] which if applied to the noodle morphology are quite exciting but beyond the scope of this study at this point. What is clear is that simply stating hydrogen evolution rates is not the only way to understanding how these structures behave, and the real key is studying the processes in depth through spectroscopy.

Conclusions and future work

This study encompassed a vast body of work, and while it was apparent that PBI based photocatalysts dispersed in water are unlikely to deliver ground-breaking hydrogen evolution rates without being paired with another functional moiety. However, what has been explored in this chapter is a complex relationship between self-assembly and hydrogen evolution rates, for 8 different amino acid functionalised PBIs. Without the use of a high throughput setup, completing the photocatalysis experiments alone would have taken months. Our approach allowed us to investigate three key variables which were amino acid functionality, pH and methanol concentration (v/v%). These variables were all found to have a significant impact on the self-assembly process, and thereby the ability to evolve hydrogen. We found that self-assembly and the size of the aggregate could control photocatalytic activity, which in itself was very exciting. In addition, we were able to correlate a particular type of aggregates which involved substantial coupling between neighbouring PBI chromophores, to activity in the HER.

From our SAXS analysis we were able to confirm that our dispersions at high pH were comprised of short chains of PBI, between 2-6 units in length. As the pH was lowered these units began to stack extensively, until they formed massive supramolecular structures on the order of 700 nm, that could no longer be quantified by SAXS analysis. We were able to induce these changes by simply lowering the pH, which opens a huge opportunity to perform similar studies on similar systems and molecules. Instead of simply investigating synthetic changes when designing future organic photocatalysts, more emphasis needs to be placed on how these molecules will behave in solution when exposed to different stimuli.

In our research paper that this chapter is based upon we used the comparison of PBI-A vs PBI-Y as it made for an effective comparison between an active and inactive photocatalyst.[49] This chapter allowed for a more thorough examination of all PBIs in this study, and thankfully strengthened our argument for the importance of type 2 aggregates. PBI-V in particular shows many parallels to the successful hydrogen evolving PBI-A data, with a clear switching on at around pH 5 coinciding with the prominence of the type 2 aggregates. Another active catalyst PBI-F also shared the requirement for type 2 aggregates, but did not develop the characteristic broadness shown by both PBI-V and PBI-A at low pH to signify the formation of type 3 aggregates. The argument was solidified by the PBI-H dataset which did not contain

any type 2 aggregates at any pH, in accordance with its inability to evolve hydrogen at any pH.

It we uncovered the same mixing of the FE and CT bands that has been demonstrated throughout the PBI photocatalysis literature, and there was a clear correlation with the UV-Vis spectra within our study. This mixing of states was a crucial factor in determining the success of the specific system, but did not completely explain why there was no hydrogen evolution at the extremes of pH. Short bonded PBIs have been shown to display the same mixing we describe in our larger structures,[151,160–162] but this did not appear to be enough to contribute to catalysis. We were also unable to determine the active species, and why certain PBIs worked and why others didn't, but this will be explored further in chapter 2. Nevertheless, the success of the fitting process to evaluate hydrogen evolution in active PBIs cannot be overstated.

Finding a suitable PBI that was able to form stable noodles came late in the timescale of the project, and despite significant efforts we were unable to complete the study due to issues with sample preparation. While the noodles themselves were undoubtably produced excellent images their activity in the HER was questionable, and there seemed no conclusive way of making them reproducibly due to small differences in solution preparation. With more time, I do believe we would have been able to form conclusively aligned and unaligned noodles, and to test the hypothesis to see whether alignment of the noodles improved charge transport. But due to time constraints a high throughput study was not achievable, and even then, the sample preparation would have been difficult. The bigger question from this study was also how the noodles behave when exposed to light, as they opened a wide variety of potential experiments. Due to their high absorbance, many spectroscopic studies would have been challenging to perform, but could have yielded many answers for how they behave. To conclude, the noodles were a potentially very interesting avenue that was not quite realised within the duration of this project.

Chapter 3: Uncovering the relationship between PBI self-assembly and photophysical properties: A transient absorption study

Introduction

In the previous chapter we explored how controlling the structure can enhance the hydrogen evolving capabilities of PBI based photocatalytic dispersions. In this chapter we wish to elucidate further our understanding of PBI photophysics, which governs the ability of a system to effectively separate and transport charges. Once excited, PBIs are known to form tightly bound excitonic species,[92,162–164] which struggle to overcome the strong coulombic attraction that governs the behaviour HER. Our self-assembled PBI samples contain non-covalently bound chromophores which interact with one another, and we propose this allows for charge distribution across many PBI units. For PBIs this comes in the form of PBI radical species, $PBI^{\cdot-}$ and $PBI^{\cdot+}$, which have the charges localised on different PBI units. This separation can be strongly affected by temperature,[165] and also solvent polarity; with more polar solvents leading to more efficient charge separation. However, at elevated temperatures the formation of the radical anion is suppressed in perylene based dimers, leading to a so-called restoration of symmetry of charge.[165] This is in reference to the term symmetry breaking charge separation (SB-CS), which refers to a lack of symmetry of charge in covalently bound perylene dimers (and trimers) as a result of photoexcitation.[151,161,162,165–169]

Transient absorption spectroscopy (TAS) allows for the detection of PBI based excited species due to the difference in absorption spectra of the PBI radical anions (and cation), relative to the neutral species. Typically, the PBI radical anion peaks are present around 730, 820 and 980 nm (for an amino acid functionalised PBI such as PBI-A) following a relaxation from the excited singlet PBI state.[85,105,142,146,170] However the PBI radical cation was harder to identify in our previous work on PBI-A,[85] despite being widely reported in the literature at a variety of wavelengths.[171–175] This was attributed to the electron donor like properties of the amino acid alanine functionality,[85] which suggested the localisation of the hole onto the alanine side chain. The oxidised alanine is likely to absorb in the UV spectral range and is therefore difficult to track while also observing the effects on the PBI core. However, there are frequent reports of excimer formation in PBI based systems,[94,174,176–178] which leads to charge carriers being bound to different PBI units, as opposed to intramolecular separation suggested in PBI-A

fibres. While the charges are formally assigned to different PBI units the reality is that the charge can be delocalised over several units, which leads to broad TA spectra encompassing multiple PBI units in a self-assembled structure, in contrast to well defined features shown in monomer species. The broadening present is a result of interchromophore coupling in π stacked structures, and is highly dependent on solvation where polar solvents with high dielectric constants can allow for more effective separation of charge.[171,178,179] There are also profound differences when considering the size of the PBI structure, and which solvent is best suited to solvating it.[180,181] For example, Wurthner *et al.* investigated the effects of chloroform vs THF in a PBI based 'folda-dimer' and elucidated that PBI stacks were more effectively solvated by THF, and individual PBI units were more effectively solvated by chloroform.[181]

Figure 49 describes the process of excimer formation, which can lead to eventual SB-CS, and was shown to yield the charge separated radical anion and cation in just 12 ps.[171] There appears to be some debate in the literature as to whether the formation of long-lived excimers is beneficial to the yield of mobile charge carriers, which can be used for solar fuel production. As several publications state that the long-lived excimer can lead to long lived states with the ability to generate charge separated species.[176,180] The matter in question centres around the mobility of this excimer state, and whether it can overcome the coulombic forces that hold it together, even at distances of between 5-10 PBI units in some cases (figure 49).[163]
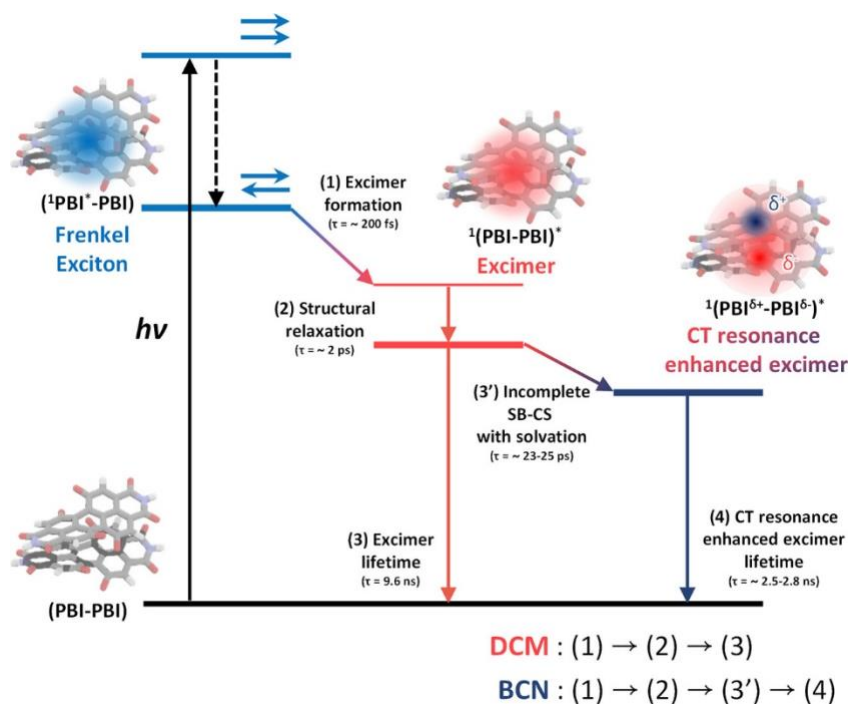
Figure 49- A Jablonski diagram which describes the excited state pathway for a PBI system from Wurthner et al. Reproduced with permission.[174]

Recent work by Spano *et al.* has highlighted the importance of short-range packing of PBI structures, with particular emphasis on the interaction between the Charge Transfer (CT) and Frenkel Exciton (FE) bands, and how subtle differences in the local geometry can have a profound effect on the fate of the excited state. The interchromophore distance appears to be a key consideration,[182] with shorter distances of 3.5 Å leading to strong coupling and therefore an excimer type state (Figure 49), but longer distances of between 6.4-10.8 A have been shown to have weaker coupling and a preference for eventual formation of SB-CS.[151,182] The distance between chromophores is often difficult to control without covalent linkages, and will therefore heavily rely on the nature of the imide functionality. In the previous chapter we did not discuss the difference in interchromophore spacing as a potential hypothesis for activity trends. But the reality of using different amino acid functionalities is that there was an effect on the electronic profile of the PBI core, and therefore the $\pi-\pi$ stacking will have also subtly changed. Unfortunately, wide angle x-ray scattering (WAXS) measurements were not performed on the PBI dispersions, so it is not possible to comment further on how significantly this affected our samples.

We have previously investigated PBI-A photophysics using TAS.[85,183] Although self-assembled structures were explored, the exact morphology was quite different and centred more on forming PBI films, and investigating changes as a result of water content, as opposed to dispersions in water. Nevertheless, these studies detail the presence of the long lived PBI radical anion, and also the likely oxidation of the amino acid functionality.[183] While the lack of stability of the PBI-A species is concerning, it does suggest the likely charge separation of the initially formed excitonic species, which goes hand in hand with the photocatalysis results from chapter 2 which showed clear generation of hydrogen. Our initial study on PBI-A films also suggests the need for methanol to effectively charge separate using visible light.[85] We investigate this requirement further in this chapter with a direct comparison between PBI-A and PBI-Y dispersions, in an attempt to uncover why PBI-A was a successful photocatalyst and PBI-Y was not.

Experimental design
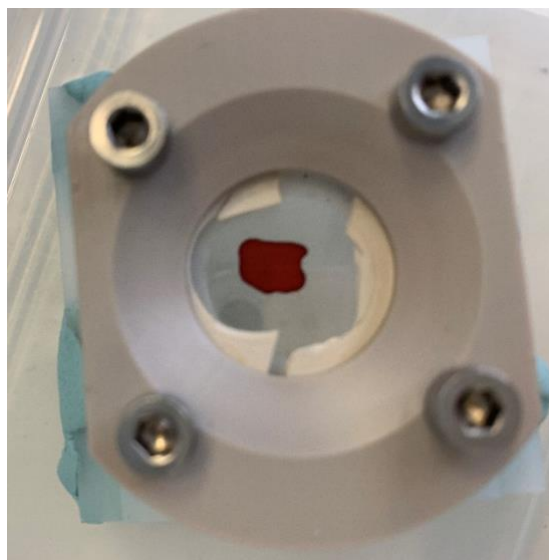
Figure 50- Image of the cell used to perform TA experiments, with a sample of PBI-A in the centre.

An Image of 3D printed cell designed by Khezar Saeed containing a PBI sample is shown in figure 50. Having already investigated the PBI dispersions as photocatalysts for hydrogen evolution, the logical next step was to attempt to uncover the reason for the activity in PBI-A and the lack in PBI-Y. A large part of the previous chapter directly compared the structural features of the successful photocatalyst PBI-A, and the perceived inability of PBI-Y to form the crucial type 2 aggregates. Although expanding this hypothesis to the other PBIs in the study potentially could weaken this hypothesis, we aimed to expand the study to compare the photophysical properties of PBI-A and PBI-Y (figure 51).
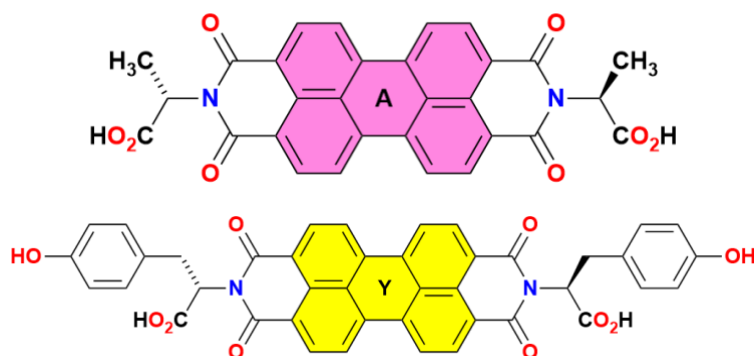
Figure 51- Molecular diagrams of both PBI-A and PBI-Y with different amino acid functionality

Due to the time-consuming nature of running and analysing TA experiments, three pH's were chosen for each PBI to demonstrate each dominant local structure type at that pH; pH 10 for type 1, pH 5 for type 2, and pH 2 for type 3. However, it quickly became clear that running samples at pH 2 would not be possible, due to the lack of homogeneity of the sample. In addition to this, running the samples in the conventional cuvettes was also not possible, as a result of high absorbance of the samples at the concentrations chosen for the photocatalysis measurements. We chose to maintain the same PBI concentration throughout all experiments, in accordance with all previous measurements in the previous chapter at 5 mg/mL (as concentration impacts assembly). This meant that we needed to design a cell with a thin path length that would be able to fit inside the spectrometer. Thankfully, another member of the research group Dr Khezar Saeed was able to design a suitable cell for the experiments. The basis of the cell was two CaF_2 windows pressed as closely together as possible, to mimic the UV-Vis measuring procedure from the previous chapter but with more control. The screws in the cell allowed for compression of the windows, and the distance between them was controlled by the spacer. Purging of the samples was not possible due the very small distances between the windows and small volumes used, with experiments on the picosecond (ps) timescale not expected to be heavily impacted by diffusion controlled processes. Another complication was that the absorption coefficients of the samples changed substantially with pH, therefore different spacers and volumes were required to obtain a similar optical density in each sample. For our measurements, the ideal optical density was around 0.4 O.D., to ensure that around 50% of the incident light was transmitted through the sample. These protocols were developed through the process of optimising the experiment over many iterations, which eventually led to the final measurements which were the best representation of how to run the experiment. The experimental setup and design iterations are detailed fully in the appendices.

Transient absorption study on PBI photocatalysis
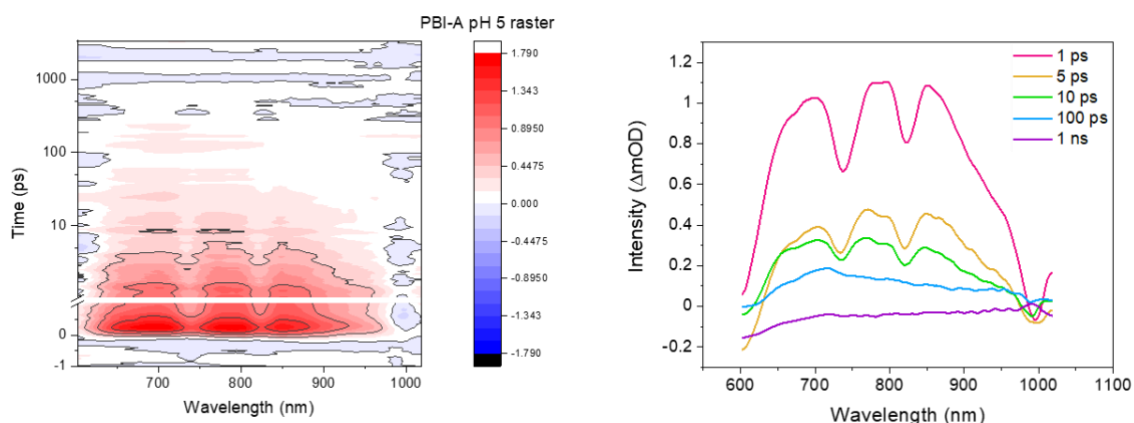
Figure 52- TA data comparing PBI-A at pH 5 with 25μm spacer. Contour plots shown on left and time slices on the right. Contour plots display most intense changes in absorbance through the experiment in red (If positive) and in blue (if negative). Key time slices illustrate the species present at that particular time period. Samples contained PBI-X 5 mg/mL, methanol v/v% and Pt nanoparticles (1 wt.%). Pump light intensity 1 mWcm^{-2}. Pump wavelength 490nm. Rastered sample.

We decided to raster the sample to prevent damage of the sample in a single spot, due to the power used in this set of experiments. However, rastering the sample led to an even more significant discovery, with significant bleaches at 730, 820 and 980 nm, which was shown in figure 52. The quality of the data was noticeably worse due to the lack of homogeneity of the sample at this pH, but the time slices clearly displayed a negative feature at each position where the expected PBI-A peaks were. These negative features persisted for the first 120 ps before being replaced by the broad photoinduced absorption (PIA) present underneath. This broad PIA had been dominated by the 3 bleaches which were indicative of the PBI radical anion being pumped to a higher state by the pump laser, and had not been seen in any previous experiments to our knowledge. Performing a double excitation (i.e. the excitation of the excited state formed by a previous pulse of the high repetition laser system) in a single experiment on this time period seemed highly unlikely, therefore it prompted the realisation that the PBI radical anion had likely been present in the sample since the previous laser shot seconds ago. The UV-Vis spectrum of the sample post illumination was also recorded and is shown by figure 53. The change in absorbance at 730 and 820 nm clearly indicates the lifetime of the PBI radical anion is far longer than the period of time used in the TA experiments, and also a large enough quantity to be detectable an hour after the measurement.
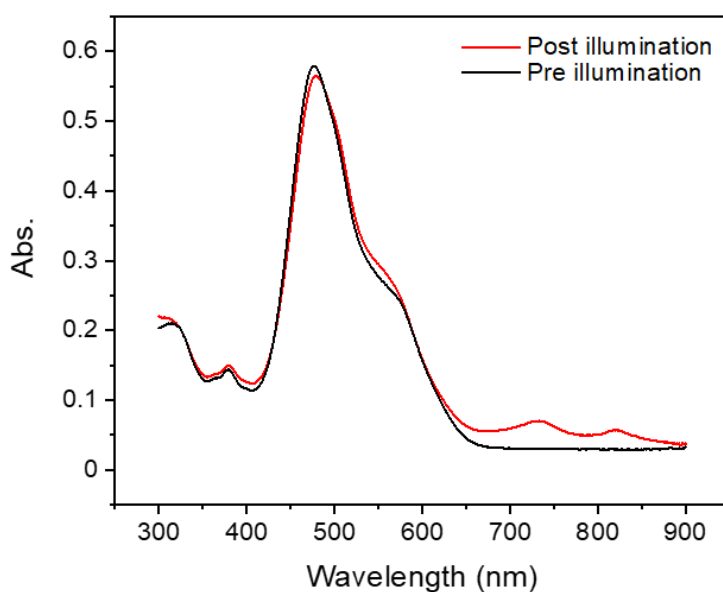
Figure 53- UV-Vis of PBI-A pH 5 sample pre and post TA experiments. Sample was illuminated with 490 nm light at 1 mWcm^{-2}. Samples contained PBI-A 5 mg/mL, methanol v/v% and Pt nanoparticles (1 wt.%).

The very long-lived species complicated proceedings, as it was shown to live longer than the time period of the experiment. This species was confirmed by the pre time zero data, the time before the species should be generated (figure 54 and 55) and meant that any data handled would have to subtract this offset from any future scans. In addition, due to the accumulation of the PBI radical anion single spot measurements on the sample were no longer suitable and rastering the sample was the only option to remove as much of the PBI radical anion as possible. It also appeared that using a single sample for multiple scans was also no longer possible, once again due to accumulation; and therefore, a new sample would be required for each measurement.
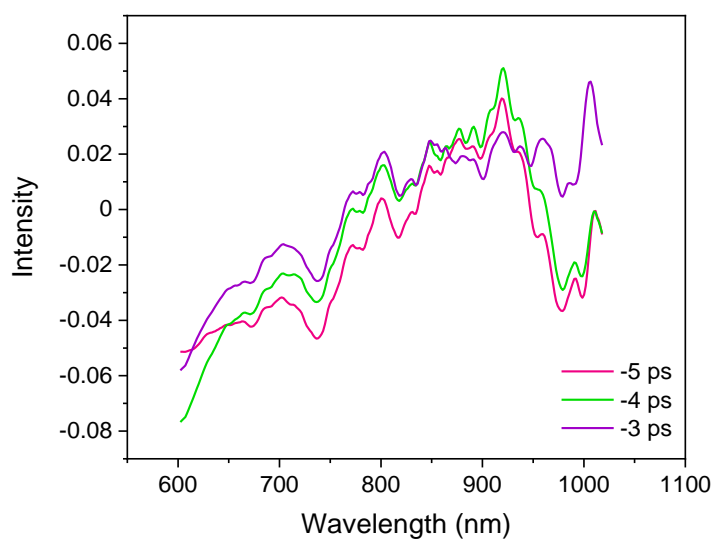
Figure 54- Pre time zero data for PBI-A pH 5 25 μm spacer showing that transient features are present from the previous excitation pulse. Samples contained PBI-A 5 mg/mL, methanol 20 v/v% and Pt nanoparticles (1 wt.%). Pump light intensity 1 mWcm^{-2}. Excitation wavelength 490nm. Rastered sample.
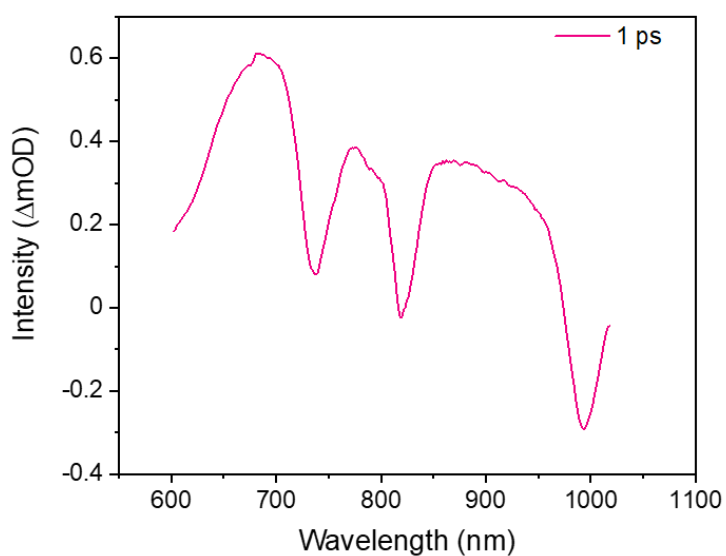
Figure 55- Single time delay for PBI-A pH 5 with a 25 um spacer, 1 mWcm^{-2}. Scan performed 5 times on a single spot on the sample. Samples contained PBI-A 5 mg/mL, methanol 20 v/v% and Pt nanoparticles (1 wt.%). Pump light intensity 1 mWcm^{-2}. Excitation wavelength 490nm.
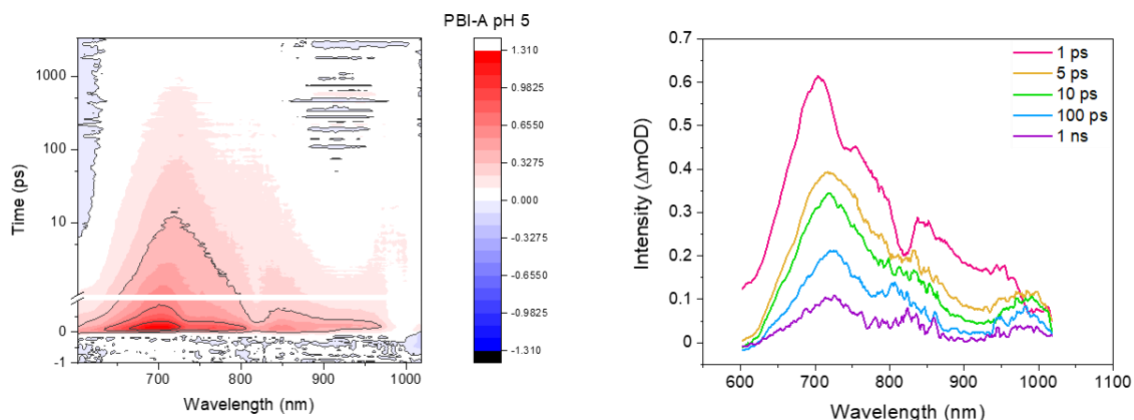
Figure 56- Full delay line PBI-A at pH 5 with a 25μm spacer, sample post single time delay measurement. Contour plots shown on left and time slices on the right. Contour plots display most intense changes in absorbance through the experiment in red (If positive) and in blue (if negative). Key time slices illustrate the species present at that particular time period. Samples contained PBI-A 5 mg/mL, methanol 20 v/v% and Pt nanoparticles (1 wt.%). Pump light intensity 1 mWcm^{-2}. Excitation wavelength 490nm. Rastered sample.

Figures 54 and 55 were performed on a single position on a PBI-A pH 5 sample without rastering (constant sample movement throughout the experiment). First a single time delay at 1 ps was performed to simulate the conditions of pumping the PBI radical anion to a higher energetic state, followed by a full delay line experiment to track the evolution of the remaining PBI-A radical species that has not been pumped. The initial bleaches in figure 56 are replicated in the full delay line, but the rate of their removal appeared to be faster to yield a typical spectrum for a PBI-A radical anion by 10 ps as opposed to 120 ps in the first instance. Therefore, if we are able to control the rate of pumping of the radical anion to make it sufficiently small, we should be able to track its transient formation and evolution effectively. If we were unable to suppress the rate of excitation to a higher order we could not perform these experiments. At this point we were unable to assign the pumped PBI radical anion species (PBI^{-})* to any transient features in this window, which suggests that the PBI^{2-} is not formed in this set of conditions due to a lack of a feature growth around 605 nm (highly solvent and substituent dependent).[73,102]

The UV activity of PBIs has been widely documented, but thus far only 490 nm has been used as the pump wavelength in the TA experiments. We were ultimately unable to incorporate 365 nm measurements into this study, due to excess generation of the long-lived PBI species.

Upon recording the background white light measurements through the sample, the background was changing so rapidly due to generation of PBI radical species it was not possible to reach a steady PBI⁻ state to perform the experiments, and therefore only visible measurements are performed from this point onwards.

Having finally arrived on a reproducible method of performing the experiments several earlier studies were repeated with the new experimental parameters (appendices). The light intensity was lowered to 100 μWcm^{-2}, to ensure the concentration of PBI anion was kept low enough for the study of its generation and lifetime to occur (10x lower than previously). The sample was also rastered on the slowest setting, due to the lack of homogeneity of the pH 5 sample, the eventual data was quite noisy and required 5x repeats. These repeats were then merged to form a single dataset for each sample, which was then used to fit the data and form models that could contribute towards the mechanism. The probe wavelength window was also shifted further to the blue in order to understand what was occurring in the neutral film, in addition to the radical species population produced.

PBI-A pH 5
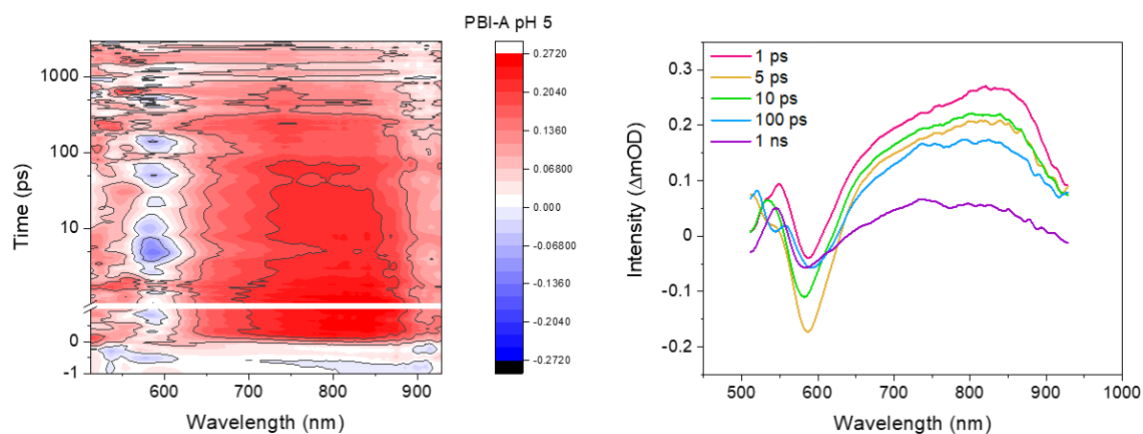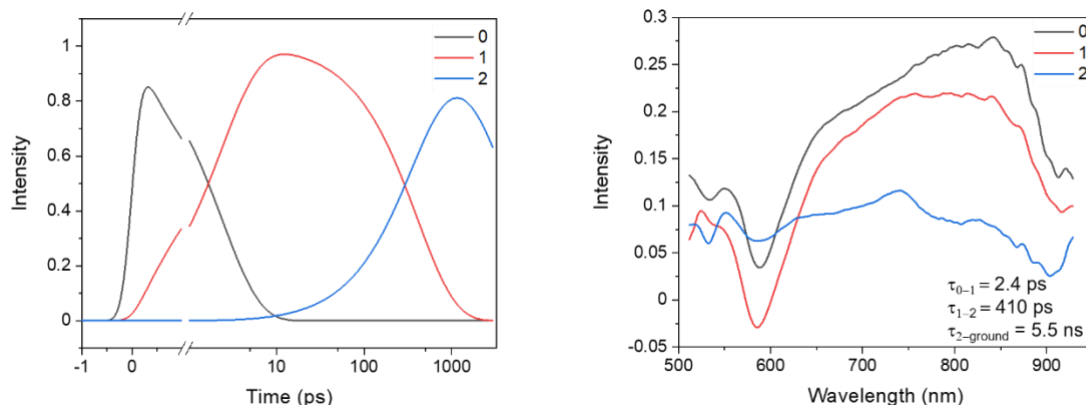
Figure 57 - TA data comparing PBI-A at pH 5 with a 25μm spacer. Contour plots shown on left and time slices on the right. Contour plots display most intense changes in absorbance through the experiment in red (If positive) and in blue (if negative). Key time slices illustrate the species present at that particular time period. Samples contained PBI-A 5 mg/mL, methanol 20 v/v% and Pt nanoparticles (1 wt.%). Pump light intensity 100 μWcm^{-2}. Pump wavelength 490nm. Rastered sample. Fittings performed in Carpetview software using global lifetime analysis, 3 compartment model.

Due to the controlled film thickness and lower absorbance the signals achieved were far lower than had previously been recorded (Appendix figures 100-112). In addition, the random sample rastering and subsequent merging of scans helped to keep the concentration of PBI radical anion low enough so that there were no pronounced bleaches assignable to PBI⁻. The resulting data is quite similar to the initial run using thicker samples with an initial broad PIA between 600-900 nm (appendix figures 102-113), which then slowly localises to yield a species which looks similar to the PBI radical anion.

The data was fitted using three compartment sequential model global analysis on Carpetview (figure 57) and produced two fits to describe how the species decays, and also what that species likely looks like. The three-compartment model was chosen after single value decomposition analysis, which suggested a 3-compartment model as the most appropriate. The initially formed species (labelled as 0) describes the rapidly formed broad species with peaks at 650, 730 and 819 nm and decayed rapidly (2.4 ps) to form the second species. The broad species aligned with what was expected of an excitonic species due to the likely charge localisation over a number of PBIs. The extent of broadening decreased from state 0 to state 1, potentially due to charge being localised over fewer PBI units.

This process is described in literature as excimer like, which explains the uncharacteristic broadening towards the blue to encompass some PBI cation like behaviour. This excimer state allows the charges to live longer than they would be able to were they to localise fully, to form a 'charge transfer enhanced excimer state' as coined by Wurthner *et al* (state 2).[184] This excimer state is highly solvent dependent and makes excellent use of the highly polar water exhibited throughout the PBI structure, to stabilise this excimer like state. The lifetime of such a state has been described on the order of multiple nanoseconds, [177,178,185] and enables the PBI structure to act as a successful hydrogen evolving photocatalyst.

We do not see any evidence of the mixing of the FE and CT bands in real time, which we have described previously due to our UV-Vis study (chapter 2). This mixing occurs on the femtosecond (fs) time scale and was likely not observable within our experimental parameters. However, we do have good agreement once again that it has indeed occurred, due to the broad species that has formed, which indicated a huge degree of delocalisation of charge. This delocalisation led to the formation of an excimer like state, which over a period of 100s of ps began to localise over a smaller number of PBI units, leading to a likely polarisation between the stack from a PBI unit baring a mostly positive charge to another baring a mostly negative charge. The final state in the model displays this character with the characteristic PBI anion peaks accompanied by a new peak at 630 nm due to the cationic character delocalised over a number of PBI units. The active species taking part in catalysis has not been revealed at this stage, due to a lack of transfer to the platinum. Nevertheless, there was evidence of a long-lived charge separated state with the potential to perform catalytic reduction.
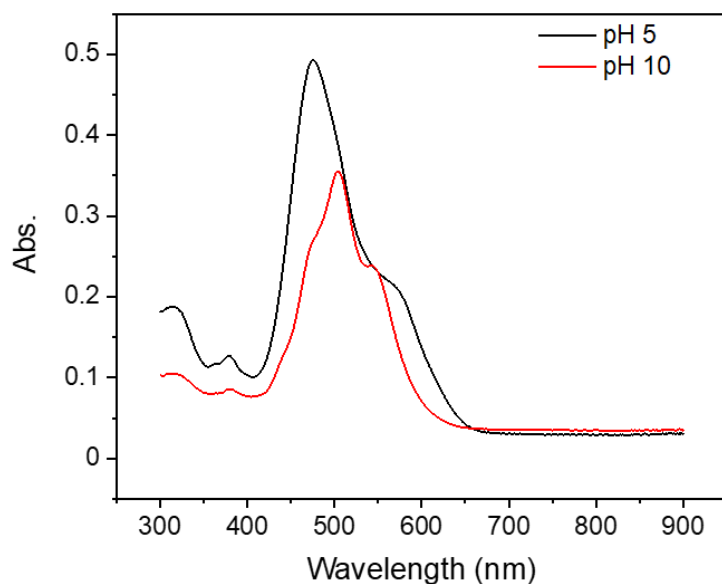
Figure 58- UV-Vis spectra of PBI-A at pH 5 using 25µm spacers and pH 10 using 10 µm spacers. Samples contained PBI-A 5 mg/mL, methanol v/v% and Pt nanoparticles (1 wt.%).
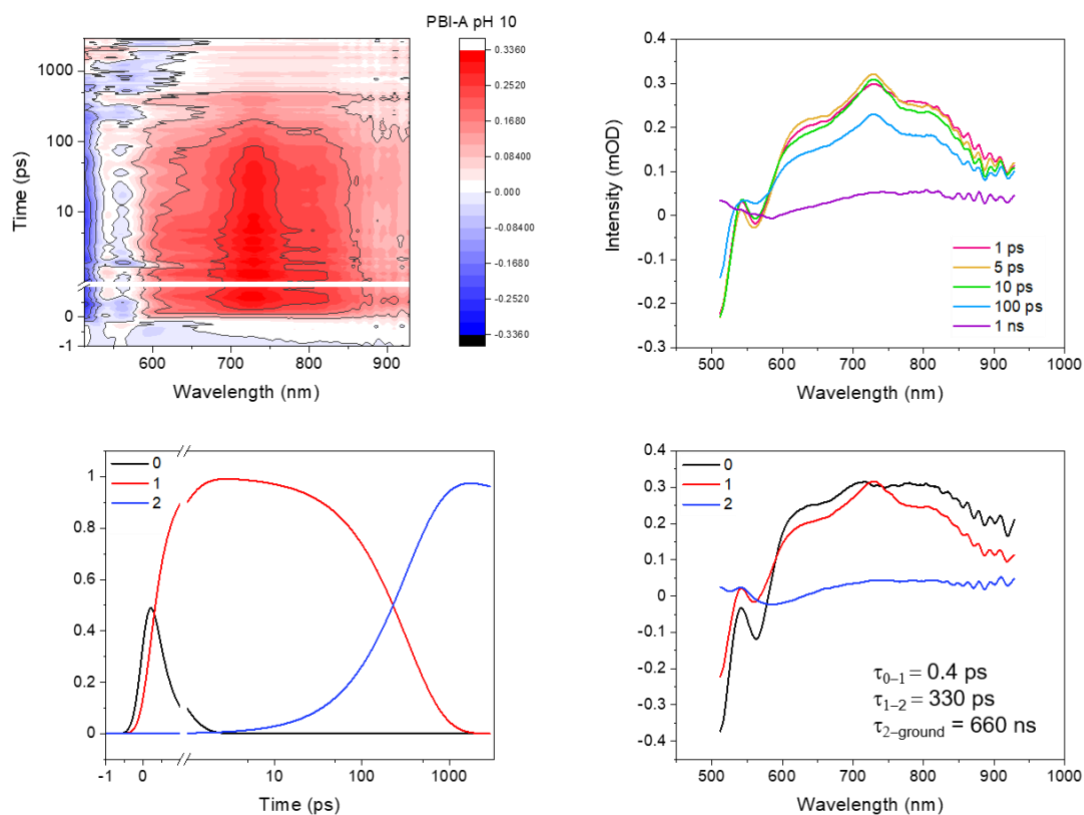

Figure 59- TA data comparing PBI-A at pH 10 with 10µm. Contour plots shown on left and time slices on the right. Contour plots display most intense changes in absorbance through the

Due to the higher absorbance of PBI-A at pH 10, samples required the thinnest spacer (10 μm) to achieve a transmittance of around 50 % (figure 58). But other than the small difference in sample preparation the data collection proceeded in accordance with the pH 5 data, as demonstrated by figure 59. First of all, the ground state bleach and stimulated emission had greater Δmo.D. (530 and 570 nm). The contour plot illustrates a dramatic difference in the early timescales, but it is better defined by the time slice traces which confirm 3 sharp peaks forming within 1 ps. There appeared to be little evolution in these peaks within the first 100 ps, either in position or broadness. In fact, the three peaks uniformly decayed throughout the measurement, but the final state does look significantly broader (figure 60). This contrasts strongly with pH 5 which formed an initially broad state that localised over 100s of ps. The final state at 3 ns in PBI-A pH 10 is broad in part due to the etalon effect between the windows that we were unable to remove, but also due to the low population present in the excited state.

Fitting the TA data once again revealed a three-state model with sensible lifetimes to describe the behaviour of the system. The initial broader state decays within 1 ps to yield three well defined peaks at 620, 730, and 807 nm (figure 60 and 61). This process occurred much quicker than in the exciton like pH 5 samples, making the pH 10 samples more singlet like in nature. At pH 10 one would expect structures of between 2-6 PBI units as shown by the SAXS study, whereas the PBI exciton has previously been shown to delocalise over as many as 10 units.[163] As a consequence of having fewer PBI units aggregated together, there was also less of an interaction between these tightly stacked chromophores simply due to fewer units being bound together by non-covalent forces. We previously described this as a lack of type 2 aggregates in our UV-Vis study, to describe a lack of mixing between the FE and CT bands, due to insignificant overlap. At pH 10 this results in the excited state exhibiting more CT character, and hence more well-defined features in the TA spectra. By 1 ps one could tentatively assign the presence of a PBI-A radical anion cation pair, due to the relative positions of the peaks (figure 61). However once again due to the highly excitonic nature of these materials, it was

more likely to be a singlet state that exhibits both cationic and anionic character over neighbouring PBI units. The lifetime of this state does not appear to be sufficient to contribute to catalysis, as evidenced by its lack of hydrogen activity. Whereas the excimer at pH 5 enabled electron transfer to the Pt catalyst.
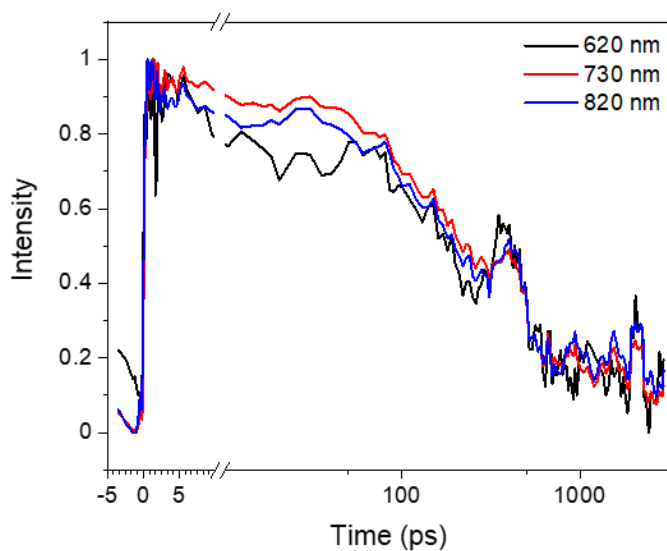
Figure 60 –Wavelength decay profiles from PBI-A pH 10. Wavelengths chosen common to PBI radical anion position, and potential cation. Samples contained PBI-A 5 mg/mL, methanol 20 v/v% and Pt nanoparticles (1 wt.%). Data was normalised.
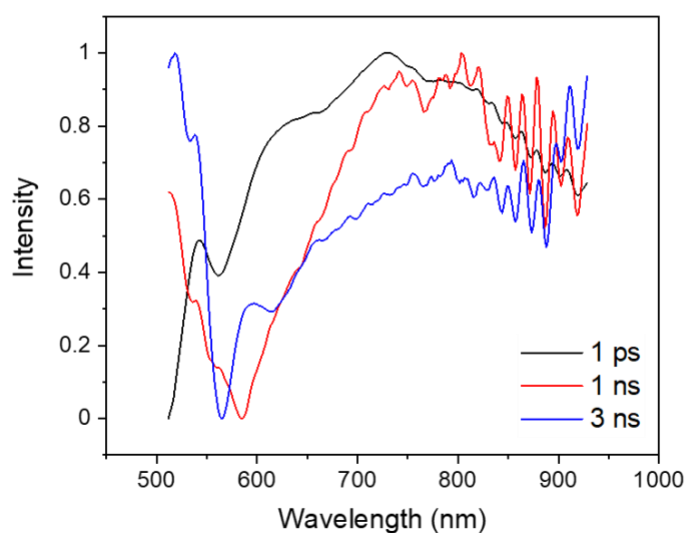
PBI-Y pH 5
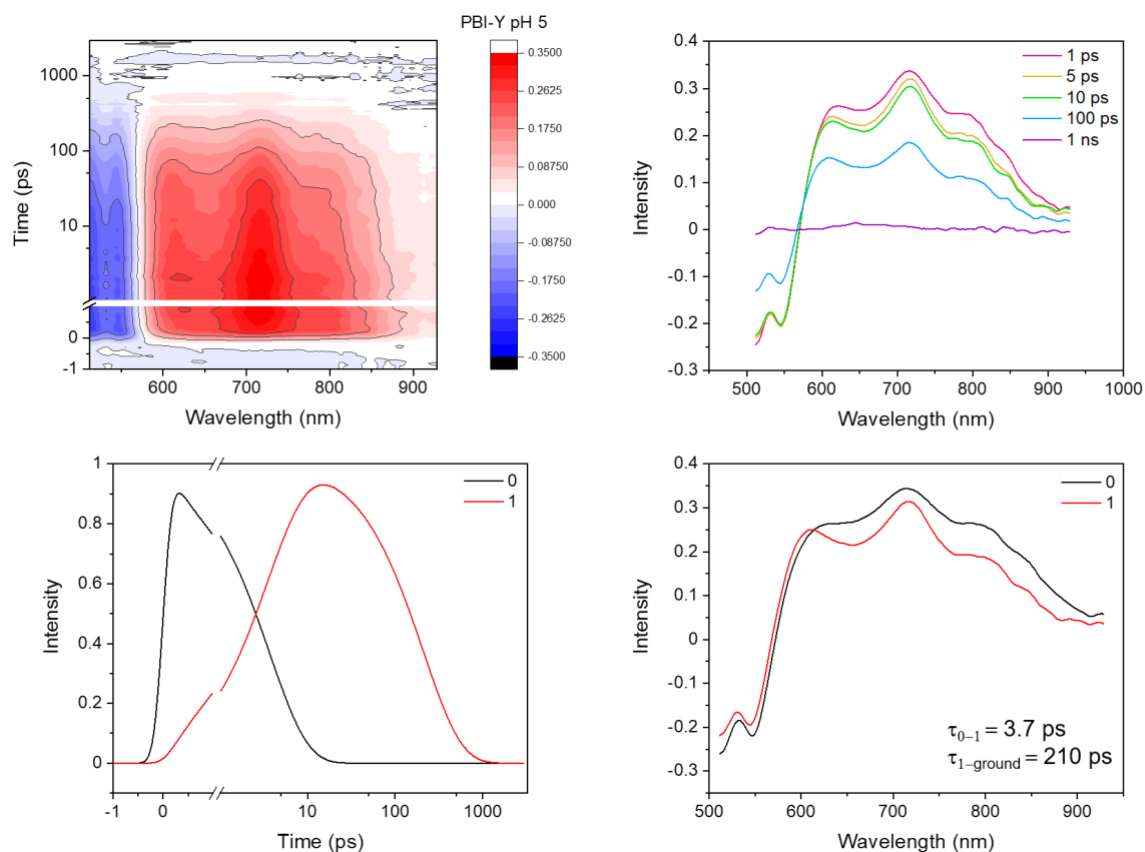
Figure 62- TA data comparing PBI-Y at pH 5 with 25μm. Contour plots shown on left and time slices on the right. Contour plots display most intense changes in absorbance through the experiment in red (If positive) and in blue (if negative). Key time slices illustrate the species present at that particular time period. Samples contained PBI-Y 5 mg/mL, methanol 20 v/v% and Pt nanoparticles (1 wt.%). Pump light intensity 100 μWcm^{-2}. Excitation wavelength 490nm. Rastered sample. Fittings performed in Carpetview software using global lifetime analysis, 2 compartment model.

The TA spectrum of PBI-Y at pH 5 was more like PBI-A at pH 10 than at pH 5, as evidenced by the narrower peak widths, which were slightly shifted in position due to the change in amino acid functionality (figure 62). This was despite the presence of the much larger self-assembled structures at PBI-Y at pH 5 vs pH 10 PBI-A. Three well defined peaks formed within 1 ps, as opposed to the broad excited species that had been seen previously at the more aggregated pH. The position of these peaks was slightly blue shifted with respect to the PBI-A spectra,

with peaks at 610, 714 and 803 nm (vs 730 and 819 nm in PBI-A). Figure 63 displays the UV-Vis spectra for PBI-Y samples at pH 5 before and after illumination and indicated the formation of the long-lived radical anion due to new peaks at 730 and 813 nm. This species was shown to be detectable via UV-Vis seconds after illumination. Once the difference in these spectra was overlaid with some crucial TA time slices it became clear that the peaks were not in the same position, but did capture the GSB and SE very well. Therefore, it was clear that there was evolution of the species, despite its perceived short lifetime in the TA experiments. The well-defined peak at 610 nm in the TA was considerably broader in the UV-Vis spectrum, and the peaks at 714 and 803 nm were blue shifted relative to their position in the UV-Vis. In addition, the relative power of the LED used to excite the sample was considerably higher than the pump laser pulse used in the TA experiments, which may have led to subsequent excitation. This difference in wavelength may have been due to an error in calibration, but due to this being thoroughly checked throughout the experiments it was unlikely. Furthermore, a peak shift from that of the radical anion suggests a singlet like species, which cooled over hundreds of ps in accordance from what was seen at pH 10 in PBI-A. The same rate of decay for the three peaks was observed, with little transient species present beyond 1 ns. This suggested a rapidly formed singlet like PBI species, which was not able to live long enough to contribute to catalysis.
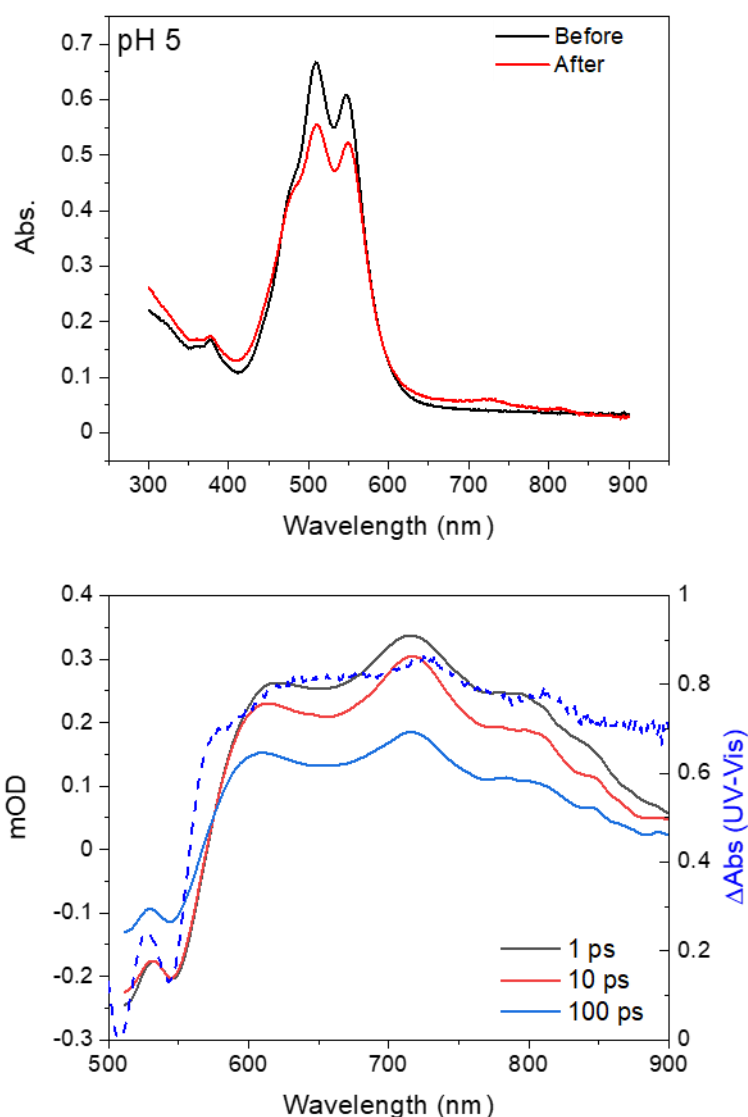
Figure 63- PBI-Y pH 5 UV-Vis before and after illumination. Difference in absorption before and after illumination (dashed line) overlaid with TA data on the same sample. Samples contained PBI-Y 5 mg/mL, methanol 20 v/v% and Pt nanoparticles (1 wt.%). Change in absorbance was normalised.

The lack of activity from PBI-Y aggregates samples around pH 5 was initially surprising, due to the presence of long-range aggregates capable of transporting charge. We initially diagnosed this lack of activity as a consequence of a lack of type 2' aggregates in the UV-Vis spectra. The TA study has strengthened this further in the case of PBI-Y, which even at pH 5 does not have long lived species which could transfer electrons to the platinum catalyst. On the other hand, the TA study cannot quite inform us why these long-lived species do not form, despite their

presence in the UV-Vis data upon illumination. The UV LED used was known to rapidly photoexcite PBIs, and therefore generate a large concentration of excited PBI molecules, so the conditions were not quite comparable in this case. From literature it was possible to suggest that the interchromophore distance between PBI-Y units was larger than that of PBI-A,[151,182] due to electronic and steric effects. Therefore, the interaction between PBI units was less significant, making the delocalisation of the excited state over more units unfavourable, and instead favoured a localised singlet like PBI, despite the potential to share over large distances. Within our original study the interchromophore distance was assumed to be fairly constant at between 3-4 Å,[49] and in hindsight this was an error. A number of other groups use covalent linkages to separate PBI units by distinct distances, which was not reproducible with our self-assembled methodology.

PBI-Y pH 10
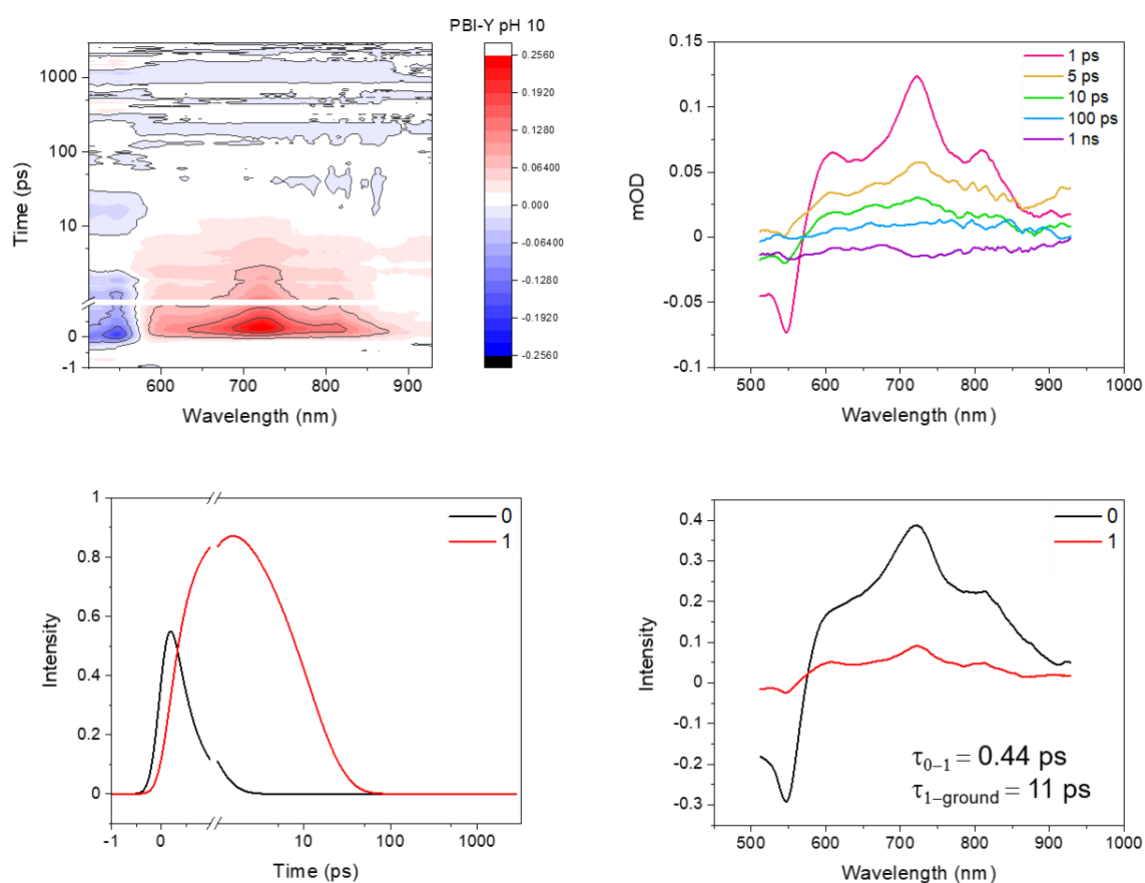
Figure 64- TA data comparing PBI-Y at pH 10 with 10 μm spacer. Contour plots shown on left and time slices on the right. Contour plots display most intense changes in absorbance through the experiment in red (If positive) and in blue (if negative). Key time slices illustrate the species

The initial spectrum at 1 ps was comparable to pH 5 in PBI-Y with three prominent peaks at 610, 720 and 810 nm, however the peaks were shifted by 5 nm to the red with respect to pH 5 (figure 64). These peaks were even more defined than those present at pH 5, likely due to the shorter aggregates of PBI to delocalise the charge over. By 5 ps there was a noticeable decrease in the resolution of these peaks, which had become much broader and lower in intensity. There were no peaks that could be assigned beyond this time period.

The lifetime of all excited species in PBI-Y at pH 10 was amazingly short. While this was not surprising due to the lack of hydrogen evolution, when compared with PBI-A at the same pH the difference truly was massive. Within 5 ps there was a noticeable decay, and once this data was fitted to a two-component model it confirmed the rapid pathway back to the ground state at around 11 ps after excitation. Figure 65 displays the massive difference in rate of decay of the 720 nm peak between PBI-Y pH 5 and pH 10 samples. At pH 5 the initial rate of decay was slow for the first hundred ps, but then rapidly decayed past 100 ps. At pH 10 the rate of decay was so rapid that the excited species was effectively gone by 100 ps. This contrasted strongly with the PBI-A samples which retained a proportion of the excited species until the end of the experiment (3 ns). The comparison between these datasets effectively confirms why PBI-Y was unable to evolve hydrogen in the photocatalysis experiments, there were quite simply not enough charge carriers present.
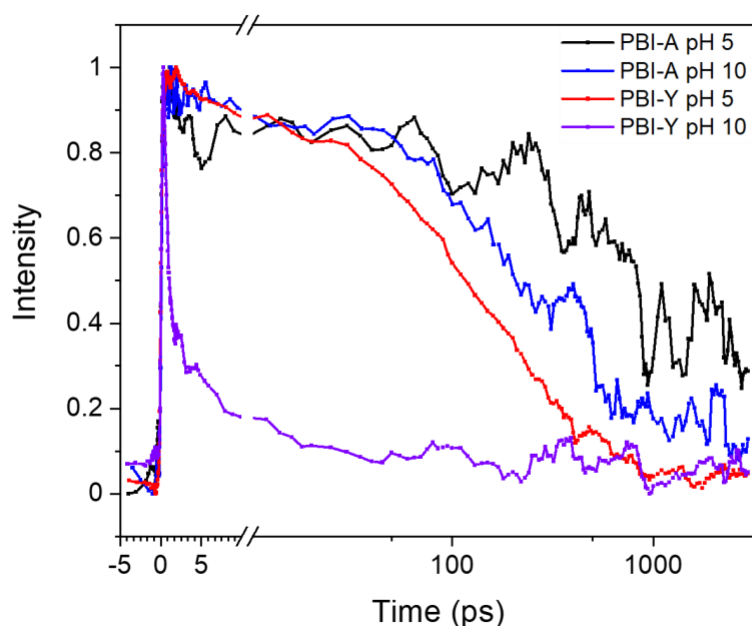
Figure 65- PBI-A and PBI-Y pH 10 and pH 5 compared at 720 nm. Data was normalised. Samples contained PBI-X 5 mg/mL, methanol 20 v/v% and Pt nanoparticles (1 wt.%).

Upon illumination with an LED there was little change in the UV-Vis spectrum for several minutes, which was much longer than was required for the pH 5 sample to display a response. It is hard to quantify whether this necessarily means a lower concentration of PBI radical was generated but, in combination with the lifetime data could suggest that less of the charge persists long enough to form the radical anion and therefore a smaller peak in the UV-Vis spectrum. Nevertheless, the small changes in the spectrum were overlaid with the TA data at 1 ps and 10 ps (figure 66) and did line up with the expected peaks for the radical anion. Once again, the likelihood was that the identity of the PBI singlet looked similar to that of the PBI radical anion, and was not in fact a fully formed species. The species that is detected by UV-Vis had been illuminated for > 5 minutes to generate a large population in the excited state, and some of this population was able to survive to yield a small quantity of the radical anion. Due to a much lower population in the excited state in our TA experiments, any population that yielded a PBI radical was not detectable, as it was unlikely that a fully formed radical would be present within 10 ps. Instead it appeared that a localised charge separated excited species formed over 1 or two PBI units, to yield what appeared to be a PBI radical (720 and 810 nm) and a PBI radical cation (610 nm). Had this species survived long enough, there was

potential to contribute to eventual photocatalysis, but the lifetime was simply too short. This process was shown by figure 65, and visualised in figure 67.
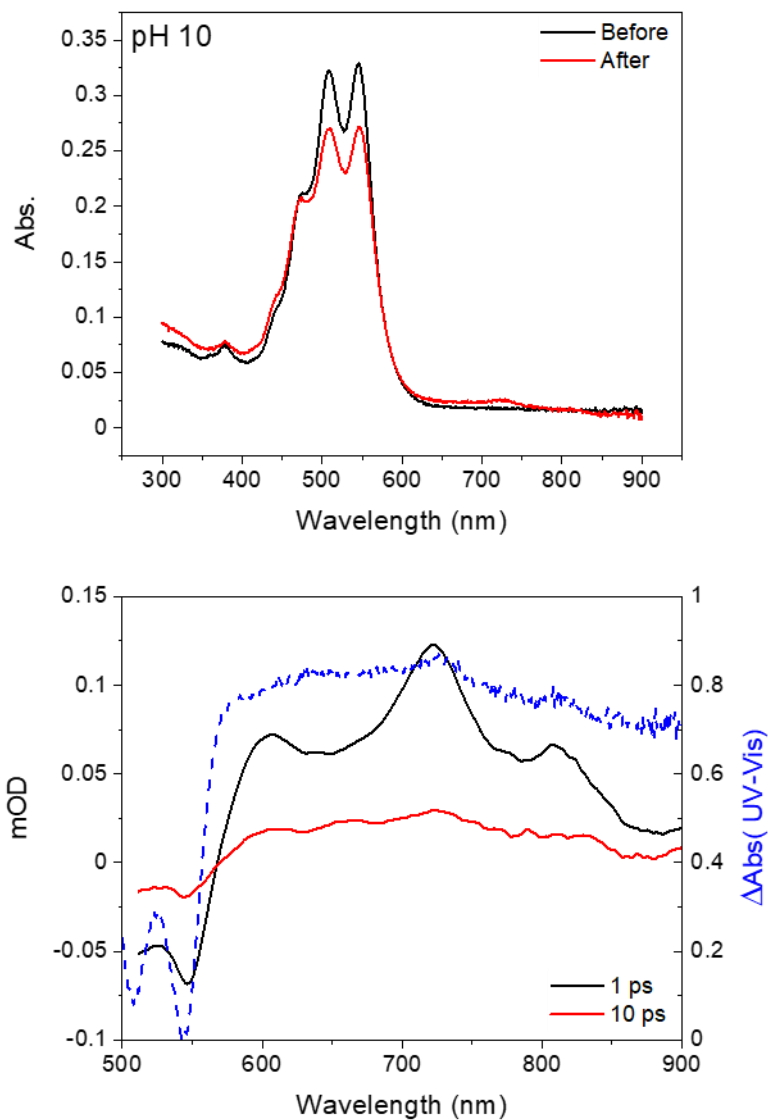
Figure 66- PBI-Y pH 10 illumination compared using UV-Vis spectra, spectra shown before and after illumination. The Changes in UV-Vis spectra were overlaid with TA time slices from previous experiment. Samples contained PBI-Y 5 mg/mL, methanol 20 v/v% and Pt nanoparticles (1 wt.%). Change in absorbance was normalised.

FE generation

hv

Strong FE/CT mixing

Singlet excited state

- Localised charges
- Short lifetime

- Extended excimer CT state
- Desired for long range charge separation within 1D stack
- Efficient electron transfer to catalyst
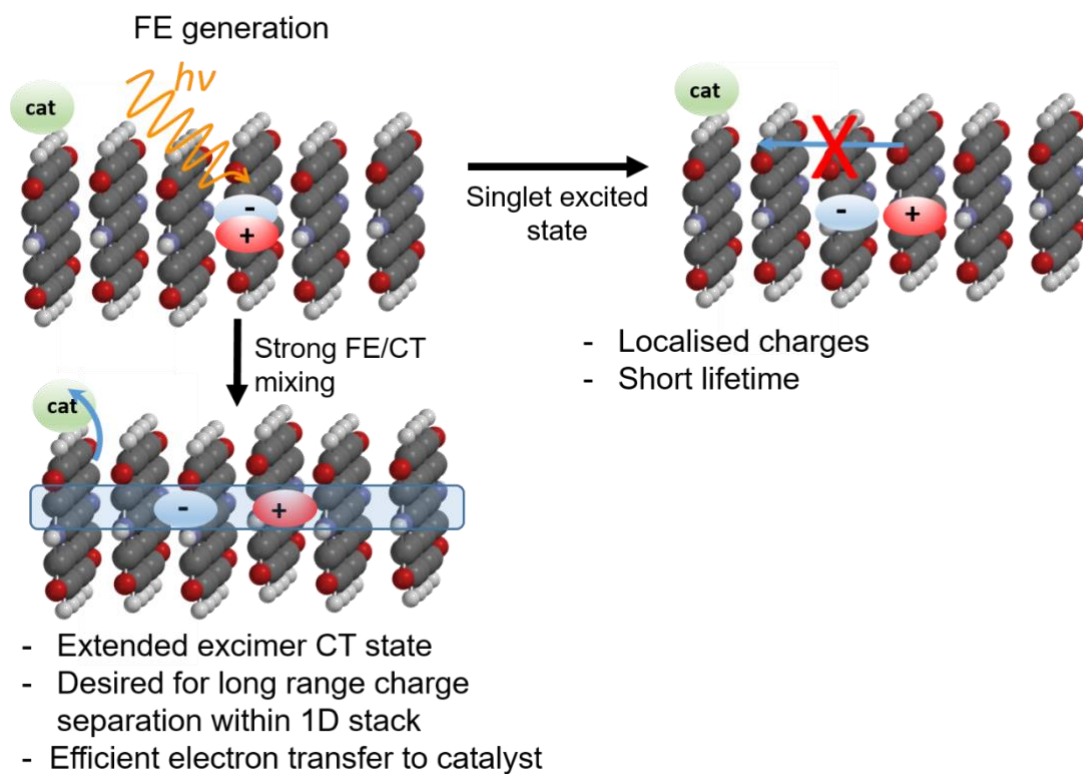
Figure 67- Molecular diagram to explain the behaviour of excimer and singlet like PBI species. Due to mixing of states PBI-A at pH 5 was able to form an excimer, which was able to live long enough to form a CT excimer and contribute to catalysis. PBI-Y at pH 5 formed a singlet like species with local charge separated character, due to a lack of mixing between states once initially excited.

Discussion

We have previously demonstrated that we are able to detect changes in the extent of self-assembly via UV-Vis and SAXS and related this to photoactivity via hydrogen evolution. Through this TA study we have now been able to expand this further to examine why some PBIs are able to perform photocatalysis and why others are not. We propose that the presence of type 2 aggregates enables the formation of these excimer-like states, which significantly extend the lifetime of the excited species which forms. Without the presence of these aggregates the lifetime of these species was significantly shorter, and did not yield any hydrogen. To this point we have been unable to examine the roles of methanol and platinum in this time period, and have not directly observed electron transfer to or from either compound. In order to determine whether methanol is acting as an electron donor in this time period, or if platinum is receiving an electron, we devised some control experiments to dive deeper into the mechanism occurring in this time period.

Samples without platinum catalyst present

To investigate whether platinum was involved in the mechanism within the 3 ns time period, it was removed from a set of control experiments. Figure 68 displays samples containing PBI-A at pH 10, but containing no Pt NP, which allowed for a direct comparison between the samples which did contain the co-catalyst. Once again, the initial spectrum at 1 ps contained three prominent positive features, alongside the GSB and SE we have seen previously in these samples. Over the first 1 ps there was clear uniform cooling to leave a broad signal at 1 ns. This compares well with what we have seen previously at pH 10 with samples containing Pt. The data was fitted to a three-compartment model, which also mirrors trends seen in the previous model. The calculated lifetimes are comparable with the initial process occurring on the time scale of 1-4 ps, which resulted in a loss of broadening from the spectra. The peaks at 605, 730 and 805 nm were more resolved in this dataset, and considerably less noisy past 800 nm, which allowed for more accurate peak picking and better data. The lifetimes for the next two processes were also similar (330 ps compared with 480 ps, and >>3ns for both) to one another, and also contain large errors on both values. State 1 depicts a localised charge separated exciton with both anionic and cationic character, signified by the peaks around 605, 730 and 805 nm. However due to their shift in position it was likely that they are not fully

charge separated, despite the narrowed peaks. The lifetime of these species was found to be on the period of hundreds of ps, to leave behind a broad species on the longer time scales. We found no evidence of any interaction with platinum in these samples.
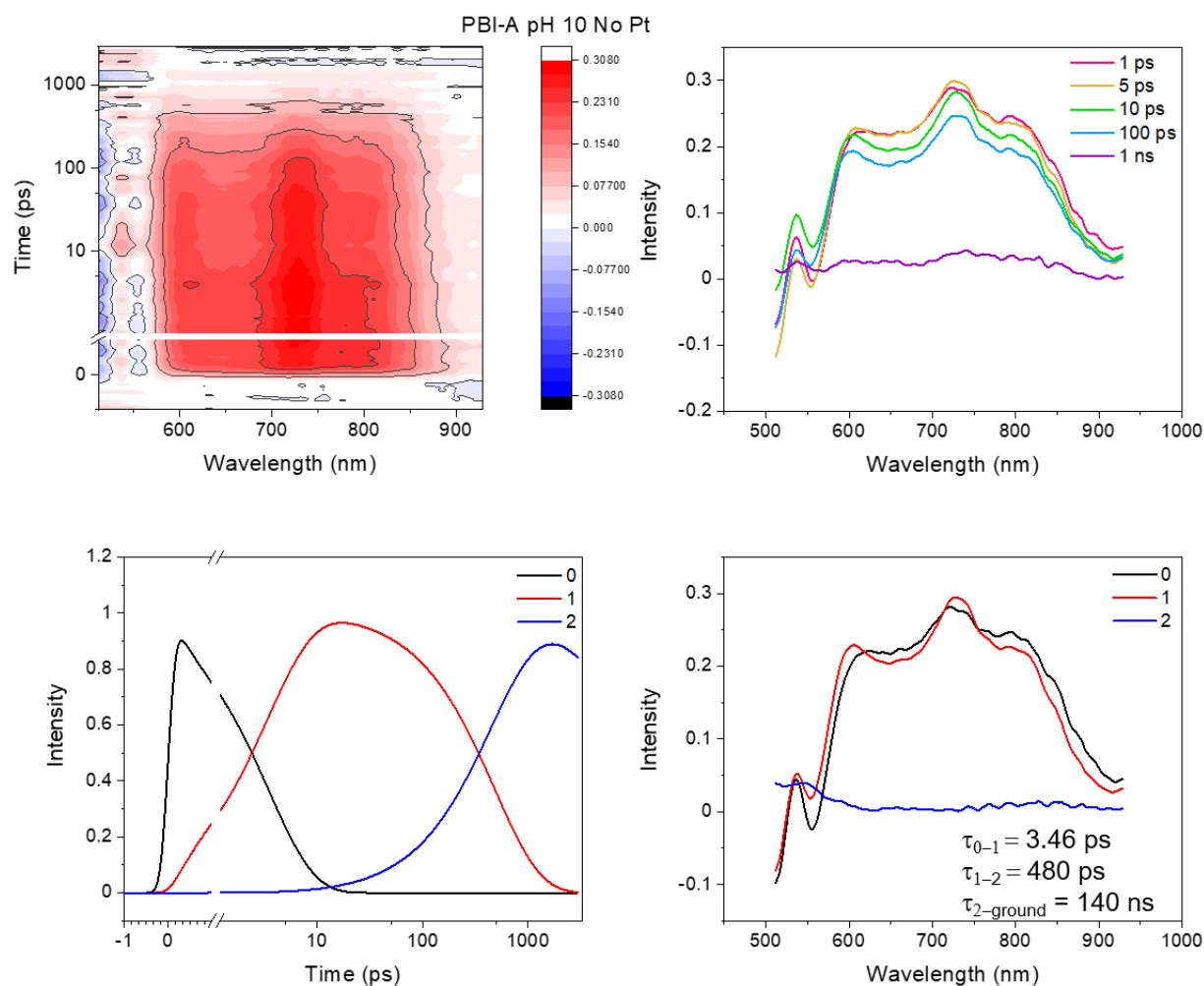
Figure 68- TA data comparing PBI-A at pH 10 with 10 μm spacer, with no Platinum nanoparticles. Contour plots shown on left and time slices on the right. Contour plots display most intense changes in absorbance through the experiment in red (If positive) and in blue (if negative). Key time slices illustrate the species present at that particular time period. Samples contained PBI-A 5 mg/mL, methanol 20 v/v% and no Pt nanoparticles (1 wt.%). Pump light intensity 100 μWcm^{-2}. Excitation wavelength 490nm. Rastered sample. Fittings performed in Carpetview software using global lifetime analysis, 2 compartment model.

PBI-A pH 5 no Pt co-catalyst: Evaluating charge transfer to catalyst in active conditions

The dataset without platinum present shared many parallels with the data from when it was present (figure 69). However, there are subtle differences in lifetimes and shape of spectra which were surprising. The same cooling is observed to leave what looked like the PBI radical

anion forming in around 1 ns, but the lifetime of the initial state is much longer than expected at around 48 ps. This seemed to indicate that the initially formed species took longer to decay without the platinum present, despite no obvious hallmarks of its involvement in any mechanism. The final state 2 from the fitting lacked the definition that was present in the equivalent state in the samples that did contain Pt, and also had a much longer lifetime (despite a large error). But the characteristic peaks at 730 and 820 nm are visible amongst the noise, which seemed to suggest the two additional peaks at 690 and 885 nm were unlikely to be real, and most likely present due to noise at longer time scales.
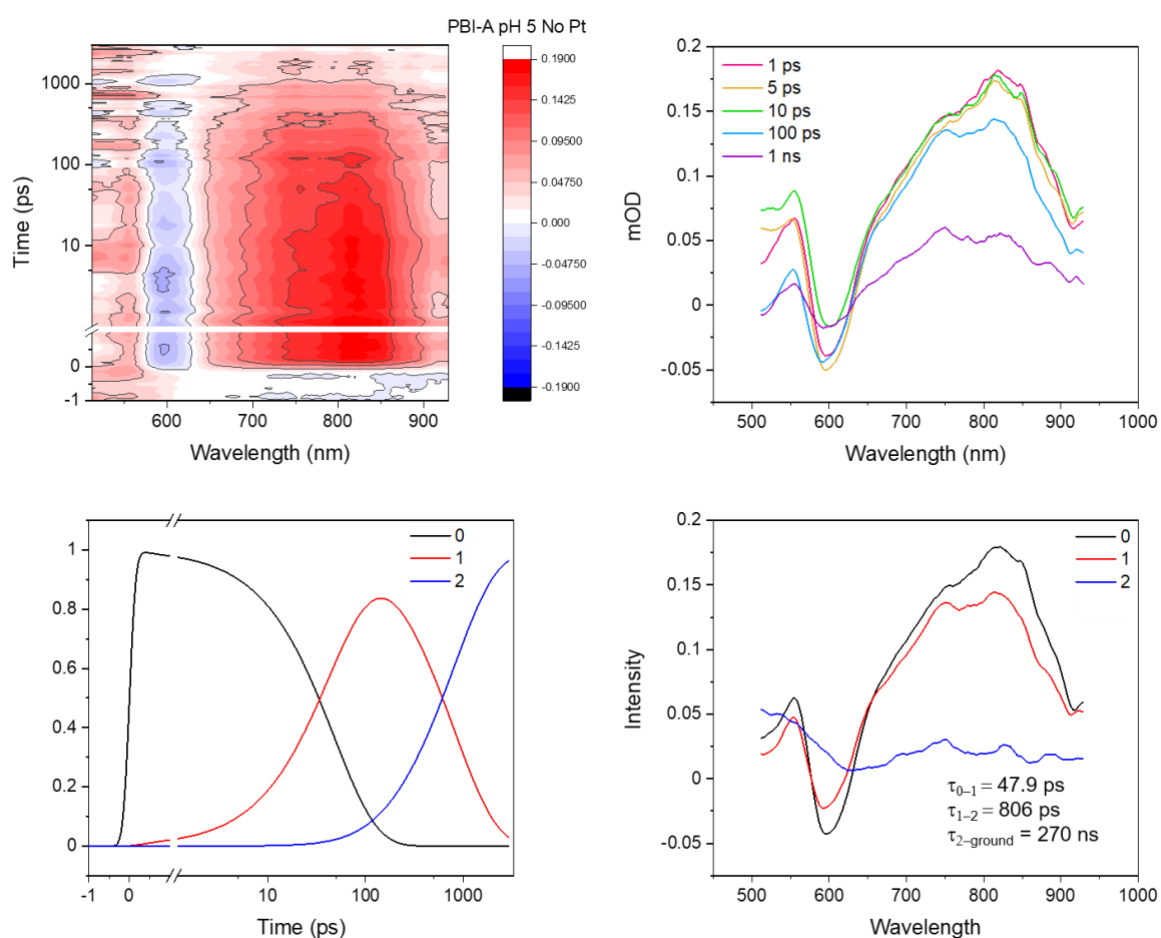
Figure 69- TA data comparing PBI-A at pH 5 with 25 μm spacer, with no Platinum nanoparticles. Contour plots shown on left and time slices on the right. Contour plots display most intense changes in absorbance through the experiment in red (If positive) and in blue (if negative). Key time slices illustrate the species present at that particular time period. Samples contained PBI-X 5 mg/mL, methanol 20 v/v% and no Pt nanoparticles (1 wt.%). Pump light intensity 100 μWcm^{-2}. Excitation wavelength 490nm. Rastered sample. Fittings performed in Carpetview software using global lifetime analysis, 2 compartment model.

The UV-Vis of the samples was also an added complication, as the lack of Pt seemed to influence the local packing. At pH 10 there were more subtle differences at 450 and 550 nm, as shown by figure 70. But at pH 5 the difference was significant broadening, normally associated with a change in pH.[49] This difference was reproducibly shown by a number of samples, which indicated that the difference was a real change as a result of the added Pt. While the behaviour looked to be the same in the TA experiments, the species being probed was not quite the same as when the platinum was present in either pH. Nevertheless, we did not observe charge transfer to platinum within the 3 ns timescale in any of our experiments, which suggested the need for long lived charges to enable successful catalysis.
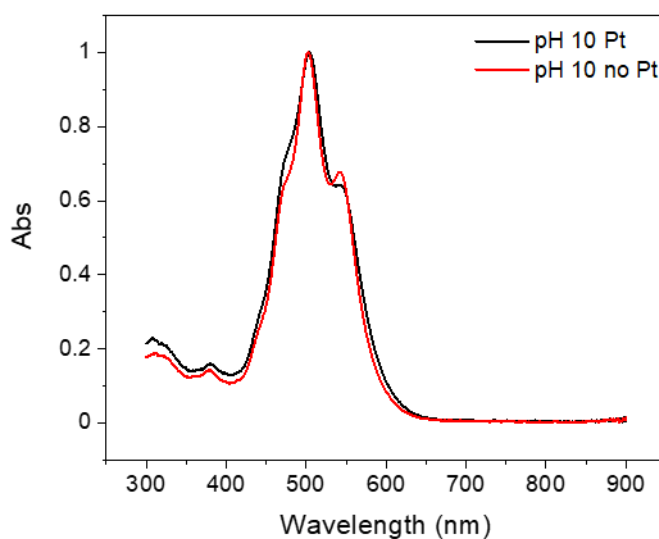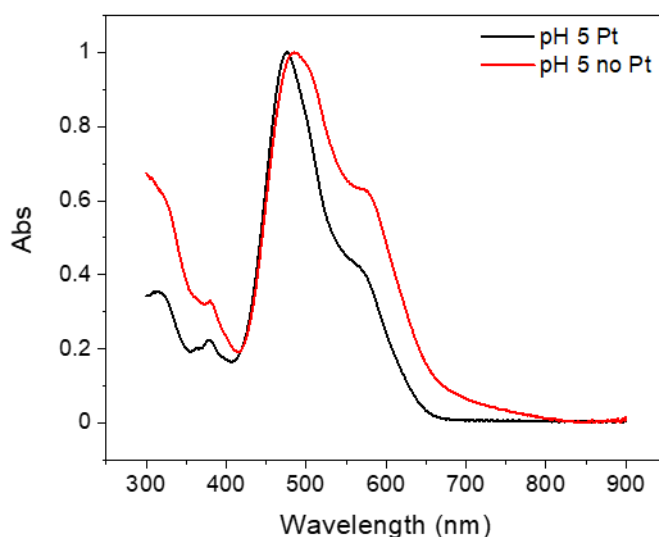
Figure 70- UV-Vis spectra of PBI-A at pH 5 and pH 10 with and without Pt NP. Samples contained PBI-X A mg/mL and methanol 20 v/v%.

Multi-faceted role of methanol

Since moving to thinner spacers to allow for light penetration of the sample, the methanol concentration has been constant through all experiments (20 v/v%). In our photocatalytic study we observed that the role of methanol went beyond simply acting as a hole scavenger, and in fact due to its polarity and dielectric constant being different to water, there were also structural implications too, due to the nature of self-assembly. With this in mind we attempted to resolve this further with our optically thick samples by varying the concentration of methanol significantly (0% to 40%) and found that there was little difference within the 3 ns time frame. We expanded this further to encompass the thinner samples to confirm that this was the case.

Figure 71 displays the data from a series of TA experiments that compare two different pHs with no methanol present. We noticed that in the original UV-Vis study and subsequent fitting that there was a lower concentration of type 2 aggregates at pH 5 when no methanol was present, and therefore little to no hydrogen evolved. But at a lower pH of 3.5 a small amount of hydrogen was evolved, and this correlated with the characteristic peak shift and broadening in the UV-Vis we named type 2 aggregates.

Without methanol present the spectra at pH 5 did not look similar to the 20 v/v% spectra, due to the inherent lack of type 2 character there was a clear lack of broadness. From 1 ps two of the three characteristic peaks were well defined, with a different intensity ratio than the standard pH 5 sample. In contrast the spectrum at 1 ps in the pH 4.5 sample was noticeably broader, and had shifted the intensity ratio from 1:2:1 to the 1:2:3 previously seen at pH 5 with 20 v/v%. We were unable to measure a sample at pH 3.5 due to the lack of homogeneity at this pH which caused a loss of signal to noise. However, a small drop of the pH from 5 to 4.5 was enough to see a significant difference in the TA spectra, due to an increase in type 2 character (figure 71 and 72). If we were able to continue with this data set we hypothesise that the spectrum at pH 3.5 would look very similar to that at pH 5 at 20 v/v%.
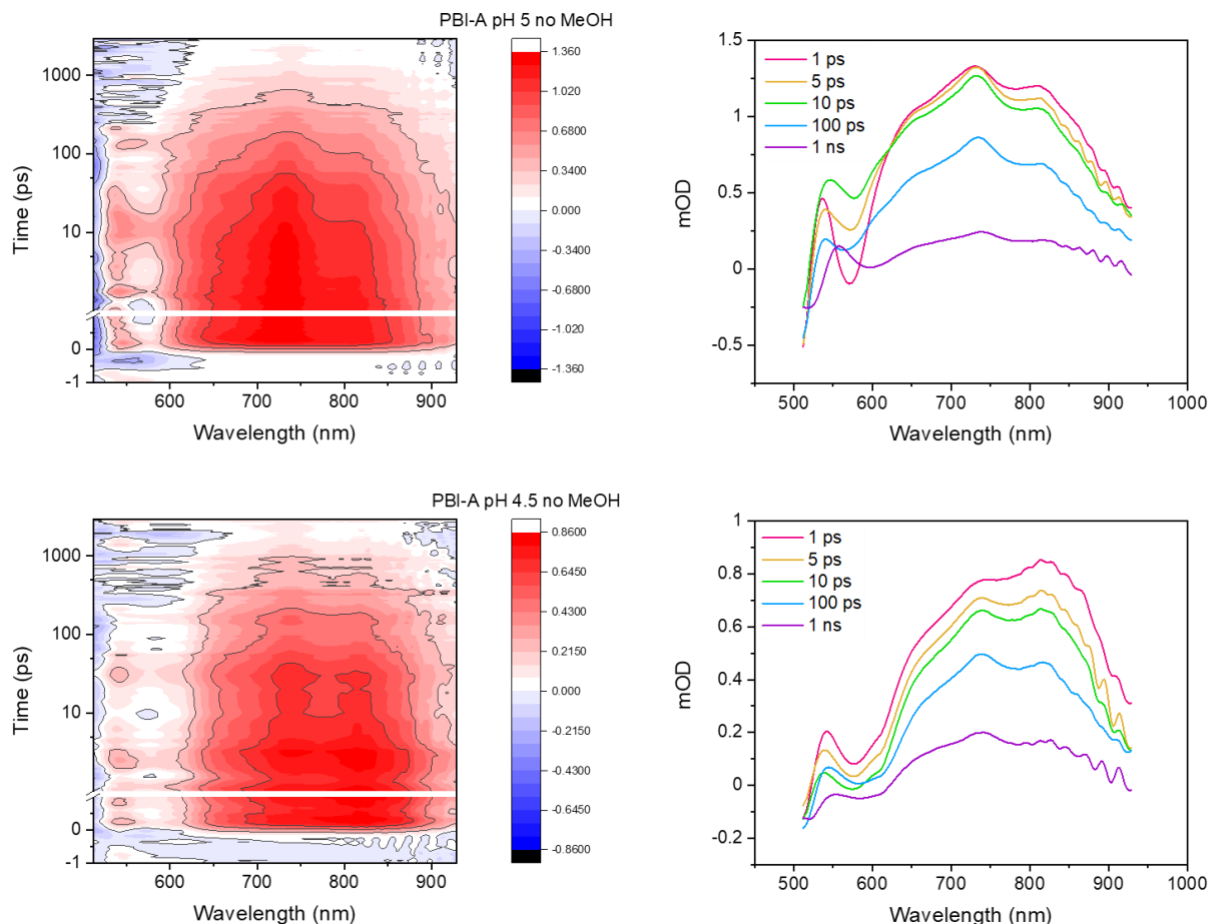
Figure 71- TA data comparing PBI-A at pH 5 and 4.5 with 25 μm spacer, with no methanol present. Contour plots shown on left and time slices on the right. Contour plots display most intense changes in absorbance through the experiment in red (If positive) and in blue (if negative). Key time slices illustrate the species present at that particular time period. Samples contained PBI-X 5 mg/mL, and Pt nanoparticles (1 wt.%). Pump light intensity 100 μWcm^{-2}. Pump wavelength 490nm. Rastered sample.
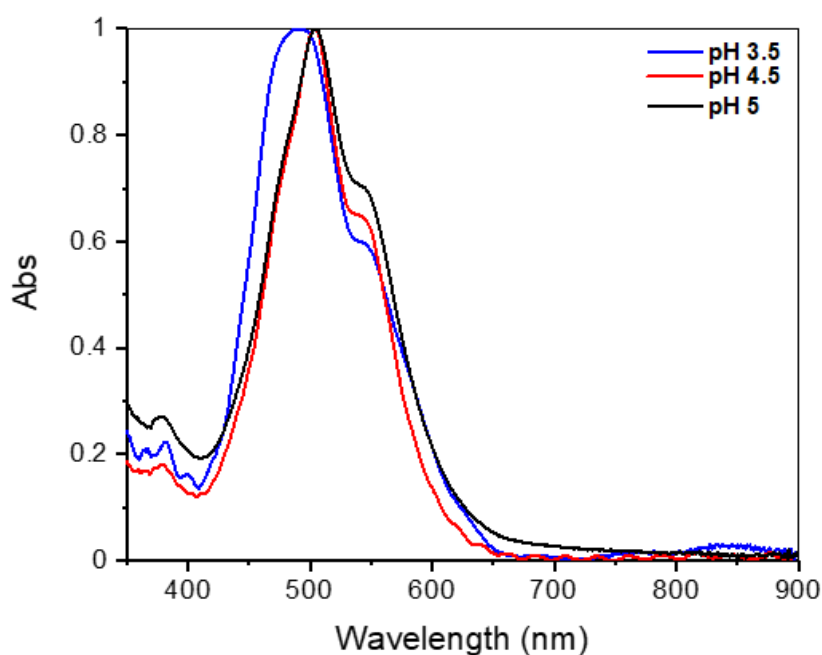
Figure 72- UV-Vis of PBI-A with no MeOH present. Samples contained PBI-A 5 mg/mL, and Pt nanoparticles (1 wt.%). Data was normalised.

Fitting of the two data sets produced very similar lifetimes for the different states in the model, despite noticeable differences in the UV-Vis and TA spectra. Figure 73 depicts how similar the lifetimes truly were for these models, but also that there was still a significant difference in the shape of the spectra to describe these states. Most notably the intensity ratio of each of the peaks for each state changed markedly for each sample. At pH 5 the most intense peak was at 730 nm throughout, whereas at pH 4.5 the initially formed excited state has the most intense peak at 820 nm, which had previously been seen for active pH 5 samples containing methanol. This intensity ratio then changes after the initially formed state decays to form state 1, so that the peaks at 730 and 820 nm are around 1:1. The data at pH 5 (with no methanol) looks like a model that would fit with pH 10 data due to the well-defined peaks and lifetimes, due to the lack of type 2 aggregates. The similarities between the lifetimes of the two datasets highlighted the issues with modelling the data in this way, and made clear how chemical intuition is required to correctly interpret these models due to the subtle differences.
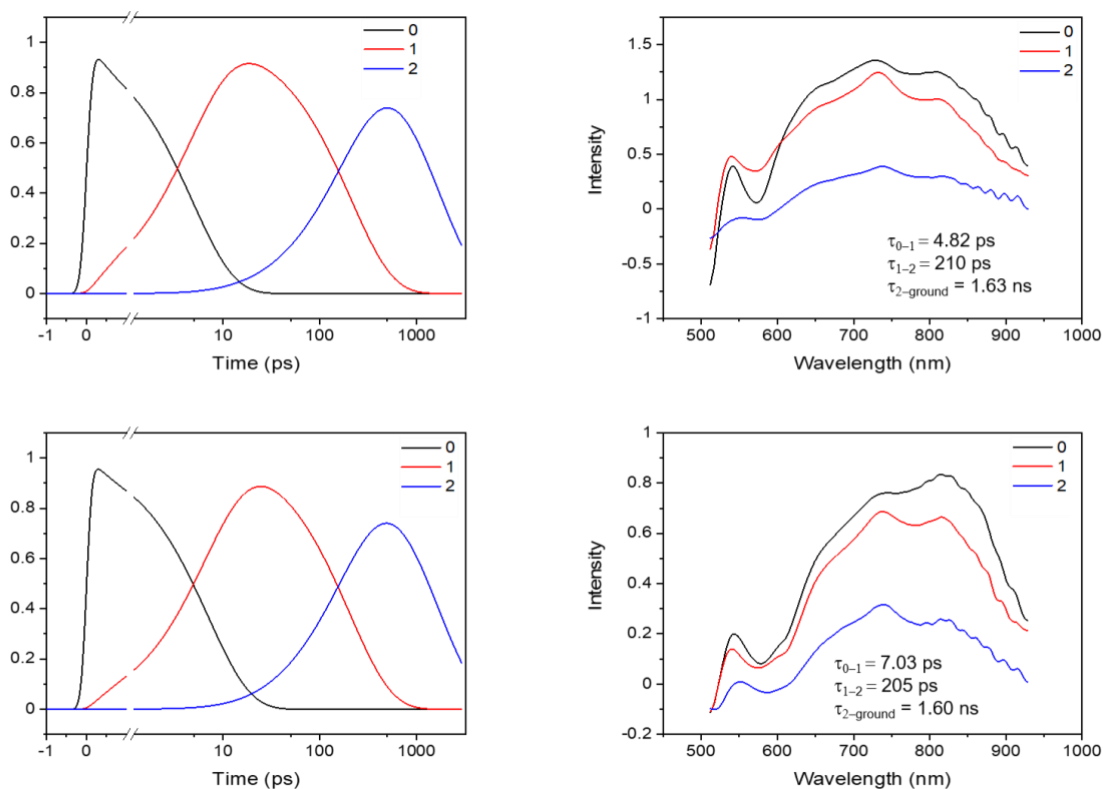
Figure 73- Fittings performed in Carpetview software using global lifetime analysis, 3 compartment model. Top data is PBI-A at pH 5, bottom data is pH 4.5. Samples do not contain methanol but do contain platinum nanoparticles (1 wt. %).

Figure 74 displays the aggregate type fittings between the pH range in the photocatalysis experiments. The fitting approach used the same non-linear combination of variables used in chapter 2, and the literature paper,[49] to fit the UV-Vis data from the 0 % MeOH study. Thankfully the fitting results were once again supported by the hydrogen evolution results, as pH 3.5 was the single point where type 2 aggregates dominated and was also the highest point of hydrogen evolution. pH 5 was normally the switching point in PBI-A samples for the dominance of type 2 aggregates, but due to the lack of methanol in these samples there was a delay in this trend; highlighting once again the importance of methanol as a structuring agent. The type 2 data point at pH 7 was surprising and suggested that either there was an error in the preparation of that sample or UV-Vis sampling, or that an interesting structure had formed at that pH. Despite this revelation, there was no hydrogen evolution at this pH, indicating a likely error. The fitting technique used throughout this study has been used many times throughout this thesis, and each time has stood up to the test and been able to explain complex photophysical trends and relate them to hydrogen evolution. Type 2 aggregates

really did appear to be of paramount importance to PBI-A and beyond. While it is difficult to assign these species to defined structures in the same way as figure 67 it is the significance in the change of intensity of peaks at early timescales which is the crucial information from this experiment.
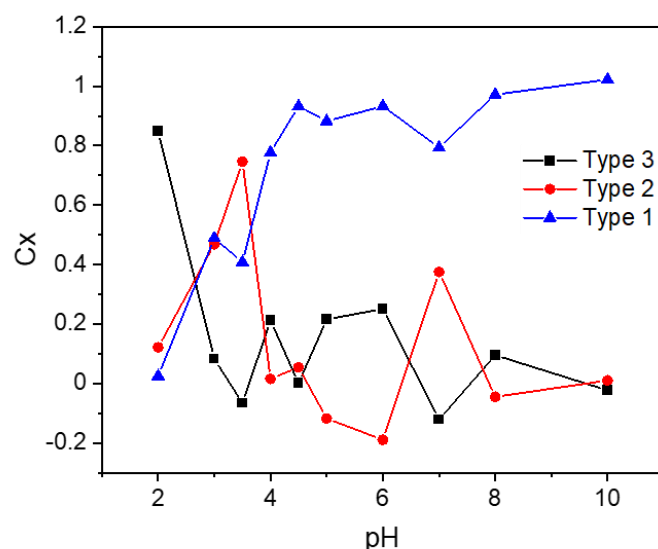
Figure 74- Fitting of PBI-A 0% MeOH UV-Vis data across pH trend. Using fitting procedure from chapter 2 using non-linear combination of variables for 3 structure types.

Having examined the effects of methanol thoroughly, it did not appear that there was a hole scavenging effect within the 3 ns time frame. While there were differences in the behaviour of the samples with and without methanol they were a result of methanol acting as a structuring agent, and not as an electron donor. The proposed mechanism for the samples containing type 2 aggregates remained the same regardless of the availability of methanol, and required a long lived PBI radical state to ensure success in the HER. This success was also determined by the presence of type 2 aggregates which enabled the formation of an excimer like state which enhanced the stability of the excited state, and prevented decay within 3 ns. We have been unable to directly observe an active species that was responsible for the formation of hydrogen, but we can conclude with some degree of confidence that excited PBI species were required for activity. In addition, we have demonstrated the formation of localised hard charges on shorter stacks of PBI were unable to live long enough to have the potential to evolve hydrogen. And finally, that PBI-Y was unable to evolve hydrogen due to

the lack of type 2 aggregates across the pH range which ultimately yielded very short-lived species not capable of transferring electrons to the platinum catalyst.

Overview of experimental results

Although there were significant changes to the experimental setup, there was a clear trend between the data sets. An initial process occurred on the period of 1-5 ps which was indicative of a broad excited state, which was likely to be the relaxation into the excimer like state. We did not see any direct evidence for the mixing of the FE and CT states in any dataset, as this mixing was likely to take place in less than 300 fs it would be within the instrument response function and not trackable. This made assigning this mixing difficult via TA analysis, but fully supported by the previous UV-Vis study in chapter 2. Therefore, our analysis took place after the mixing of states had already occurred. The next step took place over hundreds of ps, and resulted in a loss of broadening to leave behind more well-defined peaks that look more like the characteristic PBI radical anion. Through previous iterations the wavelength window of the experiment shifted considerably, and thinning the samples allowed for a more detailed look at the shorter wavelengths, which in actual fact revealed little about the mechanism, and ended up cutting off the distinctive 980 nm anion peak from most spectra. With more time the experiments would have been repeated to study the whole region, and in a dream circumstance examine the NIR and UV regions also. The process in question was likely a solvent related charge separation due to the high dielectric constant of water, which allowed for a more charge separated excimer like species to form over the period of hundreds of ps. The final species was the charge separated PBI excimer like species which could then go on to transfer an electron to the co-catalyst.

We hypothesise minimal mixing of states due to a lack of PBI units stacked together, and therefore wouldn't expect to see this even if we were able to. However, there was a consistent fast step at around 1 ps which was the formation of the PBI singlet, a charge localised over few units, which also appeared broader than expected due to the use of water as a solvent (appendix for full details). This looked like the formation of a radical cation and anion pair, but was in fact a charge separated singlet. An earlier data set from the spacer compared study confirmed this with a consistent lack of a radical anion peak at 980, as shown by figures 105-112. The pH 5 dataset in figure 75 is the clearest confirmation of the formation

of the radical anion peak at 980 nm, which was not present in any pH 10 dataset in any capacity. This was also a significant outcome due to the formation of a PBI radical anion without the presence of methanol (using visible light), in contradiction to what we previously hypothesised.[85] Due to the change in optical window we were unable to observe this for the final dataset, which was an oversight. The lifetime of the PBI singlet formed at pH 10 was not sufficient to contribute to catalysis, regardless of the experimental setup. The lifetime of the final state in the 10 μm setup was anomalously large and described a very broad state incapable of separating charge effectively.
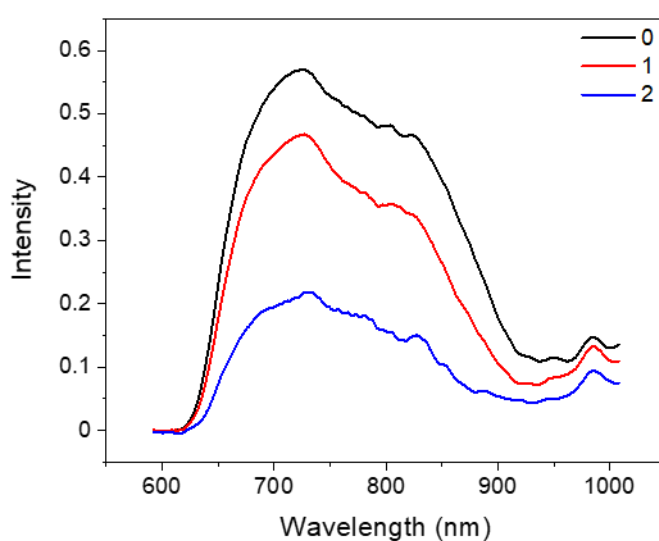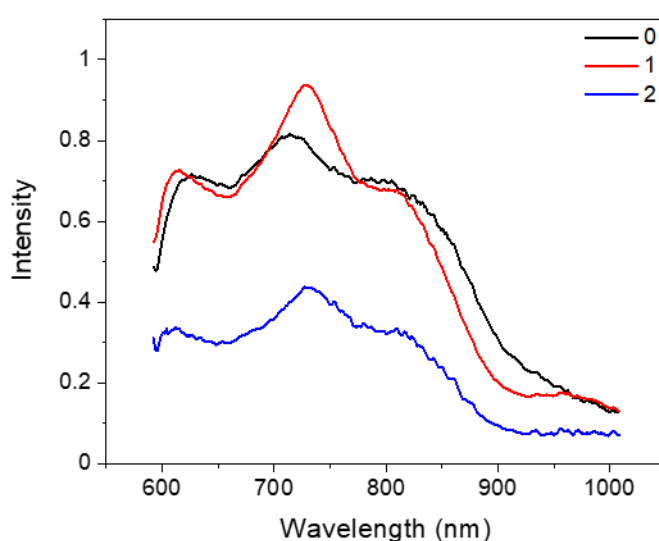
Figure 75- Fittings performed in Carpetview software using global lifetime analysis, 3 compartment model. Fitting results of PBI-A pH 10 (top) *and PBI-A pH 5* (bottom) *with no MeOH present.*

Conclusion

We endeavoured to gather more information on the photophysical behaviour of the PBI photocatalytic systems that were examined in great detail in chapter 2. This primarily centred around the use of TA spectroscopy to probe the lifetimes of excited states generated by the illumination by visible light, with the hope of uncovering an appropriate mechanism of action. PBI-A was shown to be an active photocatalyst for hydrogen evolution when self-assembled at pH 5, whereas PBI-Y was unable to evolve hydrogen significantly at any pH. PBI-A has previously been examined as a thin film, and also as a concentrated solution by our group, who proposed the formation of a PBI radical anion, and highlighted the importance of water content in the structure. Our photocatalytic dispersions were rich in water but also contained methanol as a hole scavenger, which we have described as a structuring agent in chapter 2, in addition to its photophysical role as an electron donor.

A significant portion of this work was spent on optimising the setup to perform the 'perfect experiment', as is often the case with spectroscopic studies. We eventually arrived at a reproducible method and arrived at an optically thin sample the pump and probe light could penetrate, and also rastered the sample to prevent accumulation of the long lived PBI radical anion. This involved keeping the light intensity low to prevent further pumping of this extremely long-lived species, as it was not possible to track multiple transient species at once. Our initial experiments used thicker spacers, and resulted in optically thicker samples which absorbed all of the pump and probe light. This left us at an experimental crossroads, as it was an accurate reflection of what would occur in a photocatalysis experiment, but did not let us study the species through UV-Vis spectroscopy. In addition, there were added complications of heating the front face of the sample due to the high absorbance, which may have had an effect on the TA results due to only probing the front face. Having now looked back at the fitting results of these samples, they did provide an accurate reflection of what was occurring in a photocatalysis experiment, and produced similar values to thinner samples. In retrospect these experiments were more useful than initially thought.

We were also able to explore the roles of methanol and platinum within the 3 ns time frame. From our experiments it does not appear that there was direct charge transfer to either species within this time frame, which makes sense due to longer lived charges being required for eventual transfer to a suitable co-catalyst. However, investigating the role of methanol proved to be quite a challenge due to its ability to change the process of self-assembly. We were able to demonstrate why PBI-A samples that contained no methanol did not evolve hydrogen at pH 5, despite all other samples at this pH being able to do so in abundance. As ever in this PBI study, this came down to structure, and a lack of type 2 aggregates being formed at this pH when compared with a sample containing 20 v/v%.

The lack of activity of PBI-Y was successfully deconvoluted through this TA study, with its lack of type 2 aggregates at any pH meaning that there was little delocalisation of charge over the PBI units, and therefore shorter-lived charges. The lifetime at pH 10 was incredibly short, with little to no signal at 100 ps. Meanwhile at pH 5 the lifetime was certainly longer, but localised over few PBI units, which led to sharply defined peaks indicative of a charge separated PBI singlet, with a lifetime of a few hundred ps. The reason for PBI-Y being unable to form type 2 aggregates may stem from the electronic and steric profile disturbance caused by the phenol ring of tyrosine, as opposed to alanine with a simple methyl group. It has previously been reported that larger inter PBI distances can contribute to the formation of harder charges, and a lack of delocalisation over neighbouring PBI due to a lack of coupling.[182] We were unfortunately unable to probe this further as it was assumed that inter PBI distances were constant within the SAXS study of chapter 2.[49]

Moreover, the short PBI-A stacks at pH 10 were also unable to form long lived charges, and instead formed a PBI singlet, very similar to PBI-Y in profile with three distinct peaks. This contrasted strongly with the spectra of pH 5 which were very broad, due to the formation of a mixed state of CT and FE bands. While we were unable to observe this mixing in real time due to instrumental setup, we were able to see the relaxation of this state to form a long-lived charge separated excimer like state. The lifetime of this state was in excess of 3 ns, with little evidence of charge transfer to the catalyst within this time frame. It was unclear whether this species was indeed the active species due to its ability to absorb additional photons, and

therefore form a more reductive state, but this was beyond the scope of this study; which was to once again demonstrate the control of photophysical properties using self-assembly.

Chapter 4: Controlling photoactivity by self-assembly – tuning perylene bisimide photoanodes

Introduction

The task of efficiently storing solar energy in the form of chemical bonds remains one of the greatest scientific challenges of the generation. Solar water splitting allows for this abundant source of energy to be conveniently stored as O_2 and H_2, which are both highly desirable and adaptable products in their own right.[186–188] There are 3 key stages for water oxidation; light absorption, charge separation and migration, and catalysis, each requiring optimized material design to produce an efficient device.[5,189–192] In addition to this, the proposed device must be economically more attractive than both current photovoltaic and fossil fuel-based alternatives to truly be fit for purpose. Organic molecule-based devices provide an alternative to the classic inorganic semiconductors that dominate the field of photovoltaics, and boast enhanced tunability at considerably lower cost.[38,66]

True water splitting involves both of its component half-cells, the oxygen evolving reaction (OER) and the hydrogen evolving reaction (HER). Both reactions can be performed by photoelectrodes,[193–196] photocatalysts,[49,55,61,62,65,197] or photoelectrochemical tandem cells,[29,198–200] but for organic photoelectrodes in particular long-term stability and activity is a challenge. Water oxidation is often labelled/described as the kinetic bottleneck.[201] By its very nature, this step is kinetically challenging, as it requires two molecules of water and four incident photons to overcome the barrier of +1.23 V required to evolve a single molecule of oxygen.[202] An overpotential is also required to help reaction rates,[203,204] and combat recombination that plagues organic molecule based devices due to inherently low dielectric constants and inefficient charge carrier transport.

Self-assembly and molecular design of organic molecules can enhance water splitting activities, by providing structures that facilitate charge transportation to catalytic centres and reduce recombination,[49,133,136,205,206] Stupp *et al.* have investigated improving the crystallinity of their perylene monoimide samples,[132,137] which helped to boast improved performance in generating hydrogen photocatalytically. Perylene based devices are particularly attractive due to their aromatic chromophores that absorb a large amount of visible and UV light,[207,208]

along with many synthetic avenues to develop further architectures. PBIs are known to self-assemble in water and form hydrogels,[49,142,143,170,183] which have been shown to boost charge separation.[183] The inherent incorporation of water into the hydrogel structure has been shown to increase the local dielectric constants,[183] which normally limit the storing of charge in organic materials and unlock the potential of PBIs as water splitting materials.

PBIs have frequently been employed as part of multi-layer devices for water oxidation,[15,34,66,209,210] and also several examples of photocathodes,[28] and photocatalytic mixtures.[211] Sivula *et al.* employed a bulk heterojunction with a PBI based acceptor to enable the separation of charge upon illumination, and thereby drive the photooxidation water.[32] This particular device was highly sensitive to pH due to its inclusion of an electron transport layer (ETL), which has a different optimal pH to the other constituent layers.[36] A similar heterojunction approach was used to design a photocathode system that successfully yielded a 100 % Faradaic efficiency for hydrogen via injection of photogenerated electrons into a MoS_3: MoP catalyst.[28]

Finke *et al.* have demonstrated a PBI based photoanode using a dye sensitized nanostructured system for improved photoactivity.[212–214] In this case the PBI was found to act as a light absorber and was able to separate charge effectively and allow for water oxidation with a Faradaic efficiency of 31 %.[214] However the addition of the CoO_x catalyst was found to hinder the photocurrents achieved, and in fact promote charge carrier recombination. The addition of an Al_2O_3 passivation layer was found to enhance photoactivity and reduce recombination after finding the optimal thickness. While the faradaic efficiency is lower than originally reported for this system,[213] it demonstrates the reality facing many PBI photoanode devices, which is that self-oxidation dominates and hinders both stability and performance.

Previously it was shown that thin films of amino acid modified dried PBIs were photoconductive over long distances (mm) suggesting that long range charge transfer can occur following illumination.[85,142,143] We have also reported that the nature of the amino acid can control structure of PBI aggregates/gels which modifies photocatalytic activity (chapter 2).[49] Typically PBIs photoanodes are multi-layered devices combined with a suitable water oxidation catalyst to enable efficient charge separation and transfer. Here we wish to expand

on these recent studies to explore how the nature of the amino acid functional group can control the activity of a thin film organic photoanode for use in water.

We chose one material that was an effective photoconductor (PBI-A), and one that was less effective (PBI-L). Our investigations uncovered that PBI sample radical anion generation which gives rise to photoconductivity, does not correlate with higher photocurrents or oxygen evolution yields, and in fact it was PBI-L that was the superior photoanode. We attempted to elucidate this observation through various electrochemical and spectroscopic techniques.

Results and discussion

Device design

Dried films of PBI-A have been shown to be photoconductive in air under both UV and visible light due to the presence of radical anions, which were able to effectively transport charge between contacts. For PBI based devices to be employed as photoelectrodes they needed to be submerged in electrolyte, and thereby hydrated, as opposed to being exposed to air. Depending on the electrolyte pH, a dried PBI solution photoelectrode may rapidly dissolve. Instead we have used xerogels, which were effectively gels that had been allowed to dry in air and reduce their water content (96 w.t % in hydrogel, 5 w.t % in a xerogel).[183] Hydrogels were formed after the PBI solution (7.5 mg/mL PBI-A with 1 eq of base) was pipetted onto a slide of fluorine doped tin oxide (FTO), and then exposed to an acidic atmosphere using HCl vapour. Copper wires were then attached to the top left corner of the FTO slide with silver paste and epoxy resin, in order to transport charge, and yield a device (figure 76).

While the water content within a xerogel was similar to that of a dried solution it had undergone the gelation process, and therefore effectively incorporated water into the structure by immobilizing it before evaporation. In addition, the stability of both hydrogels, prior to drying, and dried solutions was not sufficient to perform electrochemical analysis, as they often fell of the FTO slide or dissolved. We have previously shown that upon immersion in water the xerogel partially rehydrates and that incorporating water into the structure increases the effective dielectric constant of the material, enabling charge separation.[183] Therefore we anticipated that if a suitable interface with a water oxidation catalyst could be made the xerogels presented promising photoanodes.
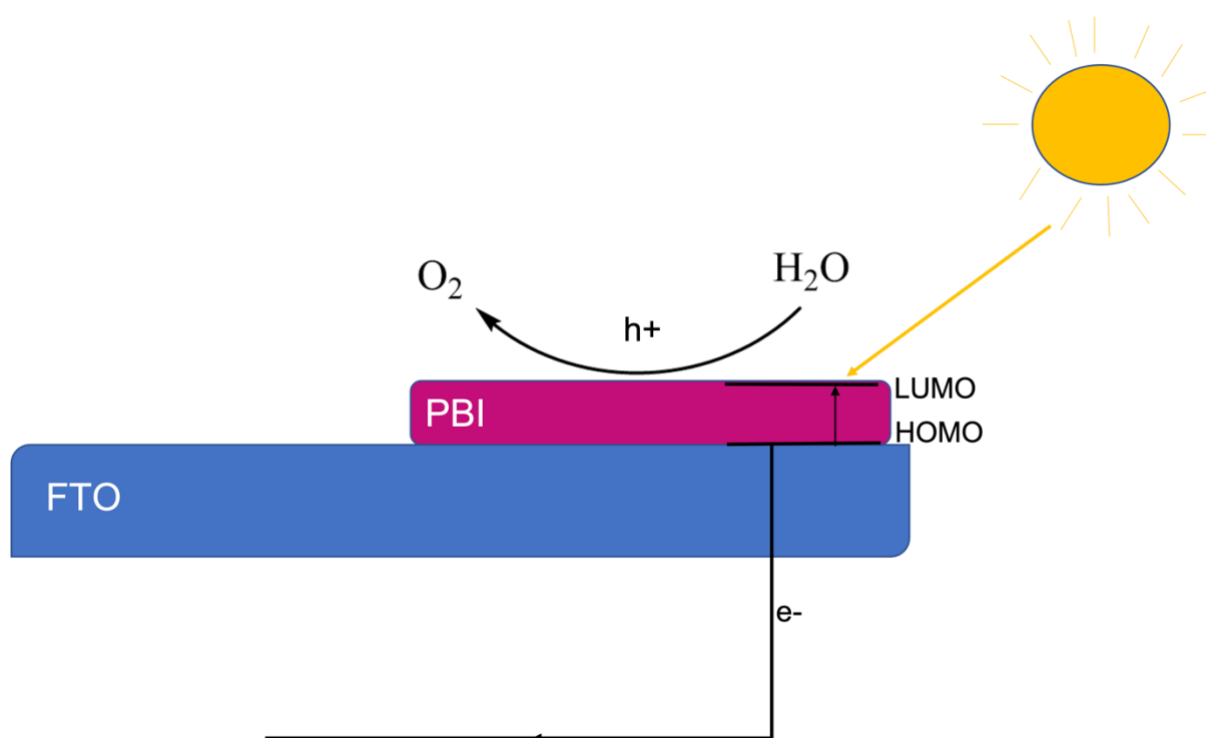
Figure 76- Schematic diagram of the PBI based photoanode placed on top of an FTO sheet of glass. The process of water oxidation is illustrated by the absorption of sunlight generating an electron and hole pair, which if correctly separated can allow the electron to flow around the external circuit, and the hole to oxidise water.

Initial PBI-A photoelectrode characterization

The PBI gelator solution used for forming electrodes was both a different concentration to that used in the photocatalysis study, but also a different initial pH as only one equivalent of base was used (1 eq of NaOH). This approach predated the photocatalysis study, and required less viscous solutions to ensure a uniform thickness across the electrode area, and therefore a lower pH solution of a higher concentration was used. The structure of PBI-A is shown in figure 77 along with the UV-Vis spectrum of the solution is shown in figure 78, in addition to the spectrum of the electrode after gelation and drying overnight. As expected the spectrum of the electrode was considerably broader due to aggregation that occurred due to the acid trigger used. The spectrum appeared to lie between that of the pH 5 photocatalysis sample (type 2) and the pH 2 sample which displays type 3 structure (discussed further in chapters 1 and 2).
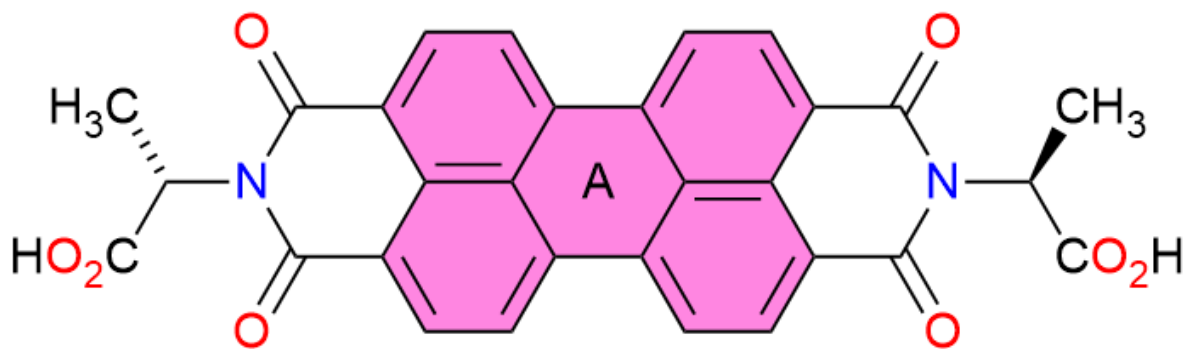
Figure 77- Chemical structure of PBI-A
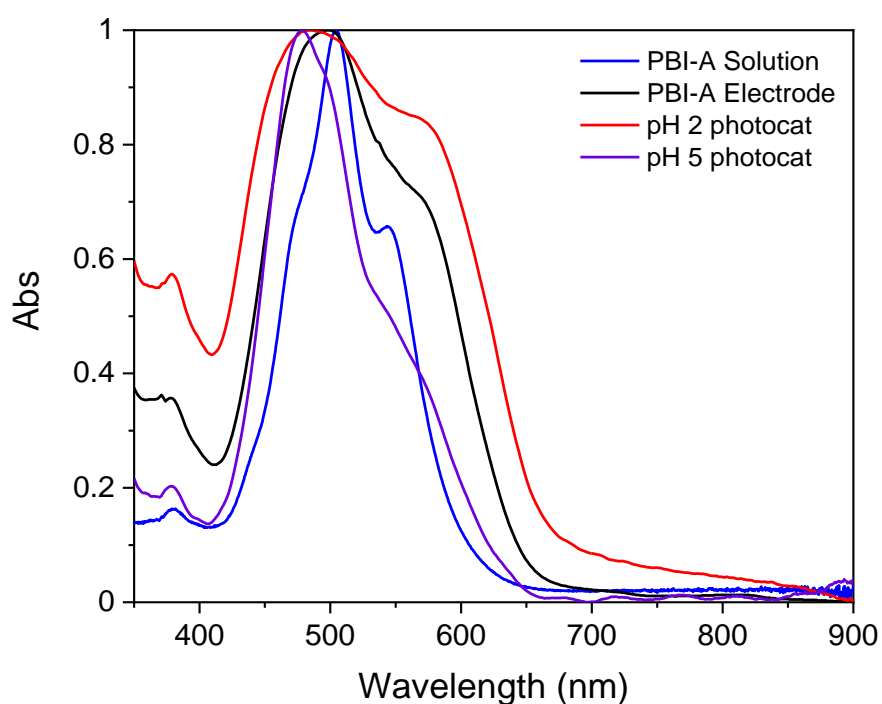
Figure 78- UV-Vis of PBI-A gelator solution and electrode compared with spectra from chapter 1 using photocatalysis samples. The PBI gelator solution was 7.5 mg/mL, and the electrode was prepared using the acid trigger method. pH 2 and pH 5 spectra taken from chapter 1 for PBI-A. All absorbance data was normalized.

Although this was not a consideration at the time of experimentation, the spectra for the electrode and gelator solution were processed using the same fitting procedure as that of the photocatalysis samples to determine the contribution of structure types. The result of this fitting is shown in figure 79, and confirmed that, as expected, the solution displayed exclusively type 1 aggregates. Interestingly the electrode spectrum displayed a dominance of

type 2 aggregates, in addition to a high concentration of type 3 aggregates. Despite the solution preparation being different for the photocatalysis and electrode solutions there were clear parallels between the local structures in solution, as confirmed by UV-Vis. The high pH of the starter electrode solution is similar to the pH 8-10 samples from the photocatalysis study, and therefore one could hypothesize a similar extent of self-assembly. Electrodes were prepared by leaving the electrode solution placed in an acidic atmosphere of HCl for 15 mins, and then allowed to dry overnight before use. Due to the variability of this preparation method the resulting electrodes may have different concentrations of type 2/type 3 aggregates depending on gelation conditions. The final electrode spectrum contained an almost equal concentration of type 2 and type 3 aggregates, and displayed the characteristic blue peak shift and broadening expected for these aggregates. But the spectrum did not display the extreme broadness expected for a type 3 aggregate dominated species. Type 2 aggregates have previously been shown to be key for preserving long lived charges needed for photocatalysis, and relating this further to photoelectrodes is an interesting avenue.
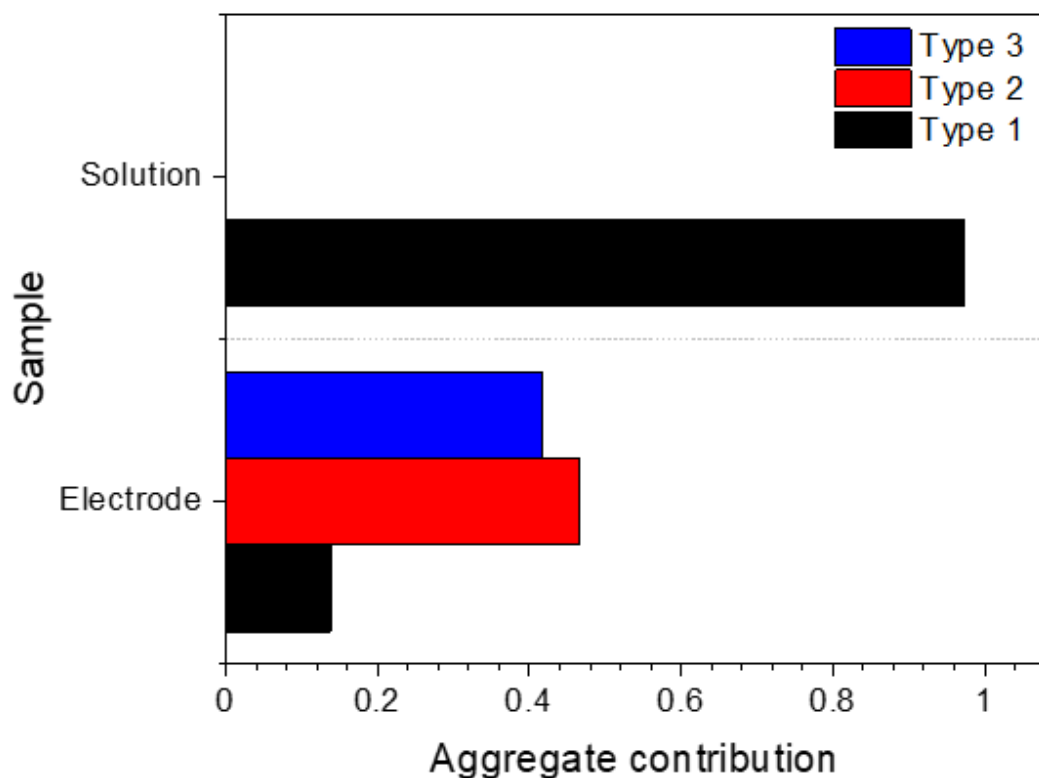
Figure 79- Illustration of fitting procedure used to calculate aggregate type contribution from the UV-Vis spectra of the PBI-A gelator solution and electrode formed.

PBI-A photoelectrochemistry

Figure 80 shows a characteristic PBI-A CV in the dark, with a prominent reduction beginning at -0.17 V (vs Ag/AgCl) and continued to -0.7 V. This peak described the PBI reduction from an initial neutral species to a single PBI radical, and then to a doubly reduced radical dianion. The peak is broad due to the extent of aggregation across the structures, and lack of formal reduction on a single PBI molecule. The experiments were performed in water with KCl (0.1 M) as the electrolyte, which was adjusted to pH 4 using 0.1 M HCl. Above pH 4 electrodes would dissolve fairly quickly, due to deprotonation of the carboxylic acid functionality. This meant that any water oxidation catalyst employed would have to be stable to acid conditions.

The linear sweep voltammogram (LSV) displayed the dark current when no light was present, and also the chopped photocurrent of the device. As expected the photocurrent increased with applied bias, and the dark current of the PBI electrode began to increase at around 1.25 V (vs Ag/AgCl) due to the onset of water oxidation . The initial photocurrent was around 2 μA at (+0.2 V vs Ag/AgCl) which was low but encouraging for an unoptimized system without a water oxidation catalyst. Similar systems such as Norimatsu *et al.* achieved 6 μA with a perylene based thin film-based device,[215,216] while Finke *et al.* had claimed a PBI based device was capable of 150 μAcm^{-2} and a faradaic efficiency of 80 %.[212] This claim was later revised to a faradaic efficiency (FE) of 31 %, with more modest photocurrents.[214]
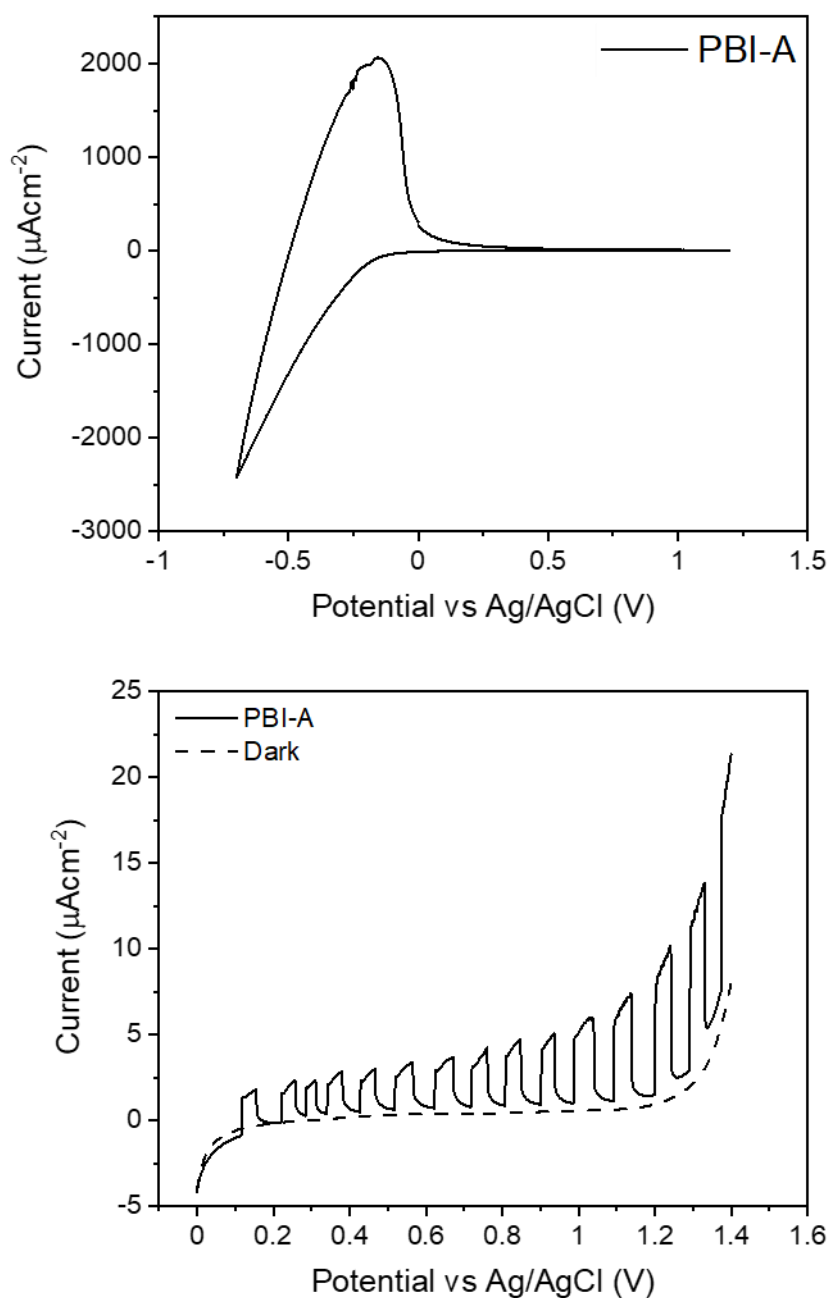
Figure 80- PBI-A CV at pH 4 0.1 M KCl using Pt wire and Ag/AgCl reference electrode. Linear sweep voltammetry using Xe lamp with KG1 with a light intensity of 100 mWcm^{-2}. Chopped light every 5 seconds. Dark current is shown by dashed line.

IrO$_x$ catalyst incorporation

Due to the lack of pH stability of our PBI-A films above pH 4 (rapid dissolution of the film), adding IrO$_x$ nanoparticles through a typical photodeposition was not possible. Therefore, we decided to incorporate K$_2$IrCl$_6$ into our gelation mixture at a low wt. %, with the hope that the

gelation process via the HCl acid trigger would have the same effect. We were not able to conclusively prove whether the addition of iridium through this manner has successful. In theory we had hoped to use photodeposition in order to deposit the catalyst at the photoactive sites where charge carriers were present. Our gelation method, were it successful, would only distribute the iridium at random through the film. The resultant photoelectrochemistry did not show any evidence of IrO_x, or significant photocurrent changes. A successful catalyst should either increase the FE of the device, or its photocurrent, but it was not conclusive whether this method was successful either way. Figure 81 displayed the CV and LSV for the resultant device, which resulted in the same photocurrent across the potential range. But there was an additional feature in both the CV and the LSV at around +0.7 V vs Ag/AgCl, which was likely iridium oxidation, so it did appear that the iridium had been integrated into the device but not affected the photocurrent. It was also not possible to examine whether IrO_x nanoparticles had formed, or gather any further information about how the iridium salt had changed upon the pH switch used for gelation of the PBI solution.
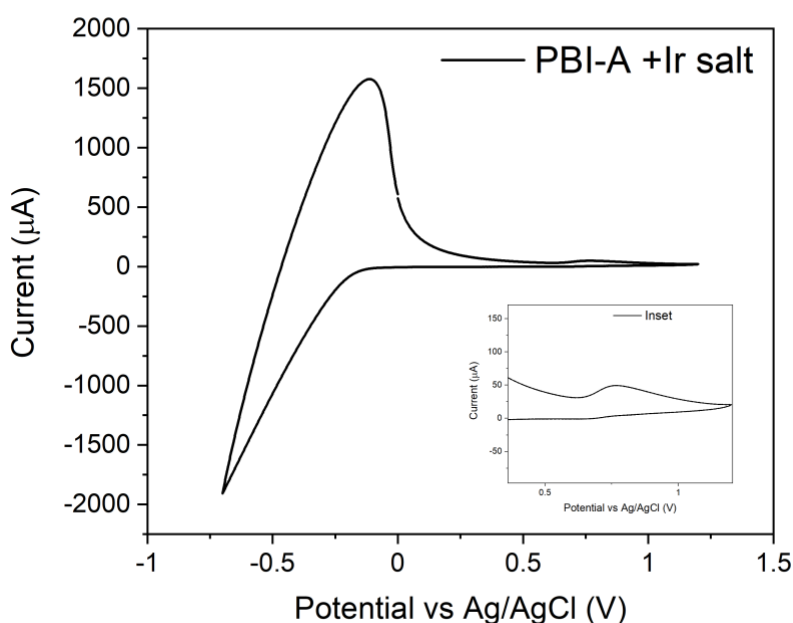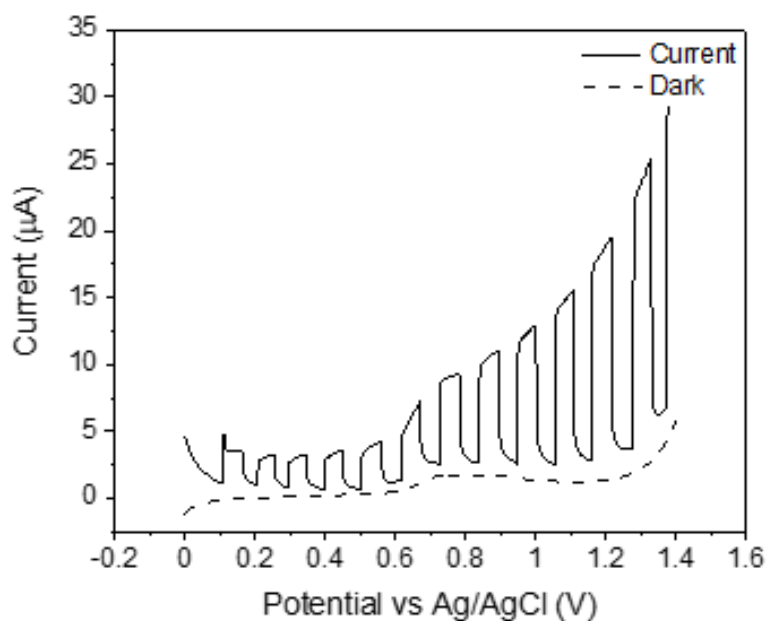
Figure 81– LSV of PBI-A + K_2IrCl_6 salt in situ gelation electrode samples. Dark measurement shown with dashed line, increase in current due to light being turned on for 5 seconds. Slow scan rate of 20 mVs^{-1} used for measurements. Xe lamp light source used with 100 mWcm^{-2} light intensity, and a KG1 filter. Electrochemistry performed in a custom 3 neck flat cell using a pH 4 KCl (0.1 M) electrolyte, with a Ag/AgCl reference electrode and platinum wire counter electrode.

Oxygen evolution testing

Following the potential integration of iridium into the PBI-A device, the next step for testing it as a photoanode was to investigate its oxygen evolving efficiency. Due to the low photocurrent the evolution of oxygen was likely to be at a very low rate, so using traditional GC type detection systems was out of the question. We employed a generator-collector method in order to effectively measure the quantity of oxygen evolved, using the charge passed within the experiment.[40] This required the use of two electrodes sandwiched together in proximity in order to create a defined area for oxygen evolution via water oxidation, and subsequent oxygen reduction using a negative potential applied to FTO. A spacer of 1 mm thickness was used to define the area between the two electrodes.
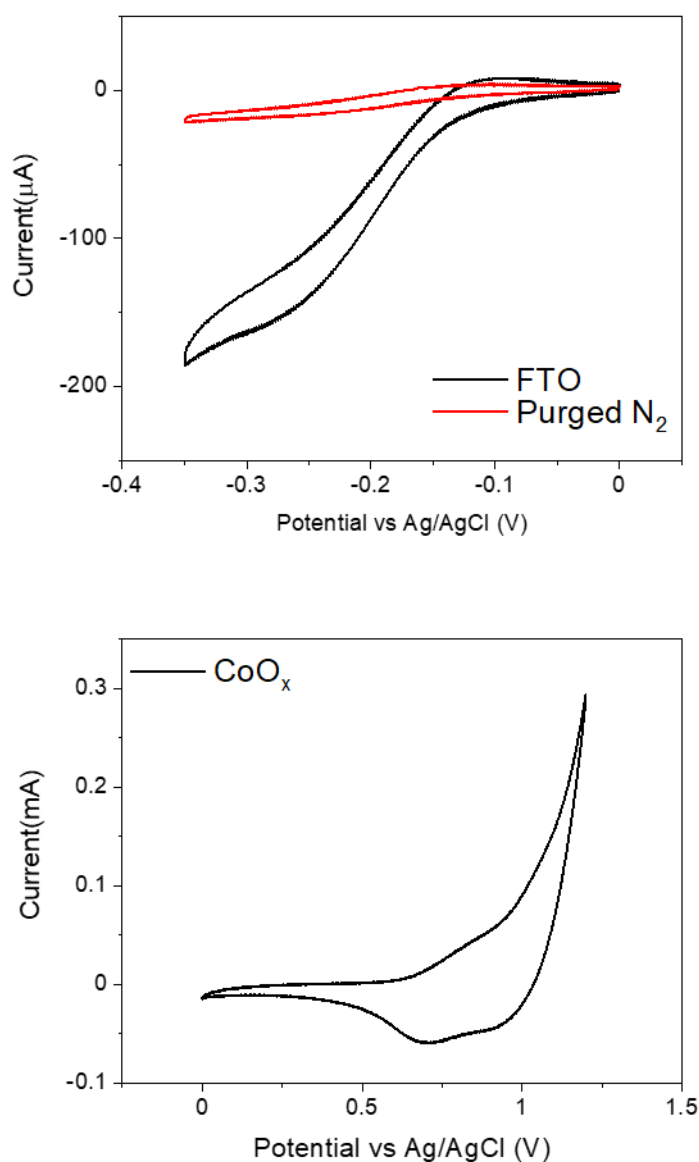
Figure 82- CVs of FTO collector and CoOx generator electrodes in pH 4 KCl electrolyte. Electrochemistry performed in a custom 3 neck flat cell using a pH 4 KCl (0.1 M) electrolyte, with a Ag/AgCl reference electrode and platinum wire counter electrode.

Control experiments used a CoO_x as the generator electrode in place of the PBI. CoO_x is a well-known dark water oxidation catalyst that operates with ~100% Faradic efficiency for O_2 evolution in water with an applied potential of +1.4 V.[42,217] The collection efficiency for this device was shown to be 54 ± 7 % at pH 4, a lower pH than standard usage for this system due to the lack of stability of CoO_x. However, the CoO_x deposition took place at pH 7 in a phosphate buffer (0.1 M), using +1.2 V applied for 30 mins to leave a brown tinge on the sheet of FTO.[42]

Custom electrochemical flat cells were purged of oxygen for 30 minutes before the experiment began, with a CV of FTO (figure 82) used to determine when the experiment was to begin. Initially there was a very large oxygen reduction peak due to dissolved oxygen from the atmosphere, but upon purging successfully this peak disappeared, meaning our experiment would not be contaminated with latent oxygen. Figure 82 displayed the classic CV for CoO_x, meaning it was suitable for electrocatalytically generating oxygen at a potential > 1 V. For the first 200 seconds of the experiment a potential of +0.2 V was applied to the generator electrode, a potential that would not generate any oxygen to be used as a baseline for the experiment. After this point a potential of + 1.4 V was applied to yield oxygen evolution, with a negative potential of -0.7 V applied to the FTO electrode throughout. The negative current shown by the FTO trace signified the reduction of oxygen as a result of it being generated by the CoO_x. The current took a considerable amount of time to peak due to diffusion across the distance between electrodes, and continued to reduce oxygen even after the potential applied to the generator had been lowered back to +0.2 V (1200 seconds). The experiment was left to run for the remainder of the hour in order to allow for the maximum amount of oxygen reduction. The collection efficiency of these electrodes was then calculated using the charge passed of the collector/ charge passed of the generator. The charge was calculate using the integrated area of current against time. A collection efficiency of less than 100 % was due to the leaking of oxygen away from the collector electrode (figure 83).
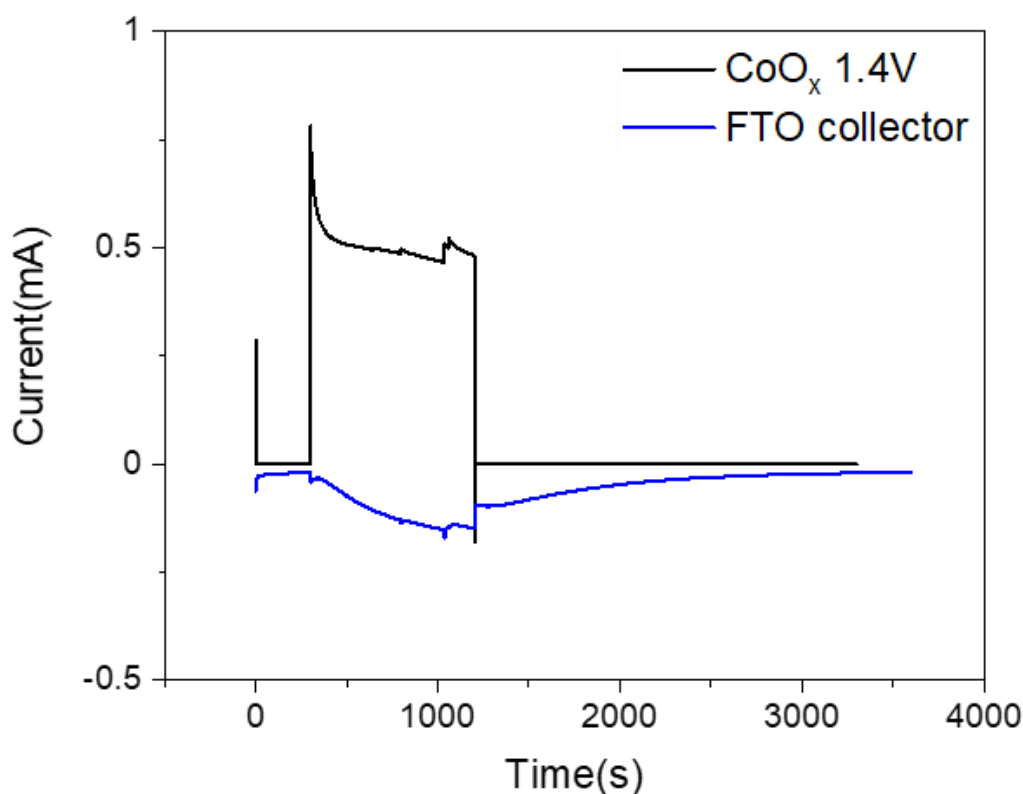
Figure 83- Generator collector method for oxygen detection. CoOₓ trace shown in black with a potential of +0.2 V applied, and then +1.4 V applied to oxidise water. FTO has an applied potential of -0.7 V throughout the experiment. Electrochemistry performed in a custom 3 neck flat cell using a pH 4 KCl (0.1 M) electrolyte, with a Ag/AgCl reference electrode and platinum wire counter electrode.

The PBI-A electrode (with added Iridium salt) was illuminated with a 490 nm LED with a light intensity of 20 mWcm^{-2} through the back face (i.e. through the FTO), reducing light intensity at the electrode, due to the need for the front face to face the FTO collector electrode. This resulted in the photocurrent of the PBI electrode being lower than normal at around 0.2 μA, which also meant a lower rate of oxygen evolution, making its detection even harder. Data recording for this set of experiments was very challenging due to the low signal to noise as a consequence of low currents. Figure 84 displays a standard experiment, which had a significant amount of noise throughout but did have a response on the FTO when the light was turned on, indicating oxygen evolution. The collection efficiency for the PBI-A device with IrO$_x$ added in situ was 30 ± 10 %, based on three repeats. Without the added iridium there was no recorded photocurrent or response from this setup. Due to the level of noise in these

measurements the results cannot conclusively state that the catalyst integration was the reason for the oxygen levels recorded relative to the device not containing the catalyst. However, the result was encouraging as we successfully measured the detection of oxygen from our device, with a faradaic efficiency of 56 ± 12%.
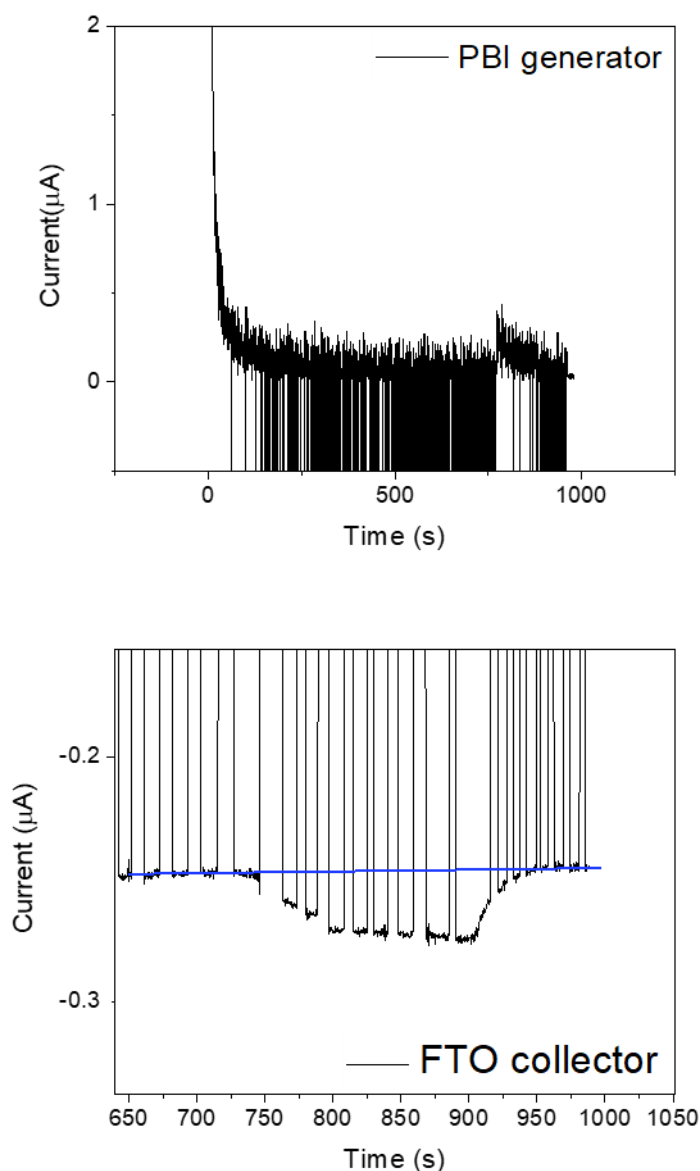
Figure 84- Generator collector setup data for PBI-A. Light source was 490 nm LED with a light intensity of 20 mWcm^{-2}, which was turned on at around 740 seconds and turned off at 900 seconds. In order to calculate charges data was fitted to remove noise. Electrochemistry performed in a custom 3 neck flat cell using a pH 4 KCl (0.1 M) electrolyte, with a Ag/AgCl reference electrode and platinum wire counter electrode. Spikes due to issues with electrical contacts, and electrical noise. Delay in oxygen detection likely due to diffusion.

CoO_x catalyst addition

Having appeared to succeed with the addition of a rare platinum group catalyst to our system, we attempted to integrate a more common catalyst as an alternative. CoO_x had been used as our model system on FTO, and appeared to be suitable for photodeposition. The initial layer of PBI was deposited in the same manner as previously followed by a photodeposition step, using a Xe lamp and an applied potential of +0.7 V. The electrolyte pH for a conventional deposition of CoO_x on FTO to use as a dark electrocatalyst is around 7, but due to the instability of the PBI electrode at that pH, the electrolyte system of KCl adjusted to pH 4 was used once again. While the electrode was more stable at pH 4, the CoO_x was likely to be unstable at low potential and dissolve, as referenced by the pourbaix diagram.[217] Cobalt catalysis for electrochemical water oxidation has been studied in detail by Nocera et al.,[217,218] with the catalytic identity highly pH dependent.[217]

This section of work was complicated by a series of surprising results where the photocurrent of the PBI-A samples appeared to increase dramatically, seemingly for no reason (figure 85). A series of experiments were carried out to determine the source of the activity, which turned out to be a layer of TiO_2 which had been deposited on the FTO glass that we had received from the supplier. In retrospect this distraction sidelined the photoelectrode work for a period of time, and it was not possible to record any measurements of successfully photodeposited CoO_x onto PBI-A.
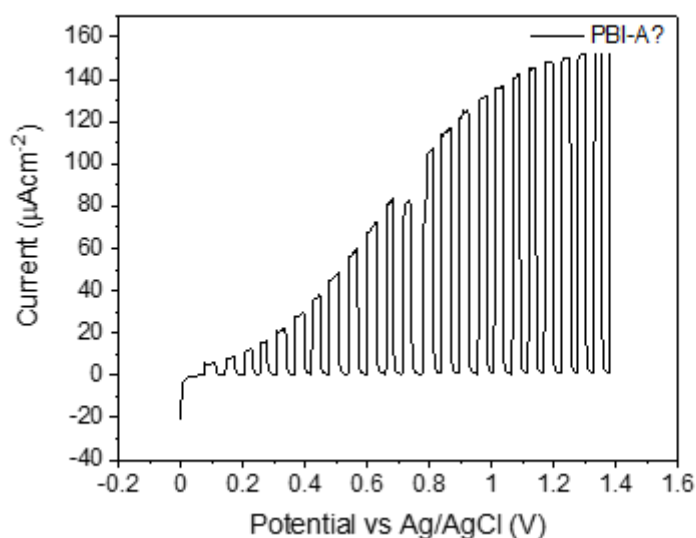
Perylene Bisimide amino phosphonate
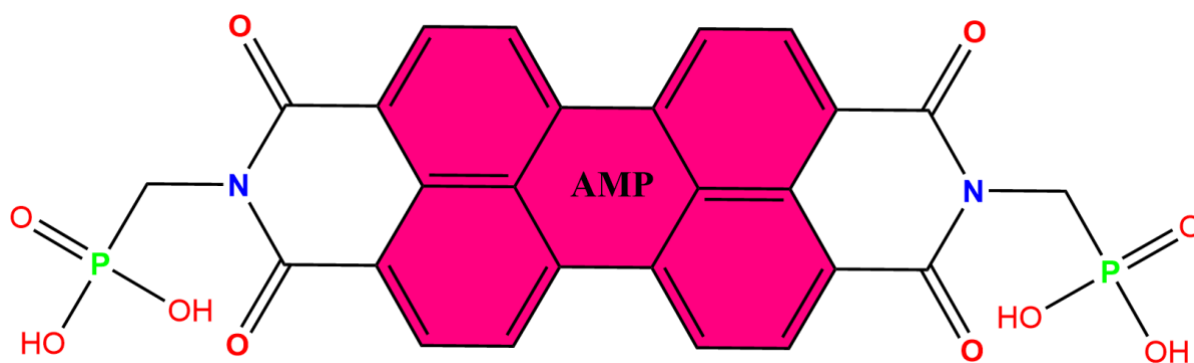
Figure 86- Chemical structure of PBI-AMP.

As finding a suitable abundant catalyst that works well in acidic conditions was beyond the scope of this project we synthesized (by D McDowall at the University of Glasgow) the PBI used by Finke et al. and performed our own electrochemical characterization, in order to understand the device further Perylene bisimide amino phosphonate (PBI-AMP, figure 86). It was hypothesized that the addition of the phosphonate groups aided the adhesion to a cobalt based catalyst at neutral conditions. The method of electrode preparation also differed greatly and required plasma cleaning of the FTO, followed by spin coating to allow for a thin layer of PBI-AMP onto the surface of the FTO. Once partially dried the sample was then dipped into a mixture of EtOH and HCl, to form an almost 'outer gel layer', although the morphology was never fully characterized by Finke *et al.*[212] In addition the PBI solution preparation was a matter of simply adding 2 mL of water and then a few drops of 1M KOH (as opposed to our standard NaOH), which led to rapid dissolution of the solid material. The resulting solution was considerably darker than that of our amino acid based PBI, as shown by the UV-Vis of the electrode, and therefore produced strikingly differently coloured electrodes. On one hand there was the difference of counter ion salt (Na^+ vs K^+), but also two different methods of forming electrodes. The spin coated (Finke method) produced much thinner samples, which appeared to be much less aggregated by the lack of UV-Vis broadening. But both samples

were stable in a pH 7 phosphate buffer electrode, regardless of preparation method, which was not possible with PBI-A (figure 87).
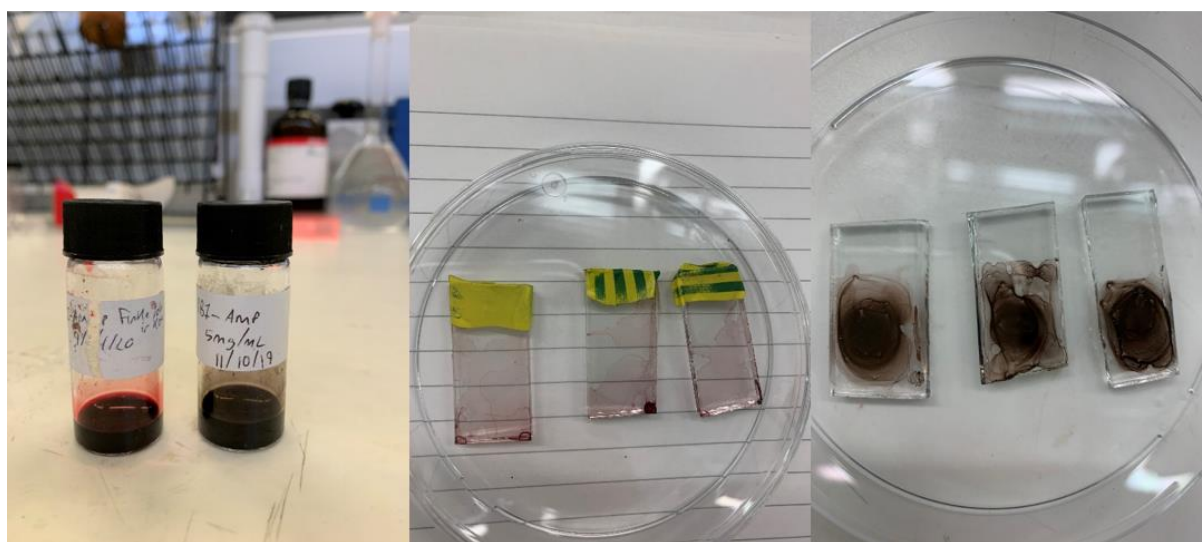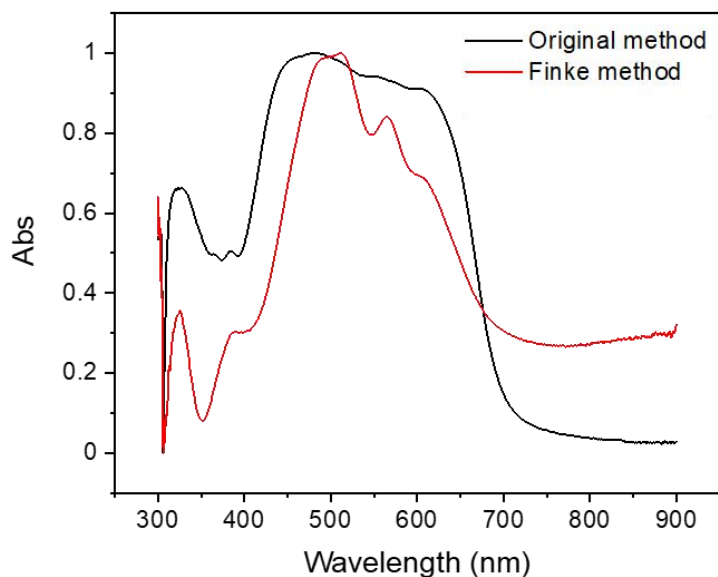
Figure 87- UV-Vis spectra of PBI-AMP using two different methods of preparation, the original acid vapour trigger and the spin coated method, which resulted in one thick and one thin sample (absorbance data is normalized to compare between films). Images of two different gelator solutions, both 5 mg/mL of PBI-AMP but containing different bases either KOH or NaOH. The solutions were clearly different colours and resulted in different coloured films and thicknesses (Pinker electrodes from K, and black electrodes from Na).

Initial PEC testing of PBI-AMP samples using our sample methodology did not yield a significant difference in the CV of the PBI, despite a more well-defined reduction (figure 88). This was also true for the chopped photocurrent experiments, which were on the order

expected for PBI-A, even at higher applied potentials. Up to this point our light illumination setup made use of a KG1 filter (300-1100 nm range), which removed a large portion of UV light from reaching the sample while still using 100 mWcm^{-2} as the light intensity. Finke *et al.* described a 'visible light assisted' system but used a light illumination source (315-700 nm light), thereby including a large amount of UV light.
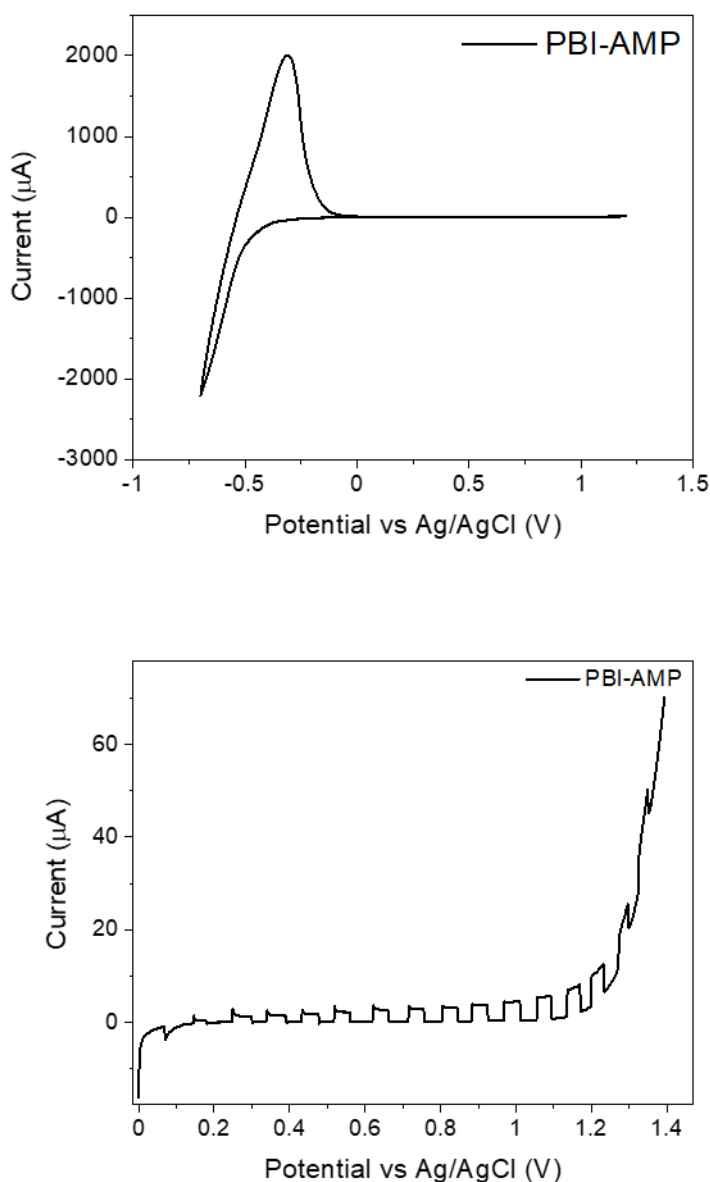
Figure 88- CV and LSV of PBI-AMP electrodes in pH 7 phosphate buffer (0.1 M). Electrochemistry performed in a custom 3 neck flat cell using a pH 4 KCl (0.1 M) electrolyte, with a Ag/AgCl reference electrode and platinum wire counter electrode. Xe lamp light source used with 100 mWcm^{-2} light intensity, and a KG1 filter.

Removing the KG1 filter and adjusting the sample position to allow for the same light intensity saw a significant increase in the photocurrents observed, and confirmed remarkable UV activity. Figure 89 displays the huge difference in photocurrent with and without the presence of the KG1 filter, with the same light intensity kept constant by moving sample position relative to the light source.
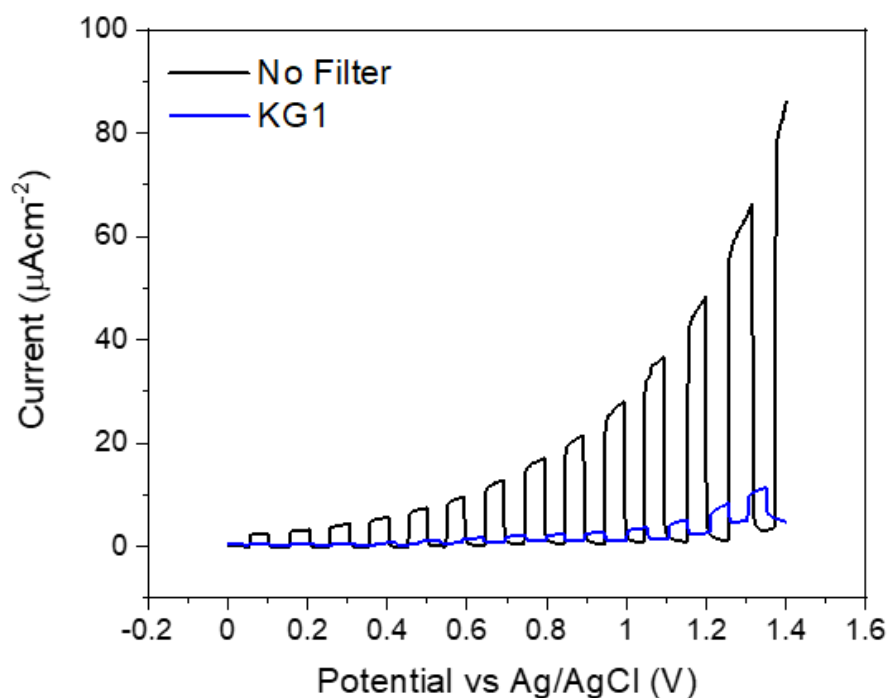
Figure 89- LSV of PBI-AMP electrodes in pH 7 phosphate buffer (0.1 M). Electrochemistry performed in a custom 3 neck flat cell using a pH 4 KCl (0.1 M) electrolyte, with a Ag/AgCl reference electrode and platinum wire counter electrode. Xe lamp light source used with 100 mWcm^{-2} light intensity, with and without a KG1 filter and the position adjusted.

Developing this further meant repeating the same experiment with our original PBI-A to determine if the biggest difference in our activity simply came from the light source used. Figure 90 shows the difference in material present on the FTO slide due to the spin coated method, and therefore less current passed from the CV. But there did not appear to be a reproducible difference in photocurrent response between samples that were spin coated, and those that used optically thicker samples. The same was also true for PBI-AMP when testing spin coated samples against thicker electrodes using our normal method. This also confirmed that the photocurrents achieved by PBI-AMP were higher than those observed

using a PBI-A, regardless of method, and that PBI-A was still not stable above pH 4 making any future Co based catalyst integration difficult.
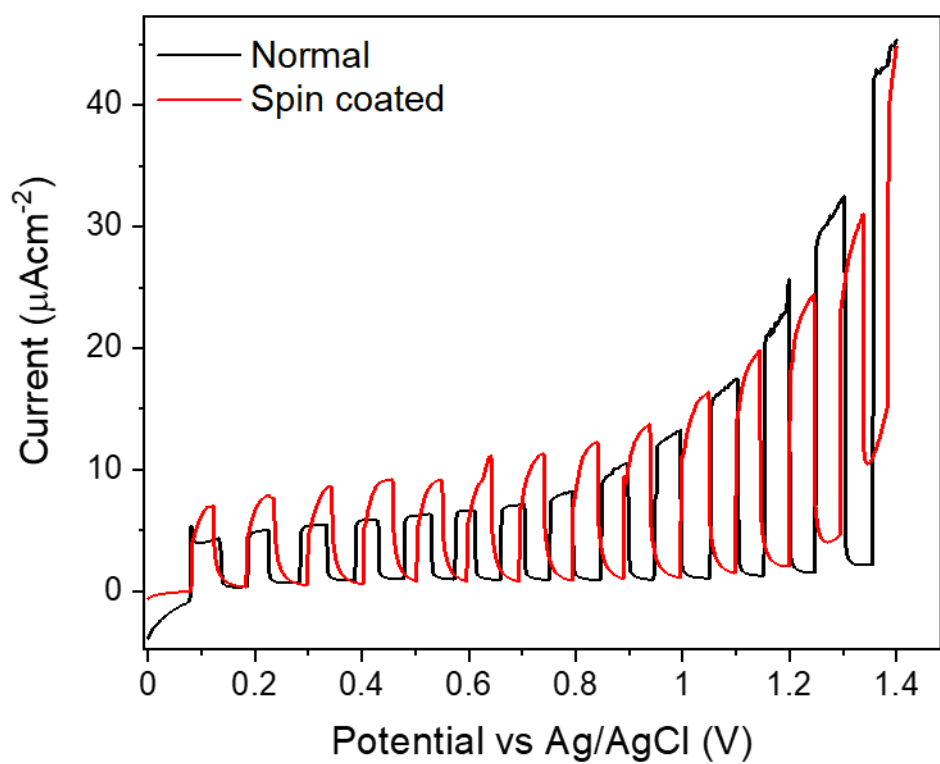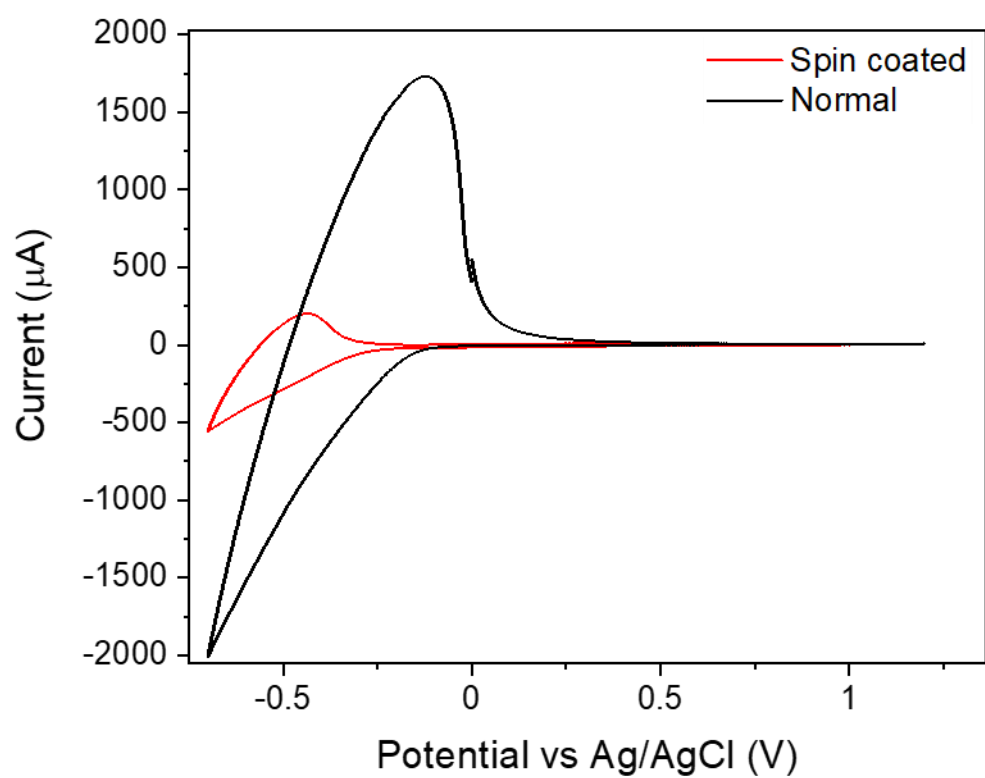
Figure 90- LSV of PBI-A electrodes, using two different electrode preparation techniques. Electrochemistry performed in a custom 3 neck flat cell using a pH 4 KCl (0.1 M) electrolyte, with a Ag/AgCl reference electrode and platinum wire counter electrode. Xe lamp light source used with 100 mWcm^{-2} light intensity, without a KG1 filter and the position adjusted.

Integrating a catalyst to PBI-AMP

Having confirmed the origin of the improved activity of PBI-AMP, we endeavored to successfully combine a water oxidation catalyst as Finke claimed in the original publication.[212] The catalyst used a CoO$_x$ based photodeposition step as done previously with PBI-A, but this time using pH 7 which should stabilize the Co based system, and not dissolve the electrode. While there was initial promise due to the added stability of the film at pH 7 (using a 0.1 M phosphate buffer), once again the addition of the catalyst was plagued with issues. Initial experiments involved photodeposition in a 50 mM Co(NO)$_3$ solution at pH 7, and resulted in presence of Co features in the resultant CV upon switching the electrolyte to remove the Co salt.

Figure 91 displays the presence of Co oxidation at around 1 V (vs Ag/AgCl), and also still contained the PBI features from PBI-AMP post deposition. The LSV post deposition did show a noticeable improvement at low applied potentials with around 20 µA at +0.2 V, but not at higher potentials where electrocatalytic features of Co were dominant as opposed to photocatalytic. The addition of Co increased the current displayed by the device with no light applied, but also appeared to decrease the maximum photocurrent observed for PBI-AMP which was 60 µA at 1.2 V applied (vs Ag/AgCl). However further testing on the electrode confirmed that the stability of this device was worse than that had not undergone addition of the catalyst. In addition, subsequent experiments on many different samples of PBI-AMP confirmed this lack of stability at pH 7, and featured lower photocurrents than described in figure 91. This was a far cry from the 'efficient coupling' as described by Finke et al. in 2014,[212] but aligned much better with the follow up paper in 2021, which described an anti-catalytic (i.e. adding a catalyst making the device perform less efficiently) style mechanism which inhibited the device.[214] Photocurrent transients from this report also displayed the higher photocurrents at lower applied potentials, with large spikes observed below +0.2 V.[214] These large spikes led to a follow up article which investigated the impurities present in the FTO, which also contributed to the anti-catalytic effect observed.[214,219] To this point we had not

seen initially high photocurrents at low applied potentials, but had certainly struggled to incorporate a catalyst successfully despite increasing photocurrents of our own devices.
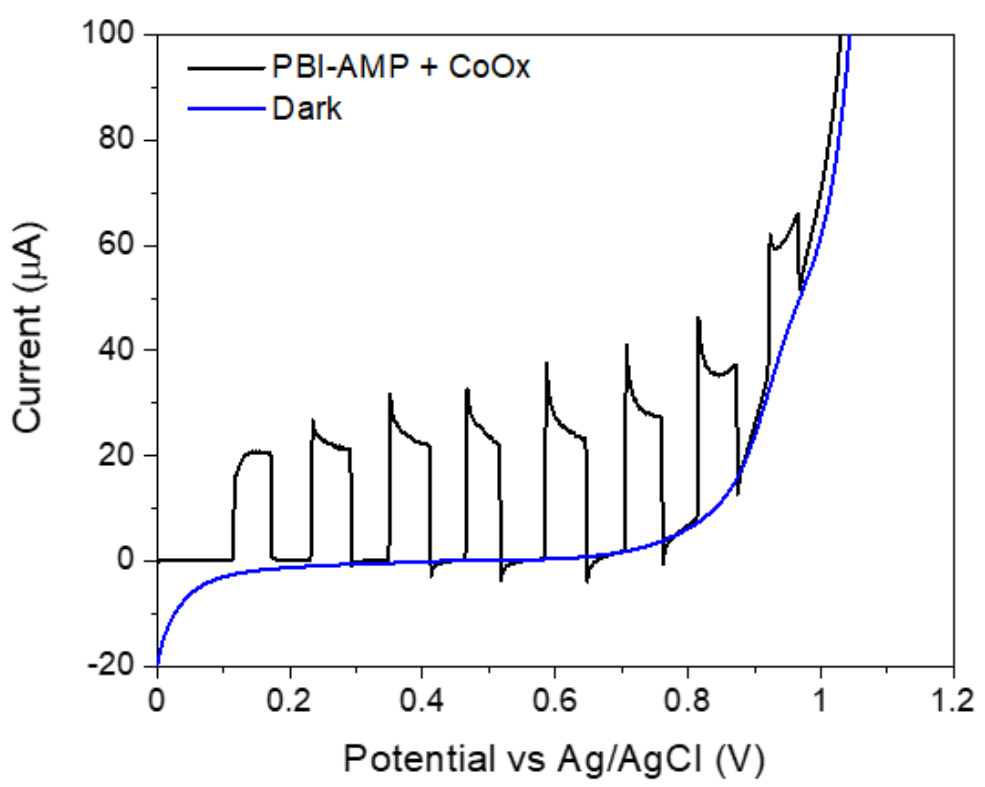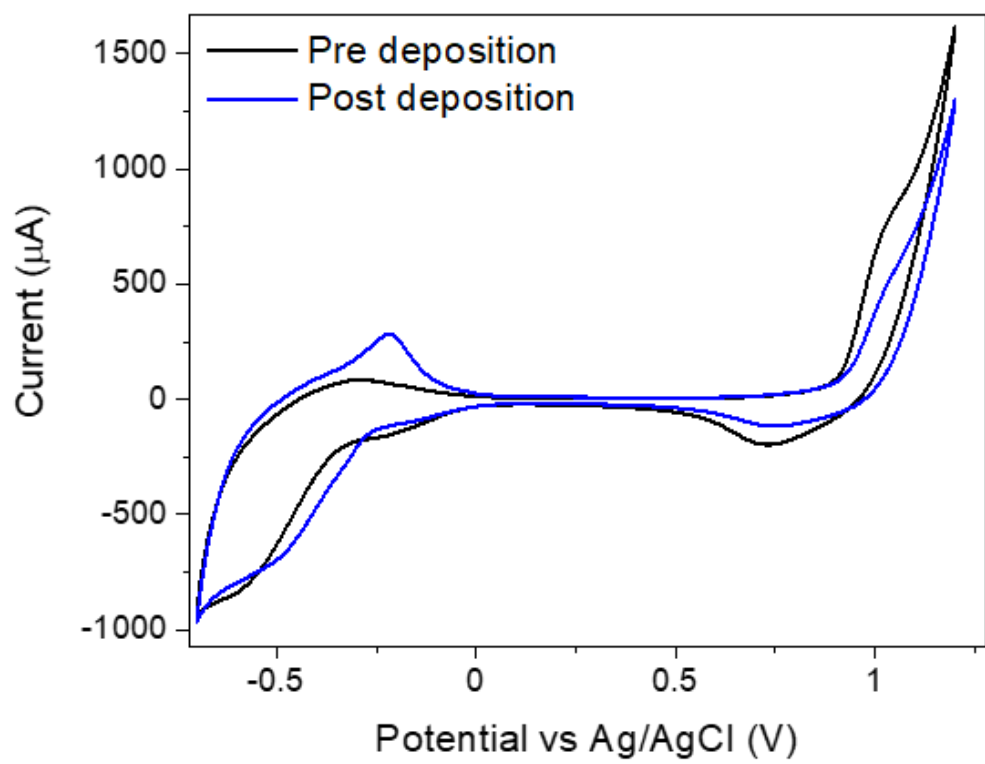
Figure 91- CV and LSV of PBI-AMP electrodes.CV before and after photodeposition step. Photodeposition took place in a pH 7 phosphate buffer with Co(NO₃)₂ 50mM present. An applied potential of +1.2 V was applied for 15 mins. Electrochemistry performed in a custom 3 neck flat cell using a pH 4 KCl (0.1 M) electrolyte, with a Ag/AgCl reference electrode and platinum wire counter electrode. Xe lamp light source used with 100 mWcm^{-2} light intensity, without a KG1 filter and the position adjusted.

New amino acid functionalized PBI photoelectrode: PBI-L

An initial aim of this project was to test multiple different PBIs electrodes at the same time, with a high throughput style methodology to explore how different PBI functionality affected photocurrent response. Unfortunately, we were unable to develop a method for testing multiple electrodes in series, in part due to COVID and logistics of cell design. As a result of this we were left with several previously synthesized amino acid functionalized PBIs, with no knowledge of which would perform best as a photoelectrode. We have previously investigated the photoconductive properties of these films,[104] and also their ability to function as photocatalysts in chapter two.[49] There appeared to be no obvious correlation between photoconductivity and hydrogen evolution through initial measurements, and so far the best performing device in literature did not feature an amino acid functionality. As part of the collaboration with the University of Glasgow there was a synthetic partnership, where our input could be used to guide synthesis of PBI molecules. We were unable to provide a definitive direction of which avenue to explore, due to limitations in speed of testing.
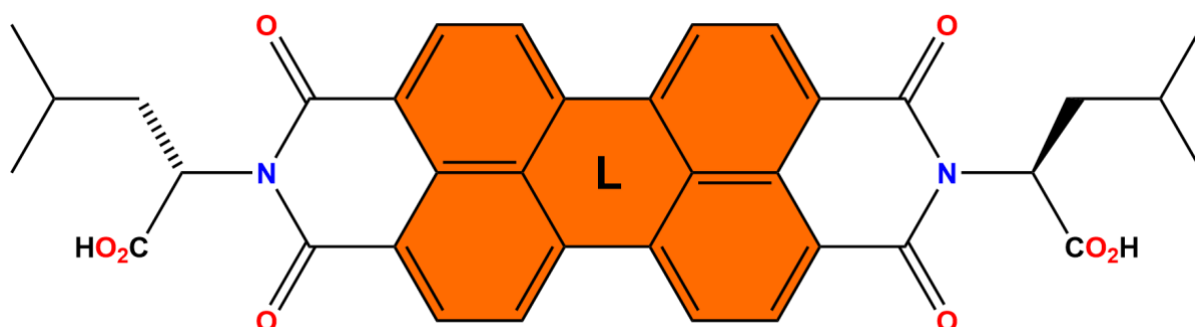
Figure 92- PBI-L molecular structure

As part of the process of choosing a PBI structure to form PBI noodles Daniel McDowall tested a number of our amino acid functionalized solutions. A key consideration for developing a system able to perform with well-established catalysts at neutral pH, instead of also having to design an acid stable alternative. This meant increasing the stability of our electrodes so they were able to withstand a higher pH electrolyte, as PBI-AMP was able to. As a consequence of testing many PBIs for the formation of PBI noodles, PBI-L was identified as a potential candidate due to its ability to form noodle- like structures stable at a variety of pHs (figure 92). For the eventual noodle work PBI-I was used as the noodles formed were more

'noodle like' than those formed by PBI-L, but by this point electrochemical devices using PBI-L had begun (I is simply an isomer of L, rather than a large difference in functionality).

The PBI concentration of the gelator solution was raised from 7.5 mg/mL to 10 mg/mL for all following electrodes, due to parallels with noodle solutions needing a higher concentration to form noodles. Initially two gelator solutions were made, one containing a single equivalent of base, and the other containing two equivalents. There was therefore a subtle difference in pH between the two solutions (6.6 vs 7.1, lower than normal due to higher concentration of PBI), which was investigated using electrochemical and UV-Vis methods. $CaCl_2$ was employed as a salt gelation trigger, rather than the acid trigger previously used for PBI-A to form electrodes. Using a new dipping method, 5 µL of gelator solution was placed onto a slide of FTO then allowed to almost dry before being dipped into a solution of $CaCl_2$. This was similar to the method used by Finke, but this time used a neutral salt rather than an acid/alcohol mix.
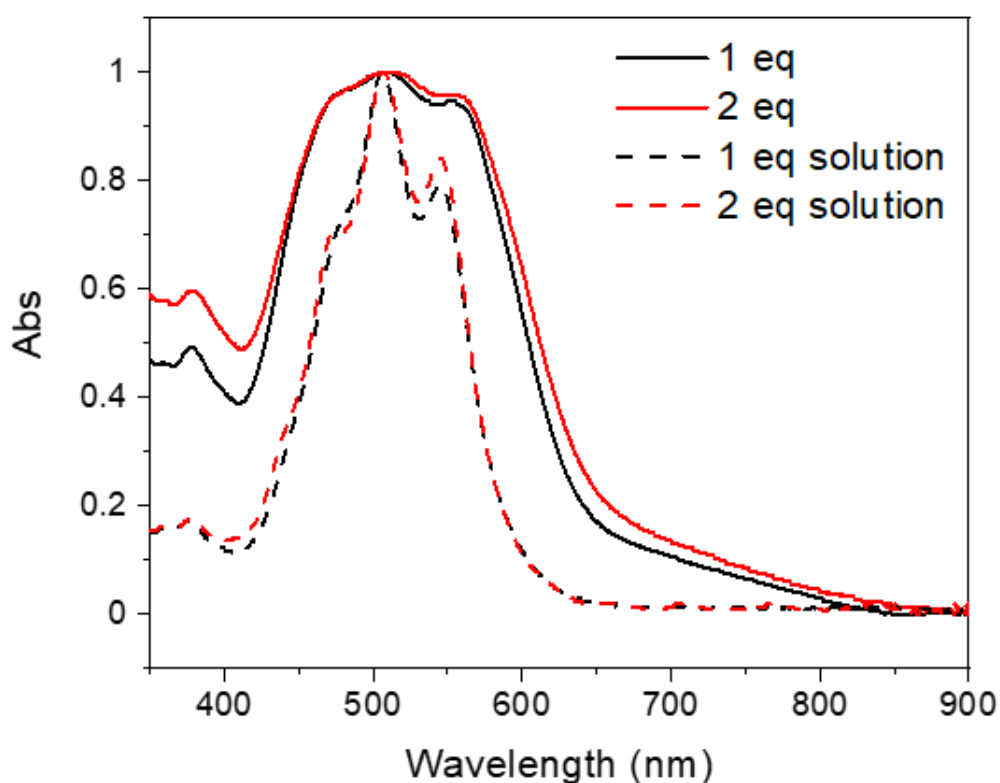
Figure 93- UV-Vis spectra of PBI-L samples containing 1 equivalent and 2 equivalents of NaOH. Spectra of electrodes formed following salt addition are displayed in a solid line, and solutions displayed by a dashed line. Absorbance data was normalized.

Figure 93 displays the UV-Vis spectra of the two PBI-L solutions with different equivalents of base, and confirmed the subtle difference in pH in this case did not yield a significant difference in the UV-Vis spectra, aside from a more pronounced peak at 550 nm. Due to the similarities of the spectra 1 equivalent was used as the standard solution from this point onwards. In retrospect a further investigation on the pH behavior of PBI-L should have been carried out, in order to form the same pH spectra for the other PBIs in the photocatalysis study, but due to issues with the purity of the PBI-L it was excluded from the initial study. Due to this we were unable to perform the same fitting to determine the contribution of aggregate types in the electrode spectrum.

PEC experiments of PBI-L electrodes took place in a new methyl phosphonic acid-based electrolyte system (adjusted to pH 6), due to its reported ability to stablise metal oxide water oxidation catalysts.[220] PBI-L electrodes were somewhat stable in solutions around pH 6, a new feature for our PBI based systems. But an additional layer of PBI solution increase this stability further, and was therefore used for electrochemical testing over longer time periods. Once the electrode had dried another 5 μL solution of PBI-L was added on top, followed by another dipping in the salt solution. The initial photocurrents were as promising as the new-found pH stability, as shown by figure 94 which demonstrated a benchmark photocurrent of 180 μAcm^{-2} for thin film PBI based devices at + 0.1 V with no scavenger present (vs Ag/AgCl). Interestingly the initial photocurrent for the device was at the lowest applied potential, and decreased with applied bias, indicating an initial oxidation process occurring within the film. The LS began at 0 V with increasing potential applied at a rate of 20mVs^{-1}, we believe this process is as a result of a chemical change that occurs due to time in solution, rather than due to applied potential. After this initial process the photocurrent stabilized above 100 μAcm^{-2} which was far higher than anything achieved before by PBI-A. The CVs of the device also displayed impressive stability with reproducible scans, which was abnormal for our PBI-A system.
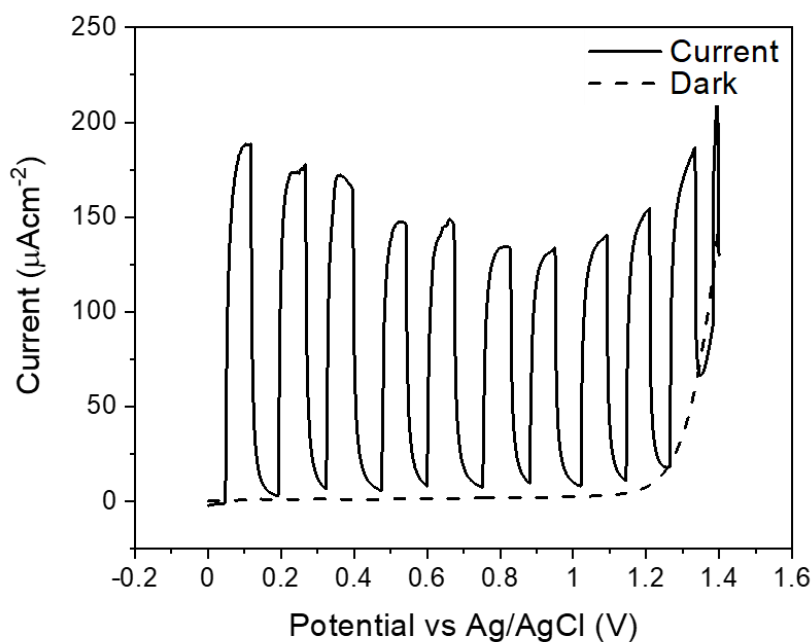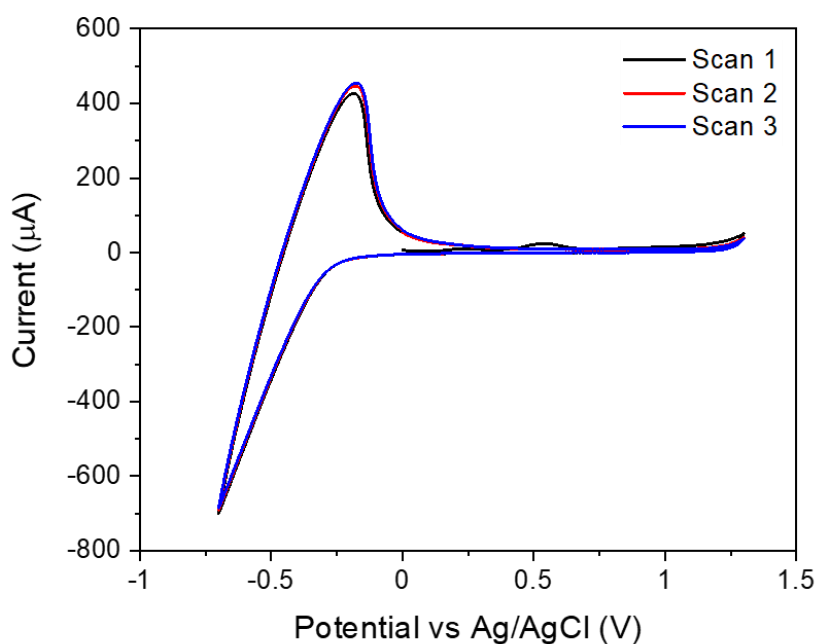
Figure 94- PBI-L CV and LSV. Electrochemistry performed in a custom 3 neck flat cell using a pH 6 MePi electrolyte (50 mM), with a Ag/AgCl reference electrode and platinum wire counter electrode. Xe lamp light source used with 100 mWcm^{-2} light intensity, without a KG1 filter and the position adjusted. 20 mVs^{-1}

Adding further layers to the PBI-L device did not increase the photocurrent further, so the number of layers was kept constant at two, but we endeavored to improve the device further

by adding a suitable water oxidation catalyst. Due to the higher pH stability of PBI-L we were hopeful of successfully incorporating CoO_x into the structure. Once again, we used a CoPi solution for photodeposition, but this time at pH 6 due to the added stability of PBI-L. Unfortunately, the resulting photocurrents post deposition were considerably lower than the device without Co present, and significantly decreased the stability of the film. This was the most striking evidence for the anti-catalytic effect of adding CoO_x to our PBI based devices, which despite the presence in the CV and in the dark current, did not improve the photoactivity of the device in any way (figure 95).
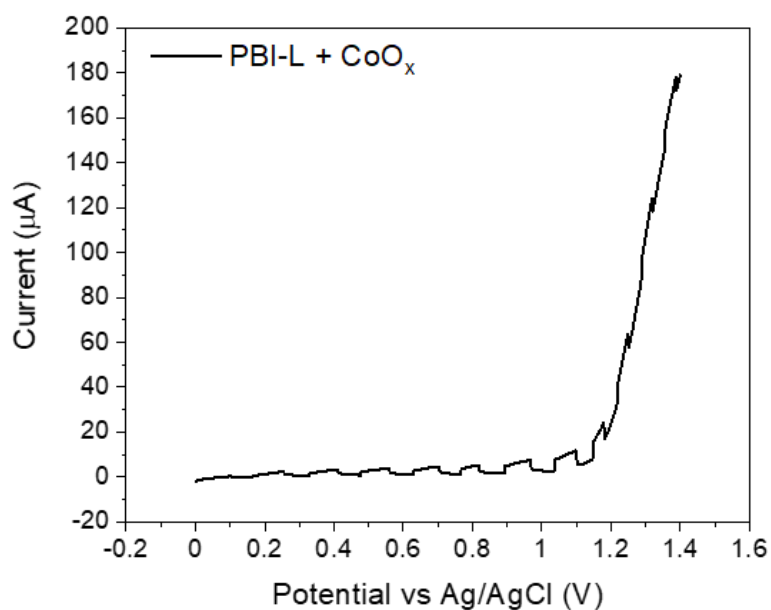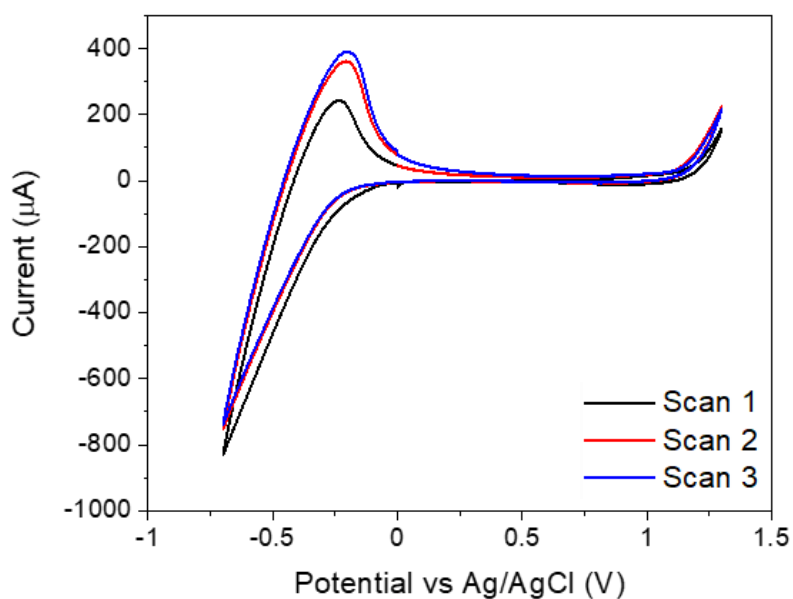
Figure 95- PBI-L with integrated CoO_x water oxidation catalyst CV and LSV. Electrochemistry performed in a custom 3 neck flat cell using a pH 6 MePi electrolyte (50 mM), with a Ag/AgCl reference electrode and platinum wire counter electrode. Xe lamp light source used with 100 mWcm^{-2} light intensity, without a KG1 filter and the position adjusted. Photodeposition used a pH 6 MePi electrolyte with Co(NO$_3$)$_2$ (50 mM) present, with a potential of 1.2 V applied for 15 mins.

Employing an IrOx catalyst with PBI-L

Having already attempted to use CoO_x as a water oxidation catalyst unsuccessfully, the final catalyst used with this device was IrO_x, as if the benchmark standard was unable to achieve a noticeable increase then it was unlikely we would find a compatible catalyst without a screening process. The catalyst was incorporated into the gelator solution as IrO_X nanoparticles synthesized by Khezar Saeed using a literature method,[221] due to the change in electrode gelation trigger for PBI-L. Resultant electrodes were then tested for oxygen evolution using the generator-collector method used for PBI-A. Due to the higher photocurrent displayed by PBI-L at the same applied bias (+ 0.2 V vs Ag/AgCl) measurements testing for the presence of oxygen were more reliable, despite still illuminating through the back face of the device (which acted as a UV filter). This made quantifying the area of the charge passed by the FTO collector electrode significantly more straightforward. Despite this the response shown by the FTO was still low at <1 μA (as shown by figure 96), but of a well-defined area. The collection efficiency for the PBI-L device was 15 ± 7 %, compared with 10 ± 3 % with the added IrO_x catalyst, signifying a marginally worse performance with the catalyst. As of a result the faradaic efficiency of the devices was 34 % for PBI-L only, and 23 % for the integrated catalyst (using a newly calculated CoPi experiment at pH 6).

These results are in line with those claimed by Finke *et al.* (31 % for PBI-AMP based device),[214] but somehow still seem unimpressive. A significant portion of this PhD was spent investigating PBI based photoanodes under the assumption that the maximum faradaic efficiency for these materials was around 80 %, due to the original publication by Finke *et al.*[212–214] However the results that we had observed throughout were not lagging behind the field, as previously thought. These results were based upon several repeats due to the complexity of performing these experiments, and appeared to confirm that the addition of the catalyst once again did not improve the performance of the device. The IrO_x nanoparticles were clearly present in the CV as referenced by the prominent oxidation at + 0.8 V vs Ag/AgCl, but due to the lack of improvement in oxygen yield the integration of the catalyst must be considered a failure and required investigation.
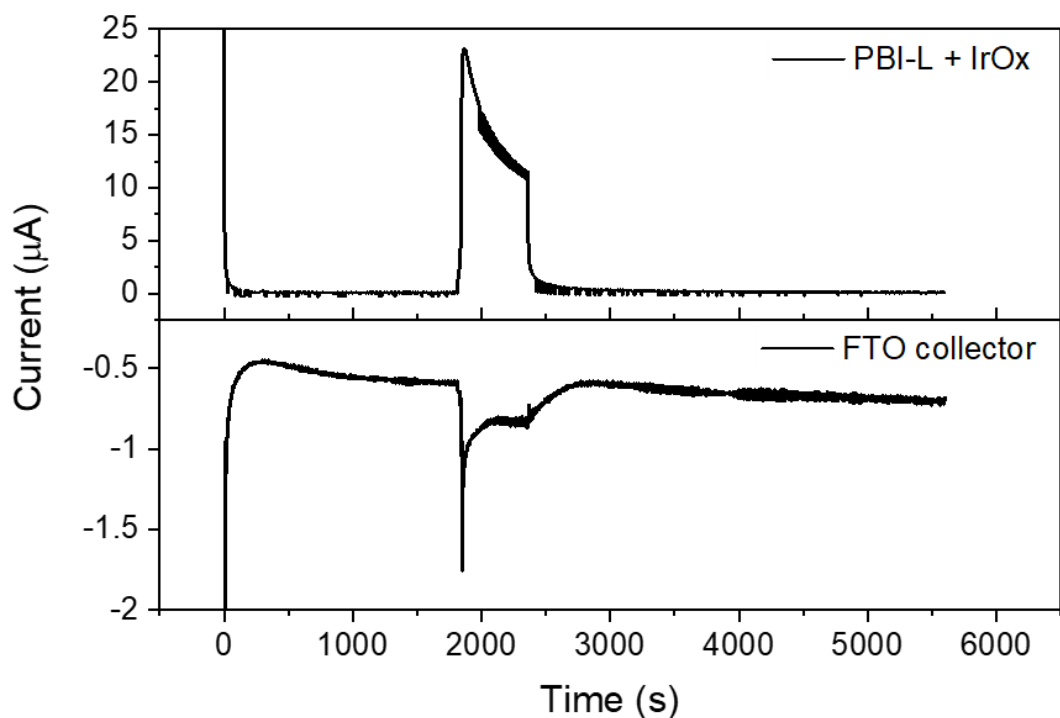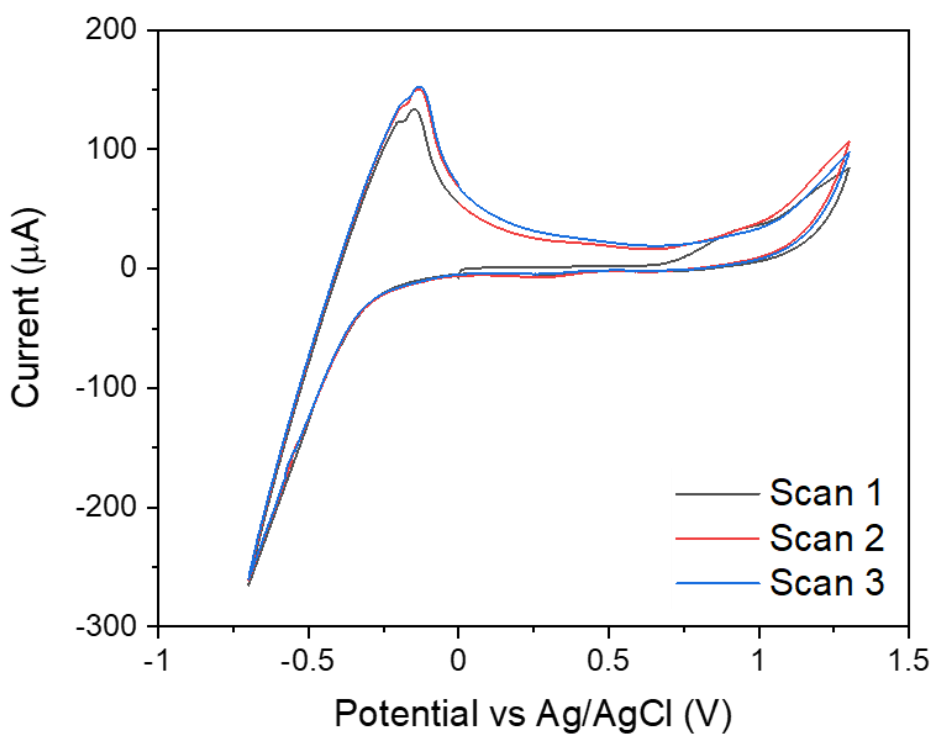
*Figure 96- PBI-L + IrOx CVs and generator collector data. Electrochemistry performed in a custom 3 neck flat cell using a pH 6 MePi electrolyte (50 mM), with a Ag/AgCl reference*

electrode and platinum wire counter electrode. Xe lamp light source used with 100 mWcm^{-2} light intensity, without a KG1 filter and the position adjusted. IrO$_x$ nanoparticles were mixed into the gelator solution, and then electrodes were prepared. Light on at 1700 seconds, and off at 2400 seconds.

Comparing between PBI-A and PBI-L with similar conditions and SEC

Increasing the photocurrents of the PBI based devices from 2 μA to around 100 μA (at + 0.2 V vs Ag/AgCl) was a notable feat. This was achieved by uncovering the UV activity of these devices, and also switching the amino acid functionality from A to L, but the oxygen measurements highlighted that the resultant device was inherently inefficient. Water oxidation as a process is highly energy intensive, as it requires two molecules of water and four photogenerated holes to produce a single molecule of oxygen. The hypothesis behind this device relies upon the ability of self-assembled fibres to be able to transfer charges to the sites that perform catalysis, when most devices use electron transport layers, and hole transfer layers to perform the task. Due to the high rates of recombination and self-oxidation, evidenced by the low oxygen evolution this hypothesis may be profoundly incorrect and require rethinking. Nevertheless, there was distinct improvement in stability and photocurrent demonstrated by PBI-L which was investigated further.
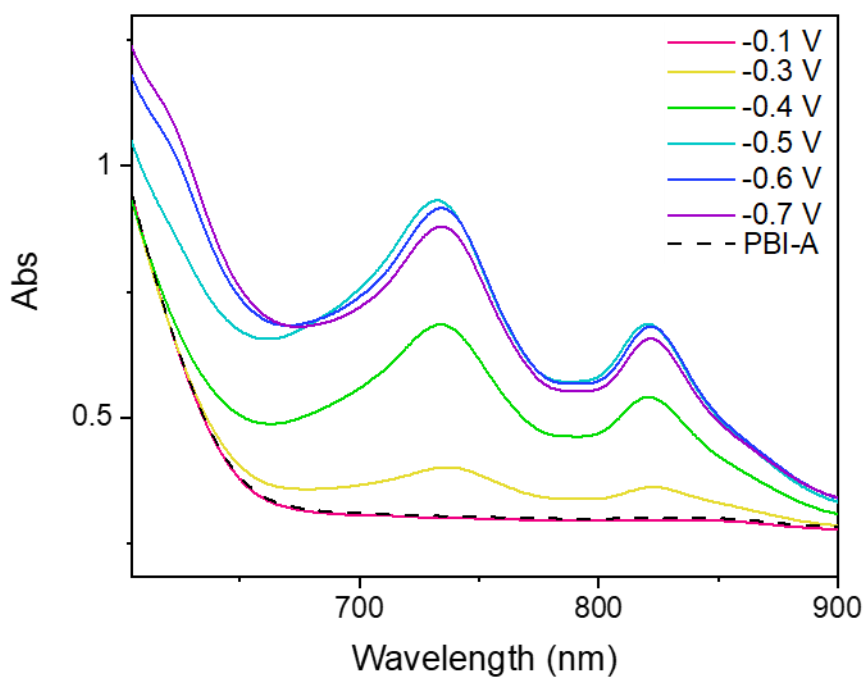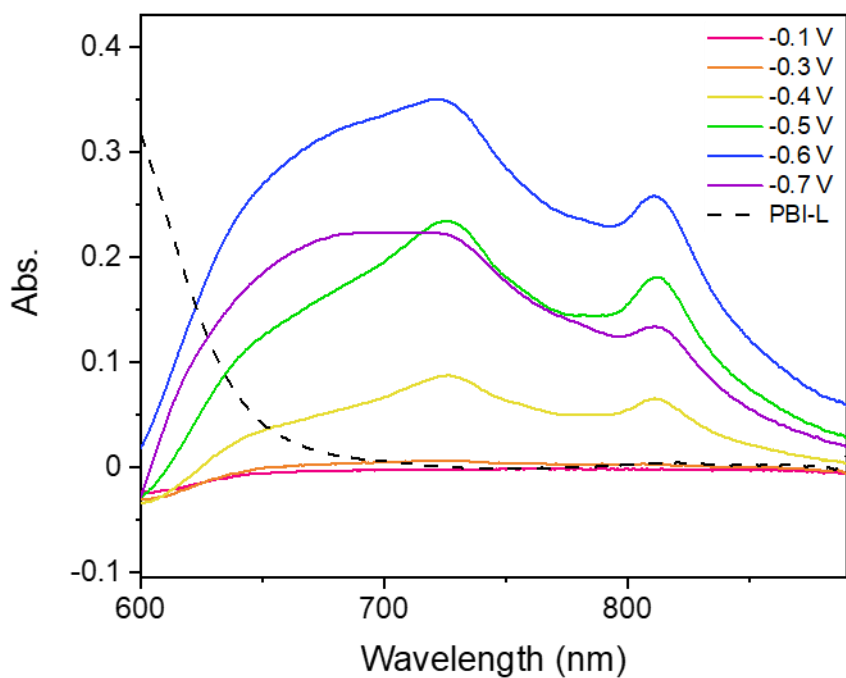
Figure 97- Spectroelectrochemistry of PBI-L and PBI-A electrodes. For PBI-L; Electrochemistry performed in a custom 3 neck cuvette cell using a pH 6 MePi electrolyte (50 mM), with a Ag/AgCl reference electrode and platinum wire counter electrode. For PBI-A; Electrochemistry performed in a custom cuvette cell using a pH 4 KCl electrolyte (0.1 M), with a Ag/AgCl

reference electrode and platinum wire counter electrode. Electrode was placed into beam of UV-Vis spectrophotometer, and spectra were recorded with applied potential.

Spectroelectrochemical studies were performed on both PBI-A and PBI-L to investigate the nature of the reductive species that occurred upon illumination. Both spectra demonstrate the formation of the PBI radical anion. For PBI-L the first prominent peaks were at -0.4 V (vs Ag/AgCl), and for PBI-A the characteristic peaks at 730 and 820 nm first occurred at -0.3 V. For a direct comparison both sets of electrochemistry occurred in pH 4 electrolyte, and appeared to indicate that PBI-A was easier to reduce at this pH. This was an intriguing outcome due to the lower photocurrent observed by PBI-A at common conditions (shown by figure 97) but reinforced the evidence that PBI-L was a superior photoanode for this setup regardless of pH. Comparing the CVs for each PBI also confirmed that the PBI-L photoelectrode was more difficult to reduce at pH 4, complementing the SEC data. The photocurrent observed for PBI-L at pH 4 was also lower than observed at pH 6, which stressed the importance of electrochemical driving force for the PBI reduction but does not consider the structural implications of the pH changes. Notably for PBI-L the initial photocurrent at low applied potential was not the highest photocurrent achieved, in stark contrast with pH 6. Instead, the photocurrent increased with applied bias, but was considerably more 'spike like' than that of PBI-A (figure 98). These devices were intended to be used for their water oxidative abilities at positive potentials, rather than negative potentials showing the reductions. The lack of availability of the equipment to perform the experiments at oxidative conditions severely hindered our understanding of their behaviour. Instead we were able to compare the ability of PBI species to be reduced and therefore pass charges through PBI structures, rather than actually oxidizing water at positive potentials. The oxidation data for PBI-A is available (as shown by figure 100).
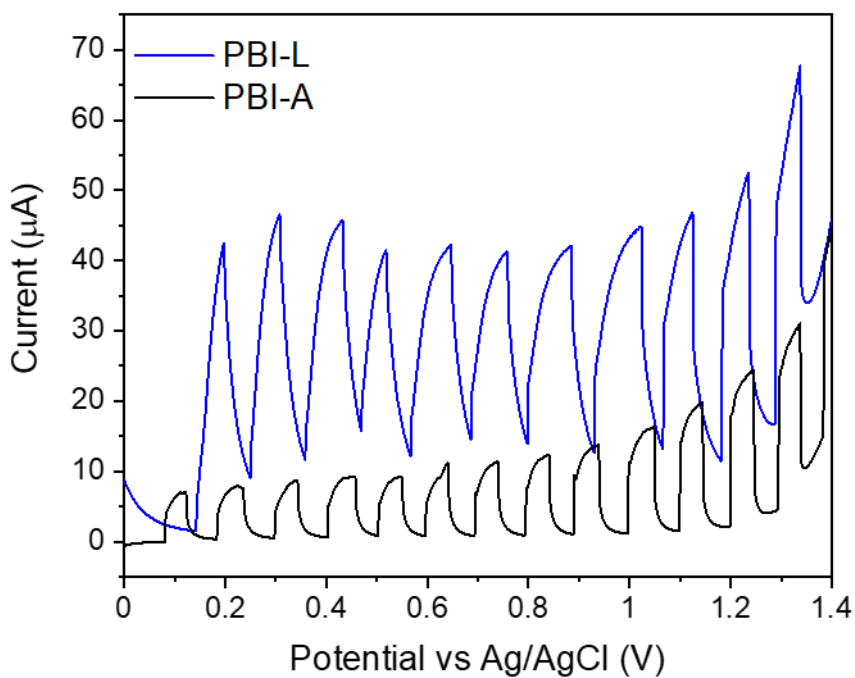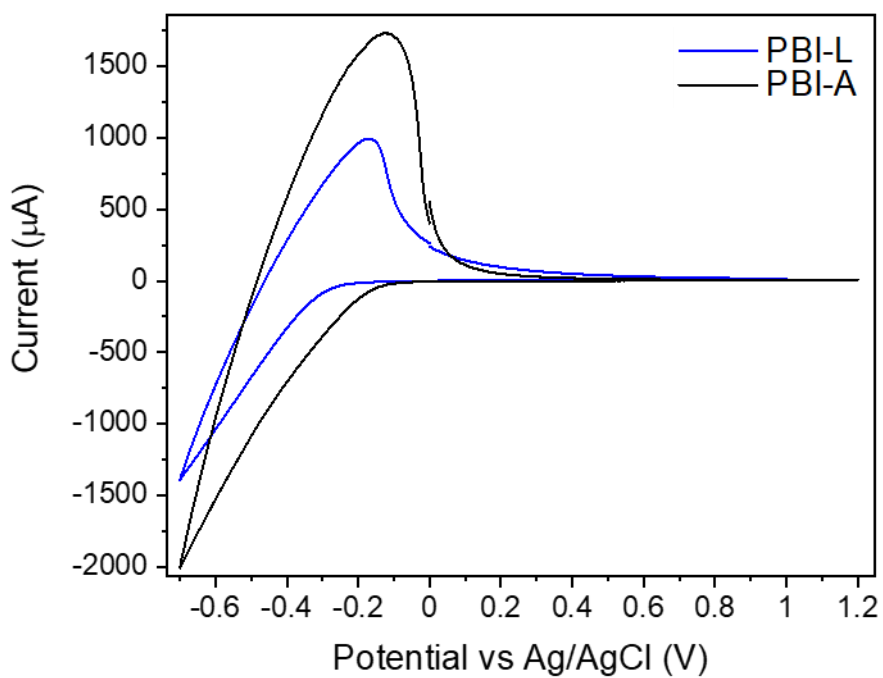
Figure 98-CV and LSV of PBI-L and PBI-A electrodes at common conditions using a pH 4 KCl electrolyte. Electrochemistry performed in a custom 3 neck cuvette cell using a pH 6 MePi electrolyte (50 mM), with a Ag/AgCl reference electrode and platinum wire counter electrode. Xe lamp light source used with 100 mWcm^{-2} light intensity, without a KG1 filter and the position adjusted.

Figure 99 displays PBI-L electrode CVs at 3 different pHs, and was therefore plotted against RHE to remove the impact of pH changes. The peak shift between pHs does not appear to be consistent with additional processes occurring, but does demonstrate the slow rate of electron transfer at all pHs, with higher applied bias required to reach a steady state as the pH is lowered. Water oxidation is a pH sensitive process, with a higher driving force at higher pH than at lower pH. In retrospect, simply assuming that a higher photocurrent at a higher pH correlated with water oxidation ability was not correct, and further testing should have been done using different scan rates and oxygen evolution at different pHs. At this point it was difficult to determine why PBI-L was able to record a better photocurrent than PBI-A, and whether that indeed facilitated a superior water oxidation current.
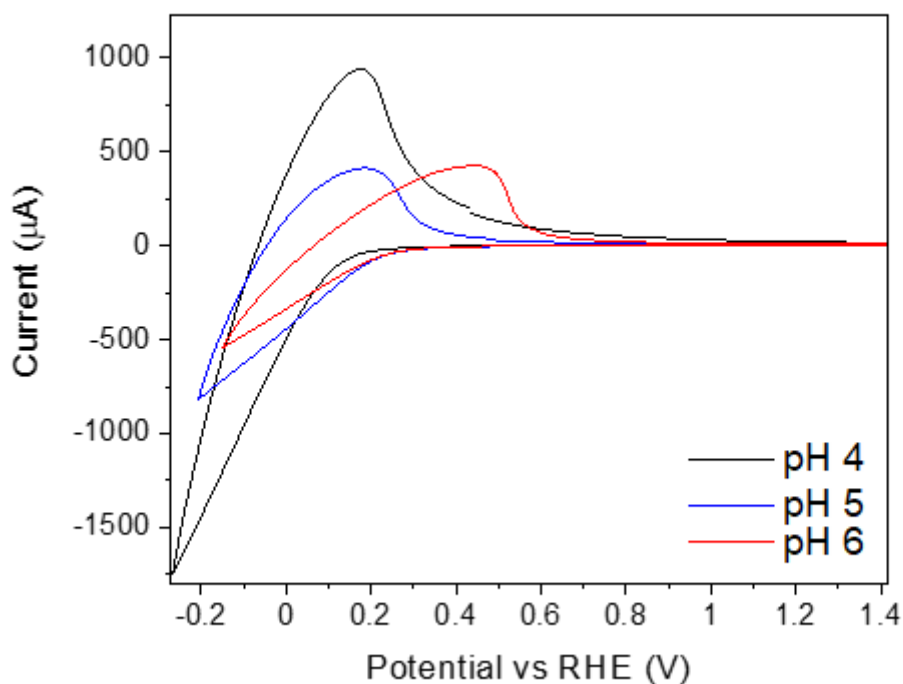
Figure 99- PBI-L CVs at different electrolyte pHs. Electrochemistry performed in a custom 3 neck cuvette cell using a MePi electrolyte (50 mM), with a Ag/AgCl reference electrode and platinum wire counter electrode. Electrolyte was adjusted using 0.1 M HCl.

We were previously able to examine PBI-A photoelectrodes oxidative processes using SEC, by depositing a film onto a SrF_2 window coated with a thin layer of ITO (conventional glassware strongly absorbs in the UV region making it unsuitable). This allowed for examination of the UV region, and allowed us to observe alanine oxidation which had been predicted by

modeling in previous research papers, with the electron residing on the perylene core and the hole oxidizing the amino acid.[85,183] A change in absorbance below 300 nm with applied positive potential was attributed to oxidation of the alanine appendage, due to its UV-Vis spectrum of that region (figure 100).[222] Around +0.8 V was required to perform this oxidation, which had long been speculated in previous literature from our group.[85,143] This oxidation is as a result of hole localization onto the amino acid unit, with the electron residing on the PBI core spatially. For photocatalysis this allowed for electron transfer between PBI units to an eventual catalyst site. For a photoelectrode to oxidise water the hole site must have sufficient driving force to perform this oxidation. The suggested alanine oxidation at around +0.8V substantially reduced the driving force for this oxidation, and therefore the efficiency of the subsequent device. Unfortunately, the specialised optical window used for these experiments was unavailable for PBI-L devices to examine the optical effects on the electrode film. The lack of this experimental data made it more difficult to establish the effect of amino acid functionality on the self-oxidation ability of the device.
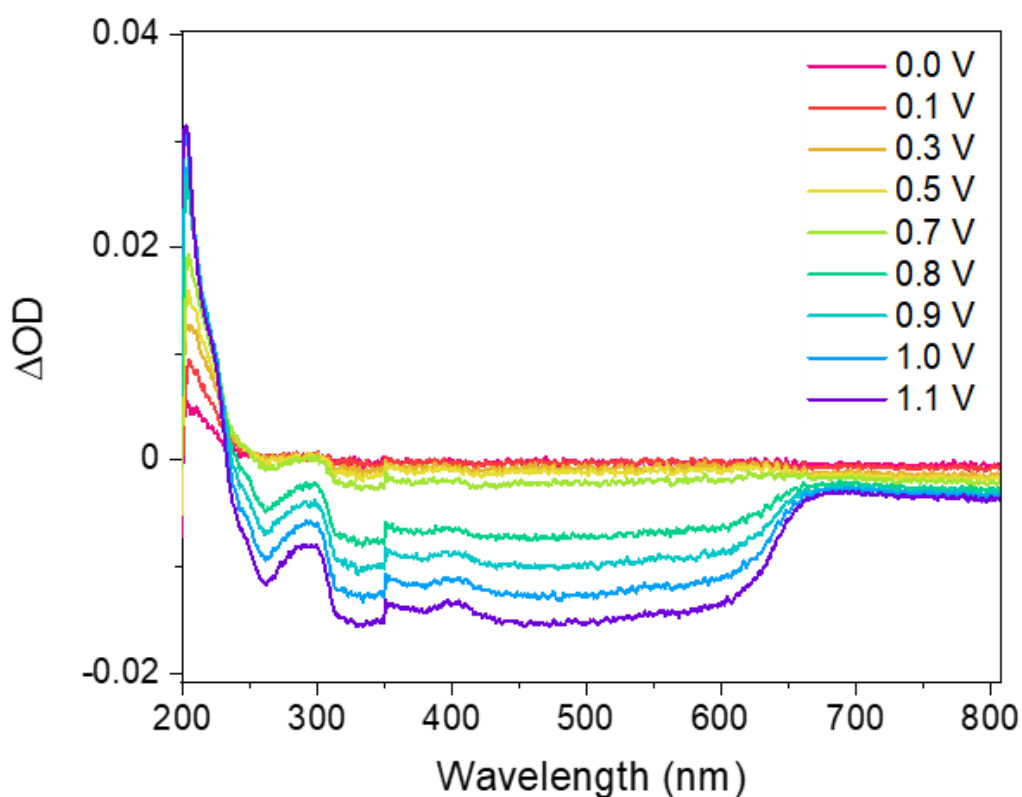
Incident photon current efficiency (IPCE) of PBI electrodes

Photocurrent measurements of a number of single wavelengths were used to calculate the IPCE (%) for several wavelengths across the visible and UV range. The trends shared between the two PBIs were very similar, and peaked in the UV region at around 2 %; which once again highlighted the striking UV activity for these materials. The photocurrents achieved at visible wavelengths were markedly lower, and thereby resulted in lower efficiencies despite lower incident light intensity. Once again it was difficult to definitively separate both of these similar PBIs, which seemed to share a number of similar properties despite large differences in photoactivity and pH stability (figure 101).
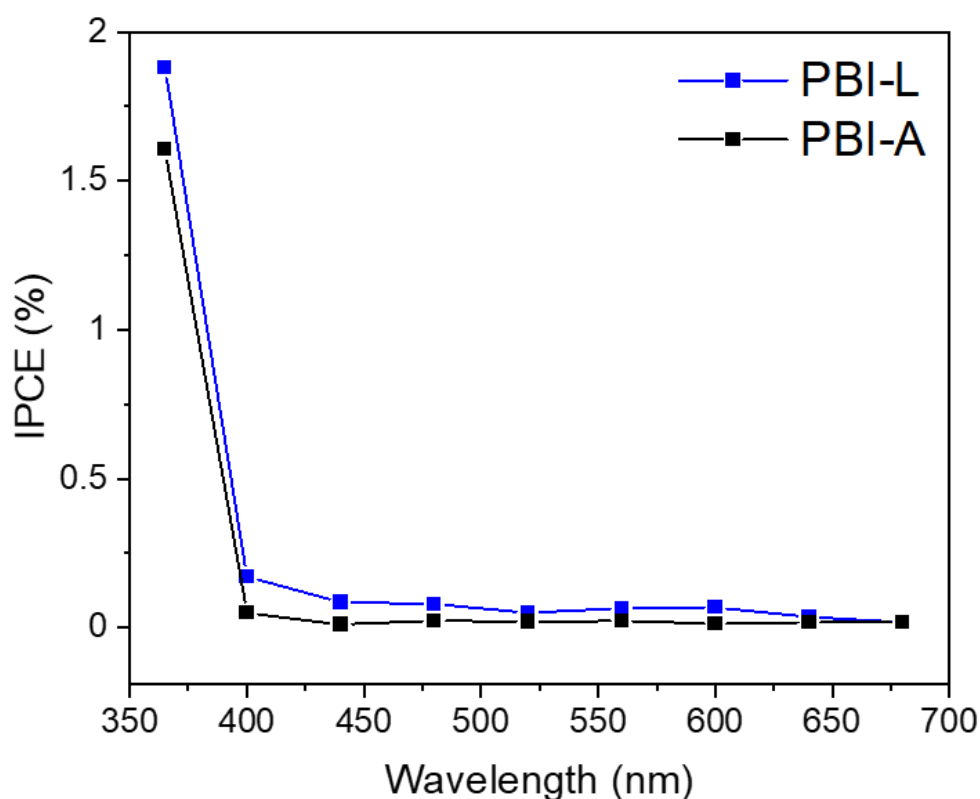
Figure 101- IPCE of PBI-L and PBI-A electrodes. Electrochemistry performed in a custom three necked cell using a pH 4 KCl electrolyte (50 mM), with a Ag/AgCl reference electrode and

platinum wire counter electrode. The light source was a Xe lamp with a monochromator for single wavelength illumination.

Final chapter thoughts

The initial scope of this chapter was vast and included successful integration of water oxidation catalyst alongside a high throughput screening of PBI photoelectrodes. Due to several factors beyond the scope of this project, this was not achieved. The initial PBI-A electrode preparation method and photocurrent results were significantly improved by switching to a PBI-L based electrode, using a salt trigger in place of a pH switch. In addition to this the new photoelectrode has been able to withstand electrolytes up to pH 6, with excellent reproducibility. However, this project in particular has been plagued with issues from the beginning, largely due to false literature precedent.[212] Having evaluated literature claims in great detail, several of them simply did not add up and held up the project due to supposed poor performance relative to the field. In reality the faradaic efficiencies for oxygen in thin film PBI based devices is low at around 30 %. But unfortunately, it has been difficult to determine how to improve this device through PBI functionality and self-assembly alone. To improve the device's outlook several new layers must be added to aid charge separation and transport, to improve efficiency. PBI based devices are excellent light absorbers, but ultimately require UV light to generate sufficient quantities of the radical anionic species to facilitate reductive reactions. The amino acid functionality allows these large aromatic hydrophobic cores to dissolve in water, but inhibits water oxidation due to their similarly lying energy levels.

There are subtle differences in the R group between A and L, which inherently have both electronic and structural effects on the PBI core, and subsequent stacking. As photocatalysts they behave similarly, and as photoelectrodes they are both capable of generating radical anionic species necessary to the formation of holes within the PBI structure. But the availability of the holes was severely hindered by the oxidation potential of the amino acid functionality, and apparent lack of integration with subsequent water oxidation catalyst. While PBI-L appeared to have a higher photocurrent than those achieved by PBI-A, it was difficult to determine why. As is often the way with PBI based devices, structure appeared to dominate the behavior of these materials in a way that required a far more comprehensive approach to uncover.

Conclusions

This thesis has explored PBIs as a class of organic materials suitable for building devices for solar fuel generation. While PBIs have proven to be a somewhat unpredictable and challenging material, there can be no denying the potential applications within the field, due the reducing power of the PBI radical anionic species, and the incredible ability to self-assemble into complex structures.

In chapter 2 PBIs proved to be successful hydrogen evolving photocatalysts, in a study partnered by the University of Glasgow. This study encompassed a vast quantity of work from both Daniel McDowall and myself, who together were able to relate the process of self-assembly to the ability of a particular amino acid based PBI to generate hydrogen. The hydrogen evolution rates for our photocatalysts were by no means vast, but instead revealed an even more pleasing insight about how structure truly governed activity, with the requirement of type 2 aggregates for any notable evolution of hydrogen. This was demonstrated by our UV-Vis study which was able to detect these subtle changes in local electronic structure in a qualitative methodology, which was then applied to more PBIs than the original publication and held up. The lack of success in the PBI noodle section was perhaps the most disappointing result of the PhD. This was largely due to time constraints, and the apparent lack of reproducibility of forming aligned PBI noodles. Within the field there are certainly a large number of functional shapes and moieties used, but the PBI noodles truly could have been a novel endeavour. With more time available this study would have been significantly expanded to even more PBIs, and far more control over the conditions of forming aligned noodles. A high throughput approach would likely have been required to perform experiments of this scope, but the difficulty in noodle preparation made this impractical to continue further. A spectroscopic approach had been suggested in order to quantify alignment, in addition to additional x-ray scattering to investigate the noodles further.

Chapter 3 was a direct follow-up of the photocatalytic study of amino acid functionalised PBIs, which once again reinforced the strong conclusions seen in chapter 2. The ability to track the excited PBI species that were generated upon excitation did not lead to a direct identification of a species responsible for catalysis. Instead TAS was able show the importance of type 2 aggregates to form long lasting charges necessary for successful catalysis. In fact, the excited

species generated lived so long it complicated the experiment considerably, as it appeared to be excited once again by incident light of the same wavelength. The PBI photocatalytic field has exploded In recent years, with more attention being given to how local packing can govern the behaviour of the whole system, and this study sits very well with the interest in this area. Once again given more time this section would be comprised of all of the PBIs studied in chapter 2 with a variety of conditions, and spectroscopic windows investigated to explore whether the trends seen in PBI-A and PBI-Y were mirrored further.

Chapter 4 was the most frustrating section of the PhD, as it represented the largest amount of time spent with the smallest gain in terms of understanding. We were able to improve our PBI based photoelectrode system, in terms of pH stability and photocurrent, but were unable to conclusively state why it had occurred. PBI photoelectrodes are intrinsically subtle in their behaviour, where the smallest difference in conditions can have a profound effect on the resulting device. It was also the project which suffered the most as a result of COVID restrictions, as they led to delays in proposed studies on more PBI photoelectrodes. In summary PBI photoelectrodes are an exciting class of materials which require far more development to improve their oxygen evolving ability than was possible within this thesis. Looking back, several avenues would have been investigated further, such as a spectroscopic study on thinner electrodes (due to high absorption). In actual fact it may have been prudent to make the electrodes thinner throughout to study their behaviour more easily with spectroscopic instrumentation, but as ever this is as a consequence of the highly concentrated PBI gelator solution which gives rise to self-assembly, and may have differed greatly at different concentrations.

Experimental methods

Materials

Milli-Q water (18.2 MΩ) was used throughout (Millipore Corp). All chemicals were obtained from Sigma-Aldrich and used as received. All PBI amino acid based gelators were synthesised using previously documented literature procedures at the University of Glasgow.[143,223] PBI-AMP was based on synthesis by Finke et al.[212] Argon and nitrogen were purchased from BOC at pure shield grade.

Chapter 2 (photocatalysis)Click or tap here to enter text.

PBI solution and photocatalytic sample preparation

PBI-X solutions were prepared to a final concentration of 5 mg/mL for uniform photocatalytic testing per unit weight. Solutions were dissolved in water containing two molar equivalents of the chosen base NaOH.

Samples were prepared with PBI in combination with the hole scavenger methanol, and platinum nanoparticles (1 mol. %). Due to different amino acid functionalities different volumes of platinum were required between different samples to maintain a constant molar %. Once combined the samples were adjusted with either 2M HCl or 2M NaOH, while stirred. The pH was measured by Hanna HI 8424 microcomputer pH meter with an FC200 probe.

Photocatalysis hydrogen evolution experimentation

10 mL Agilent GC vials were used to contain the solution, with a 5 mL headspace. A ChemSpeed Technologies SWING system was used to cap and purge the vials with N_2 over three hours. After purging the samples were placed onto a roller bed under a solar simulator lamp (Newport Oriel Sol3A class AAA with a 12 x 12 inch output beam) for a further three hours (100 mWcm^{-2}). A Shimadzu Trace 2010 with a barrier ionisation discharge detector was used to detect headspace gases such as hydrogen. Sampling of vials was aided by an HS-20 autosampler. Due to long sample waiting times, it is possible that there was some gas leakage from samples.

UV-Vis spectroscopy

All UV-Vis measurements were performed using a Shimadzu UV-2600 spectrophotometer. Due to high absorbance of samples, two microscope slides were used to create a thin path length for light penetration of the sample. Slides were sealed with Parafilm to prevent any leaking.

Fitting UV-Vis data

Each aggregate type is used as a linear combination of spectra, as detailed in previous publications.[49,150] Using PBI-A we determined that three pH ranges (10-6, 5-3, <3) corresponded to each type of structure. In this study we focus mainly on type 1 and type 2 structure, due to the low contributions of type 3 structure at the higher pHs.

$$A_{pH}(\lambda) = \sum C_x A_x(\lambda)$$

C_x is the coefficient of each aggregate contribution towards the structure at a given pH.

Electrochemistry

Measurements were performed in a 40 mL vial in order to not stain traditional electrochemical cells. An Emstat potentiostat was used with a three electrode setup to perform CVs and LSVs. PBI gelator solutions were placed into the vial having been adjusted to the correct pH. A supporting electrolyte of 0.1 M NaCl was used. The working electrode was a glassy carbon disk electrode, with a platinum wire counter, and a Ag/AgCl reference electrode equipped with a double junction to prevent contamination. The vial was sealed with a septum and purged for 30 minutes with N_2.

CVs began at +0.3 V and scanned to -1 V with a scan rate of 100 mVs^{-1}, and an equilibration time of 30 seconds. SWVs measurements required a lot of optimisations with regards to the frequency and amplitude. 1s Equilibration time, 0.01 amplitude, and 1 Hz frequency were used for final measurements.

SAXS

PBI sample preparation was as described previously, and measurements were performed by Daniel McDowall. Samples were run at the Diamond light source. Additional information and further characterisation are available in the publication, or in the appendices.[49]

Action spectrum

A sample of PBI-A at pH 5 was illuminated by a 300 W Xe lamp (100 mWcm^{-2}) after being purged for 30 minutes under N_2. The sample contained both MeOH and Pt nanoparticles in order to effectively simulate photocatalytic conditions. A gas headspace injection (500 μL) was performed to establish effective catalysis, which was confirmed by GC analysis. The solution was repurged to remove remaining hydrogen. A monochromated light source was then used to illuminate the sample with a single wavelength of light. The sample was illuminated for 1 hour per wavelength, which was then followed by sampling the headspace.

A quartz cuvette cell equipped with headspace was used to allow for UV light from the Xe lamp light source. Low light intensities were used for monochromator. Sample was stirred throughout.

PBI-I noodles

Solution preparation

10 mg/mL solutions of PBI-I were prepared (2 mL) using two equivalents of NaOH to dissolve the PBI solid, with the remainder being topped up with distilled water. In order to form noodles the solution pH was lowered using HCl (2M), with stirring throughout. Noodles were able to form around pH 6.5, but required a lower pH (between 6-6.30) to form aligned noodles. Throughout testing a uniform pH for alignment could not be established.

Testing aligned noodles

A microscope setup was established in partnership with Daniel McDowall in order to record the noodles as they were forming. The noodles were pipetted into a vial (10 μL) containing $CaCl_2$ (50 mM) dissolved in water to trigger gelation. A smartphone camera was used to record and image noodles. A white light source was placed behind a sheet of paper to disperse the light, with two polarisers perpendicular to one another. Birefringent noodles rotated the

plane of incident light, and appeared bright in the images, with unaligned samples appearing dark. A fixed brightness was used on all images using software MAVIS from the app store.

Forming unaligned noodles

Unaligned noodles were formed using the same PBI-I solution as aligned noodles (10 mg/mL). The noodles were pipetted into distilled water which did not contain any salt to trigger gelation. The noodles appeared to lose any alignment over a period of 1 minute, at that point a concentrated solution of $CaCl_2$ was added to trigger gelation, and maintain noodle shape.

Hydrogen evolution

For hydrogen testing platinum nanoparticles (1 mol.%) were added to the PBI-I gelator solution (10 mg/mL). Noodles (28 x 10 μL) were pipetted into a prepurged quartz cuvette (with N_2 for 30 mins) with headspace, prepurged methanol was also added at this point to act as hole scavenger. The sample was then illuminated by a 300 W Xe lamp, with no filters for 3 hours (100 mWcm^{-2}). Gas headspace analysis was performed every hour in order to check for any hydrogen evolution (250 μl). Due to latent hydrogen remaining on the GC column from previous injections there appeared to be a detectable amount of hydrogen in every injection. This did not appear to be as a result of PBI noodles, which were unable to decisively evolve hydrogen above a baseline.

UV-Vis spectroscopy of PBI noodles

All UV-Vis measurements were performed using a Shimadzu UV-2600 spectrophotometer. Microscope slides were used to sandwich noodle samples, measurements were performed in absorbance mode.

Chapter 3 (TAS)

Transient absorption (TAS) and fluorescence spectroscopy are often employed to track the species that form as a result of photoexcitation, and also provide an insight into the mechanism that occurs. TAS is an example of pump-probe spectroscopy, which examines how excited species behave on typically very fast time scales (femtosecond). Following an excitation with the pump pulse beam (which is typically in the range of 300-900 nm), the formation and decay of such species is tracked in terms of the change in absorbance (ΔmOD) of the sample over the time period of the experiment (shown by equation 1). The change in absorbance is probed by a second light pulse, which typically encompasses a range of wavelengths of light in the visible range, to essentially provide the user with a UV-Vis spectrum over a defined time period. Conversely, traditional UV-Vis spectra record simply the ground state absorbance of the sample, whereas TAS can observe the difference between the ground state and the excited states as a result of the pump beam. This can provide an insight into the lifetimes of charge carriers that form as a result of the initial pump pulse, which is of particular importance for possible photocatalytic applications.

$$\Delta A = \log(I_t/I^*)$$

Equation 1- The equation is used to calculate the change in absorbance ΔA, using the initial transmitted light intensity I^* and the light intensity at time t I_t.

Understanding what is happening in your sample from TA spectra can be huge challenge due to the layered contributions of many simultaneous processes. These include a ground state bleach (GSB) which describes a decrease in ground state population which can be promoted to the excited state by the pump pulse, and results in a negative signal in the spectrum where the ground state absorption would normally be present. Stimulated emission (SE) is a process where photoabsorption leads to emissive decay of the excited state, which can yield both positive and negative features in the spectrum. The positive signal in the TA spectrum is often assigned to an excited state absorption, which is when the incident wavelength causes an excitation in your sample and therefore a change in the spectrum as a result of the new species present. When trying to deconvolute your spectrum you must consider these three processes, but there are also thermal effects to consider,[224] particularly with highly absorbing samples which do not allow the incident light to penetrate the sample in its entirety.

How to best record a TA spectrum

The initial spectrometer settings were based upon previous research,[85,183] and used a 200 μW pump pulse of 490 nm light to excite the sample before the arrival of the probe pulse. This meant that the pump and probe beams had to overlap spatially and temporally, to ensure that the sample was being illuminated on the same spot, and for correct determination of time zero; which establishes the start of the experiment. Due to our prior expectation of the generation of the PBI radical anion our experimental window was between 600-900 nm, with a view to potentially expanding into the near infra-red (NIR), and also exploring UV excitation. Finding a good TA signal for these samples was very simple due to the high absorbance values, but in retrospect the data only represented probing the front of the sample.

TA procedure

Measured using a printed cell from Protolabs to use a thin pathlength. A small volume of PBI solution (either 5 or 7uL depending on pH) was placed in between 2 CaF_2 windows with a suitable spacer and tightly assembled. A UV-Vis spectrum was recorded before every measurement using a Shimadzu UV-2600 spectrophotometer.

TA instrumentation

Using setup previously described in literature.[225] Ultra-fast measurements carried out using a Harpia TA spectrometer from Light conversion. The chosen pump wavelengths used were 490 nm and 365 nm which were generated by a Pharos-SP-10W (light conversion, FWHM ~ 140 fs, 10 kHz, 1030 nm), combined with an Orpheus with a 2nd harmonic generation stage. The probe light is generated using Pharos laser focused onto a sapphire crystal within the spectrometer. Carpetview is used for data analysis and fittings.

Chapter 4 (photoelectrode)

Preparation of PBI electrodes

All PBI electrodes were prepared on FTO (TEC-15). PBI solution concentrations were 7.5 mg/mL for all samples and contained 1 equivalent of NaOH, unless stated otherwise. PBI-A electrodes were prepared in petri dishes with dampened blue paper roll placed inside them with 20 μL of PBI solution on the FTO electrode. Concentrated HCl was then dropped onto the blue roll to create an acidic vapour and trigger gelation. After 15 minutes the electrodes were removed from the petri dishes and allowed to dry overnight. When tested after drying the electrodes were treated as xerogels.

PBI-L electrodes used 5 μl of a gelator solution placed onto an FTO slide (area of electrodes was 0.6 x 0.8 cm), which was then dipped into a $Ca(NO_3)_2$ (50 mM) dipping solution. This process was then repeated once more to create a double layer of PBI. These electrodes were also allowed to dry overnight.

PBI-AMP solutions were prepared using 5 mg in 1 mL of water and 2 drops of KOH as described by Finke *et al.*[212] Electrodes were prepared via spin coating, in addition to the method used for PBI-A.

Spin coated PBI electrodes

FTO was cleaned using plasma cleaner for 15 minutes, and then directly spin coated at 200 rpm for 60 seconds. Electrodes were then dipped in a 2M HCl/ ethanol mix for 30 seconds to allow for an outer layer of gelation and allowed to dry before use.

Photoelectrochemical measurements

Measurements took place in a custom 3 necked cell, or inside a quartz cuvette with a headspace. The working electrode was the PBI electrode, which was connected with a crocodile clip, or a nickel wire using silver paste. The reference electrode was Ag/AgCl (3.5 M), with a platinum wire counter electrode. All measurements used a Palmsens 3 potentiostat, or an Emsat potentiostat. Cyclic voltammograms were performed in pH 4 KCl (0.1 M) for PBI-A, pH 7 phosphate buffer (0.1 M) for PBI-AMP, and pH 6 MePi (50 mM) between +1.2 to -0.7 V for 3 scans for PBI-L. Linear sweep measurements were recorded between 0 to +1.4 V for all measurements, with 5 second light on/light off measurements. Xe

lamp used had an intensity of ~100 mW/cm^2 with either a KG1 filter, or no filters used, depending on the specified experiment.

Oxygen measurements required the use of the generator-collector method,[40] and thereby needed 2 reference electrodes and counter electrodes. Calibration experiments used a CoOx WOC electrodeposited on FTO for 25 minutes at +1.2 V. Oxygen evolution potential chosen was +1.6 V (held at +0.6 V to initially stabilise current), with -0.6 V applied to the FTO working electrode to selectively reduce oxygen and allow for a direct charge comparison. No lamps were required for the electrocatalytic experiment.

For PBI oxygen experiments the applied potentials of +0.2 V on PBI, and -0.6 V were applied throughout the experiment. After x minutes to let the current settle, the PBI sample was then illuminated with a light source (either a Xe lamp or LED) for 10 minutes, the light source was then turned off while still monitoring the current. This allowed for any latent oxygen to diffuse and be collected.

CoO$_x$ photodeposition

Various experimental conditions were attempted in order to successfully deposit CoO$_x$ as a functional water oxidation catalyst. Preparation of CoPi initially used Co(NO)$_3$ solution, before dilution in a pH 7 phosphate buffer (0.5 mM Co^{2+}). Photoelectrochemical deposition was then attempted using a 300 W Xe lamp light source, with the CoPi acting as the electrolyte. The PBI electrode sample was illuminated for 15 minutes at an applied potential of +0.7 V (vs Ag/AgCl). LSVs were then performed with chopped light on measurements every 5 seconds.

Different pH solutions were used for various deposition attempts. For PBI-A, pH 4 was used, for PBI-AMP pH 7, and for PBI-L pH 6.

IrO$_x$ integration into PBI electrodes

K$_2$IrCl$_6$ was mixed into the gelator solution for PBI-A, before electrode preparation had begun. The acid vapour method was then used to integrate the catalyst into the structure.

Pre-made IrO$_x$ nanoparticles were prepared by Khezar Saeed and mixed into the PBI gelator solution before electrode preparation. This solution was then used to form electrodes using acid vapour, and salt addition gelation methods as previously described.

UV-Vis Spectroscopy

All UV-Vis measurements were performed using a Shimadzu UV-2600 spectrophotometer. Electrode samples were placed inside the spectrophotometer without using a cuvette with blue tack.

Annealing PBI electrode gelator solutions

Premade PBI-L solution was heated to 80°C for 30 minutes and then allowed to cool overnight. Electrodes were formed using the Ca gelation method.

Spectroelectrochemistry

PBI-A samples were prepared using the acid vapour method and required a pH 4 KCl electrolyte. PBI-L samples used the double dip salt gelation method, with pH 6 MePi electrolyte (50 mM).

Performed inside UV-Vis spectrophotometer using a quartz cuvette, a platinum wire counter electrode, and an Ag/AgCl reference electrode. Initial PBI-L film shown at +0.2 V (vs Ag/AgCl) and used as background for future measurements. Potential was then stepped down by -0.1 V per run and a spectrum was recorded.

IPCE (Incident photon to current efficiency)

Measurements were carried out using a 100 W Xe lamp equipped with a monochromator, in order to select a certain wavelength. A custom three necked flat cell was used to house the electrochemical cell, containing the PBI working electrode, platinum wire counter, and Ag/AgCl reference electrode. The area of the electrode was calculated relative to the size of the beam to account for total power across electrode. Photocurrents were measured using a Palmsens3 potentiostat.

Appendices

Chapter 2 photocatalysis

A vast quantity of SAXS analysis was performed by Daniel McDowall in order to understand the behaviour of PBI based photocatalysts across the pH range. The supplemental tables and fits are available from the publication,[49] with tables for PBI samples displayed here.

Model	pH	Length / nm	Kuhn length / nm	Cylinder radius / nm	Sphere radius / nm	Reduced Chi squared
Flexible cylinder with polydispersity of radius 0.25	3	152 ± 0.60	15.2 ± 0.00	4.0 ± 0.00	-	4.06
Flexible cylinder with polydispersity of radius 0.25	3.5	157 ± 0.70	15.7 ± 0.00	4.1 ± 0.00	-	1.96
Flexible cylinder with polydispersity of radius 0.25	4	179 ± 0.42	12.7 ± 0.05	3.9 ± 0.00	-	4.30
Flexible cylinder with polydispersity of radius 0.25	4.5	181 ± 0.41	13.5 ± 0.05	4.1 ± 0.00	-	4.64
Flexible cylinder with polydispersity of radius 0.25	5	175 ± 0.39	13.0 ± 0.05	4.1 ± 0.00	-	4.56
Flexible cylinder with polydispersity of radius 0.25	6	130 ± 0.41	22.6 ± 0.07	4.2 ± 0.00	-	3.22
Flexible cylinder with polydispersity of radius 0.25	7	88 ± 0.29	40.0 ± 0.10	4.3 ± 0.00	-	3.89
Cylinder + Sphere	8	51 ± 0.55	-	25.5 ± 0.00	0.9*	<1
Sphere	10	-	-	-	0.9 ± 0.00	1.00

*Table A3- SAXS fitting results for **PBI-H** at 5 mg/mL with 20 v/v% MeOH at different pH. *No fitting error available. Sphere radius fixed based on pH 10 fit.*

Model	pH	Length / nm	Kuhn length / nm	Cylinder radius / nm	Axis ratio	Sphere radius / nm	Power law	Reduced Chi squared
Flexible cylinder with a polydispersity of radius 0.3	2	400*	13.0 ± 0.06	5.0 ± 0.01	-	-	-	7.5
Flexible cylinder with a polydispersity of radius 0.3	3	420*	13.7 ± 0.05	4.8 ± 0.00	-	-	-	8.6
Flexible cylinder with a polydispersity of radius 0.3	3.5	470*	9.4 ± 0.08	4.5 ± 0.01	-	-	-	8.9
Flexible cylinder with a polydispersity of radius 0.3	4	500*	9.4 ± 0.08	4.6 ± 0.01	-	-	-	9.8
Flexible cylinder with a polydispersity of radius 0.3	4.5	400*	13.9 ± 0.04	4.6 ± 0.00	-	-	-	10.3
Flexible elliptical cylinder	5	700 ± 21.73	2.7 ± 0.10	1.1 ± 0.01	4.6 ± 0.01	-	-	3.4
Sphere + Flexible cylinder	6	300*	13.5 ± 0.70	8.5 ± 0.04	-	1.0†	-	1.2
Sphere	7	-	-	-	-	1.0 ± 0.00	-	<1
Power law	7	-	-	-	-	-	2.7 ± 0.01	<1
Sphere	8	-	-	-	-	1.0 ± 0.00	-	<1
Power law	8	-	-	-	-	-	2.7 ± 0.01	<1
Sphere	10	-	-	-	-	1.0 ± 0.00	-	<1
Power law	10	-	-	-	-	-	2.5 ± 0.02	<1

*Table A4- Model fitting results for **PBI-F** at 5 mg/mL and 20 v/v% MeOH at a range of pH. * No fitting error available. Further fitting of the length went to an unrealistically large number. Length left and other parameters fitted to finish the fitting. This suggests that the length is larger than can be measured with this SAXS setup. †No fitting error available. Bump at high Q attributed to small aggregates as seen at high pH. Sphere radius set to 1.0 nm based on the high pH fitting.*

Model	pH	Length / nm	Kuhn length / nm	Cylinder radius / nm	Sphere radius / nm	Power law	Reduced Chi squared
Flexible cylinder with a polydispersity of radius 0.2 + power law	2	680*	5.9 ± 0.08	3.2 ± 0.01	-	2.7 ± 0.00	3.4
Flexible cylinder with a polydispersity of radius 0.2 + power law	3	680*	5.7 ± 0.07	3.1 ± 0.01	-	2.7 ± 0.00	1.3
Flexible cylinder with a polydispersity of radius 0.2 + power law	3.5	680*	5.6 ± 0.06	3.0 ± 0.01	-	2.7 ± 0.00	3.7
Flexible cylinder with a polydispersity of radius 0.25	4	680*	6.3 ± 0.05	3.0 ± 0.00	-	-	3.9
Flexible cylinder with a polydispersity of radius 0.3	4.5	220 ± 2.7	24.3 ± 0.07	3.5 ± 0.00	-	-	3.4
Flexible cylinder with a polydispersity of radius 0.25 + Sphere	5	130 ± 0.52	22 ± 0.08	3.5 ± 0.00	1.0†	-	2.7
Sphere + Power law	6	-	-	-	1.0 ± 0.00	2.6 ± 0.01	1.0
Sphere	7	-	-	-	1.0 ± 0.00	-	<1
Sphere	8	-	-	-	1.0 ± 0.00	-	<1
Sphere	10	-	-	-	1.0 ± 0.00	-	<1

*Table A5- Model fitting results for **PBI-A** at 5 mg/mL at 20 v/v% MeOH at a range of pHs. No fitting error available. Length increased to an unrealistically large number with further fitting. Length set to 680 nm and a power law added to capture the intensity at low Q. This suggests the presence of structures longer than measurable by this SAXS setup. † No fitting error available. Bump at high Q attributed to small aggregates as seen at high pH. Sphere radius set to 1.0 nm based on the high pH fitting.*

Model	MeOH / v/v%	pH	Length / nm	Kuhn length / nm	Cylinder radius / nm	Sphere radius / nm	Power law	Reduced Chi squared
Sphere	0	7	-	-	-	1.1 ± 0.00	-	<1
Flexible cylinder with polydispersity of radius 0.3	0	4.5	99 ± 0.03	24 ± 0.09	3.0 ± 0.00	-	-	4.0
Not fitted	0	2					-	
Sphere	5	7	-	-	-	1.0 ± 0.00	-	<1
Flexible cylinder with polydispersity of radius 0.3	5	4.5	104 ± 0.45	26 ± 0.00	3.1 ± 0.00	-	-	5.0
Flexible cylinder with polydispersity of radius 0.3	5	2	690 ± 13.01	6.7 ± 0.08	2.9 ± 0.01	-	-	1.3
Sphere	10	7	-	-	-	1.0 ± 0.02	-	<1
Flexible cylinder with polydispersity of radius 0.3	10	4.5	87 ± 0.30	22 ± 0.00	3 ± 0.00	-	-	6.0
Flexible cylinder with polydispersity of radius 0.3	10	2	510 ± 5.66	6.0 ± 0.08	2.9 ± 0.01	-	-	1.9
Sphere	30	7	-	-	-	1.0 ± 0.00	-	<1
Flexible cylinder with polydispersity of radius 0.3	30	4.5	190 ± 1.15	19 ± 0.00	3.6 ± 0.00	-	-	3.1
Flexible cylinder with polydispersity of radius 0.3 + power law	30	2	700*	7.4 ± 0.05	3.3 ± 0.01	-	2.5 ± 0.01	3.6
Sphere	40	7	-	-	-	1.0 ± 0.00	-	<1
Flexible cylinder with polydispersity of radius 0.3 + Sphere	40	4.5	230 ± 0.88	17.5 ± 0.05	4.1 ± 0.02	1.0†	-	2.9
Flexible cylinder with polydispersity of radius 0.3 + Power law	40	2	700*	8.6 ± 0.09	3.9 ± 0.01	-	2.8 ± 0.00	8.0

*Table A6- Model fitting results for **PBI-A** at 5 mg/mL at a range of MeOH and pH. * No fitting error available. Length increased to an unrealistically large number with further fitting. Length set to 700 nm and a power law added to capture low Q scattering intensity. This suggests the presence of structures longer than measurable by this SAXS setup.* †*No fitting error available. Bump at high Q attributed to small aggregates as seen at high pH. Sphere radius set to 1.0 nm based on the high pH fitting.*

Model	pH	Length / nm	Kuhn length / nm	Cylinder radius / nm	Axis ratio	Sphere radius / nm	Reduced Chi squared
Flexible elliptical cylinder	3	280 ± 0.00	70.5 ± 0.66	2.7 ± 0.00	7.1 ± 0.01	-	4.8
Flexible elliptical cylinder	3.5	370 ± 0.00	93 ± 2.43	2.7 ± 0.00	7.2 ± 0.01	-	10.4
Flexible elliptical cylinder	4	280 ± 2.00	13.4 ± 0.04	1.7 ± 0.00	8.0 ± 0.02	-	3.3
Flexible elliptical cylinder	4.5	240 ± 2.28	19.5 ± 0.08	1.9 ± 0.00	7.7 ± 0.02	-	4.1
Flexible elliptical cylinder	5	290 ± 2.18	13.2 ± 0.03	1.7 ± 0.00	8.1 ± 0.02	-	2.6
Flexible elliptical cylinder + Sphere	6	580 ± 20.33	5.9 ± 0.28	2.9 ± 0.03	4.6 ± 0.04	1.0*	1.9
Flexible cylinder with a polydispersity of radius 0.25 + Sphere	7	405 ± 13.41	11.7 ± 0.55	7.3 ± 0.05	-	1.0*	5.8
Flexible cylinder with a polydispersity of radius 0.25 + Sphere	8	314 ± 14.06	10.8 ± 0.69	7.3 ± 0.06	-	1.0*	2.3
Flexible cylinder with a polydispersity of radius 0.25 + Sphere	10	282 ± 15.10	10.2 ± 0.79	7.0 ± 0.07	-	1.0*	2.5

*Table A7- Model fitting results for **PBI-V** at 5 mg/mL and 20 v/v% MeOH at a range of pH. *No fitting error available. Bump at high Q attributed to small aggregates. High Q bump region fitted independently to sphere model and this radius used as a fixed value in the fit of the whole Q range.*

Model	pH	Length / nm	Kuhn length / nm	Cylinder radius / nm	Axis ratio	Sphere radius / nm	Power law	Reduced Chi squared
Power law	2	-	-	-	-	-	3.5 ± 0.02	<1
Not fitted	3							
Not fitted	3.5							
Not fitted	4							
Flexible elliptical cylinder	4.5	640*	12.2 ± 0.07	3.3 ± 0.00	-	-	-	11.3
Flexible elliptical cylinder + Sphere	5	640 ± 0.18	64.0 ± 13.08	3.2 ± 0.00	8.0 ± 0.03	1.0†	-	2.1
Flexible elliptical cylinder + Sphere	6	570*	27.7 ± 0.43	4.7 ± 0.01	3.7 ± 0.02	1.0†	-	1.1
Flexible cylinder + Sphere	7	300*	10.9 ± 0.29	5.8 ±0.02	-	1.0†	-	1.6
Flexible cylinder + Sphere	8	130 ± 0.00	31.8 ± 0.80	7.0 ± 0.02	-	1.0†	-	1.8
Sphere	10	-	-	-	-	1.0 ± 0.00	-	<1
Power	10	-	-	-	-	-	1.9 ± 0.07	<1

Table A8- Model fitting results for **PBI-Y** at 5 mg/mL and 20 v/v% MeOH at a range of pH. The pH 3 to 4 data could not be adequately fitted to a model. This is believed to be due to scattering from the fibre network, which also results in the observed drop in scattering intensity at pH 3 and pH 2. * No fitting error available. Further fitting of the length went to an unrealistically large number. Length left and other parameters fitted to finish the fitting. This suggests that the length is larger than can be measured with this SAXS setup. † No fitting error available. Bump at high Q attributed to small aggregates as seen at pH 10. Sphere radius set to 1.0 nm based on the high pH fitting.

Model	MeOH / v/v%	pH	Length / nm	Kuhn length / nm	Cylinder radius / nm	Sphere radius / nm	Power law	Reduced Chi squared
Flexible cylinder + sphere	0	7	710*	8.7 ± 0.88	5.6 ± 0.06	1.0†	-	1.9
Could not fit	0	4.5						
Flexible cylinder with polydispersity of radius 0.3	0	2	560*	10.6 ± 0.29	5.0 ± 0.03	-	-	1.9
Flexible cylinder + sphere	5	7	680*	8.9 ± 0.85	5.6 ± 0.05	1.0†	-	1.7
Flexible cylinder with polydispersity of radius 0.25 + power law	5	4.5	1000*	6.3*	3.0*	-	4.8 ± 0.02	5.3
Flexible cylinder with polydispersity of radius 0.3	5	2	430*	11.6 ± 0.22	5.7 ± 0.02	-	-	4.3
Flexible cylinder + sphere	10	7	530*	9.2 ± 0.64	5.6 ± 0.04	1.0†	-	1.5
Flexible cylinder with polydispersity of radius 0.3 + power law	10	4.5	940*	8.2*	3.4*	-	6.2 ± 0.05	4.0
Flexible cylinder with polydispersity of radius 0.3	10	2	360 ± 29.92	11.5 ± 1.42	6.4 ± 0.13	-	-	<1
Flexible cylinder with polydispersity of radius 0.1 + sphere	30	7	440*	9.4 ± 0.33	5.5 ± 0.02	1.0†	-	1.2
Flexible cylinder with polydispersity of radius 0.3	30	4.5	1200*	10.0 ± 0.64	5.0 ± 0.01	-	-	9.8
Flexible cylinder with polydispersity of radius 0.3	30	2	250*	21.0 ± 1.23	12.3 ± 0.08	-	-	1.5
Not fitted	40	7						
Not fitted	40	4.5						
Not fitted	40	2						

*Table A9- Model fitting results for **PBI-Y** at 5 mg/mL at a range of MeOH and pH. Good fits to the 40 v/v% MeOH data could not be achieved. * No fitting error available. Further fitting of the length went to an unrealistically large number. Length left and other parameters fitted to finish the fitting. This suggests that the length is larger than can be measured with this SAXS setup. † No fitting error available. Bump at high Q attributed to small aggregates. High Q bump region fitted independently to sphere model and this radius used as a fixed value in the fit of the whole Q range.*

Initial TA experiments and optimisation of experimental design

The first run of TA experiments was designed to replicate the conditions used in the photocatalysis experiments. A PBI dispersion was made up to 5 mg/mL in PBI concentration, also containing 20 (v/v%) methanol, and platinum nanoparticles. The solution was placed on one of the windows before being separated by a 100 μm spacer, and sealed by another window. This meant there was an attempt to minimise compression of the sample, but also to spread the sample enough to allow light to penetrate it. An error in cell design meant that the compression applied to the windows was not as reproducible as first thought, but this was not known at this stage. The optical density of the samples measured was far higher than the desired value of 0.4 o.D. (figure 102). This was not a desirable situation as it meant we were unable to directly compare changes shown in the TA to the initial species we had, and also created the problem of potential heating processes at the front of the sample.[11] The high absorbance meant that we could not penetrate the sample fully below 600 nm and would not be able to monitor the GSB. We could however study the wavelength region between 600-900 nm which gives information about the excited species and potential radical anions which govern the activity in the HER.
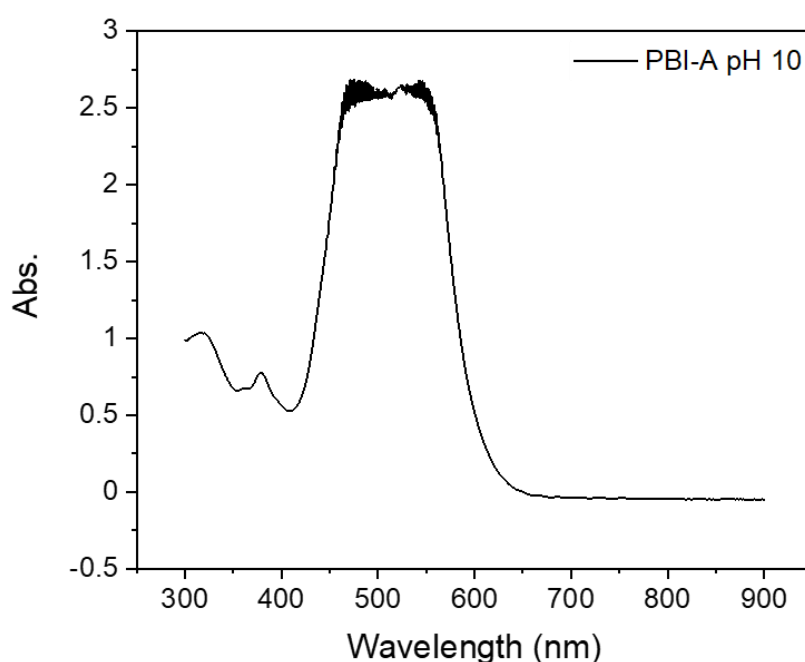
Figure 102- A UV-Vis spectrum of PBI-A pH 10 which maxed out the detector, indicated by thick line between 450-600 nm. Recorded in TA cell with 100 μm spacer.

Analysis of optically thick samples

TA spectra at 2 pHs of PBI-A and PBI-Y are shown by figure A103. This allowed for a direct comparison between dominant aggregate types (type 2 vs type 1) and provided an insight into the likely excited state species and mechanism of action. As expected there were clear differences in the spectra produced by both changes in pH, and also PBI amino acid functionality. For PBI-A at pH 5 (at 1ps) the spectrum is noticeably broader than for the other samples in this study, with peaks becoming more defined at later time scales > 1 ns. The peak wavelengths for this spectrum occurred at around 740 and 830 nm, which were in the region expected for the PBI radical anion although slightly blue shifted, and significantly broadened. For PBI-A at pH 10 the peaks were more well defined than at pH 5, with two major features at 734 and 820 nm, in addition to an additional peak at 610 nm which was not present at pH 5. Interestingly the intensity ratio between peaks also changed, with the peak at 820 nm becoming the most intense at pH 10. Due to the level of aggregation present at pH 5, it was not surprising that the peaks were broader, given that the inter chromophore coupling between PBI units was more extensive due to the far greater length of fibres. In the SAXS study detailed by chapter 1, PBI structures at pH 10 were shown to be between 2-6 PBIs in length, compared to structures greater than 130 nm at pH 5. The striking difference between these samples was the lifetime of the excited species, which is best demonstrated by figure 103. The rate of decay for PBI-A at 738 nm was similar for the first 50 ps at both pHs, but beyond 100 ps the pH 10 TA signal decayed more rapidly, with no significant quantity remaining at 3 ns (the end of the experiment). In contrast, the pH 5 sample had around 20 % of the excited species remaining, which indicated a striking difference in lifetime with just a subtle change in pH.
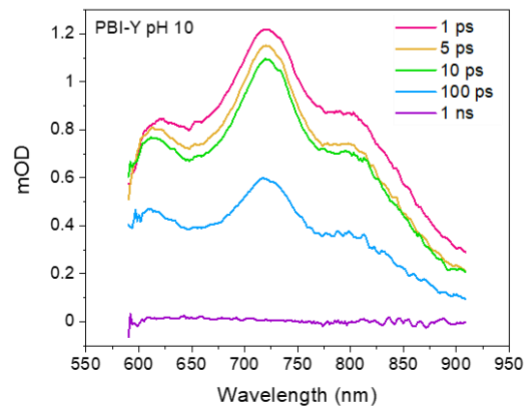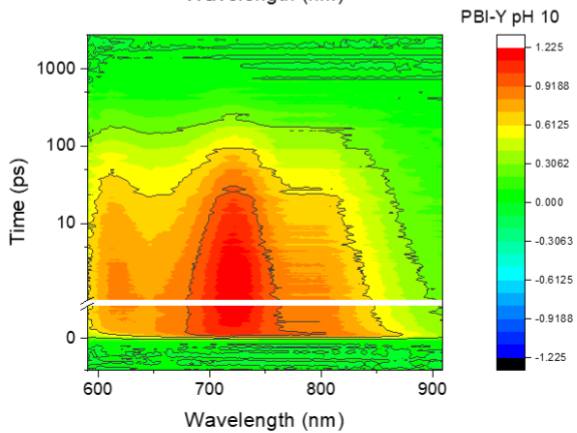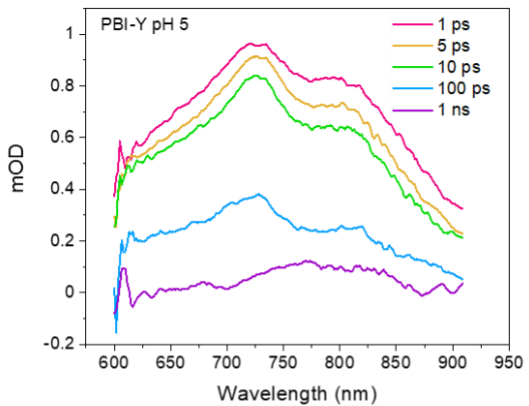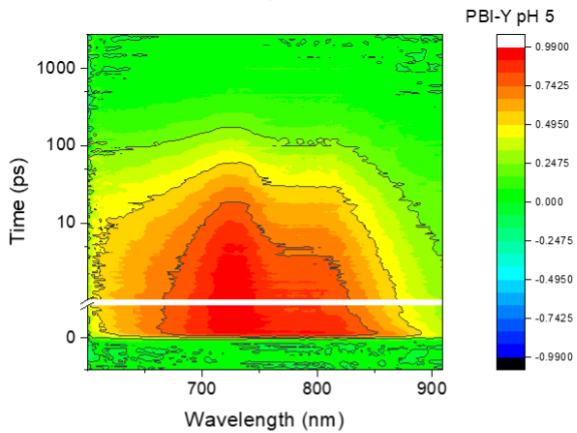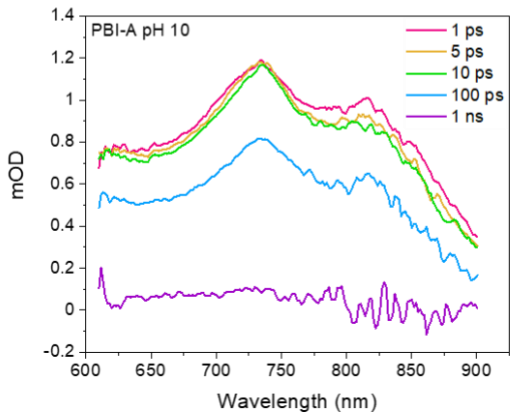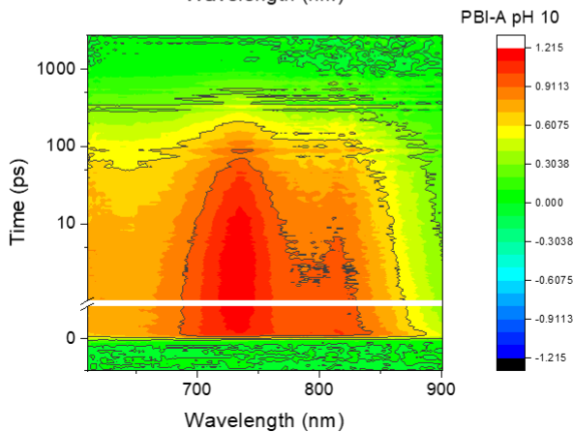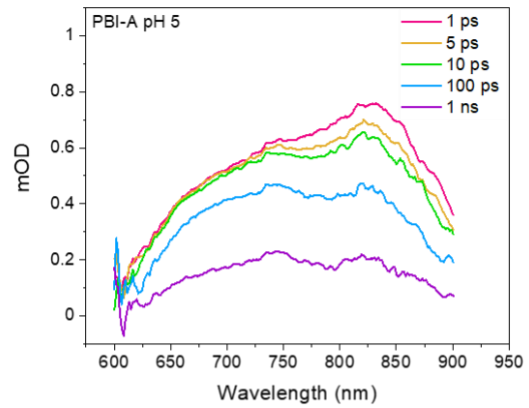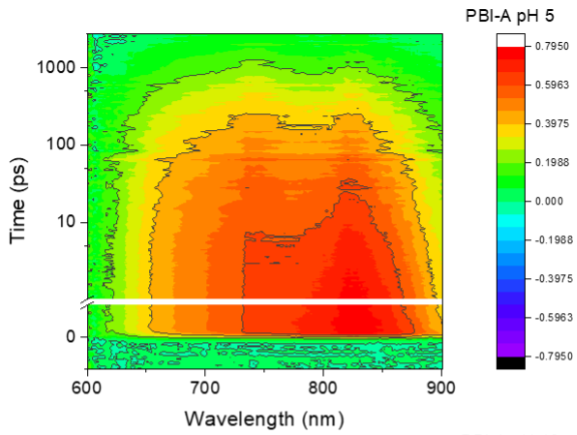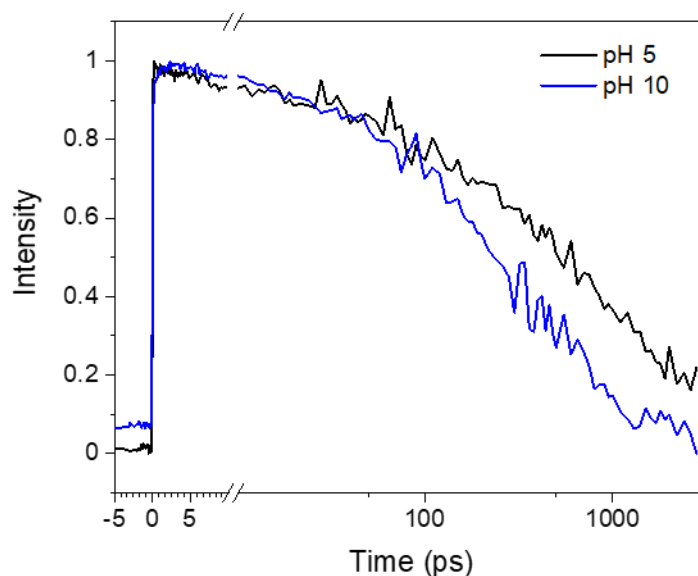
Figure 104- Single wavelength decay trace for PBI-A at 2 pHs. Wavelength chosen was 739 nm, due to common high intensity. Data was normalised.

The spectrum for PBI-Y at pH 5 displayed little broadening, and looked strikingly similar to data obtained for PBI-A at pH 10 slightly red shifted. This was despite displaying even larger assembled structures at pH 5 (confirmed via SAXS), characterised by a UV-Vis peak at 640 nm. The lack of broadening in PBI-Y truly highlights the impact of amino acid functionality on local packing, which has a profound effect on the interaction between neighbouring chromophores. Unfortunately, interchromophore measurements were not carried out in this study, which could have uncovered whether the addition of the phenol ring contributed to a greater distance between PBI units; through a combination of steric bulk and electronic effects. The peak at 620 nm was less well defined than in PBI-A (at pH 10), and appeared as a shoulder to the most intense peak at 723 nm, but otherwise the intensity ratios of the peaks were quite similar to PBI-A at high pH. There was a noticeable difference in the intensity ratios for the peak absorbance change in the PBI-Y pH 10 sample, which was initially 1:3:1 at 1 ps (610, 720, 805 nm) and the decay profile is shown in figure 104.
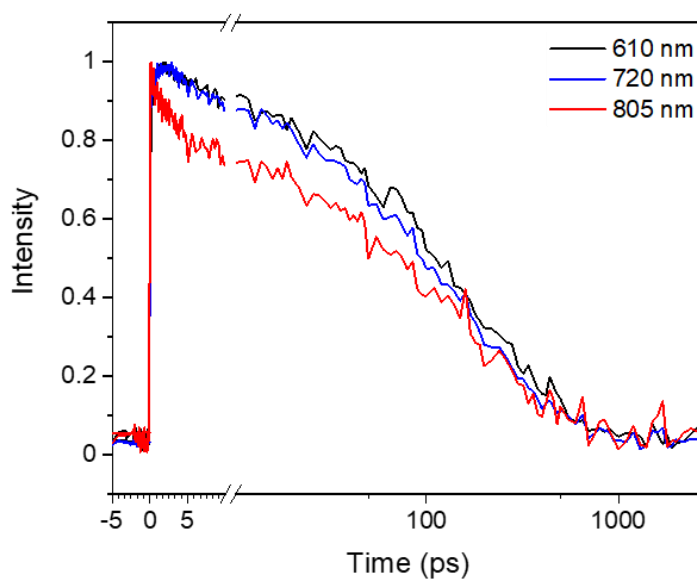
Figure 105- Single wavelength decay trace for PBI-Y at pH 10. Wavelengths chosen were 610,720 and 805, due to common high intensity. Data was normalised.

For PBI-Y at pH 10, the rate of decay of the peaks at 720 and 610 nm was the same throughout the experiment, whereas the peak at 805 initially cooled rapidly for the first 10 ps before slowing to match the other two features. Once again for a pH 10 sample there was a low concentration of the excited species at the end of the experiment, but also at pH 5 there was significantly less remaining excited than in PBI-A. The true difference in rates of excited state decay are displayed in figure 106, which illustrates how much longer PBI-A takes to return to the neutral species. This may help explain why the rate of hydrogen evolution is significantly higher in PBI-A, despite the same large structures forming in both samples. Without a long lives excited species, it is unlikely to lead to successful extraction of charge due to nature of the typically tightly bound excitons formed in these organic materials.
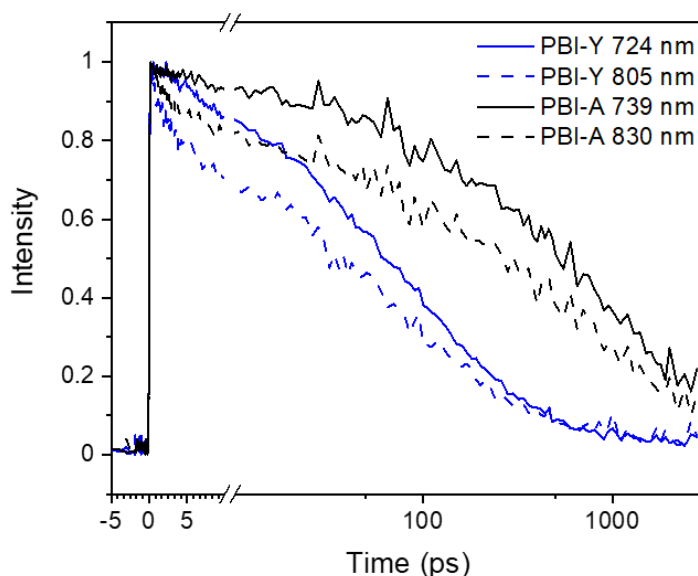
Figure 106- Comparing lifetimes of PBI-A and PBI-Y at pH 5, using peaks that are typical for a PBI radical anion. Data was normalised.

Varying the methanol concentration of optically thick samples

Having already explored the role of methanol as a structuring agent in chapter 2, the next logical step was to examine its hole scavenging effects in more detail. Once again, the samples used in this study were optically thick, due to the use of a 100 μm spacer not effectively compressing the sample. However, on this occasion rubber was used to more effectively compress the windows, which ensured the sample spread out more than in the previous set of experiments. PBI-A samples in this study used a range of methanol concentrations between 0-40 v/v%, to compare with the standard concentration used in the study of 20 v/v%. The wavelength window was also shifted slightly due to the level of noise below 600 nm due to the high absorption, which also allowed for a greater insight into the NIR region beyond 900 nm.

Figure 107 displays the contour plots of the TA data, and also the time slices at key intervals. At a first glance the data is strikingly similar for both data sets (0% vs 40% v/v% MeOH), despite a huge difference in the amount of methanol present in the sample. However, there were subtle differences which can explain why one sample was able to evolve hydrogen successfully and the other was not. Due to the extended range of these experiments, we were also able to track the region between 900-1000 nm, which has previously been shown to

contain the third peak for the PBI-A radical anion.[143] Although it was difficult to rationalise, there was clear evidence of a peak at 970 nm in both samples (particularly at 1 ns in 40 % MeOH). In fact, as the experiment progressed from 1 ps to 1 ns there was a distinct narrowing of the peaks present, and a growth of the feature at 970, which could indicate cooling of the initial transient species to form the PBI radical anion as known to literature.[143] This path is less clear in the no methanol data set, which did display a more prominent PBI radical anion signature at 100 ps, but not as clearly by 1 ns to 3 ns. Normalising the traces at 3 ns allowed for a direct comparison of the species remaining at the end of the experiment (shown by figure 108). And while the relative quantities of the transient species could not be obtained, it appeared that the same species was present in both samples. This also suggested that methanol was not involved in a hole scavenging role within the time frame of this experiment, and required a longer-lived species to participate in the eventual mechanism.
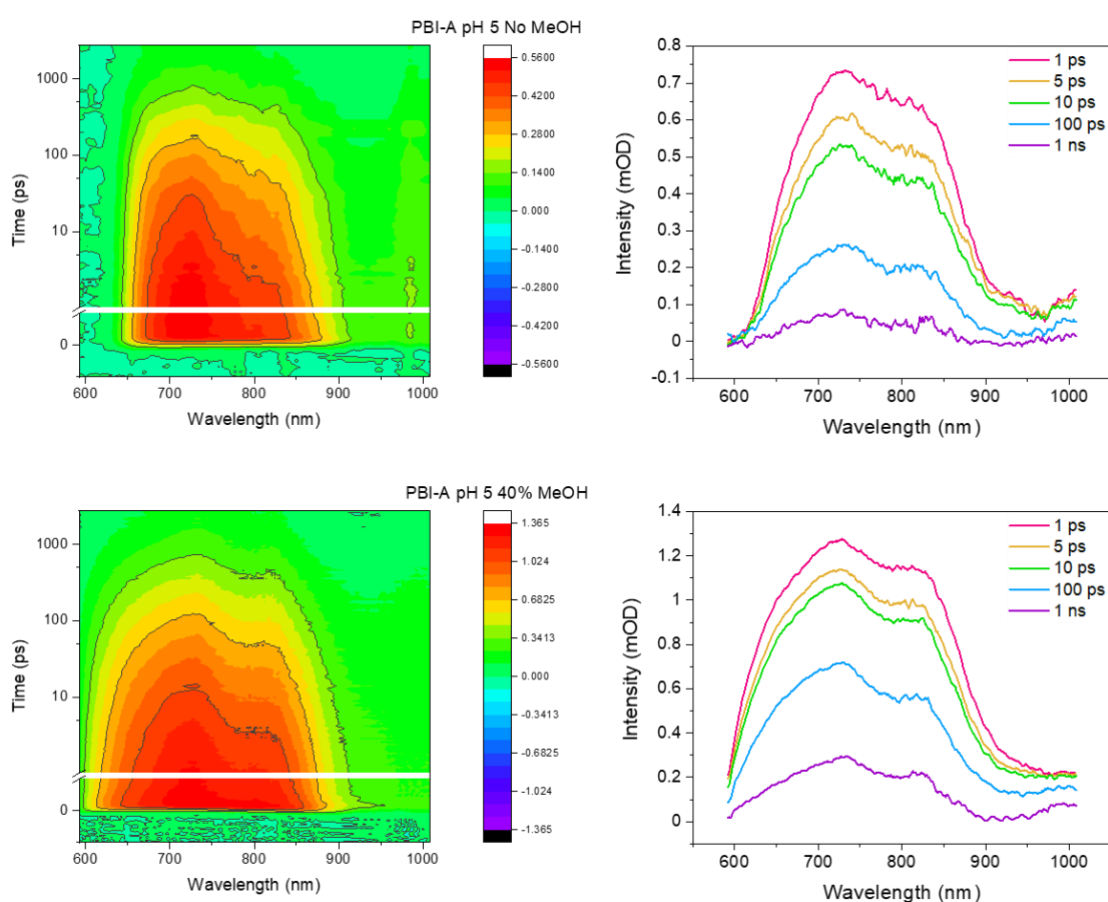
Figure 107- TA data comparing PBI-A at pH 5 at two different methanol concentrations 0 v/v% and 40 v/v%., Contour plots shown on left and time slices on the right. Samples were recorded

in the TA cell using a 100 μm spacer. Contour plots display most intense changes in absorbance through the experiment in red (If positive) and in blue (if negative). Key time slices illustrate the species present at that particular time period. Samples contained PBI-X 5 mg/mL, methanol v/v% and Pt nanoparticles (1 wt.%). Pump wavelength was 490 nm, light intensity of 200 μWcm^{-2}.
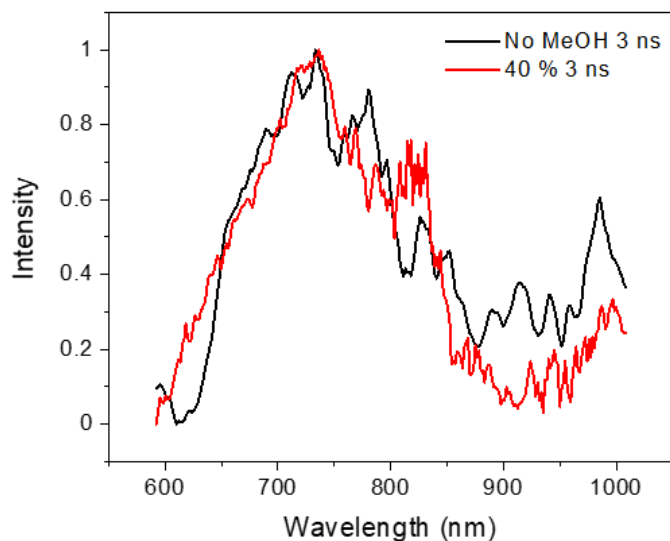
Figure 108 – 3 ns time slices from PBI-A pH 5 methanol study. Samples contained PBI-X 5 mg/mL, methanol v/v% and Pt nanoparticles (1 wt.%).

Investigating spacer thickness

Previous experiments used a 100 μm spacer to ensure uniform thickness and compression through the samples. Nevertheless, due to an error in the design of the cell the windows were not pressed together in a reproducible manner, and required rubber gaskets to maintain pressure evenly over the windows. As a result, spacers of varying thickness' were used to examine whether sample compression was resulting in a difference in behaviour.
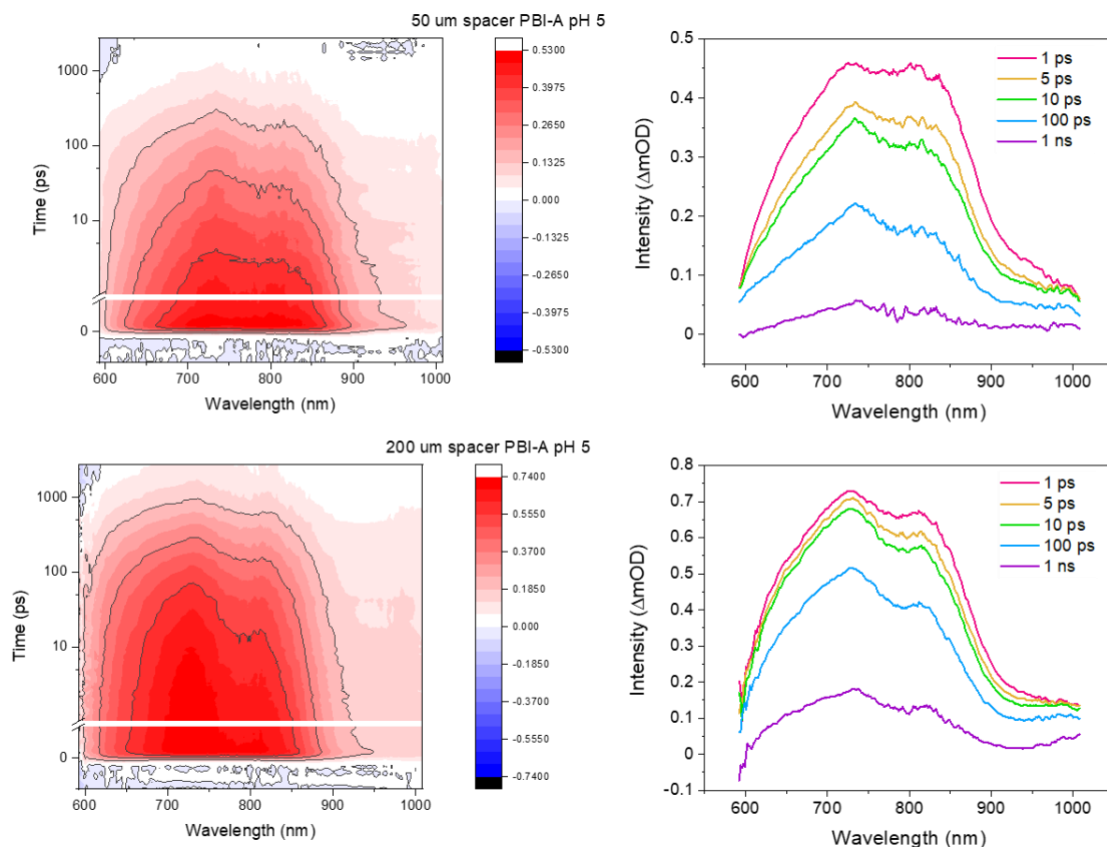
Figure 109- TA data comparing PBI-A at pH 5 at two different spacer thicknesses, 50 and 200 μm. Contour plots shown on left and time slices on the right. Samples were recorded in the TA cell using a 100 μm spacer. Contour plots display most intense changes in absorbance through the experiment in red (If positive) and in blue (if negative). Key time slices illustrate the species present at that particular time period. Samples contained PBI-X 5 mg/mL, methanol v/v% and Pt nanoparticles (1 wt.%). Light intensity was 200 μWcm^{-2}, and pump wavelength was 490 nm.

As the sample in both experimental setups was the same, the ideal outcome was that the data would look the same regardless of the spacer used. While there was no doubt that the same species are present in both samples, the lifetimes observed and the rates of decay of the transient species are quite different (figure 109). Therefore, the choice of spacer was having an effect on the outcome of the experiment, which would also complicate any potential models that would be produced by this data. This was elucidated further by figure 110 which clearly displays the different rates of decay of the prominent peaks at 729 and 819 nm.
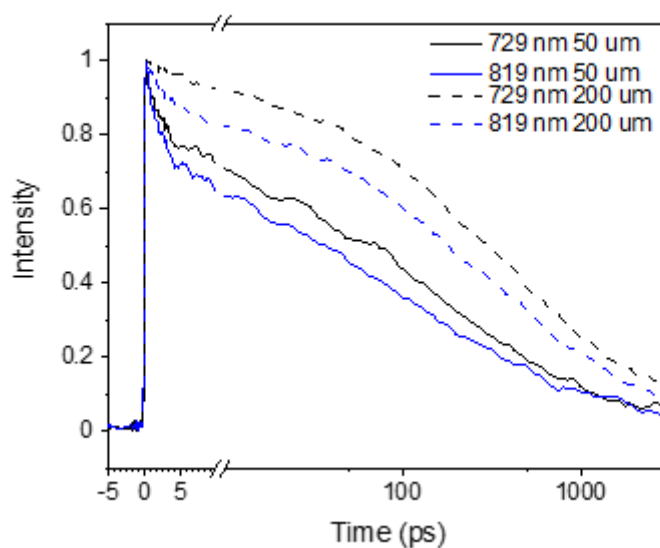
Figure 110–Wavelength decay profiles from PBI-A pH 5 thickness study. Wavelengths chosen common to PBI radical anion position. Samples contained PBI-X 5 mg/mL, methanol v/v% and Pt nanoparticles (1 wt.%).

Upon initial sample preparation there was a clear difference in the size of the sample spot for a given volume of PBI solution, depending on which spacer was used. This was due to a lack of compression from the larger 200 μm spacer (with respect to the 50 μm), which therefore spread the sample out less. The result of this was more absorbing sample (due to its smaller area and constant volume) which could not be measured by a traditional UV-Vis spectrophotometer, but yielded large transient measurements. The legitimacy of these measurements was however questionable due to limited penetration through the sample, and lack of reproducibility depending on volume chosen for the sample. Choosing a sample volume was also difficult as the surface tension and how much it spread was proportional to the volume, and therefore the absorbance could be controlled by volume. Having to control all these additional variables left the experiments at a crossroads, as the setup and results were similar to those recorded previously within this group, but meant there was a lack of reproducibility across the samples due to the largely arbitrary choice of spacer without sufficient compression.

We have previously demonstrated the formation of the PBI-A radical anion in PBI-A suspensions and thin films from both UV and visible light on the ultrafast timescale.[85] But the visible pump light required methanol vapour to form a charge separated PBI radical anion,

with the hole likely localising on the alanine functional group and the electron on the PBI core. Without the added hole scavenger there was instead a short lived PBI singlet species present, as confirmed by the shifted peaks in the TA spectrum. The difference in dielectric constant for the two sample preparation methods (solution or dried film) were quite striking, due to the loss of water in the drying process. In addition, the concentration of the solutions used was 47 mM at pH 9, around 2x the concentration used in our own study but somewhat comparable with our own PBI-A solutions tested at pH 10 while also containing methanol and Pt nanoparticles (shown in figure 111). Due to the much lower extent of aggregation at pH 10 the viscosity of the pH 10 samples was strikingly different to that at pH 5, and might explain why they do not seem to be as dependent on the spacer used. Our previous measurements were performed on samples that were also optically thick due to the high concentration, meaning that it was likely that the measurements were only probing the face of the solution as opposed to the bulk transmission. With this in mind the results from both studies on PBI share many parallels, due to the initially formed broad species which appear to localise to yield what looks like the PBI radical anion. However, in our study we appear to have been able to generate the same species without methanol, due to striking similarities between the 0 and 40 v/v% samples. But in order to gain a better understanding of how our samples truly behaved in a non-static measurement, we endeavoured to find a way to increase the transmission and standardize conditions across our experiments.
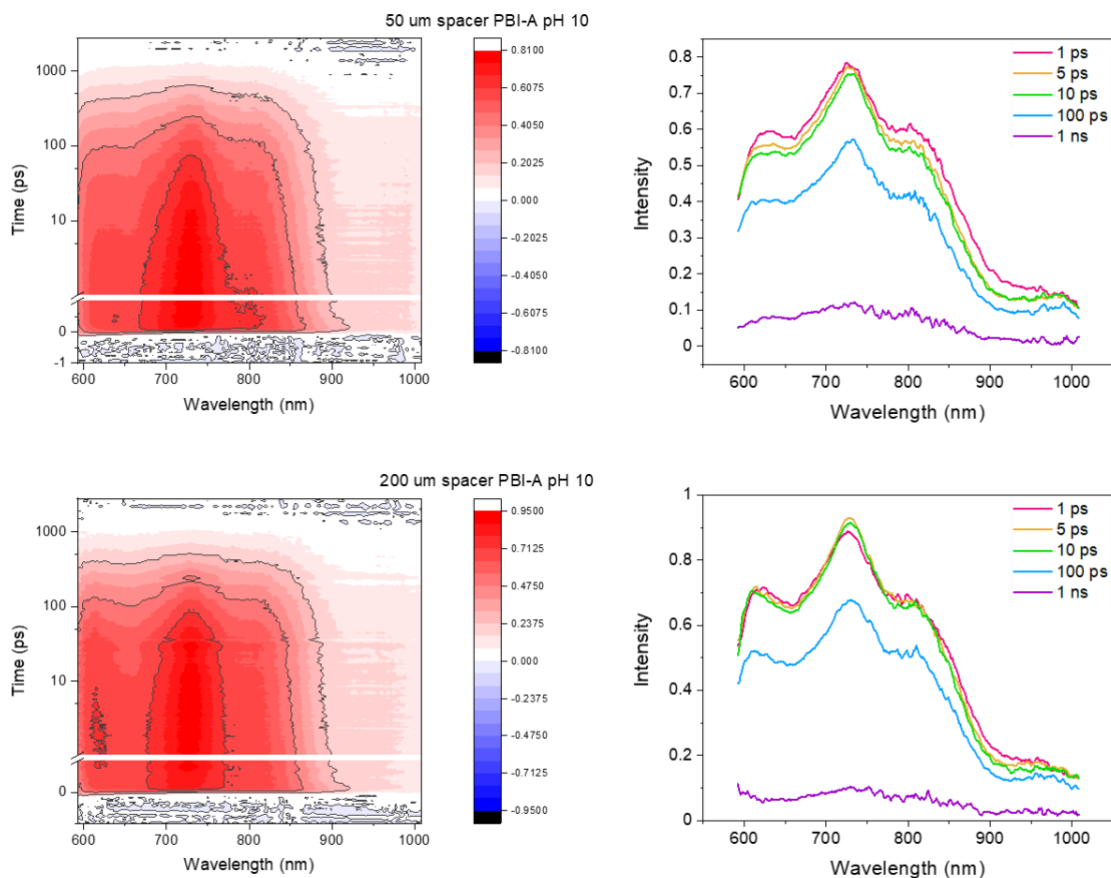
*Figure 111- TA data comparing PBI-A at pH 10 with two different spacers, 50 and 200 μm. Contour plots shown on left and time slices on the right. Contour plots display most intense changes in absorbance through the experiment in red (If positive) and in blue (if negative). Key time slices illustrate the species present at that particular time period. Samples contained PBI-X 5 mg/mL, methanol v/v% and Pt nanoparticles (1 wt.%). Pump light intensity was 200 μWcm^{-2}. Pump wavelength was 490 nm.*

Thinner spacers to allow for more light penetration

Figure 112 clearly displays that there was a difference in absorption coefficient between PBI-A pH 5 and pH 10 samples. This phenomenon has been previously tracked in amino acid PBI samples,[146] and due to aggregation, the absorbance falls with pH. This meant that not only were thinner spacers required, but also it was likely that different spacers would be required for each pH to achieve a comparable absorbance.
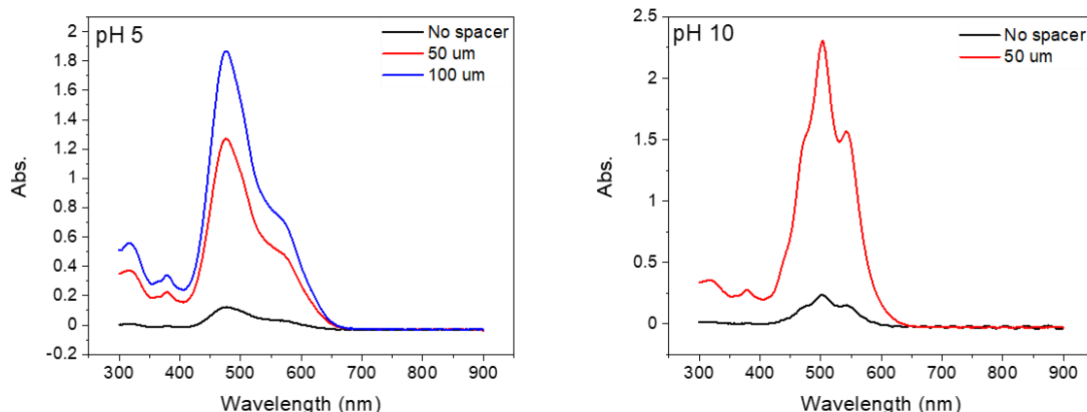
Figure 112- UV-Vis spectra of original spacers compared PBI-A at pH 5 and pH 10.
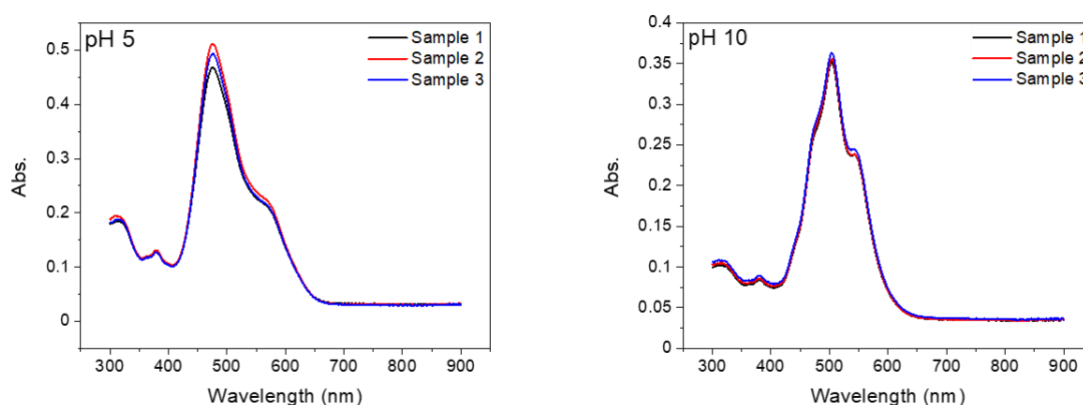
Figure 113- UV-Vis spectra of PBI-A at pH 5 and 10 using 25um spacers and 10 um spacers.

After a period of testing out a few different spacers two were chosen, 25 µm for pH 5 and 10 µm for pH 10. Figure A113 displays the reproducibility of performing the experiments over multiple runs, with minimal difference in the UV-Vis spectrum between samples. The absorbance was also at a level where around 50 % of the light was being transmitted through the sample, meaning for the first time we were able to consider the whole sample in our discussions and not simply the front face.

Comparing between experiment setups

Throughout the period of studying the PBI photocatalytic samples there were a number of different experimental setup iterations, and therefore a significant amount of data analysis. Upon arriving at the 'perfect setup' we had highest level of confidence in our results, and had hoped to minimise other factors which would lower our confidence in these results (such as

lowering the light intensity and thickness of samples). Having completed the experimental dataset, it was important to look back with hindsight and compare the results between each iteration to see how truly different the results are from one another.

PBI-A pH 5

Sample	Light intensity	oD of sample at λ_{max}	τ_{01}	τ_{12}	τ_{22}	Comments
50 μm spacer	200 μW	>1	1.12 ps	36.0 ps	582 ps	Shorter than expected
200 μm spacer	200 μW	>1	3.90 ps	151 ps	1.36 ns	
40 % MeOH 200 μm spacer	200 μW	>1	2.60 ps	77 ps	1.50 ps	
0% MeOH 200 μm spacer	200 μW	>1	4.37 ps	133 ps	1.66 ns	
25 μm spacer final run	100 μW	0.4	400 ps	4.4 ns		
100 μm spacer Original run	200 μW	>1	90.7 ps	1.53 ns		

Table A10- Comparing experimental conditions and fitted model lifetimes for PBI-A pH 5

PBI-A pH 10

Sample	Light intensity	oD of sample at λ_{max}	τ_{01}	τ_{12}	τ_{22}	Comments
Original run 100 um	200 μW	>>1	0.87 ps	96.0	447 ps	
50 um spacer	200 μW	>>1	2.03 ps	71.7 ps	590 ps	
200 um spacer	200 μW	>>1	0.87 ps	164 ps	530 ps	
Final run 10 um spacer	100 μW	0.4	0.74 ps	333 ps	260 ns	V large final value seems unlikely

Table 11- Comparing experimental conditions and fitted model lifetimes for PBI-A pH 10.

Due to the high extinction coefficient the choice of spacer was even more crucial to ensure light penetration through the sample. Despite this the results of the models have very similar lifetimes to one another, in some cases even closer than for pH 5.

References

1   C. C. L. McCrory, S. Jung, I. M. Ferrer, S. M. Chatman, J. C. Peters and T. F. Jaramillo, *J Am Chem Soc*, 2015, **137**, 4347–4357.

2   P. Kumar and A. Kumar, in *Handbook of Ecomaterials*, 2018, pp. 1–38.

3   A. J. Bard and M. A. Fox, *Acc. Chem. Res*, 1995, **28**, 141–145.

4   O. Dumele, L. Dordević, H. Sai, T. J. Cotey, M. H. Sangji, K. Sato, A. J. Dannenhoffer and S. I. Stupp, *J Am Chem Soc*, 2022, **144**, 3127–3136.

5   F. Li, H. Yang, W. Li and L. Sun, *Joule*, 2018, **2**, 36–60.

6   S. Bai, W. Yin, L. Wang, Z. Li and Y. Xiong, *RSC Adv*, 2016, **6**, 57446–57463.

7   A. Kirubakaran, S. Jain and R. K. Nema, *International Journal of Recent Trends in Engineering*, 2009, **1**, 157–161.

8   J. Jia, L. C. Seitz, J. D. Benck, Y. Huo, Y. Chen, J. W. D. Ng, T. Bilir, J. S. Harris and T. F. Jaramillo, *Nat Commun*, 2016, **7**, 1.

9   A. Fujishima and K. Honda, *Nature*, 1972, **238**, 37–38.

10   X. T. Xu, L. Pan, X. Zhang, L. Wang and J. J. Zou, *Advanced Science*, 2019, 6, 1801505.

11   J. K. Cooper, S. E. Reyes-Lillo, L. H. Hess, C. M. Jiang, J. B. Neaton and I. D. Sharp, *Journal of Physical Chemistry C*, 2018, **122**, 20642–20652.

12   A. W. Hains, Z. Liang, M. A. Woodhouse and B. A. Gregg, *Chem Rev*, 2010, **110**, 6689–6735.

13   T. Hisatomi, J. Kubota and K. Domen, *Chem Soc Rev*, 2014, **43**, 7520–7535.

14   H. Gerischer, M. E. Michel-Beyerle, F. Rebentrost and H. Tributsch, *Electrochim Acta*, 1968, **13**, 1509–1515.

15   A. Sekar and K. Sivula, *Chimia (Aarau)*, 2021, 75, 169–179.

16   R. R. Lunt, J. B. Benziger and S. R. Forrest, *Advanced Materials*, 2010, **22**, 1233–1236.

17   T. Tang, J. Qu, K. Müllen and S. E. Webber, *Langmuir*, 2006, **22**, 7610–7616.

18   M. M. Alam and S. A. Jenekhe, *Chemistry of Materials*, 2004, **16**, 4647–4656.

19   T. W. Kim and K.-S. Choi, 2014, **343**, 990–995.

20   T. H. Reilly, A. W. Hains, H. Y. Chen and B. A. Gregg, *Adv Energy Mater*, 2012, **2**, 455–460.

21   M. Dehghan and A. Behjat, *RSC Adv*, 2019, **9**, 20917–20924.

22   M. Gilbert Gatty, S. Pullen, E. Sheibani, H. Tian, S. Ott and L. Hammarström, *Chem. Sci.*, 2018, 4983–4991.

23   Y. Z. Zhao, K. X. Li, S. Y. Ding, M. Zhu, H. P. Ren, Q. Ma, Z. Guo, S. P. Tian, H. Q. Zhang and Z. C. Miao, *Russian Journal of Physical Chemistry A*, 2018, **92**, 1261–1265.

24   J. Belić, A. Förster, J. P. Menzel, F. Buda and L. Visscher, *Physical Chemistry Chemical Physics*, 2022, **24**, 197–210.

25   C. P. Lee, C. T. Li and K. C. Ho, *Materials Today*, 2017, **20**, 267–283.

26   R. Grisorio, L. de Marco, C. Baldisserri, F. Martina, M. Serantoni, G. Gigli and G. P. Suranna, *ACS Sustain Chem Eng*, 2015, **3**, 770–777.

27   B. A. Gregg, *Soft Matter*, 2009, **5**, 2985–2989.

28   L. Yao, N. Guijarro, F. Boudoire, Y. Liu, A. Rahmanudin, R. A. Wells, A. Sekar, H. H. Cho, J. H. Yum, F. le Formal and K. Sivula, *J Am Chem Soc*, 2020, **142**, 7795–7802.

29   I. C. Kaya, S. Akin, H. Akyildiz and S. Sonmezoglu, *Solar Energy*, 2018, **169**, 196–205.

30   H. C. Rojas, S. Bellani, F. Fumagalli, G. Tullii, S. Leonardi, M. T. Mayer, M. Schreier, M. Grätzel, G. Lanzani, F. di Fonzo and M. R. Antognazza, *Energy Environ Sci*, 2016, **9**, 3710–3723.

31   Z. Zhao, S. Zhan, L. Feng, C. Liu, M. S. G. Ahlquist, X. Wu, K. Fan, F. Li and L. Sun, *ACS Appl Mater Interfaces*, 2021, **13**, 40602–40611.

32   K. Sivula, A. Sekar, J. M. Moreno-Naranjo, Y. Liu, J. H. Yum, B. P. Darwich, H. H. Cho, N. Guijarro and L. Yao, *ACS Appl Mater Interfaces*, 2022, **14**, 8191–8198.

33   K. R. Wee, B. D. Sherman, M. K. Brennaman, M. v. Sheridan, A. Nayak, L. Alibabaei and T. J. Meyer, *J Mater Chem A Mater*, 2016, **4**, 2969–2975.

34   H.-H. Cho, L. Yao, J.-H. Yum, Y. Liu, F. Boudoire, R. A. Wells, N. Guijarro, A. Sekar and K. Sivula, *Nat Catal*, 2021, **4**, 431–438.

35   S. S. Patil, M. A. Johar, M. A. Hassan, D. R. Patil and S. W. Ryu, *Solar Energy*, 2019, **178**, 125–132.

36   L. Yao, Y. Liu, H. H. Cho, M. Xia, A. Sekar, B. Primera Darwich, R. A. Wells, J. H. Yum, D. Ren, M. Grätzel, N. Guijarro and K. Sivula, *Energy Environ Sci*, 2021, **14**, 3141–3151.

37   J. T. Kirner and R. G. Finke, *J Mater Chem A Mater*, 2017, **5**, 19560–19592.

38   J. M. Yu, J. Lee, Y. S. Kim, J. Song, J. Oh, S. M. Lee, M. Jeong, Y. Kim, J. H. Kwak, S. Cho, C. Yang and J. W. Jang, *Nat Commun*, 2020, **11**, 1–9.

39   G. A. Volpato, M. Marasi, T. Gobbato, F. Valentini, F. Sabuzi, V. Gagliardi, A. Bonetto, A. Marcomini, S. Berardi, V. Conte, M. Bonchio, S. Caramori, P. Galloni and A. Sartorel, *Chemical Communications*, 2020, **56**, 2248–2251.

40   B. D. Sherman, M. v. Sheridan, C. J. Dares and T. J. Meyer, *Anal Chem*, 2016, **88**, 7076–7082.

41   M. K. Brennaman, R. J. Dillon, L. Alibabaei, M. K. Gish, C. J. Dares, D. L. Ashford, R. L. House, G. J. Meyer, J. M. Papanikolas and T. J. Meyer, *J Am Chem Soc*, 2016, 138, 13085–13102.

42   C. A. Kent, J. J. Concepcion, C. J. Dares, D. A. Torelli, A. J. Rieth, A. S. Miller, P. G. Hoertz and T. J. Meyer, *J Am Chem Soc*, 2013, **135**, 8432–8435.

43   D. Zhu and Q. Zhou, *Environ Nanotechnol Monit Manag*, 2019, 12.

44   H. Miao, J. Yang, G. Peng, H. Li and Y. Zhu, *Sci Bull (Beijing)*, 2019, **64**, 896–903.

45   T. An, J. An, Y. Gao, G. Li, H. Fang and W. Song, *Appl Catal B*, 2015, **164**, 279–287.

46   J. Chen, P. Wagner, L. Tong, G. G. Wallace, D. L. Officer and G. F. Swiegers, *Angewandte Chemie - International Edition*, 2012, **51**, 1907–1910.

47   T. Hasobe, H. Oki, A. S. D. Sandanayaka and H. Murata, *Chemical Communications*, 2008, 724–726.

48   G. F. Moore, J. D. Blakemore, R. L. Milot, J. F. Hull, H. E. Song, L. Cai, C. A. Schmuttenmaer, R. H. Crabtree and G. W. Brudvig, *Energy Environ Sci*, 2011, **4**, 2389–2392.

49   D. McDowall, B. J. Greeves, R. Clowes, K. McAulay, A. M. Fuentes-Caparrós, L. Thomson, N. Khunti, N. Cowieson, M. C. Nolan, M. Wallace, A. I. Cooper, E. R. Draper, A. J. Cowan and D. J. Adams, *Adv Energy Mater*, 2020, **10**, 1–10.

50   F. Yu, Z. Wang, S. Zhang, K. Yun, H. Ye, X. Gong, J. Hua and H. Tian, *Appl Catal B*, 2018, **237**, 32–42.

51   I. Kim, H. M. Haverinen, Z. Wang, S. Madakuni, J. Li and G. E. Jabbour, *Appl Phys Lett*, 2009, **95**, 93–96.

52   P. C. Rieke, C. L. Linkous and N. R. Armstrong, *Journal of Physical Chemistry*, 1984, **88**, 1351–1357.

53   X. Feng, X. Ding and D. Jiang, *Chem Soc Rev*, 2012, **41**, 6010–6022.

54   N. W. Ockwig, A. P. Cote, M. O. Keeffe, A. J. Matzger and O. M. Yaghi, *Science (1979)*, 2005, **310**, 1166–1171.

55   X. Wang, L. Chen, S. Y. Chong, M. A. Little, Y. Wu, W. H. Zhu, R. Clowes, Y. Yan, M. A. Zwijnenburg, R. S. Sprick and A. I. Cooper, *Nat Chem*, 2018, **10**, 1180–1189.

56   Z. Xiong and Y. Xu, *Chemistry of Materials*, 2007, **19**, 1452–1458.

57   C. Yan, J. Dong, Y. Chen, W. Zhou, Y. Peng, Y. Zhang and L. ning Wang, *Nano Res*, 2022, 15, 3835–3858.

58   Y. Tan, X. Dai, Y. Li and D. Zhu, *J Mater Chem*, 2003, **13**, 1069–1075.

59   A. W. Mureithi, Y. Sun, T. Mani, A. R. Howell and J. Zhao, *Cell Rep Phys Sci*, 2022, **3**, 100889.

60   Q. Wang, S. Okunaka, H. Tokudome, T. Hisatomi, M. Nakabayashi, N. Shibata, T. Yamada and K. Domen, *Joule*, 2018, **2**, 2667–2680.

61   D. J. Woods, R. S. Sprick, C. L. Smith, A. J. Cowan and A. I. Cooper, *Adv Energy Mater*, 2017, **7**, 1–6.

62   Y. Bai, L. Wilbraham, B. J. Slater, M. A. Zwijnenburg, R. S. Sprick and A. I. Cooper, *J Am Chem Soc*, 2019, **141**, 9063–9071.

63   B. Burger, P. M. Maffettone, V. v. Gusev, C. M. Aitchison, Y. Bai, X. Wang, X. Li, B. M. Alston, B. Li, R. Clowes, N. Rankin, B. Harris, R. S. Sprick and A. I. Cooper, *Nature*, 2020, **583**, 237–241.

64   M. Marchini, A. Gualandi, L. Mengozzi, P. Franchi, M. Lucarini, P. G. Cozzi, V. Balzani and P. Ceroni, *Physical Chemistry Chemical Physics*, 2018, **20**, 8071–8076.

65   M. Rahman, H. Tian and T. Edvinsson, *Angewandte Chemie - International Edition*, 2020, 59, 16278–16293.

66   K. Sivula, *ACS Energy Lett*, 2020, **5**, 1970–1973.

67   K. Sivula, *Chem*, 2018, **4**, 2490–2492.

68   Y. Bai, K. Hippalgaonkar and R. S. Sprick, *J Mater Chem A Mater*, 2021, **9**, 16222–16232.

69   P. A. LEWIS, in *Applied Polymer Science: 21st Century*, eds. C. D. Craver and C. E. B. T.-A. P. S. 21st C. Carraher, Pergamon, Oxford, 2000, pp. 493–526.

70   L. Perrin and P. Hudhomme, *European J Org Chem*, 2011, 5427–5440.

71   C. Huang, S. Barlow and S. R. Marder, *J Org Chem*, 2011, **76**, 2386–407.

72   L. Chen, C. Li and K. Müllen, *J Mater Chem C Mater*, 2014, **2**, 1938–1956.

73   M. Pakseresht, J. B. Bodapati and H. Icil, *J Photochem Photobiol A Chem*, 2018, **360**, 270–277.

74   L. Zhong, F. Xing, W. Shi, L. Yan, L. Xie and S. Zhu, *ACS Appl Mater Interfaces*, 2013, **5**, 3401–3407.

75   E. E. Neuteboom, S. C. J. Meskers, P. A. van Hal, J. K. J. van Duren, E. W. Meijer, R. A. J. Janssen, H. Dupin, G. Pourtois, J. Cornil, R. Lazzaroni, J. L. Brédas and D. Beljonne, *J Am Chem Soc*, 2003, **125**, 8625–8638.

76   S. M. Mackinnon and Z. Y. Wang, *J Polym Sci A Polym Chem*, 2000, **38**, 3467–3475.

77   F. Würthner, *Chemical Communications*, 2004, **4**, 1564–1579.

78   D. Ke, A. Tang, C. Zhan and J. Yao, *Chemical Communications*, 2013, **49**, 4914–4916.

79   C. Schierl, A. Niazov-Elkan, L. J. W. Shimon, Y. Feldman, B. Rybtchinski and D. M. Guldi, *Nanoscale*, 2018, **10**, 20147–20154.

80   D. Liu, J. Wang, X. Bai, R. Zong and Y. Zhu, *Advanced Materials*, 2016, **28**, 7284–7290.

81   A. K. Dwivedi, M. Pandeeswar and T. Govindaraju, *ACS Appl Mater Interfaces*, 2014, **6**, 21369–21379.

82   A. Weißenstein, C. R. Saha-Möller and F. Würthner, *Chemistry - A European Journal*, 2018, **24**, 8009–8016.

83   T. Takada, A. Ashida, M. Nakamura and K. Yamana, *Bioorg Med Chem*, 2013, **21**, 6011–6014.

84   F. Würthner, C. R. Saha-Möller, B. Fimmel, S. Ogi, P. Leowanawat and D. Schmidt, *Chem Rev*, 2016, **116**, 962–1052.

85   J. J. Walsh, J. R. Lee, E. R. Draper, S. M. King, F. Jäckel, M. A. Zwijnenburg, D. J. Adams and A. J. Cowan, *The Journal of Physical Chemistry C*, 2016, **120**, 18479–18486.

86   F. C. Spano, *Acc Chem Res*, 2010, **43**, 429–439.

87   H. Wu, L. Xue, Y. Shi, Y. Chen and X. Li, *Langmuir*, 2011, **27**, 3074–3082.

88   K. A. Kistler, C. M. Pochas, H. Yamagata, S. Matsika and F. C. Spano, *Journal of Physical Chemistry B*, 2012, **116**, 77–86.

89   S. Ghosh, X. Q. Li, V. Stepanenko and F. Würthner, *Chemistry - A European Journal*, 2008, **14**, 11343–11357.

90   S. Basak, N. Nandi, A. Baral and A. Banerjee, *Chem Commun (Camb)*, 2015, **51**, 780–3.

91   N. J. Hestand and F. C. Spano, *Journal of Chemical Physics*, 2015, **143**, 244707.

92   R. Ghosh and F. C. Spano, *Acc Chem Res*, 2020, **53**, 2201–2211.

93   N. J. Hestand and F. C. Spano, *Chem Rev*, 2018, **118**, 7069–7163.

94   A. L. Bialas and F. C. Spano, *Journal of Physical Chemistry C*, 2022, **126**, 4067–4081.

95   N. J. Hestand and F. C. Spano, *Acc Chem Res*, 2017, **50**, 341–350.

96   C. Lu, M. Fujitsuka, A. Sugimoto and T. Majima, 2016, **120**, 12734–12741.

97   T. Huang, A. Zhang, N. Xue, W. Jiang and Z. Wang, *Dyes and Pigments*, 2021, **193**, 109489.

98   D. Gosztola, M. P. Niemczyk, W. Svec, A. S. Lukas and M. R. Wasielewski, *Journal of Physical Chemistry A*, 2000, **104**, 6545–6551.

99   V. v. Roznyatovskiy, D. M. Gardner, S. W. Eaton and M. R. Wasielewski, *Org Lett*, 2014, **16**, 696–699.

100   D. Gosztola, M. P. Niemczyk, W. Svec, a S. Lukas and M. R. Wasielewski, *Journal of Physical Chemistry A*, 2000, **104**, 6545–6551.

101   P. Mentzel, M. Holzapfel, A. Schmiedel, I. Krummenacher, H. Braunschweig, A. Wodyński, M. Kaupp, F. Würthner and C. Lambert, *Physical Chemistry Chemical Physics*, 2022, **24**, 26254–26268.

102   R. Renner, M. Stolte, J. Heitmüller, T. Brixner, C. Lambert and F. Würthner, *Mater Horiz*, 2022, **9**, 350–359.

103   Z. Zhao, F. Niu, P. Li, H. Wang, Z. Zhang, G. J. Meyer and K. Hu, *J Am Chem Soc*, 2022, **144**, 7043–7047.

104   E. R. Draper, L. J. Archibald, M. C. Nolan, R. Schweins, M. A. Zwijnenburg, S. Sproules and D. J. Adams, *Chemistry - A European Journal*, 2018, **24**, 4006–4010.

105   M. C. Nolan, J. J. Walsh, L. L. E. Mears, E. R. Draper, M. Wallace, M. Barrow, B. Dietrich, S. M. King, A. J. Cowan and D. J. Adams, *J Mater Chem A Mater*, 2017, **5**, 7555–7563.

106   I. Papadopoulos, D. Gutiérrez-Moreno, Y. Bo, R. Casillas, P. M. Greißel, T. Clark, F. Fernández-Lázaro and D. M. Guldi, *Nanoscale*, 2022, **14**, 5194–5203.

107   J. K. Gallaher, E. J. Aitken, R. A. Keyzers and J. M. Hodgkiss, *Chemical Communications*, 2012, **48**, 7961.

108   J. M. Giaimo, J. v. Lockard, L. E. Sinks, A. M. Scott, T. M. Wilson and M. R. Wasielewski, *Journal of Physical Chemistry A*, 2008, **112**, 2322–2330.

109   E. Benazzi, K. Rettenmaier, T. Berger, S. Caramori, S. Berardi, R. Argazzi, M. Prato and Z. Syrgiannis, *The Journal of Physical Chemistry C*, 2020, **124**, 1317–1329.

110   J. D. Yuen, V. A. Pozdin, A. T. Young, B. L. Turner, I. D. Giles, J. Naciri, S. A. Trammell, P. T. Charles, D. A. Stenger and M. A. Daniele, *Dyes and Pigments*, 2019, **174**, 108014.

111   J. R. McKone, N. S. Lewis and H. B. Gray, *Chemistry of Materials*, 2014, **26**, 407–414.

112   S. Chen, Y. Li and C. Wang, *RSC Adv*, 2015, **5**, 15880–15885.

113   Y. Zhou, L. Zhang and K. Zhou, *Appl Surf Sci*, 2021, **543**, 148792.

114   J. Warnan, J. Willkomm, Y. Farré, Y. Pellegrin, M. Boujtita, F. Odobel and E. Reisner, *Chem Sci*, 2019, **10**, 2758–2766.

115   S. Chen, C. Wang, B. R. Bunes, Y. Li, C. Wang and L. Zang, *Appl Catal A Gen*, 2015, **498**, 63–68.

116   P. E. Keivanidis, V. Kamm, W. Zhang, G. Floudas, F. Laquai, I. McCulloch, D. D. C. Bradley and J. Nelson, *Adv Funct Mater*, 2012, **22**, 2318–2326.

117   C. Lu, M. Fujitsuka, A. Sugimoto and T. Majima, *Journal of Physical Chemistry C*, 2017, **121**, 4558–4563.

118   S. Chen, P. Slattum, C. Wang and L. Zang, *Chem Rev*, 2015, **115**, 11967–11998.

119   Y. Guo, Q. Zhou, J. Nan, W. Shi, F. Cui and Y. Zhu, *Nat Commun*, 2022, **13**, 1–10.

120   N. Kihal, A. Nazemi and S. Bourgault, *Nanomaterials*, 2022, 12.

121   K. Dirian, S. Bauroth, A. Roth, Z. Syrgiannis, F. Rigodanza, M. Burian, H. Amenitsch, D. I. Sharapa, M. Prato, T. Clark and D. M. Guldi, *Nanoscale*, 2018, **10**, 2317–2326.

122   E. R. Draper, L. Wilbraham, D. J. Adams, M. Wallace, R. Schweins and M. A. Zwijnenburg, *Nanoscale*, 2019, **11**, 15917–15928.

123   S. Ahmed, K. N. Amba Sankar, B. Pramanik, K. Mohanta and D. Das, *Langmuir*, 2018, **34**, 8355–8364.

124   C. Schaack, A. M. Evans, F. Ng, M. L. Steigerwald and C. Nuckolls, *J Am Chem Soc*, 2022, **144**, 42–51.

125   S. Ahmed, B. Pramanik, K. N. A. Sankar, A. Srivastava, N. Singha, P. Dowari, A. Srivastava, K. Mohanta, A. Debnath and D. Das, *Sci Rep*, 2017, **7**, 1–13.

126   G. L. Eakins, J. P. Wojciechowski, A. D. Martin, J. E. A. Webb, P. Thordarson and J. M. Hodgkiss, *Supramol Chem*, 2015, **27**, 746–756.

127   Y. Sun, C. He, K. Sun, Y. Li, H. Dong, Z. Wang and Z. Li, *Langmuir*, 2011, **27**, 11364–11371.

128   W. Wei, D. Liu, Z. Wei and Y. Zhu, *ACS Catal*, 2017, **7**, 652–663.

129   W. Wei, S. Ouyang and T. Zhang, *Journal of Semiconductors*, 2020, **41**, 091708.

130   Y. Xu, J. Zheng, J. O. Lindner, X. Wen, N. Jiang, Z. Hu, L. Liu, F. Huang, F. Würthner and Z. Xie, *Angewandte Chemie - International Edition*, 2020, **59**, 10363–10367.

131   K. Kong, S. Zhang, Y. Chu, Y. Hu, F. Yu, H. Ye, H. Ding and J. Hua, *Chemical Communications*, 2019, **55**, 8090–8093.

132   A. S. Weingarten, A. J. Dannenhoffer, R. v. Kazantsev, H. Sai, D. Huang and S. I. Stupp, *J Am Chem Soc*, 2018, **140**, 4965–4968.

133   N. J. Hestand, R. V. Kazantsev, A. S. Weingarten, L. C. Palmer, S. I. Stupp and F. C. Spano, *J Am Chem Soc*, 2016, **138**, 11762–11774.

134   A. S. Weingarten, R. v. Kazantsev, L. C. Palmer, D. J. Fairfield, A. R. Koltonow and S. I. Stupp, *J Am Chem Soc*, 2015, **137**, 15241–15246.

135   A. S. Weingarten, R. v. Kazantsev, L. C. Palmer, M. McClendon, A. R. Koltonow, A. P. S. Samuel, D. J. Kiebala, M. R. Wasielewski and S. I. Stupp, *Nat Chem*, 2014, **6**, 964–970.

136   A. Dannenhoffer, H. Sai, D. Huang, B. Nagasing, B. Harutyunyan, D. J. Fairfield, T. Aytun, S. M. Chin, M. J. Bedzyk, M. Olvera de la Cruz and S. I. Stupp, *Chem Sci*, 2019, **10**, 5779–5786.

137   A. J. Dannenhoffer, H. Sai, B. Harutyunyan, A. Narayanan, N. E. Powers-Riggs, A. N. Edelbrock, J. v Passarelli, S. J. Weigand, M. R. Wasielewski, M. J. Bedzyk, L. C. Palmer and S. I. Stupp, *Nano Lett*, 2021, **21**, 3745–3752.

138   A. S. Weingarten, R. v. Kazantsev, L. C. Palmer, M. McClendon, A. R. Koltonow, A. P. S. Samuel, D. J. Kiebala, M. R. Wasielewski and S. I. Stupp, *Nat Chem*, 2014, **6**, 964–970.

139   H. Yamagata, D. S. Maxwell, J. Fan, K. R. Kittilstved, A. L. Briseno, M. D. Barnes and F. C. Spano, *Journal of Physical Chemistry C*, 2014, **118**, 28842–28854.

140   A. Oleson, T. Zhu, I. S. Dunn, D. Bialas, Y. Bai, W. Zhang, M. Dai, D. R. Reichman, R. Tempelaar, L. Huang and F. C. Spano, *Journal of Physical Chemistry C*, 2019, **123**, 20567–20578.

141   A. M. Castilla, E. R. Draper, M. C. Nolan, C. Brasnett, A. Seddon, L. L. E. Mears, N. Cowieson and D. J. Adams, *Sci Rep*, 2017, **7**, 1–10.

142   E. R. Draper, J. R. Lee, M. Wallace, F. Jäckel, A. J. Cowan and D. J. Adams, *Chem Sci*, 2016, **7**, 6499–6505.

143   E. R. Draper, J. J. Walsh, T. O. McDonald, M. A. Zwijnenburg, P. J. Cameron, A. J. Cowan and D. J. Adams, *J. Mater. Chem. C*, 2014, **2**, 5570–5575.

144   E. R. Draper, O. O. Mykhaylyk and D. J. Adams, *Chemical Communications*, 2016, **52**, 6934–6937.

145   E. R. Draper, M. Wallace, D. Honecker and D. J. Adams, *Chemical Communications*, 2018, **54**, 10977–10980.

146   J. G. Egan, G. Brodie, D. McDowall, A. J. Smith, C. J. C. Edwards-Gayle and E. R. Draper, *Mater Adv*, 2021, **2**, 5248–5253.

147   G. Klebe, F. Graser, E. Hädicke and J. Berndt, *Acta Crystallogr B*, 1989, **45**, 69–77.

148   Z. Chen, B. Fimmel and F. Würthner, *Org Biomol Chem*, 2012, **10**, 5845–5855.

149   Z. Chen, V. Stepanenko, V. Dehm, P. Prins, L. D. A. Siebbeles, J. Seibt, P. Marquetand, V. Engel and F. Würthner, *Chemistry - A European Journal*, 2007, **13**, 436–449.

150   G. L. Eakins, J. K. Gallaher, R. A. Keyzers, A. Falber, J. E. A. Webb, A. Laos, Y. Tidhar, H. Weissman, B. Rybtchinski, P. Thordarson and J. M. Hodgkiss, *Journal of Physical Chemistry B*, 2014, **118**, 8642–8651.

151   C. Lin, T. Kim, J. D. Schultz, R. M. Young and M. R. Wasielewski, *Nat Chem*, 2022, **14**, 786–793.

152   D. McDowall, M. Walker, M. Vassalli, M. Cantini, N. Khunti, C. J. C. Edwards-Gayle, N. Cowieson and D. J. Adams, *Chemical Communications*, 2021, **57**, 8782–8785.

153   L. Hu, R. Zhang and Q. Chen, *Nanoscale*, 2014, 6, 14064–14105.

154   L. Jiang, H. Dong and W. Hu, *Soft Matter*, 2011, 7, 1615–1630.

155   Y. Shoji, M. Yoshio, T. Yasuda, M. Funahashi and T. Kato, *J Mater Chem*, 2010, **20**, 173–179.

156   V. Duzhko, J. Du, C. A. Zorman and K. D. Singer, *Journal of Physical Chemistry C*, 2008, **112**, 12081–12084.

157   S. Zhang, M. A. Greenfield, A. Mata, L. C. Palmer, R. Bitton, J. R. Mantei, C. Aparicio, M. O. de La Cruz and S. I. Stupp, *Nat Mater*, 2010, **9**, 594–601.

158   M. M. L. Arras, C. Grasl, H. Bergmeister and H. Schima, *Sci Technol Adv Mater*, 2012, **13**, 1.

159   M. Abramowitz and M. W. Davidson, Optical Birefringence, https://www.olympus-lifescience.com/en/microscope-resource/primer/lightandcolor/birefringence/.

160   M. Koch, M. Myahkostupov, D. G. Oblinsky, S. Wang, S. Garakyaraghi, F. N. Castellano and G. D. Scholes, *J Am Chem Soc*, 2017, **139**, 5530–5537.

161   J. M. Alzola, N. A. Tcyrulnikov, P. J. Brown, T. J. Marks, M. R. Wasielewski and R. M. Young, *Journal of Physical Chemistry A*, 2021, **125**, 7633–7643.

162   E. Sebastian and M. Hariharan, *J Am Chem Soc*, 2021, **143**, 13769–13781.

163   J. M. Lim, P. Kim, M. C. Yoon, J. Sung, V. Dehm, Z. Chen, F. Würthner and D. Kim, *Chem Sci*, 2013, **4**, 388–397.

164   C. Rehhagen, M. Stolte, S. Herbst, M. Hecht, S. Lochbrunner, F. Würthner and F. Fennel, *Journal of Physical Chemistry Letters*, 2020, **11**, 6612–6617.

165   H. Khandelwal, A. R. Mallia, R. T. Cheriya and M. Hariharan, *Physical Chemistry Chemical Physics*, 2012, **14**, 15282–15285.

166   C. E. Ramirez, S. Chen, N. E. Powers-Riggs, I. Schlesinger, R. M. Young and M. R. Wasielewski, *J Am Chem Soc*, 2020, **142**, 18243–18250.

167   V. Markovic, D. Villamaina, I. Barabanov, L. M. Lawson Daku and E. Vauthey, *Angewandte Chemie - International Edition*, 2011, **50**, 7596–7598.

168   E. Sebastian and M. Hariharan, *ACS Energy Lett*, 2022, **7**, 696–711.

169   J. Kong, W. Zhang, G. Li, D. Huo, Y. Guo, X. Niu, Y. Wan, B. Tang and A. Xia, *Journal of Physical Chemistry Letters*, 2020, **11**, 10329–10339.

170   E. R. Draper, B. J. Greeves, M. Barrow, R. Schweins, M. A. Zwijnenburg and D. J. Adams, *Chem*, 2017, **2**, 716–731.

171   Y. Wu, R. M. Young, M. Frasconi, S. T. Schneebeli, P. Spenst, D. M. Gardner, K. E. Brown, F. Würthner, J. F. Stoddart and M. R. Wasielewski, *J Am Chem Soc*, 2015, **137**, 13236–13239.

172   F. Würthner, C. Thalacker, S. Diele and C. Tschierske, *Chemistry - A European Journal*, 2001, **7**, 2245–2253.

173   M. K. Brennaman, M. R. Norris, M. K. Gish, E. M. Grumstrup, L. Alibabaei, D. L. Ashford, A. M. Lapides, J. M. Papanikolas, J. L. Templeton and T. J. Meyer, *Journal of Physical Chemistry Letters*, 2015, **6**, 4736–4742.

174 W. Kim, A. Nowak-Król, Y. Hong, F. Schlosser, F. Würthner and D. Kim, *Journal of Physical Chemistry Letters*, 2019, **10**, 1919–1927.

175 B. S. Veldkamp, W. S. Han, S. M. Dyar, S. W. Eaton, M. A. Ratner and M. R. Wasielewski, *Energy Environ Sci*, 2013, **6**, 1917–1928.

176 J. Sung, A. Nowak-Król, F. Schlosser, B. Fimmel, W. Kim, D. Kim and F. Würthner, *J Am Chem Soc*, 2016, **138**, 9029–9032.

177 M. Son, K. H. Park, C. Shao, F. Würthner and D. Kim, *Journal of Physical Chemistry Letters*, 2014, **5**, 3601–3607.

178 R. E. Cook, B. T. Phelan, R. J. Kamire, M. B. Majewski, R. M. Young and M. R. Wasielewski, *Journal of Physical Chemistry A*, 2017, **121**, 1607–1615.

179 J. M. Giaimo, A. v. Gusev and M. R. Wasielewski, *J Am Chem Soc*, 2002, **124**, 8530–8531.

180 W. Kim, A. Nowak-Król, Y. Hong, F. Schlosser, F. Würthner and D. Kim, *Journal of Physical Chemistry Letters*, 2019, **10**, 1919–1927.

181 A. Nowak-Król, B. Fimmel, M. Son, D. Kim and F. Würthner, *Faraday Discuss*, 2015, **185**, 507–527.

182 A. F. Coleman, M. Chen, J. Zhou, J. Y. Shin, Y. Wu, R. M. Young and M. R. Wasielewski, *Journal of Physical Chemistry C*, 2020, **124**, 10408–10419.

183 C. L. Smith, L. L. E. Mears, B. J. Greeves, E. R. Draper, J. Doutch, D. J. Adams and A. J. Cowan, *Physical Chemistry Chemical Physics*, 2019, **21**, 26466–26476.

184 W. Kim, A. Nowak-Król, Y. Hong, F. Schlosser, F. Würthner and D. Kim, *Journal of Physical Chemistry Letters*, 2019, **10**, 1919–1927.

185 K. E. Brown, W. A. Salamant, L. E. Shoer, R. M. Young and M. R. Wasielewski, *Journal of Physical Chemistry Letters*, 2014, **5**, 2588–2593.

186 N. S. Lewis and D. G. Nocera, *Proc Natl Acad Sci U S A*, 2006, 103, 15729–15735.

187 P. Dimitriou and T. Tsujimura, *Int J Hydrogen Energy*, 2017, **42**, 24470–24486.

188 J. S. Wallace and C. A. Ward, *Int. J. Hydrogen Energy,* 1983, **8**, 255–268.

189 B. Turan, J. P. Becker, F. Urbain, F. Finger, U. Rau and S. Haas, *Nat Commun*, 2016, **7**, 1–9.

190 B. Eftekharinia, A. Moshaii, A. Dabirian and N. S. Vayghan, *J Mater Chem A Mater*, 2017, **5**, 3412–3424.

191 Z. Wang, X. Zong, Y. Gao, J. Han, Z. Xu, Z. Li, C. Ding, S. Wang and C. Li, *ACS Appl Mater Interfaces*, 2017, **9**, 30696–30702.

192 Z. Zhang and P. Wang, *Energy Environ Sci*, 2012, **5**, 6506–6512.

193 Y. He, T. Hamann and D. Wang, *Chem Soc Rev*, 2019, 48, 2182–2215.

194 I. Holmes-Gentle, F. Bedoya-Lora, F. Alhersh and K. Hellgardt, *Journal of Physical Chemistry C*, 2018, **123**, 17–28.

195 A. J. Cowan and J. R. Durrant, *Chem Soc Rev*, 2013, **42**, 2281–2293.

196 P. Bornoz, M. S. Prévot, X. Yu, N. Guijarro and K. Sivula, *J Am Chem Soc*, 2015, **137**, 15338–15341.

197 H. J. Lee, J. Kim, A. Abudulimu, J. Cabanillas-Gonzalez, P. C. Nandajan, J. Gierschner, L. Lüer and S. Y. Park, *Journal of Physical Chemistry C*, 2020, **124**, 6971–6978.

198 L. Meng, Y. Zhang, X. Wan, C. Li, X. Zhang, Y. Wang, X. Ke, Z. Xiao, L. Ding, R. Xia, H. L. Yip, Y. Cao and Y. Chen, *Science (1979)*, 2018, **361**, 1094–1098.

199 F. Li, K. Fan, B. Xu, E. Gabrielsson, Q. Daniel, L. Li and L. Sun, *J Am Chem Soc*, 2015, **137**, 9153–9159.

200 Y. H. Lai, D. W. Palm and E. Reisner, *Adv Energy Mater*, 2015, **5**, 1–11.

201 M. G. Walter, E. L. Warren, J. R. McKone, S. W. Boettcher, Q. Mi, E. A. Santori and N. S. Lewis, *Chem Rev*, 2010, **110**, 6446–6473.

202 K. Maeda and K. Domen, *Journal of Physical Chemistry Letters*, 2010, **1**, 2655–2661.

203 H. Tributsch, *RSC Energy and Environment Series*, 2018, **2018-Janua**, 1–28.

204 C. Xiang, K. M. Papadantonakis and N. S. Lewis, *Mater Horiz*, 2016, **3**, 169–173.

205   A. S. Weingarten, R. V. Kazantsev, L. C. Palmer, M. McClendon, A. R. Koltonow, A. P. S. Samuel, D. J. Kiebala, M. R. Wasielewski and S. I. Stupp, *Nat Chem*, 2014, **6**, 964–970.

206   N. Grabicki, O. Dumele, H. Sai, N. E. Powers-Riggs, B. T. Phelan, M. H. Sangji, C. T. Chapman, J. v Passarelli, A. J. Dannenhoffer, M. R. Wasielewski and S. I. Stupp, *Chemistry of Materials*, 2021, **33**, 706–718.

207   F. Zhang, Y. Ma, Y. Chi, H. Yu, Y. Li, T. Jiang, X. Wei and J. Shi, *Sci Rep*, 2018, **8**, 1–11.

208   T. M. Halasinski, J. L. Weisman, R. Ruiterkamp, T. J. Lee, F. Salama and M. Head-Gordon, *Journal of Physical Chemistry A*, 2003, **107**, 3660–3669.

209   L. Yao, A. Rahmanudin, N. Guijarro and K. Sivula, *Adv Energy Mater*, 2018, **8**, 1802585.

210   D. Zhang, H. H. Cho, J. H. Yum, M. Mensi and K. Sivula, *Adv Energy Mater*, 2022, **12**, 2202363.

211   Z. Lin, Y. Wang, Z. Peng, Y. C. Huang, F. Meng, J. L. Chen, C. L. Dong, Q. Zhang, R. Wang, D. Zhao, J. Chen, L. Gu and S. Shen, *Adv Energy Mater*, 2022, **12**, 2200716.

212   J. T. Kirner, J. J. Stracke, B. A. Gregg and R. G. Finke, *ACS Appl Mater Interfaces*, 2014, **6**, 13367–13377.

213   J. T. Kirner and R. G. Finke, *ACS Appl Mater Interfaces*, 2017, **9**, 27625–27637.

214   C. F. Jewell, A. Subramanian, C.-Y. Nam and R. G. Finke, *Sustain Energy Fuels*, 2021, **5**, 5257–5269.

215   T. Abe, K. Nagai, S. Kabutomori, M. Kaneko, A. Tajiri and T. Norimatsu, *Angewandte Chemie - International Edition*, 2006, **45**, 2778–2781.

216   T. Abe, K. Nagai, T. Ogiwara, S. Ogasawara, M. Kaneko, A. Tajiri and T. Norimatsu, *Journal of Electroanalytical Chemistry*, 2006, **587**, 127–132.

217   M. L. Rigsby, R. D. Britt, J. B. Gerken, J. Y. C. Chen, J. G. McAlpin, S. S. Stahl and W. H. Casey, *J Am Chem Soc*, 2011, **133**, 14431–14442.

218   M. W. Kanan and D. G. Nocera, *Science*, 2008, **321**, 1072–1075.

219   C. F. Jewell, A. Subramanian, C. Y. Nam and R. G. Finke, *ACS Appl Mater Interfaces*, 2022, **14**, 25326–25336.

220   M. Huynh, D. K. Bediako, Y. Liu and D. G. Nocera, *Journal of Physical Chemistry C*, 2014, **118**, 17142–17152.

221   Y. Zhao, N. M. Vargas-Barbosa, E. A. Hernandez-Pagan and T. E. Mallouk, *Small*, 2011, **7**, 2087–2093.

222   R. Abu-Eittah, A. Obaid, S. Basahl and E. Diefallah, *Bull Chem Soc Jpn*, 1988, **61**, 2609–2613.

223   S. Roy, D. Kumar Maiti, S. Panigrahi, D. Basak and A. Banerjee, *RSC Adv*, 2012, **2**, 11053–11060.

224   K. E. Knowles, M. D. Koch and J. L. Shelton, *J Mater Chem C Mater*, 2018, **6**, 11853–11867.

225   M. Forster, D. W. F. Cheung, A. M. Gardner and A. J. Cowan, *Journal of Chemical Physics*, 2020, 153, 1.